# Contents

# Figures

# Tables

# 8.0 Seismic Source Characterization

This chapter provides a description of the elements of the SSC model that are used as input to the Hanford PSHA. The chapter begins with an overview of the SSC model and the approach taken to develop the model. This is followed by a detailed description of each element of the model: the characteristics of the Cascadia subduction zone sources, crustal seismic source zones, and the fault sources. The goal in this chapter is to provide the reader with a full understanding of all elements of the SSC model that are included in the HID (hazard input document) provided in Appendix D.

## 8.1 Building the SSC Model: Overview and Approach

This section describes the conceptual framework for the SSC model, the manner in which data were evaluated by the SSC TI Team, the types of seismic sources that are included in the model, an overview of the sources that are characterized, and the structure of the logic tree that defines the SSC model.

An SSC model in a PSHA defines the seismogenic potential, locations, sizes, and rates of future earthquakes. To be useful, the SSC model must include elements that are appropriate to the tectonic environment for which it is developed. For example, the Hanford Site lies within a tectonic environment that is adjacent to major plate boundaries, but has generally undergone more recent tectonic deformation than the stable continental region to the east. As a result, there is generally a lack of a clear definition of the causative faults giving rise to the observed seismicity, so the SSC methodology should include our knowledge of fault location and behavior as well as seismic source zones to account for the unknown locations of the faults giving rise to the "background" seismicity. Similarly, geodetic data on contemporary crustal strain are currently limited in their duration; in addition, available physical models are unable to make a reliable association between geodetic strain and earthquake processes. Therefore, although such data may be useful in assisting with the evaluation of seismic source characteristics, the methodology should not rely on knowledge of the relationship between short-term crustal strain data and future earthquake characteristics.

Mindful of the tectonic setting and precedents for methods available to identify and characterize seismic sources within similar tectonic environments, an approach was taken that begins with consideration of hazard-significant technical issues; prioritization of the data according to their importance to addressing important SSC issues; compilation of available data to address the issues; gathering and evaluation of new data; evaluation of applicable data, models, and methods; identification of seismic sources according to defined criteria; and characterization of each seismic source, including the associated uncertainties using a logic-tree approach. An overview of this approach to developing the SSC model is given in Sections 8.1.1 through 8.1.5.

### 8.1.1 Criteria for Defining Seismic Sources

The SSC process for the Hanford PSHA began with the identification of criteria that would be used by the TI Team to define seismic sources. These criteria were identified based on due consideration of the tectonic regime, the types of seismic sources that might be present (e.g., fault sources and source zones), and precedent from recent SSC models developed for similar tectonic environments and for

nuclear facilities. Based on these considerations, unique seismic sources are defined to account for distinct spatial differences in the following criteria:

- earthquake recurrence rate
- maximum earthquake magnitude (Mmax)
- expected future earthquake characteristics (e.g., style of faulting, rupture orientation, seismogenic thickness)
- probability that a fault is seismogenic.

By "differences," it is meant that a given potential seismic source would differ significantly in one or more of these criteria from its neighbor such that identifying a unique seismic source is justified. It is important to note that, although the criteria are defensible because they are related to seismic source characteristics that can be important to seismic hazard, they do not lead to a unique set of seismic sources. The definition of a source zone boundary, for example, is interpretive and based on the expert judgment of the TI Team given the available data. Therefore, given a particular set of data and a specific set of seismic source criteria, there is no assurance that different experts will identify seismic sources in exactly the same way. The goal then should be to completely document the criteria that were used to define seismic sources and to document on a source-by-source basis the technical justification for the seismic sources that are included in the SSC model.

Examples will assist in illustrating the application of the seismic source criteria for the Hanford SSC model. To begin, consider the Hanford region and the first criterion of differences in earthquake recurrence rate. The methodologies used to characterize earthquake recurrence for the SSC model are described in Sections 8.3.2.8 and 8.4.3.7. In general, the record of past earthquakes is obtained from the historical/instrumental catalog and from the paleoseismic record of prehistoric earthquakes. For a fault source such as the faults identified in the Yakima Fold Belt (YFB), fault slip rate and other paleoseismic evidence are used to define the source's recurrence rate and that it is distinct from the seismic source zone within which it lies. Another example of identifying distinct seismic sources based on differences in recurrence would be observed differences in the spatial distribution and density (number of events per unit area) from one region to another. These differences can be accounted for either by spatial smoothing of recurrence parameters or by drawing a source boundary between the regions. The choice of either approach is based on the judgment of the TI Team and can include considerations such as uncertainties in the locations of observed epicenters, distance from the source to the site of interest, and the magnitudes of observed seismicity. Because both approaches are identifying spatial changes in recurrence rate from one region to another, the choice of one approach over the other (or the weights associated with each approach, if they are both included as alternatives in the SSC model) should have little hazard significance. Embedded within the concept of either spatial smoothing or drawing the source boundary is the notion of spatial stationarity; that is, the pattern of past earthquakes is a predictor of the pattern of future earthquakes. Studies in intraplate tectonic settings have concluded that this is a reasonable interpretation (Kafka 2007; Tiampo et al. 2010). Further, because the historical record of observed earthquakes is short relative to the recurrence intervals for large-magnitude earthquakes, there is an assumption that the spatial distribution of observed smaller-magnitude earthquakes is related to the spatial distribution of larger magnitude earthquakes. One consideration with regard to the decision about whether or not a source boundary should be drawn, which is described in Section 8.3.2.9, is that of the spatial homogeneity of epicenters within a seismic source zone (Musson 2000). Finally, because the observed record of moderate-to-large magnitude earthquakes is typically short relative to the recurrence intervals for those earthquakes, the use of seismotectonic features and boundaries can serve as indicators

of potential differences in the rates of future earthquakes. Such features may also provide indications of potential differences in Mmax and/or future earthquake characteristics, as discussed below.

A second criterion for subdividing the region into seismic sources is differences in Mmax. The methodologies used to assess Mmax for the SSC model are described in Sections 8.3.2.7 and 8.4.3.8. The assessment of Mmax for fault sources is based on consideration of the dimensions of possible future ruptures and models that relate the magnitude of the characteristic magnitude (Mchar) to Mmax. As discussed in Section 8.3.1, two types of seismic source zones are identified depending on whether or not fault sources are characterized within the boundaries of the seismic source zone of interest. The Mmax assessment for the fault sources within a seismic source zone places an upper limit on the Mmax for the source zone. Thus, the differences in Mmax between the fault sources and the host zone for those fault sources is a reason for calling out the fault sources specifically in the SSC model.

A third criterion for identifying distinct seismic sources in the Hanford region is the expected differences in future earthquake characteristics, such as the style of faulting, orientation of earthquake ruptures (strike and dip), seismogenic thickness, and depth distribution. The methodologies used to characterize the future earthquake characteristics for the Hanford PSHA seismic source zones are described in Section 8.3.2.5. In seismic hazard models, future earthquakes are modeled as faults having finite dimension, magnitude-dependent rupture dimensions, orientations, and depth extent. This is because these characteristics are important to modern ground motion prediction equations, including those that were developed for the Hanford PSHA. In some cases, differences in future earthquake characteristics provided a basis for identifying the boundary between seismic source zones.

A fourth criterion is the identification of particular faults that are assessed to have the potential to localize seismicity; that is, they are assessed to have a seismogenic probability p[S] greater than zero. The criteria for evaluating p[S] are described in Section 8.4.1. If a fault is assessed to be seismogenic, then future earthquakes will be localized on the fault and its source characteristics (e.g., recurrence rate, Mmax, geometry) will be specific to that fault. If the feature has a p[S] less than 1.0, then there is a finite probability, 1–p[S], that the fault is not seismogenic, future earthquakes will not be localized on the fault, and only the seismic source zone within which the fault lies will be the source of seismicity in the vicinity of the fault.

### 8.1.2 Data Evaluation Process

As defined in NUREG-2117 (NRC 2012b), the goal of a Senior Seismic Hazard Analysis Committee (SSHAC) process is the following:

> "The fundamental goal of a SSHAC process is to properly carry out and completely document the activities of evaluation and integration, defined as:
>
> *Evaluation*: The consideration of the complete set of data, models, and methods proposed by the larger technical community that are relevant to the hazard analysis.
>
> *Integration*: Representing the center, body, and range of technically defensible interpretations in light of the evaluation process (i.e., informed by the assessment of existing data, models, and methods)."

Following this paradigm, the activities of the seismic source characterization began the evaluation process by identifying hazard-significant SSC issues, identifying available data, and augmenting the available database by gathering new data. This process was enhanced by the activities associated with Workshop 1 (WS1) during which the results of hazard sensitivity analyses were presented as a means of identifying hazard-significant SSC issues, and by the presentations by numerous resource experts of the wide range of geologic, seismicity, and geophysical data that were available for potential use by the TI Team (PNNL 2013a).

The goal of the SSC process is to develop an SSC model that is used in the PSHA. Because the ultimate use of the model is for hazard analyses, it is important that the development process be conducted using a hazard-informed approach. Thus, an early step in the project entailed hazard calculations conducted to identify hazard-sensitive SSC issues, as well as consideration of the results of other PSHAs regarding hazard importance (Section 8.3.3). As discerned by the TI Team from the hazard calculations and sensitivity analyses presented and discussed during WS1, the evaluation of the relative hazard significance of SSC issues was as follows:

- Relatively High Significance
  - sources within about 20 km from the site (boundary of the Hanford Site)
  - drivers of recurrence of M 5.5 to 6.5 (slip rates, paleoseismic evidence, observed seismicity)
  - p[S] of Yakima folds and the methods used to assess activity
  - source zone(s) constrained by geodetic deformation rate
- Relatively Moderate Significance
  - thick vs. thin-skin structural model (downdip geometries of faults)
  - potential eastern extension of Yakima Ridge
  - sources within 20−50 km
  - Cascadia subduction zone (CSZ) plate interface for long-period ground motions
- Relatively Low Significance
  - CSZ sources, including eastern extent of plate interface
  - sources beyond about 50 km
  - basement source zones characterized by observed seismicity.

In addition to the site-specific hazard sensitivity calculations conducted prior to WS1, the SSC TI Team also considered the results of sensitivity analyses conducted for other PSHAs, both at the Hanford Site and in similar tectonic regions. For example, other such studies show that the detailed characteristics of nearby faults are often important, while the characteristics of faults that lie at greater distances are not important. Typically, hazard studies also show that the seismic source zone that hosts the site is often a significant contributor to the hazard at annual frequencies of interest for a nuclear plant. In turn, the earthquake recurrence rate of the host zone and those aspects of the SSC model that are important to estimating that recurrence rate (e.g., the earthquake catalog and associated magnitude conversions, catalog completeness) are also important and hazard-significant.

With knowledge of the hazard-significant issues, the TI Team then embarked on the process of data compilation that marks the evaluation part of a SSHAC process. The evaluation process consists of consideration of the data, models, and methods that have been developed by the larger technical community. Most of the data that are included in the project database consist of reports and professional

publications that relate to seismic source characteristics both locally, regionally, and by analogy to other parts of the world. To organize the data topically, an outline of topics and subtopics was developed into which all SSC data could then be assigned.

A key activity in the process of evaluation is the identification of data that have been developed by the larger technical community and WS1 was important in that data evaluation process. A number of resource experts participated in the workshop and presented their particular data sets to the TI Team (PNNL 2013a). The data that were identified during the workshop included the following:

- seismic reflection and refraction data
- compilations of regional and local geologic borehole data
- geodetic data
- potential field geophysical data
- paleoseismic data
- Quaternary geologic data
- crustal structure interpretations
- historical and instrumental seismicity data
- earthquake focal mechanisms
- Hanford Quaternary mapping database.

As part of their presentations, each resource expert provided a list of pertinent references that they felt would be useful to the TI Team. Likewise, the proponent and resource experts who discussed their models and methods during Workshop 2 (WS2) provided reference lists that were a useful resource to the TI Team's identification of data developed by the larger technical community (PNNL 2013b). The identified data also provided a useful framework for focusing the ongoing and new data collection activities in the areas where fewer data currently existed and where new data would best supplement the existing data.

An important part of the data evaluation process is the documentation of the data that were considered by the TI Team during the course of the study. For the SSC model, this documentation was accomplished in two ways: in this project report and through the use of data tables (described in Section 8.1.2.1 below).

The data, models, and methods that were used by the TI Team directly in the development of the SSC model are cited, as appropriate, in the respective parts of this PSHA report that relate to the various aspects of the SSC model. This includes the information that was compiled as part of the project database as well as the new data that were collected as part of the Hanford PSHA project, which are included as appendices to the report. All references cited are included in the Hanford PSHA project portal in the "HPSHA References" folder.

#### 8.1.2.1 Data Tables

With their introduction under the Central and Eastern United States (CEUS) SSC project (NRC 2012a), data tables have been used to assist in the documentation of the SSC data evaluation process. The data tables begin with the basic reference information for data that were identified by the TI Team and an identification of the potential relevance of each data source to the SSC model. For data that were actually used in the construction of the SSC model, additional information is included in the data tables to document the quality of the data, their relevance to the SSC model, and the degree of reliance placed on

each data source. The data tables for the Hanford SSC model resided on the Hanford PSHA project portal during the time of their development to facilitate the entry of information by the SSC TI Team members. The tables are currently held as data files within Appendix G of this report.

The data tables represent the SSC information sources that were considered during the evaluation and integration phases of the project. Each reference is identified by the basic information:

- Document or Report Number
- Author
- Year
- Full reference citation
- Link to abstract/file (for federally funded research and/or publicly released studies).

References are further characterized with regard to the specific topics and subtopics to which they pertain. A text box was available to explain the basis for assigning a particular reference to a subtopic (listed below) and to explain the potential relevance of that reference to the SSC model, as needed:

- Neotectonic Setting
  - Tectonic Stress Regime
  - Plate Motion Models
  - Geodetic Data
  - Uplift Mechanisms and Rates Data
  - Paleoseismic Evidence
  - Neotectonic Setting − Other
- Geophysical Data and Crustal Structure
  - Gravity and Magnetic Data
  - Seismic Refraction and Reflection Profiling
  - Basin Geometry/Sub-Basalt Structure
- Pliocene-Quaternary
  - Stratigraphy
  - Geomorphology
  - Flood Deposits-History
  - Geochronology Studies
  - Pliocene-Quaternary − Other
- Previous SSC Models
  - MidC Project
- Regional Geologic and Tectonic Setting
  - Tectonic Events
  - Mapped Locations of Cratons and Orogenic Belts, Basement Structures and Tectonic Boundaries
  - Stratigraphy of CRB (Columbia River Basalt)
  - Regional Geologic and Tectonic Setting − Other

- Regional Structures
  - Structures and Structural Analyses
  - Bedrock Structural Models
  - Yakima Fold and Thrust Belt-General
  - YFTB-Ahtanum-Rattlesnake Hills
  - YFTB-Columbia Hills
  - YFTB- Frenchman Hills
  - YFTB-Horse Heaven Hills
  - YFTB-Manastash Ridge
  - YFTB-Rattlesnake Mountain
  - YFTB-Saddle Mountains
  - YFTB-Toppenish Ridge
  - YFTB-Umtanum
  - YFTB-Wallula Fault
  - Badger Mountain Anticline
  - Pinto Fault
  - Regional Structures − Other
- Future Earthquake Characteristics
  - Rupture Geometry
  - Seismogenic Thickness
  - Style of Faulting
  - Future Earthquake Characteristics − Other
- SSC Framework
  - Seismic Source
  - Spatial Stationarity
  - Use of Geodetic/Strain Rates
- Earthquake Catalog Data
  - Earthquake Epicenter Locations
  - Earthquake Depths
- Earthquake Catalog Processing
- Recurrence Calculations
  - Recurrence Models
  - Mmax
  - Calculation of Recurrence Parameters
  - Recurrence Calculations − Other
- Cascadia Subduction Zone
  - Downdip Extent of Interface

The very nature of the SSC activity and the models and parameters that compose an SSC model are multidisciplinary and involve a wide range of potential data sources. Thus, it is not unusual for a particular journal article on, say, the regional geologic setting to not contain much information that is pertinent to seismic source characterization. Likewise, some papers are based on data that are of poor quality or that have been superseded by subsequent studies. In these cases, the potential relevance to seismic source characterization would be included in the relevant data table to document the fact that the data were considered, but the answer to whether the data were relied upon for the SSC model would be "no." In cases where the data were relied upon, additional information is provided, as described below.

A subset of the references was actually used and relied upon during the construction of the SSC model. The next field of the data table asks whether or not the data were used in developing the SSC model; i.e.:

- Data used in SSC Model: Yes/No.

For references that were used in the development of the SSC model, additional information is given in the data table. First, the particular element of the SSC model where the reference was used is identified and sorted according to the major elements of the SSC model. For example, if a particular paper provides information that has been used to define the boundaries of a seismic source zone, then that would be indicated here. In addition to identifying the SSC element(s) in which the data were used, the data tables also document the expert evaluator's subjective assessment of the quality of the data for the evaluation and integration for seismic source characterization (with a rating of 1 to 5) and the degree of reliance placed on the data in assessing the identified characteristic (rating of 1 to 5). This information provides important insights to readers of the report regarding which information sources are perceived to have the highest quality and were relied upon most heavily by the TI Team. The tables also provide any additional information describing the use of the information or its relevance to the SSC model, as follows:

The expert evaluator was asked to rate any of the following subtopics 1−5 where 5 is high with regard to quality and degree of reliance, and to provide any additional description or relevance.

- Fault or Seismic Source Characteristics:
  - Seismogenic Probability
  - Seismic Source or Fault Geometry
  - Recurrence/Recency & Slip Rate/Recurrence Intervals
  - Mmax
- Future Earthquake Characteristics
  - Rupture Geometry (strike, dip)
  - Style of Faulting
  - Seismogenic Thickness.

### 8.1.3 Evaluation of Models and Methods

In addition to the compilation and evaluation of data, the evaluation process includes consideration of the models and methods that are currently proposed by members of the larger technical community. For this activity to occur, the TI Team must review the professional literature, draw on its experience from other PSHAs, and interact with members of the technical community. One of the key tools used in the Hanford PSHA to discuss and debate alternative models and methods was WS2 (PNNL 2013b). The

workshop was specifically designed to include proponents of alternative models and methods, as well as resource experts who could report on the viability of the alternatives based on their experience in other projects. The models and methods that were presented and discussed at the workshop were the following:

- historical seismicity of eastern Washington
- seismicity catalog analysis for the Mid-Columbia dams project (JBA 2012) and proposed approach for the Hanford PSHA
- methods for high-resolution reprocessing of network seismicity data; case histories from the Diablo Canyon project
- slip rates on Yakima folds and implications for contemporary tectonics; models of thick- and thin-skin faulting
- large-scale splay faults on a strike slip fault system: the Yakima folds
- implications of fault geometry for seismic source characterization
- SSC model developed for the Mid-Columbia dams project
- assessment of the probability of activity of Yakima folds and faults for the Mid-Columbia PSHA
- methods and criteria for assessing seismogenic potential of the faults of the YFB
- use of geodetic data in the BC Hydro project
- characterizing seismic source zones in the Mid-Columbia dams project
- use of seismicity and geodetic data for characterizing seismic source zones
- approaches to modeling fault-specific and source zone recurrence
- Quaternary study of Manastash Ridge
- applicability of Quaternary methods to the YFB
- paleoseismic studies at Wenas Valley and Boyleston Mountains; implications for other Yakima folds
- use of paleoseismic data in Hanford SSC model
- status of screening structural analyses of Yakima folds and new data collection activities
- connection of the YFB to active faults in the Puget Lowland, Washington.

To ensure that all applicable SSC issues of concern to the TI Team were addressed, each proponent and resource expert was provided with a list of questions or comments from the TI Team that were addressed during the course of the presentations. Further, adequate amounts of time were reserved on the agenda to allow for discussions among the TI Team members and the various proponent and resource experts. During these discussions, the TI Team probed the technical bases for the models and methods being proposed. Consistent with their role as expert evaluators, the TI Team also questioned the presenters about the uncertainties in their interpretations and asked them to compare their preferred models and methods with those proposed by others. All presenters were asked to provide a list of pertinent references so that the TI Team could consider these references during the course of the evaluation process.

As a result of the large range of data, models, and methods reviewed during the evaluation phase of the SSC sub-project, the TI Team was well prepared to move into the model-building integration phase of the project.

### 8.1.4 Types of Seismic Sources Identified and Characterized in the SSC Model

As discussed in Section 8.1.1, a series of criteria were identified early in the project for defining seismic sources. The advantage of identifying the criteria early is that they could then be used to prioritize the data identification process and could be included explicitly in the data evaluation process and the associated documentation in the data tables. As the project moved into the integration phase, the TI Team developed the preliminary and final SSC models by applying the seismic source criteria and arriving at a series of seismic source zones and fault sources. The conceptual bases for identifying these seismic source zones and fault sources are discussed subsequently in this section and the technical details are given in Sections 8.2, 8.3, and 8.4 of this report.

For clarity and consistency, the term "Yakima Fold Belt" or YFB is used to describe the tectonic region that includes the faults and folds that have traditionally been called the Yakima folds. The term "Yakima Fold and Thrust Belt" or YFTB is used exclusively to refer to the name of the seismic source zone, so it will typically be followed by the word "zone." The seismic source zones are defined and characterized in Section 8.2.

Three sets of seismic sources are included in the SSC model and the names of the sources are given below:

- Cascadia subduction zone (discussed in Section 8.2)
  - Plate interface source
  - Intraslab source
- Seismic source zones (discussed in Section 8.3)
  - Yakima Fold and Thrust Belt (YFTB)
  - Zone B
  - Zone C
  - Zone D
- Fault sources (discussed in Section 8.4)
  - Ahtanum Ridge (AR)
  - Arlington (AF)
  - Cleman Mountain (CM)
  - Columbia Hills (CH)
  - Frenchman Hills (FH)
  - Horn Rapids Fault (HR)
  - Horse Heaven Hills (HHH)
  - Laurel (LF)
  - Luna Butte (LB)
  - Manastash Ridge (MR)
  - Maupin (MF)
  - Rattles of the Rattlesnake-Wallula (RAW) alignment
  - Rattlesnake Hills (RH)
  - Rattlesnake Mountain (RM)
  - Saddle Mountains (SM)
  - Seattle Fault (SFZ)

- Selah Butte (SB)
- Toppenish Ridge (TR)
- Umtanum Ridge (UR)
- Wallula Fault (WF)
- Yakima Ridge (YR).

As discussed in Section 8.1.1, the process of identifying and characterizing seismic sources for the SSC model was hazard-informed such that highest priority would be given to aspects of the model that had the highest potential hazard significance. Likewise, the level of complexity of the SSC model was consistent with current knowledge and importance to hazard. For example, hazard sensitivity analyses presented at WS1 (see V. Montaldo-Falero presentation at WS1) (PNNL 2013a) show that the host zone is the most important source to the mean hazard estimates and, as a result, details of the source geometry could be important to the calculated hazard. Accordingly, uncertainties in future earthquake characteristics within the YFTB zone, which hosts the Hanford Site, such as the sense of slip and geometries of future ruptures are included explicitly in the SSC model. Conversely, uncertainties in the detailed characterization of more distant source zones are not included in the model because of the lack of hazard significance. Likewise, any attempt to identify and characterize more distant fault sources is not needed due to the dominant contribution that the nearby faults make to the hazard.

The region over which the SSC model was developed was designed to extend somewhat beyond the distances that would be expected to contribute significantly to the site hazard, based on the hazard sensitivity analyses conducted prior to WS1 and confirmed by sensitivity analyses conducted using the preliminary SSC model prior to Workshop 3 (WS3). For example, hazard sensitivity analyses show that the contribution of source Zones B, C, and D is very low, so that they would not necessarily need to be included in the model. Nevertheless, they are included if only to demonstrate that all potentially significant seismic sources are part of the SSC model.

Consistent with the definition of seismic sources used in other projects (e.g., NRC 2012a; JBA 2012), the seismic sources identified in the SSC model are judged to have relatively uniform seismic source characteristics within their boundaries relative to adjacent regions. That is, unless otherwise indicated, the recurrence rate, Mmax, and future earthquake characteristics within seismic source zones, which are the criteria used to define each source in the first place, are judged to be relatively uniform within each source. An exception is the case where the spatial distribution of recurrence rate is defined by the spatial smoothing of observed seismicity. For fault sources, individual segments of faults are defined by uniform source characteristics (e.g., sense of slip, dip, slip rate).

The SSC model is based on the notion that an appropriate SSC model should be one that it is no more complex or detailed than required by the pertinent data. The conceptual framework for the seismic sources of the SSC model is described below.

#### 8.1.4.1 Cascadia Subduction Zone Sources

Sensitivity analyses conducted early in the Hanford PSHA project showed that the plate interface seismic source of the CSZ could contribute to long-period ground motions at annual frequencies of exceedance of interest to the Hanford Site. For completeness, both the plate interface and the intraslab sources are included in the SSC model. Fortunately, the recently completed SSHAC Level 3 PSHA conducted by BC Hydro (2012) provided a technically defensible source model that includes a full

characterization of uncertainties. The activities associated with the Hanford PSHA included updating the earthquake catalog and evaluating new data relative to the need to refine the BC Hydro model. Only minor revisions were necessary in light of new data to make the CSZ characterization up to date and appropriate for application to the Hanford PSHA.

#### 8.1.4.2 Seismic Source Zones

In this section the conceptual bases for the seismic source zones are discussed in general terms to familiarize the reader with the conceptual bases that were used to define the source zones in the SSC model. The detailed seismic source zone characteristics and their technical bases are given in Section 8.3. The seismic source zones defined for the SSC model are shown in Figure 8.1, together with the earthquake epicenters from the project catalog. Unless indicated otherwise, all magnitudes shown in seismicity maps and plots in this report are E[**M**] and the minimum magnitude is 1.85 (see discussion in Section 6.5.5). Two types of seismic source zones are identified: the YFTB source zone is a "background" zone to the fault sources of the YFB, and Zones B, C, and D are source zones that do not include identified fault sources. The exceptions are the Arlington, Luna Butte, Laurel, and Maupin faults that exist within the YFTB source zone and extend into adjacent Zone D. However, additional faults within Zone D have not been identified separately as fault sources. The reason for the two types of source zones is the relative contribution that nearby sources make to the hazard at the site. Sensitivity analyses show that the fault sources contribute most to the site hazard, followed by the YFTB source zone, followed by the other source zones. Because of their distance from the site, individual faults within Zones B, C, and D are not specifically identified and characterized. Rather, the faults that exist within these source zones are modeled by "virtual faults" whose locations are random within each zone and whose characteristics are assessed in the SSC model.

Unlike fault sources, which must be evaluated for their seismogenic probability (Section 8.4.1), seismic source zones are assessed to be seismogenic with a probability of unity. That is, all seismic source zones in the SSC model are judged to have the ability to generate moderate-to-large ($M \geq 5$) earthquakes. Consistent with current SSC practice for PSHAs and consistent with the ground motion prediction equations developed for the Hanford PSHA, the occurrence of future earthquakes within seismic source zones is modeled by virtual faults that have random locations within the zone. The future earthquake characteristics on the virtual faults are modeled by their style of faulting, 3-D rupture geometry, magnitude-dependent rupture dimensions, and relationship with zone boundaries (see Section 8.3.2). Thus, although any individual mapped fault within a seismic source zone would not necessarily be considered a localizer of seismicity, the characteristics of the modeled virtual faults within the zone incorporate source-specific seismotectonic information.

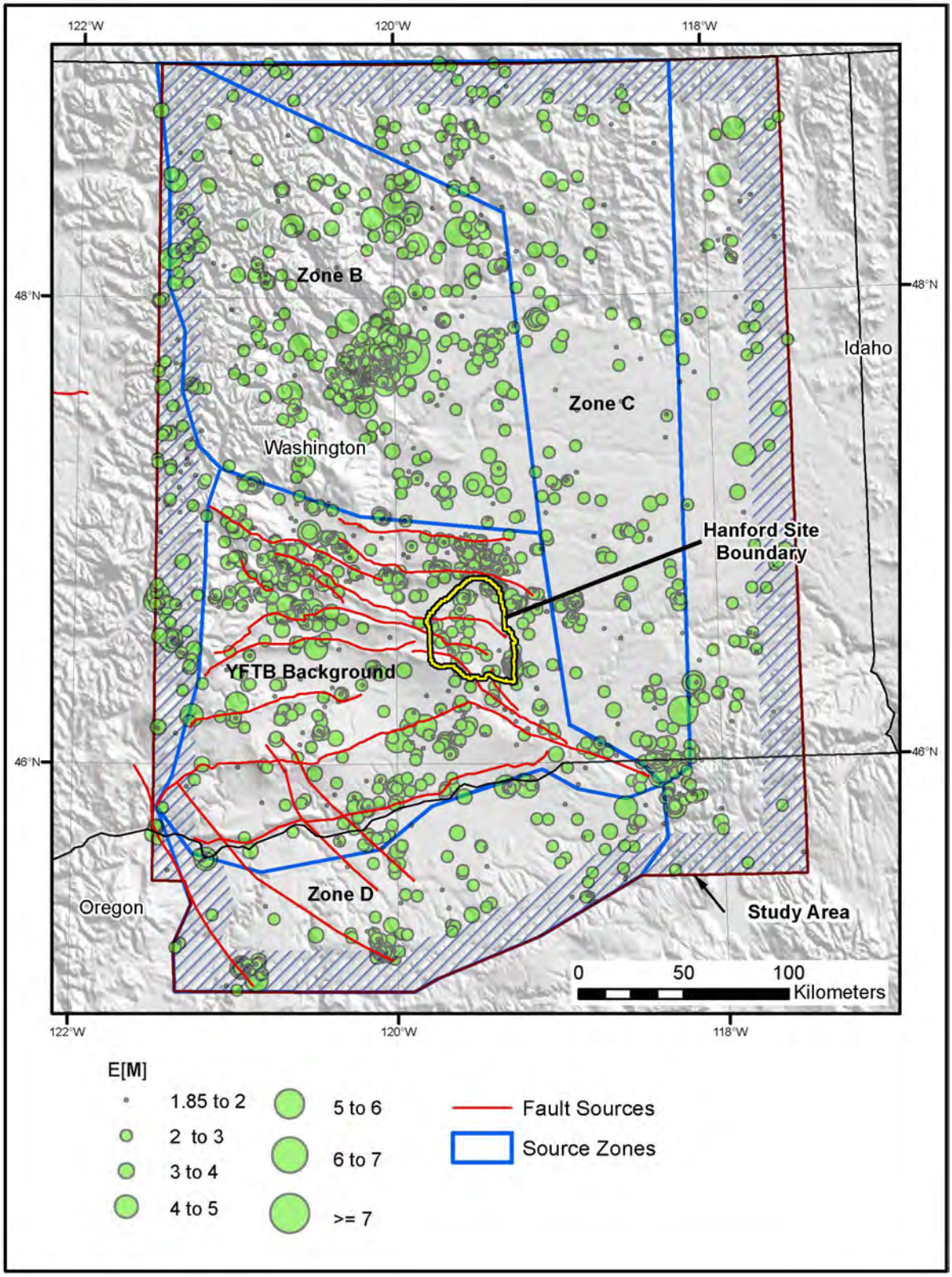


**Figure 8.1**. Seismic source zones characterized in the SSC model and earthquake epicenters in the Hanford PSHA crustal catalog having E[**M**] ≥ 1.85. Fault sources are also shown by the red lines.

Important SSC characteristics assessed for each source zone are their Mmax, recurrence rates, and spatial variation in recurrence parameters. As discussed in Section 8.3.2, these assessments are source-zone specific and account for the specific data differences among the zones. In the case of the YFTB source zone, the fault sources within the zone are characterized separately, thus leaving a background source zone whose Mmax is judged to be somewhat lower than the Mmax distributions for the other source zones. This is because the faults whose dimensions would suggest their ability to generate larger earthquakes have not been specified in the other source zones. In all cases, the assessment of earthquake recurrence incorporates fully the earthquake catalog, uncertainties in the magnitude estimates for each event, incompleteness of the record, and the contribution from dependent events (foreshocks and aftershocks). In addition, an assessment was made of the spatial homogeneity of the observed earthquake epicenters to discern whether or not spatial variations of the activity rate (a-values) should be modeled using a spatial smoothing approach (Section 8.3.2.9).

As in all SSC models developed for purposes of PSHA, the seismic source zones drawn are not unique and other configurations are possible, given the same set of criteria. Based on thorough evaluation of the set of source zones, the TI Team concluded that it is defensible relative to the criteria used, is consistent with available data, and modest variations in the geometry of the boundaries will not lead to significant differences in hazard at the site. This is confirmed by the very small contributions to hazard made by the sources adjoining the YFTB source zone (V. Montaldo-Falero presentation at WS3) (PNNL 2014) and the relatively lower recurrence rates of these adjoining regions.

#### 8.1.4.3 Fault Sources

The 20 faults whose closest approach lies within about 20 km of the site and that were assessed to have a seismogenic probability greater than zero are included in the SSC model (Figure 8.2). In addition, as discussed in Section 8.4, the Seattle fault is included in the model for completeness. Sensitivity analyses show that it does not contribute significantly to the hazard at the site because of its distance from the site but it is included in the model as being representative of faults that exist within the Puget Sound region.

The criteria used by the TI Team to evaluate seismogenic probability are given in Section 8.4.1. The criteria relate primarily to geologic evidence for involvement within the contemporary tectonic regime, evidence that they are capable of generating $M > 5$ earthquakes, and hazard significance that suggest that they should be represented as a fault source that localizes seismicity above the background source zone. The most important geologic indicators in this regard are the geomorphic surfaces and deposits that are Quaternary (<2.6 Ma) in age or that show evidence of deformation post-Columbia River Basalt (CRB) (post about 6−10 Myr). Such a time period is judged by the TI Team to be reasonably indicative of the potential for continuing activity during the contemporary tectonic regime. Fifteen of the faults identified within the YFB, as well as the Seattle fault, were evaluated by the TI Team and assessed to have a seismogenic probability of $p[S] = 1$. Four of the YFB faults were assessed to have a lower seismogenic probability.

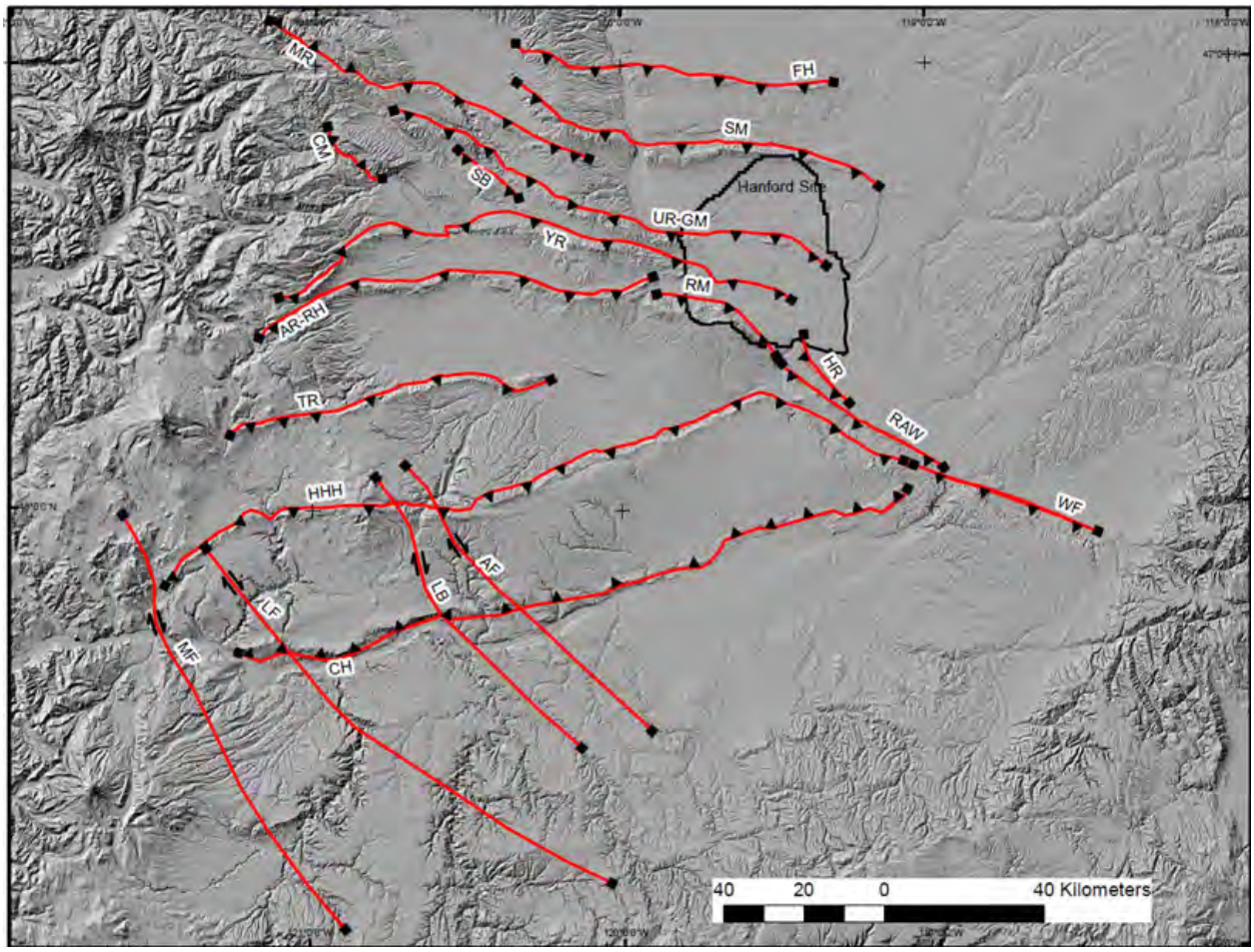


**Figure 8.2.** Fault sources included in the SSC model. Teeth are shown on the hanging wall of the faults. Arrows indicate relative sense of movement of strike slip faults.

As discussed in Section 4.4, the observed seismicity in the study region shows rather swarm-like spatial patterns of earthquake epicenters and hypocenters in the YFB region within which faults were identified and evaluated for this study. This is especially true of the seismicity in the shallow crust that represents the Columbia River basalts (mapped location shown in Figure 8.1, and includes the entire YFTB Background Source shown in Figure 8.1). As part of the high-resolution seismicity relocation analyses (Section 5.3 and Appendix F), Drs. Waldhauser and Thurber considered the spatial distribution of earthquake hypocenters and evaluated whether or not the hypocenters showed alignments that could represent active faults. They also evaluated whether the hypocenters appeared to be aligned with the subsurface projections of mapped faults. The general conclusion of these studies was that no such alignments were evident and that associations with mapped faults could not be identified with confidence.

Based on the relocation analyses as well as evaluations of studies to evaluate the seismogenic potential of preexisting faults within similar tectonic settings, the TI Team concluded that the mere spatial coincidence of observed small-magnitude epicenters in map view, or of hypocenters in cross section, in the vicinity of faults is not a very diagnostic indicator of seismogenic probability. This is in accord with the findings of other detailed studies of small-magnitude earthquakes, which conclude that, even in plate boundary regions with known active faults, "…large earthquakes are more common close to the PSZs

[principal slip zones, or Quaternary faults], and they are more likely to occur at greater depth than small earthquakes. In contrast, small quakes can occur at any geographical location…" (Hauksson et al. 2012).

Although the use of small-magnitude seismicity data is judged to provide only limited information regarding the seismogenic probability of individual faults, geologic evidence of faulting, and particularly paleoseismic data, within the time frame of the contemporary tectonic setting are judged to be very valuable in this regard. This conclusion is drawn based not only on the data that have been developed in the Hanford Site region, but on studies conducted in non-plate boundary locations worldwide. For example, the following conclusion was stated in the CEUS SSC project report (NRC 2012a):

> "An additional insight gained during the past 20 years, due largely to a number of geologic studies conducted over that period, is that paleoseismicity is important and its potential for hazard assessment is very significant. Beyond the observed historical and instrumental seismicity record, no single data set has had a more profound influence on matters of maximum size of SCR [stable continental region] earthquakes, their spatial distribution over periods much longer than the historical record, and the rates and behavior of currently active seismic sources." (NRC 2012a, p. 4−12)

Consistent with this conclusion, the Quaternary geologic studies (QGS) were conducted with the specific intention of identifying Quaternary geological deposits and geomorphic surfaces that could be dated and mapped to define the presence or absence of fault displacement or other deformation. In this respect, the QGS greatly added to the applicable database needed to identify potentially seismogenic faults and to assess their recency of displacement. As discussed in Section 8.4.3.6, these studies provided a basis for comparing the Quaternary rates of deformation for some faults with the long-term rates assessed over the past 6–10 Myr. In doing so, the evidence clearly shows that the long-term rates are comparable and that the post-CRB deformation rates of the faults of the YFB have been relatively constant over that time period.

It is important to consider the implications in the SSC model and the hazard analysis of a fault having a seismogenic probability that is zero or greater than zero. If it is greater than zero, then the fault localizes seismicity and the geometry, Mmax, and recurrence rate are all specified for the fault source. Because all seismic source zones are considered to have a seismogenic probability of unity, the particular background seismic source zone within which the fault lies (e.g., the YFTB source) is also considered to be a seismic source in the hazard analysis. In the case where a fault is assessed to be nonseismogenic, the fault does not localize seismicity and is not separately characterized for the hazard analysis. However, as discussed above in Section 8.1.4.2 on seismic source zones, the source zone that hosts the fault is characterized by random virtual faults that incorporate the available seismotectonic information for that zone. Therefore, a virtual fault could occupy the position of the nonseismogenic fault, but the fault would not be a preferred localizer of seismicity above any other location within the source zone.

As discussed in Section 8.4.3, many of the characteristics of the fault sources in the SSC model are defined by their structural geologic features. For example, the mapped location and spatial pattern of structural relief is used to identify potential lengths of rupture segments and, in turn, the range of magnitudes that would define Mchar for the fault source. The mapped pattern of structural relief also provides information related to the dip of the fault at depth, and the amount of relief is used together with assessments of the deformation start time to assess the vertical rates of slip. Importantly, the information related to structural relief, such as the relationship between topographic relief and structural relief, and the

relationship between the slip rates derived from the cumulative structural relief of the CRBs and from deformation of Quaternary deposits, has been defined and documented where this type of information exists. The careful consideration of this type of local geologic evidence has provided a firm technical basis for assessing the characteristics of all of the fault sources within the YFB.

### 8.1.5 Structure of the SSC Model Logic Trees

This section describes the structure of the logic trees that compose the SSC model. The goal is to identify all of the components of the trees, describe the underlying logic for the elements and sequencing of the nodes of the trees, and provide the reader with pointers to where the technical bases for the assessments included in the trees can be located in this report.

A logic tree is a tool for displaying the epistemic uncertainties that are part of the inputs to the PSHA. Each node of the tree represents an element of the model and the alternative branches at each node represent the alternative models or parameter values for that given element. Each branch is assigned a relative weight, treated as a probability in the calculations, which expresses the TI Team's degree of belief that it is a more appropriate model or parameter value. Ideally, epistemic uncertainties can be reduced or even eliminated with additional data and information. The technical assessments that underlie the identification of the nodes of the trees, the alternative branches, and the weights assigned to each branch are documented in this report (Sections 8.2 through 8.4).

Distinct from epistemic uncertainty is aleatory variability, which expresses those aspects of a model that we consider to be random and, at least at the level of our current knowledge, not amenable to reduction with the consideration of additional data and information. For example, the time and size of the next earthquake that will occur on a seismic source have aleatory variability. When multiple states of a model or parameter can both exist—say, a region that is assessed to include both strike slip and normal faulting seismic sources—then the assessment for purposes of the SSC model is considered to be aleatory (e.g., the styles of faulting occur randomly with respect to any given future earthquake) and the relative percentages assigned to each state are expressions of the relative frequency with which each state is expected to occur. For example, for the seismic source assessed to host both strike slip and normal faulting earthquakes, perhaps the assessed relative frequency of these events is 80 percent and 20 percent, respectively, meaning that the future relative number of strike slip and normal faulting earthquakes is expected to have this relative frequency. Because logic trees, by convention, are intended to represent epistemic uncertainties exclusively and the branches are assessed as mutually exclusive alternatives, aleatory assessments are not typically presented in a logic-tree format. For clarity in this report, aleatory assessments will be clearly indicated as such, and the relative frequencies of aleatory alternatives will be indicated as percentages within parentheses (35%) rather than relative weights as used for epistemic alternatives within square brackets [0.35]. This convention is also used in the Final HID (Appendix D).

The CSZ sources are the intraslab source zone and the plate interface and, although the model developed for the BC Hydro (2012) project includes a number of elements, there are only two attributes of that model that are updated epistemic uncertainties in the Hanford PSHA (Figure 8.3). These are the depth extent of the intraslab source, which defines its closest approach to the Hanford Site, and the easternmost extent of the seismogenic plate interface, which defines the closest approach of the interface source to the Hanford Site. Both of these assessments were made in light of new data that have been made available subsequent to the finalization of the BC Hydro SSC model: a new earthquake catalog has been developed for defining the intraslab source and new studies of episodic and tremor events have been considered in defining the eastern extent of the plate interface (see Section 8.2).

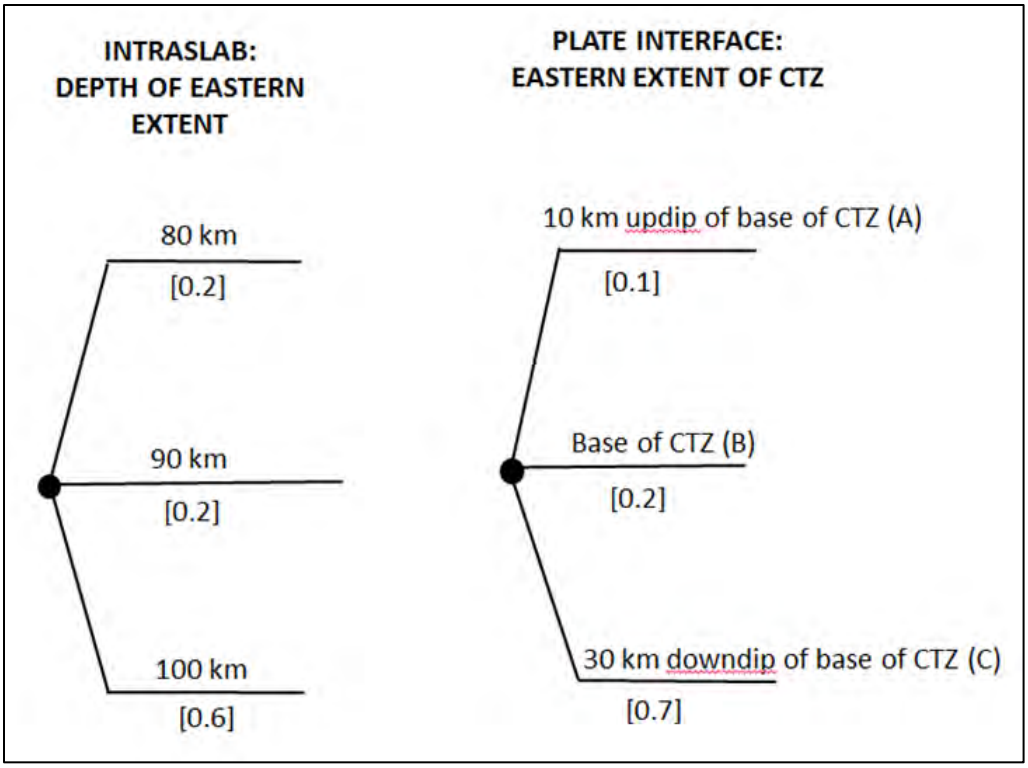


**Figure 8.3**. Logic tree for the Cascadia subduction zone sources, which include the intraslab source zone and the plate interface. "CTZ" indicates the coseismic transition zone.

The logic tree for the seismic source zones is shown in Figure 8.4. Following the convention for displaying logic-tree elements, the elements that reflect epistemic uncertainties are indicated by a node (black filled circle) and multiple branches, which represent the alternatives and weights associated with each alternative. The weights associated with all branches at a node sum to 1.0, indicating that the branches represent the "collectively exhaustive" set of options. Likewise, each model or parameter value associated with a branch at a node is "mutually exclusive" of other branches. Also shown in Figure 8.4, is a vertical bar without a node, which indicates that subsequent elements of the tree are assessed on a source-by-source basis. In general, a logic tree is structured such that more general assessments occur earlier in the tree (i.e., to the left) and more specific assessments, which may be dependent on the general elements, are shown later in the tree (i.e., to the right). For example, alternative conceptual models and their relative weights would occur first in the logic tree, and the parameter values associated with each model would follow in nodes that are conditional on each particular model.

In the seismic source zone logic tree in Figure 8.4, the first node of the tree is common to all source zones and is therefore shown to the left on the tree. Subsequent assessments are source zone-specific, as shown by the vertical bar. The next two epistemic assessments for each source zone are maximum magnitude and spatial variation of recurrence parameters. As shown on the tree, the branch values and the weights associated with each branch are source-specific. An additional epistemic assessment for the YFTB source zone only is whether or not the observed seismicity is associated with the fault sources included within the zone.

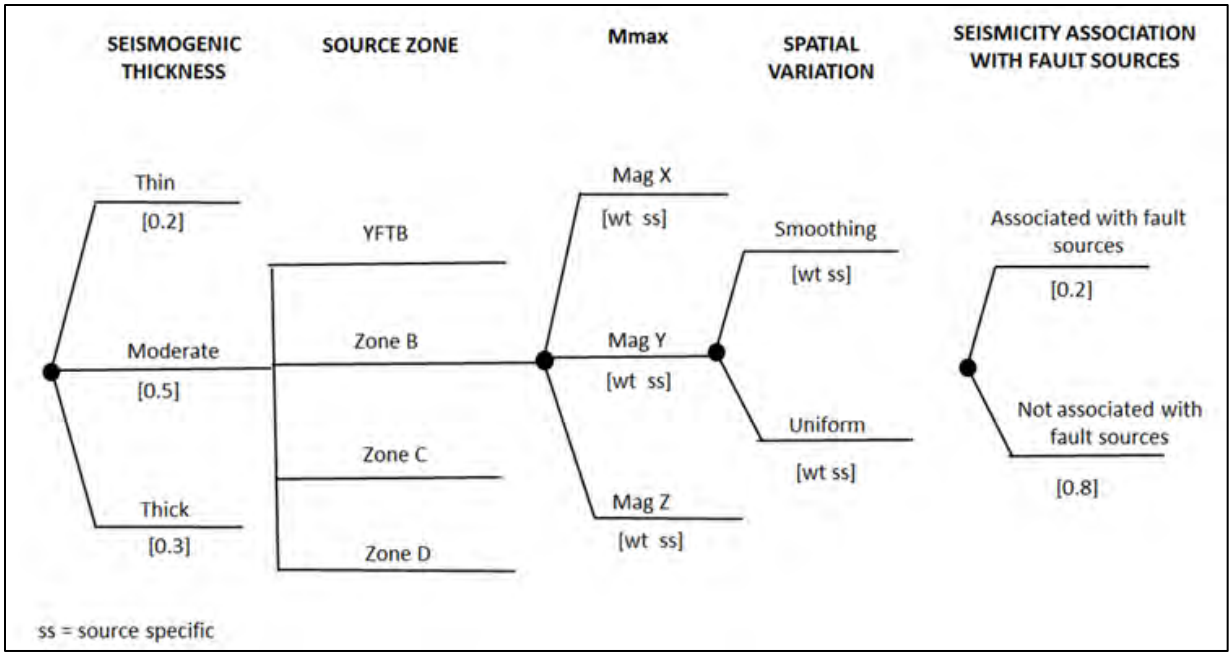


**Figure 8.4**. Logic tree for seismic source zones. The assessment of seismicity association with fault sources is applicable to the YFTB source zone only.

Aleatory (relative frequency) assessments define the characteristics of future ruptures within the source zones. The aleatory assessments are given in Table 8.1, but, because they are aleatory and not epistemic, they are not shown in the logic tree. All of the characteristics for the seismic source zones and the technical justification for the treatment of the aleatory and epistemic uncertainties are given in Section 8.3 of this report.

**Table 8.1**. Summary of seismic source zone characteristics in the SSC model.

| Characteristics | YFTB[(a)] | Zone B | Zone C | Zone D |
|---|---|---|---|---|
| Seismogenic Thickness | 13 km [0.2]<br>16 km [0.5]<br>20 km [0.3] | 10 km [0.2]<br>12 km [0.5]<br>15 km [0.3] | 13 km [0.2]<br>16 km [0.5]<br>20 km [0.3] | 15 km [0.2]<br>20 km [0.5]<br>24 km [0.3] |
| Style of Faulting | Reverse (60%)<br>Normal (20%)<br>Strike slip (20%) | Reverse (60%)<br>Strike slip (40%) | Reverse (60%)<br>Strike slip (40%) | Reverse (60%)<br>Strike slip (40%) |
| Strike of Ruptures | <u>Reverse</u><br>40º (20%)<br>90º (60%)<br>140º (20%)<br><u>Normal</u><br>10º (20%)<br>90º (60%)<br>140º (20%)<br><u>Strike slip</u><br>60º (50%)<br>150º (50%) | 0−360° uniform (100%) | 0−360° uniform (100%) | 0-360° uniform (100%) |

**Table 8.1**. (contd)

| Characteristics | YFTB[a] | Zone B | Zone C | Zone D |
|---|---|---|---|---|
| Dip of Ruptures | Reverse<br>30º (20%)<br>50º (60%)<br>70º (20%)<br>Normal<br>40º (20%)<br>60º (60%)<br>80º (20%)<br>Strike slip<br>70º (40%)<br>90º (60%)<br>Dip direction is random | Not modeled[b] | Not modeled[b] | Not modeled[b] |
| Mmax | 6.5 [0.3]<br>6.75 [0.4]<br>7.0 [0.3] | 6.5 [0.2]<br>6.75 [0.5]<br>7.0 [0.2]<br>7.25 [0.09]<br>7.5 [0.01] | 6.5 [0.2]<br>6.75 [0.5]<br>7.0 [0.2]<br>7.25 [0.09]<br>7.5 [0.01] | 6.5 [0.2]<br>6.75 [0.5]<br>7.0 [0.2]<br>7.25 [0.09]<br>7.5 [0.01] |
| Max Observed[c] | M 4.79 1918-11-17 | M 7.06[d]<br>1872-12-15 Lake Chelan | M 5.98<br>1936-07-16 Milton-Freewater | M 4.8<br>1893-03-06 |
| Seismicity Association | Assoc. with faults [0.2]<br>Not assoc. [0.8] | Not applicable | Not applicable | Not applicable |
| Spatial Variation of Recurrence Parameters | Uniform [0.8]<br>Smoothing [0.2] | Smoothing [1.0] | Uniform [1.0] | Uniform [0.8]<br>Smoothing [0.2] |

(a) Epistemic weights are given as probabilities in [brackets] and aleatory relative frequencies are given as percentages in (parentheses).
(b) Because of the large distance to the sites, the dip of ruptures is not modeled but is assumed to be vertical.
(c) Magnitudes given are the expected magnitudes, E[M], in the Hanford PSHA earthquake catalog.
(d) The Bakun et al. (2002) magnitude estimate is M 6.5 – 7.0 at the 95th confidence level.

The fault sources within the SSC model are characterized using three logic trees that provide a full expression of the knowledge and uncertainties regarding important fault source characteristics (see Section 8.4.3). Given the nature of the available data, which show differences in the geometry and structural relief along the lengths of individual faults, the faults are characterized according to the segments identified along their lengths. The SSC model also provides assessments of the manner in which future earthquake ruptures could involve more than one segment. For example, the model allows for ruptures on one segment to include all or portions of adjacent segments, but the seismic moment rate constraints (defined by the net-slip rate and fault geometry) are maintained for each fault segment.

The first logic tree for the fault sources is shown in Figure 8.5. It includes the characteristics that define the 3-D geometry and net-slip rate for each fault segment. The first two nodes of the tree are common for all fault segments, and the subsequent parts of the tree are fault segment-specific. The assessment of seismogenic probability is source-specific and subsequent nodes of the tree are dependent on the fault segment being seismogenic. The sense of slip is also source-specific, duly accounting for a variety of geologic and seismologic data, and the factor for calculating net slip is a function of the particular sense of slip. The final assessment in the tree is the start time for calculating net-slip rate and

each combination of net slip and start time leads to a distribution of segment-specific net-slip rates, as shown at the end of the logic tree. These distributions are then used as input to the logic tree related to earthquake recurrence rates. As discussed in Section 8.4.3.6.2, a few of the faults have documented evidence for Quaternary deformation and, as a result, Quaternary slip rates have also been assessed and these are combined in the logic tree with the long-term slip rates as weighted alternatives.

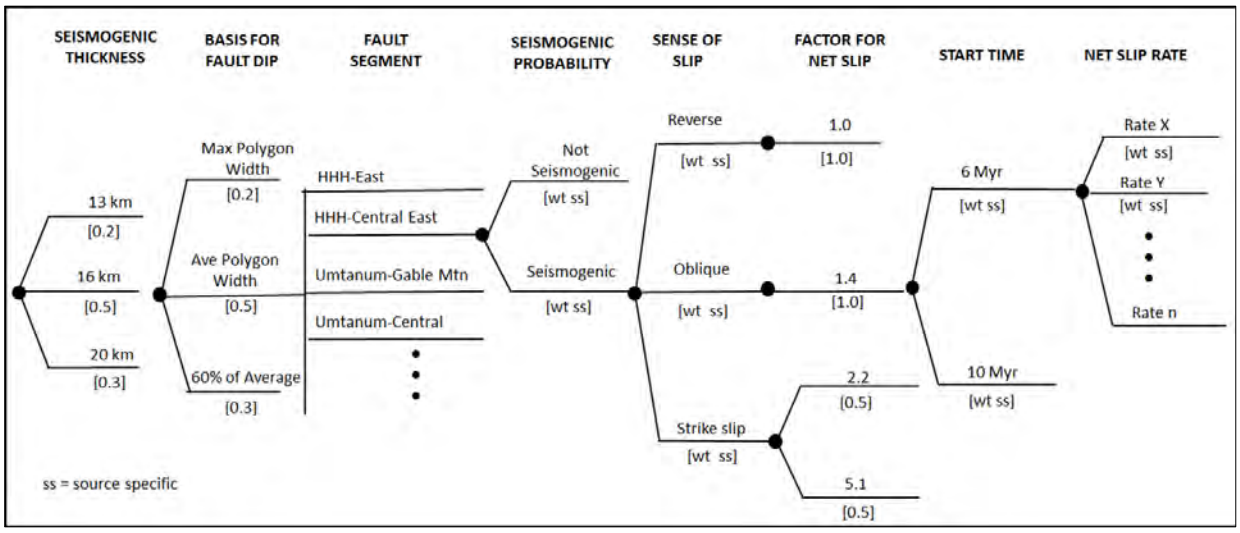


**Figure 8.5**. Logic tree for the fault segment geometry and slip rate.

The second logic tree for fault sources is shown in Figure 8.6 and includes the assessments that lead to a distribution of characteristic magnitudes, Mchar. The assessments relate to the expected dimensions of rupture, defined by the seismogenic thickness, rupture length, and average width (and hence area). These assessments are used in combination with the previous assessments of the downdip width that comes from a consideration of the dip of each fault segment (Figure 8.5). Given estimates of rupture length and rupture area, alternative approaches to calculating Mchar are included in the logic tree as well as alternative rupture versus magnitude relationships for a given approach. As before, the logic tree includes assessments that are common to all fault segments (to the left) as well as assessments that are source-specific (to the right).

The third logic tree is shown in Figure 8.7 and provides the assessments that lead to earthquake recurrence rates for each fault segment. An element common to all fault segments is the temporal scale factor, which accounts for the possibility of non-Poissonian behavior related to a renewal process of earthquake generation. The factor is multiplied by the Poissonian recurrence rate to account for the large uncertainties that exist for the timing of past earthquakes on these fault sources. For three fault sources, sufficient data exist to estimate earthquake recurrence intervals as well as slip rate, hence these alternative approaches to recurrence estimation are included in the logic tree. For all fault segments the net-slip rates combined with the dimensions of the fault define the seismic moment rate, which is input to a magnitude frequency distribution to arrive at the equivalent Poisson rate for all magnitudes up to the maximum, Mmax. The final distributions are then input directly into the seismic hazard model.

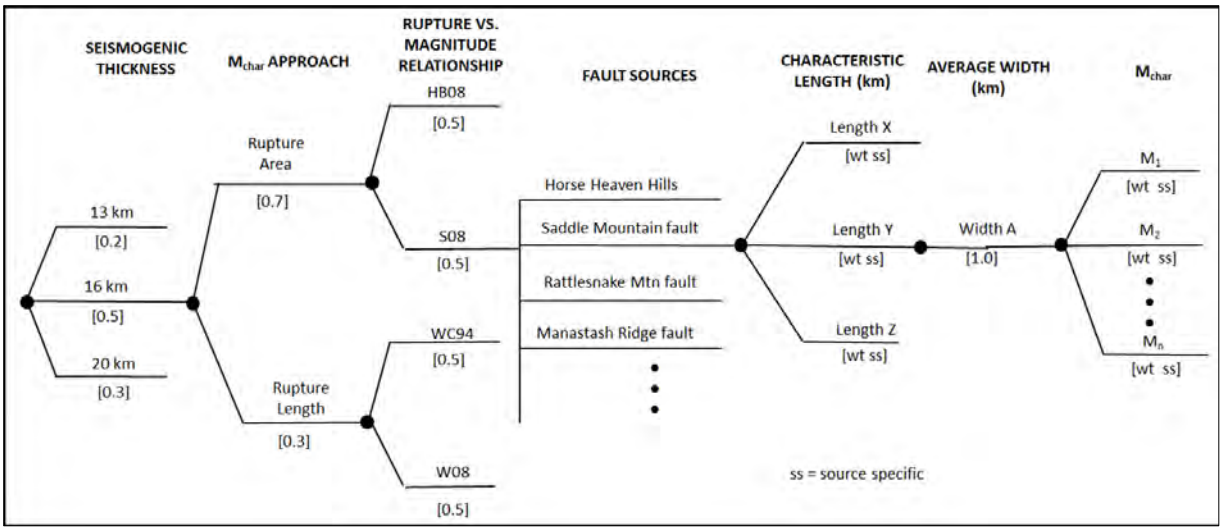


**Figure 8.6**. Logic tree for characteristic magnitudes of fault sources.

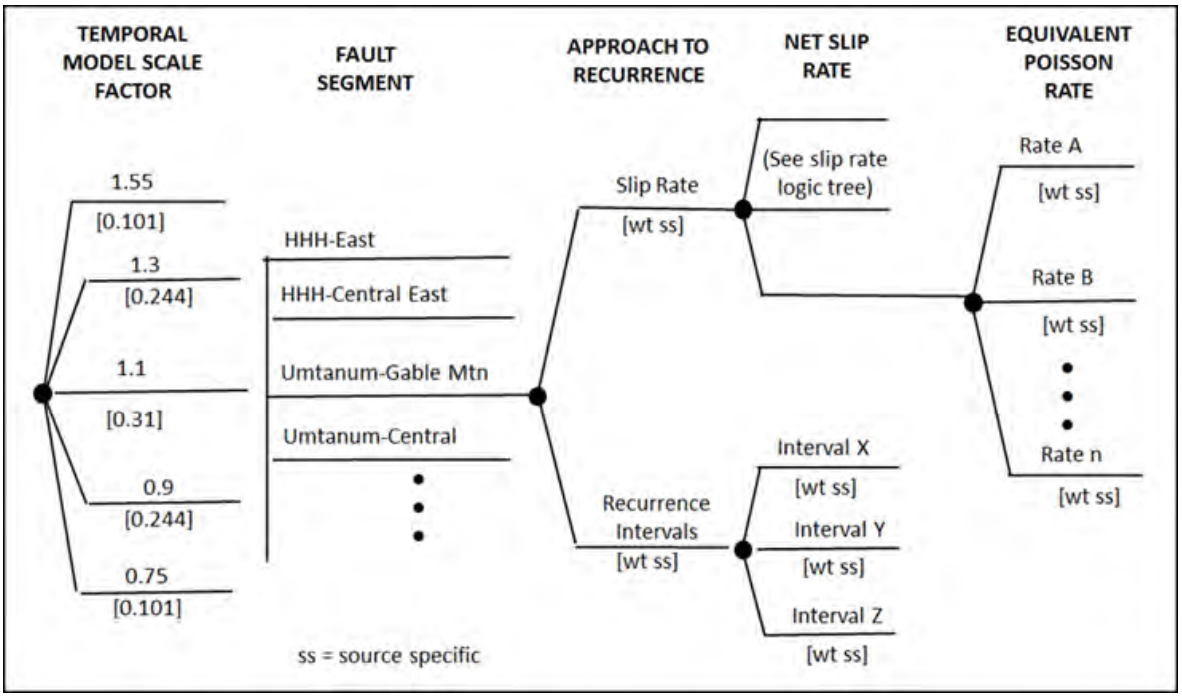


**Figure 8.7**. Logic tree for the recurrence characteristics of fault segments.

Sections 8.2 to 8.4 of this report are intended to provide a detailed discussion of all aspects of the SSC model. This includes identification of the key elements of the model, the manner in which uncertainties in those elements have been quantified, and the technical justification for all assessments made by the TI Team. Relevant data, models, and methods will be cited to provide the reader with an indication of the manner in which the information was evaluated and integrated into the SSC model. In some cases, some models and methods that exist within the technical community were evaluated and found by the team to not be part of the center, body, and range of the technically defensible interpretations and, as a result, were not incorporated into the SSC model. That technical justification is also included in this report.

## 8.2 Cascadia Subduction Zone Sources

Sensitivity analyses conducted as part of the Hanford PSHA show that the seismic sources associated with the CSZ have the potential to contribute to the seismic hazard at the Hanford Site. The analyses show that the contribution of seismic sources to total hazard is relatively small due to their large distances from the site, but may be significant for the assessment of long-period ground motions. As a result, CSZ sources are included in the SSC model. The sensitivity studies indicate that the most important aspects of the CSZ source characteristics are those that relate to the closest approach of the sources to the Hanford Site. The two CSZ sources are the intraslab source zone and the plate interface source. The intraslab source is modeled as a seismic source zone and the plate interface is a fault source. As discussed in Section 8.2.1, the CSZ source characteristics used in the Hanford SSC model come from recent previous studies. Evaluation by the SSC TI Team of information developed subsequent to those studies, discussed in Sections 8.2.2 and 8.2.3, confirms that nearly all of the existing CSZ models continue to be representative of the center, body, and range of the technically defensible interpretations, with the exception of two characteristics discussed in those sections. In addition, a significant effort was devoted to updating the earthquake catalog to include recent earthquakes, to ensure that a uniform moment magnitude is assigned for all events, and to analyze the catalog for purposes of recurrence calculations.

### 8.2.1 Approach Using Previous Studies and the Evaluation of New Data

As discussed in Chapter 2.0, the evaluation stage of a SSHAC Level 3 process requires that data, models, and methods be compiled and reviewed for their potential applicability to the SSC and GMC models for the PSHA. This review is informed and prioritized by preliminary hazard calculations presented at WS1 (presentation by V. Montaldo-Felero) (PNNL 2013a) and previous hazard studies, which allow the TI Teams to understand the potential hazard significance of the available information. In the case of the Hanford Site, previous hazard studies conducted for the site and nearby locations (Geomatrix 1996; JBA et al. 2012) suggested that the CSZ sources could potentially contribute to the site hazard, particularly at low annual frequencies of exceedance and for longer period ground motions. A very fortunate circumstance was that the BC Hydro SSHAC Level 3 PSHA (BC Hydro 2012) had recently been completed and included a complete characterization of the CSZ sources. Several members of the Hanford PSHA SSC TI Team had also participated in the development and review of the BC Hydro SSC model and are thus in a good position to understand its technical basis.

The BC Hydro CSZ model includes the characterization of both the intraslab seismicity occurring within the down-going Juan de Fuca slab (also called the Wadati-Benioff zone) and the plate interface between the Juan de Fuca and the North American plates. These seismic sources are shown diagrammatically in Figure 8.8.

The geometry of the intraslab source is defined from analyses of the observed seismicity and a host of geophysical studies (e.g., McCrory et al. 2006, 2012). The TI Team decided that the earthquake catalog development activity for the Hanford PSHA would include a complete update of the CSZ seismicity, conversion of all earthquake size measures to moment magnitude, analysis of the catalog to assign events to the slab or continental crust, analyses to decluster the catalog and correct for incompleteness, calculation of recurrence parameters, and spatial smoothing of those parameters to account for spatial variations. With respect to the characterization of the intraslab source, all elements of the BC Hydro SSC logic trees were reviewed by the TI Team and any new data were considered for their potential impact on the source characteristics. As discussed in Section 8.2.2, the only assessment that was judged to be

potentially significant was the maximum depth of the slab, which influences the easternmost extent of the source and its closest approach to the Hanford Site.

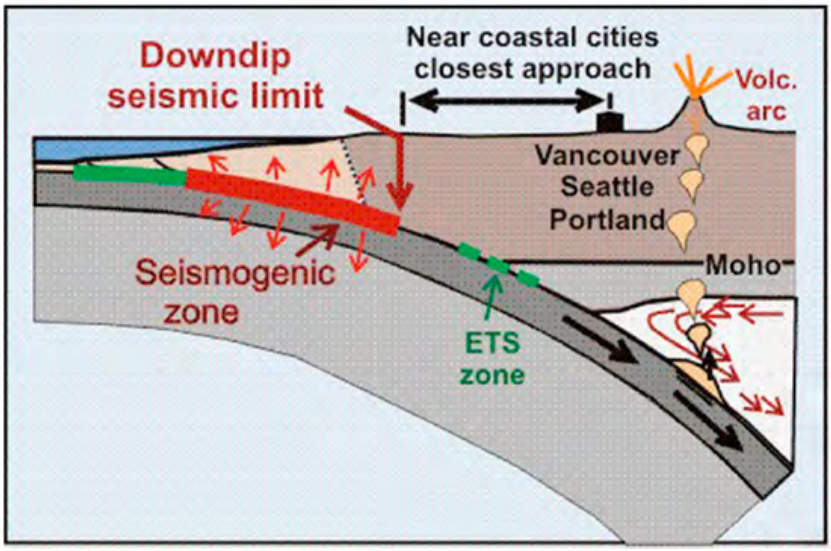


**Figure 8.8**. Diagrammatic depiction of the seismic sources and other elements related to the CSZ (Hyndman 2013). The plate interface source is shown in red and labeled "seismogenic zone." The intraslab source is shown by the down-going black arrows within the Juan de Fuca plate. Episodic tremor and slip (ETS) earthquakes are labeled "ETS zone." The landward extent of the plate interface, which is a key aspect of the SSC model, is labeled "downdip seismic limit" (Hyndman 2013). The location of Hanford Site lies east (to the right) of the Cascade volcanic arc.

The plate interface source is defined and characterized in the BC Hydro SSC model based on a comprehensive review and analysis of a variety of geologic, paleoseismic, geophysical, and seismologic databases. Although the interface has been essentially quiescent during historical time, ample paleoseismic evidence has been developed for the repeated occurrence of large-magnitude earthquakes in the recent geologic past. As part of the BC Hydro study, a comprehensive and first-of-its-kind statistical analysis was conducted of the paleoseismic evidence for the timing of paleo-earthquakes and evidence for temporal and spatial clustering of activity. Careful review and evaluation of new information developed since the conclusion of the BC Hydro study serve to confirm that all important elements of the model are judged to be current. The only element of the plate interface model with potential significance to the Hanford Site that was deemed by the TI Team to be worthy of reassessment was the position of the easternmost extent of the seismogenic interface. The three alternative locations in the BC Hydro model were judged to be appropriate in light of new data, but their relative weights were adjusted to make them more defensible in light of recent data and information, as discussed in Section 8.2.3.

### 8.2.2 Intraslab Source, Including Catalog Analyses

Unlike the CSZ plate interface, the intraslab source shows abundant evidence of seismic activity in the historical and instrumental record. Although the seismic hazard at nearby locations such as Puget Sound is significantly affected by the intraslab source, sensitivity analyses conducted for the Hanford Site show a very minor contribution to hazard at that site other than for long-period ground motions (V. Montaldo-Falero presentation at WS1 and WS3) (PNNL 2013a, 2014). Two potentially significant

source characteristics are the Mmax and the easternmost location of the source, which establishes the closest approach to the site. To assist in the assessment of both of these characteristics, as well as the assessment of earthquake recurrence, a significant effort was devoted to updating and analyzing the earthquake catalog. In addition, pertinent information in the professional literature that had become available since the completion of the BC Hydro SSC model was reviewed.

The development and analysis of the CSZ earthquake catalog (the "subduction" catalog) are described in detail in Chapter 6.0 and the catalog is provided in Appendix C. The catalog covers the time span from the earliest historical earthquakes in the 19th century to April 30, 2013, and has been compiled from a number of sources. Criteria were established for categorizing earthquake hypocenters as intraslab events versus crustal events, using the 3-D slab geometry developed by McCrory et al. (2006). That geometry was updated slightly by McCrory et al. (2012), but no significant differences were made to the slab location in relationship to the Hanford Site. Thus, that slab configuration is supported by a number of data sets and is endorsed for use in the SSC model.

The assessment of Mmax for the intraslab source was performed in the BC Hydro study based on consideration of the largest observed earthquakes (i.e., the 2001 **M** 6.8 Nisqually event) and consideration of the thickness of the slab (Kao et al. 2008) and thermal modeling of the slab to assess its seismogenic thickness (Wong 2005). The section of the slab that is pertinent to the Hanford PSHA is south of the bend in the slab, which is termed the "Puget Sound Deep" source in the BC Hydro report. The assessed Mmax for that source is given by the following distribution:

6.8 [0.2]
7.0 [0.7]
7.5 [0.1].

Studies related to the CSZ intraslab source conducted subsequent to the BC Hydro PSHA have tended to agree with the earlier findings. For example, Wada et al. (2010) use earthquake focal mechanisms to model the intraslab stresses throughout Cascadia. They conclude that "deviatoric stresses in the Juan de Fuca slab appear to be very low, resulting in very low intraslab seismicity" in the southern part of the slab south of the bend. Based on consideration of the BC Hydro assessment and evaluation of new information, the TI Team concluded that the Mmax assessment from that study does not need to be updated.

The spatial distribution of earthquakes in the subduction catalog and the depth contours on the top of the slab (McCrory 2006) are shown in Figure 8.9. For the BC Hydro study, the focus was primarily on the configuration of the slab and the location of the intraslab source to the north of the bend in the slab in central and northern Washington. Therefore, the assessment of the "depth contour defining the downdip boundary" for the slab was given in the logic tree as follows:

60 km [0.2]
70 km [0.6]
80 km [0.2].

However, from the standpoint of the Hanford PSHA, the TI Team reviewed the seismicity shown in Figure 8.9 and considered the potential depth extent of the intraslab source on the southern side of the bend.

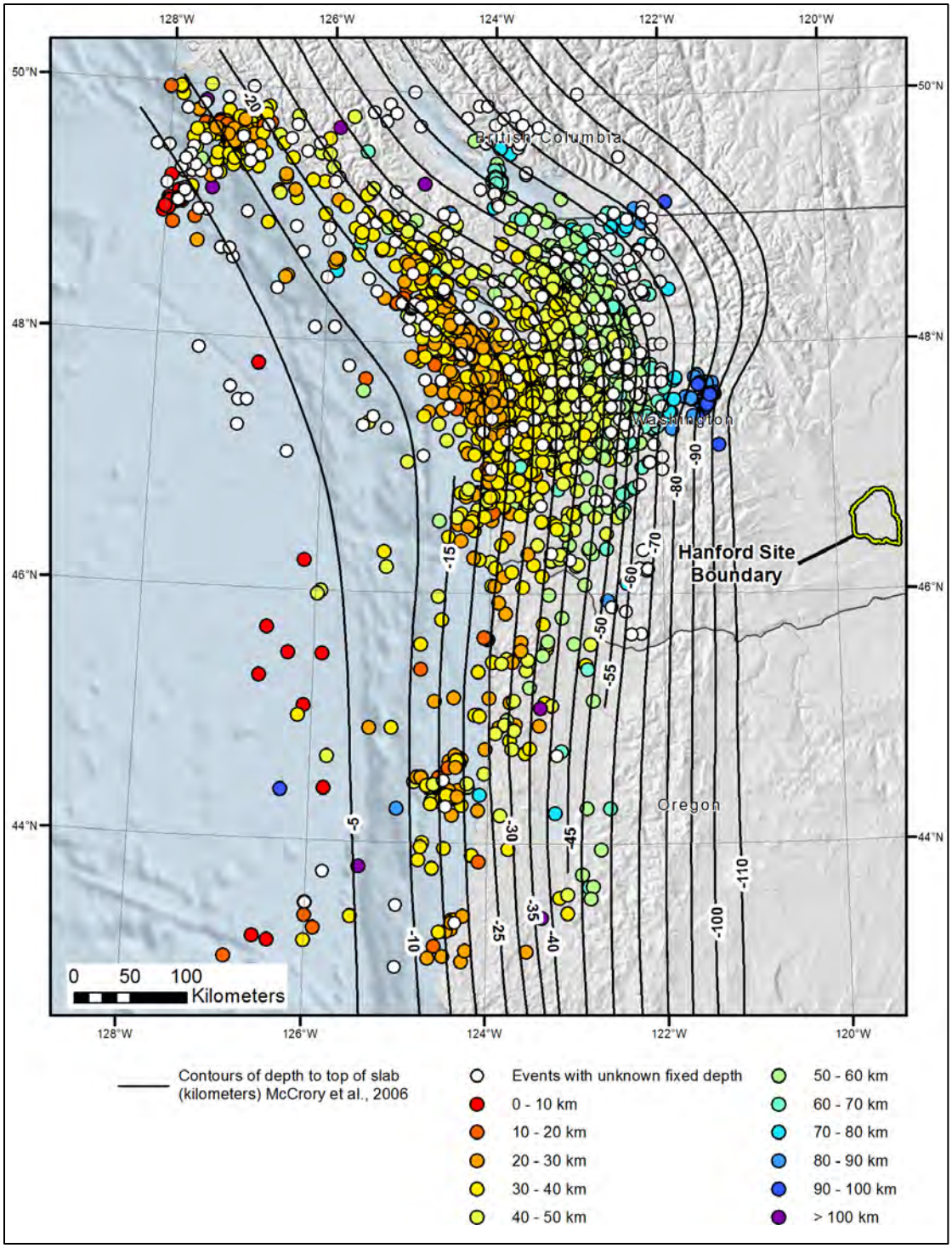


**Figure 8.9**. Distribution of seismicity in the area covered by the subduction earthquake catalog. Hypocenters are color-coded for each 10 km of depth.

As can be seen in the cross section taken through the intraslab seismicity along the southern part of the bend in the slab (Figure 8.10), the deepest earthquakes in that area are at depths of about 100 km. South of the bend and at the latitude of the Hanford Site, the deeper part of the slab appears to be quiescent seismically based on the observed seismicity. The TI Team reviewed the evidence based on the

subduction seismicity catalog and concluded that the assessment of the maximum depth of the intraslab source at latitudes applicable to the Hanford Site needed to be updated. The new distribution for the depth contour defining the easternmost extent of the intraslab source allows for the possibility that at the latitude of the site the deeper part of the slab is seismogenic, as observed along the southern part of the slab bend:

80 km [0.2]
90 km [0.2]
100 km [0.6].

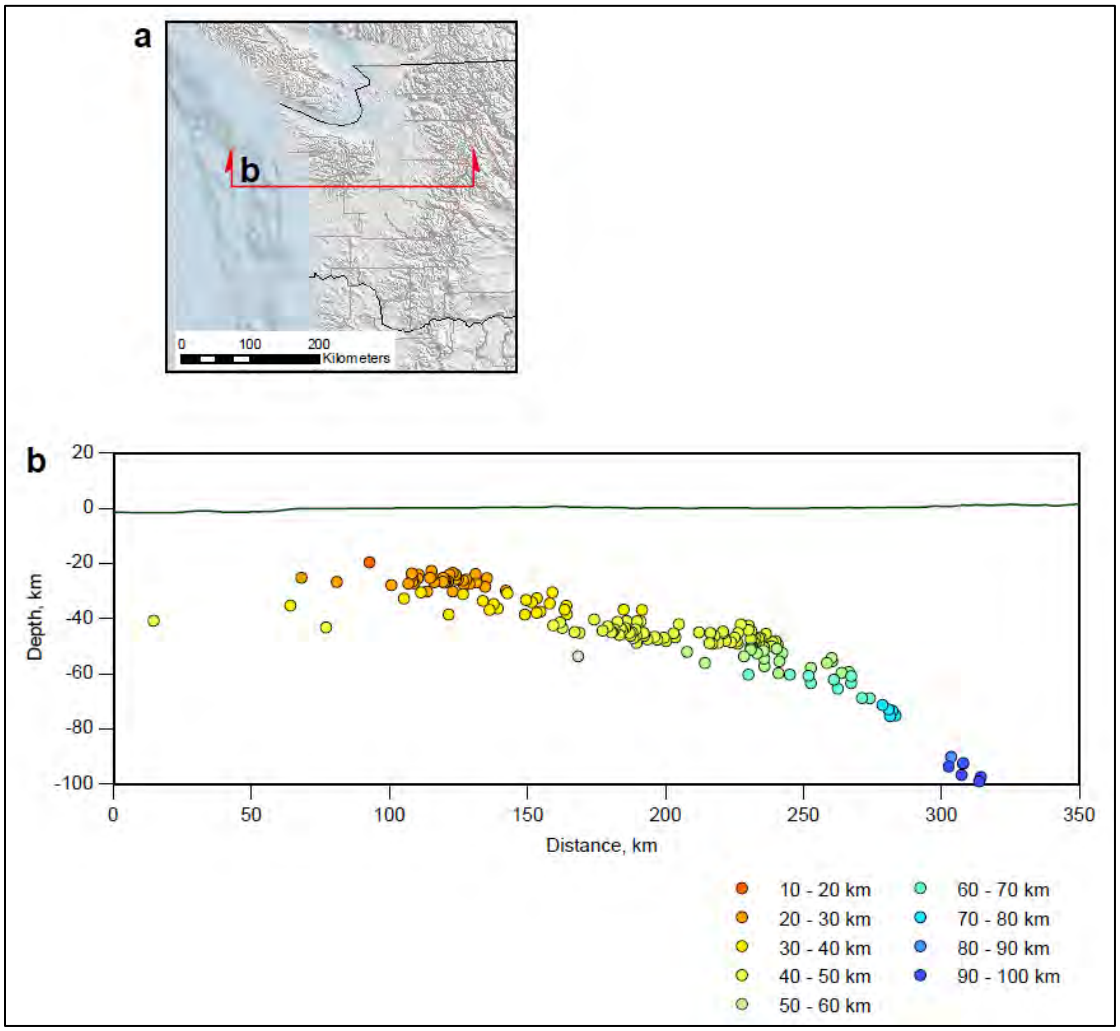


**Figure 8.10**. Cross section of intraslab seismicity along the line of section shown in panel (a). Hypocenters are color-coded for each 10 km of depth.

A key use of the subduction catalog is the development of earthquake recurrence parameters. As discussed in Chapter 6.0, the catalog has been developed to include the uncertainties in the magnitude for each event, and those uncertainties are incorporated into the recurrence calculations using the N* approach. Analysis of the catalog for purposes of evaluating completeness and declustering were also conducted. Based on the spatial distribution of intraslab earthquakes along the length of the CSZ, the TI Team concluded that spatial smoothing of the activity rate (i.e., the N* per unit area) is appropriate in

representing the future spatial variation in recurrence rate for the intraslab source. For example, the elevated levels of seismicity associated with the bend in the slab and associated shallowing of the slab downdip are expected to persist in the future for purposes of the PSHA. In contrast, the b-value recurrence parameter was judged to be relatively constant spatially within the intraslab source. To calculate the b-value, the recurrence rate for the intraslab source was calculated. Based on the assessment that $\mathbf{M} \geq 3.5$ is complete from 1970 and that $\mathbf{M} \geq 5$ is complete from 1880, 189 earthquakes are used for the recurrence calculation (shown in Figure 8.11). The b-value derived is $0.624 \pm 0.056$, which is used in the recurrence calculations.

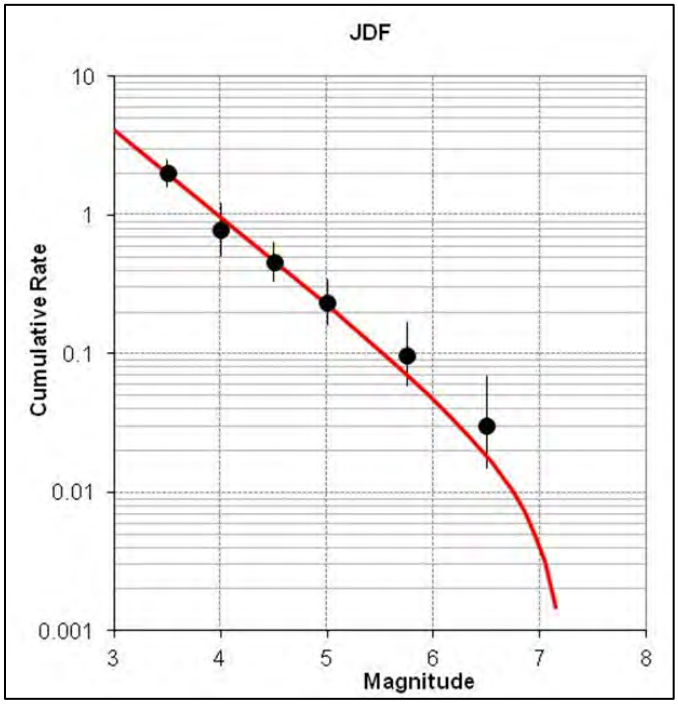


**Figure 8.11**. Earthquake recurrence curve for the intraslab source. Observed counts are shown as black dots with their associated errors. The calculated b-value is $0.624 \pm 0.056$. The b-value is held constant while the recurrence rate is spatially smoothed within the intraslab source.

The approach taken for spatial smoothing is the approach recommended by Stock and Smith (2002) as a preferred approach to the fixed smoothing kernel approach because it uses an adaptive kernel (Silverman 1986). In this approach, the kernel size is adjusted throughout the study region, decreasing in size in areas of higher data density and increasing in size in areas of sparse data. An initial kernel bandwidth (h) equal to 15 km was selected for these source zones by testing values of h from 5 to 100 km, in 5-km increments and maximizing the log-likelihood according to the procedure given by Silverman (1986). The adaptive kernel method was then used to define the final spatial density for the hazard calculations.

### 8.2.3 Plate Interface Source

As shown diagrammatically in Figure 8.8, the seismogenic plate interface is a characterized as a fault source in the Hanford PSHA. Given its tectonic position, its expected style of faulting is reverse and its lateral and downdip dimensions imply the potential to generate very large earthquakes. The Cascadia

plate interface is different than most subduction zones in its near absence of observed thrust-faulting earthquakes in the instrumental record. However, abundant paleoseismic evidence, both from offshore turbidite sequences and from onshore evidence of coastal subsidence and tsunami deposits, confirms its seismogenic potential in the contemporary tectonic regime. Fortunately, the BC Hydro SSC model (BC Hydro 2012) included a comprehensive review and evaluation of applicable data, models, and methods at the time the study was being conducted, and the plate interface model includes all pertinent aspects of the source geometry, Mmax, and recurrence characteristics. Sensitivity analyses conducted for the Hanford PSHA showed that the most important aspect of the CSZ plate interface model is the easternmost extent of the plate interface, thus defining the closest approach of the source to the site. Lesser sensitivity is related to the plate interface Mmax and recurrence rates.

The evaluation phase of the Hanford PSHA included a comprehensive review of data developed after completion of the BC Hydro model related to the eastern extent of the plate interface, Mmax, and recurrence. This evaluation by the TI Team led to the need to modify slightly the plate interface logic tree to better represent the uncertainties regarding the eastern extent of the interface, which has been the subject of considerable research in recent years. Other aspects of the model related to Mmax and recurrence were judged to not require updating in light of new information.

In the absence of direct evidence in observed instrumental seismicity, the location and geometry of the plate interface has been interpreted based on a number of geophysical, thermal, geodetic, and seismological analyses. All of these data types were evaluated as part of the BC Hydro study and work has continued in the research community since the time of that study. For example, studies integrating thermal, geodetic, geophysical, and other data have continued (e.g., Hyndman 2013; Cozzens and Spinelli 2012; McCrory et al. 2014). Considerable research has evolved related to the spatial configuration of nonvolcanic episodic tremor and slip (ETS) events (e.g., Wech and Creager 2011; Hyndman 2013) and the spatial relationship between the updip extent of ETS events and the downdip location of the seismogenic plate interface. ETS events were known and mapped in the Vancouver Island part of the CSZ plate interface at the time of the BC Hydro study, but subsequent work has focused on the ETS data in the southern part of the CSZ.

To illustrate the range of interpretations published after the BC Hydro study of the landward extent of the seismogenic plate interface, a few representative examples are included here. The location of the thermally defined landward extent of the seismogenic plate interface has varied depending on assumptions related to the presence of fluids. Figure 8.12 and Figure 8.13 show the locations of isotherms on the interface, and locking depths are generally assumed to exist down to at least the 350°C isotherm and perhaps as deep as the 450°C isotherm. In general, the thermal models tend to agree with the models of the landward extent of locking depths derived from geodetic data, but seaward of the location of the seismogenic interface interpreted from ETS.

Since the completion of the BC Hydro CSZ model, research has continued regarding the spatial distribution of ETS events and their potential significance in identifying the downdip extent of the seismogenic plate interface. This has been particularly true in the region to the south of the bend in the slab, which is of most interest to the Hanford model. Figure 8.14 and Figure 8.15 show the spatial distribution of ETS and alternative interpretations of their spatial relationship to the locked or seismogenic plate interface. In Figure 8.14, Hyndman (2013) postulates that a gap is evident and persists between the updip (seaward) extent of ETS and the locked plate interface, defined principally from the 350°C isotherm. Locally, this gap is about 50−70 km wide in the part of the interface of interest for the

Hanford study. Alternatively, as shown in Figure 8.15, Wech and Creager (2011) postulate that the seismogenic interface is located closer to and just updip from the ETS events. They acknowledge that transient events (seen primarily in geodetic data) may occur in the transition between the fully locked region and the ETS region, but large rupture events would be assumed to include the interface down to the top of the ETS zone.

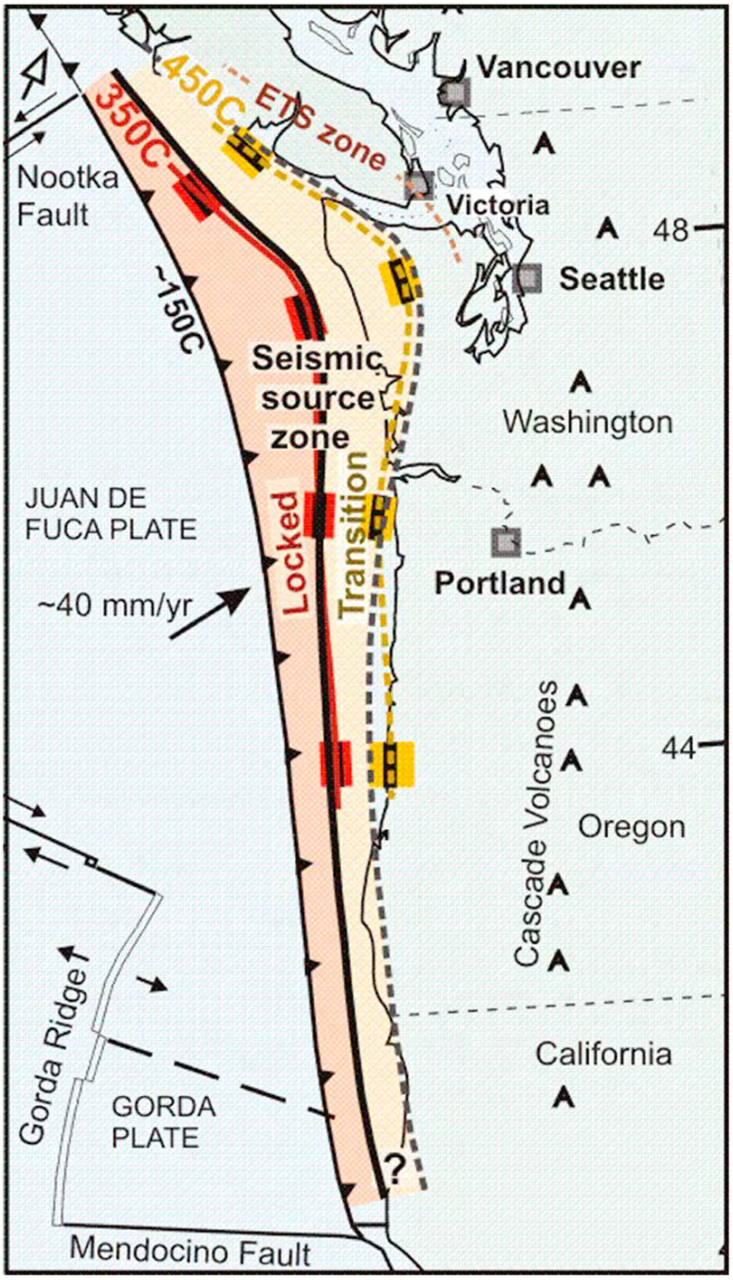


**Figure 8.12**. Figure from Hyndman (2013) summarizing the landward limits of the fully locked (to solid black line) and linear transition (to dashed gray line) zones based on leveling and tide gauge geodetic data. The thermal limits of seismic behavior, 350 and 450°C, from thermal models are shown as the red and yellow lines and uncertainties are shown as boxes. It is concluded that the thermal model and geodetic limits are in agreement within the uncertainties, and these are both seaward of the limits given by ETS.

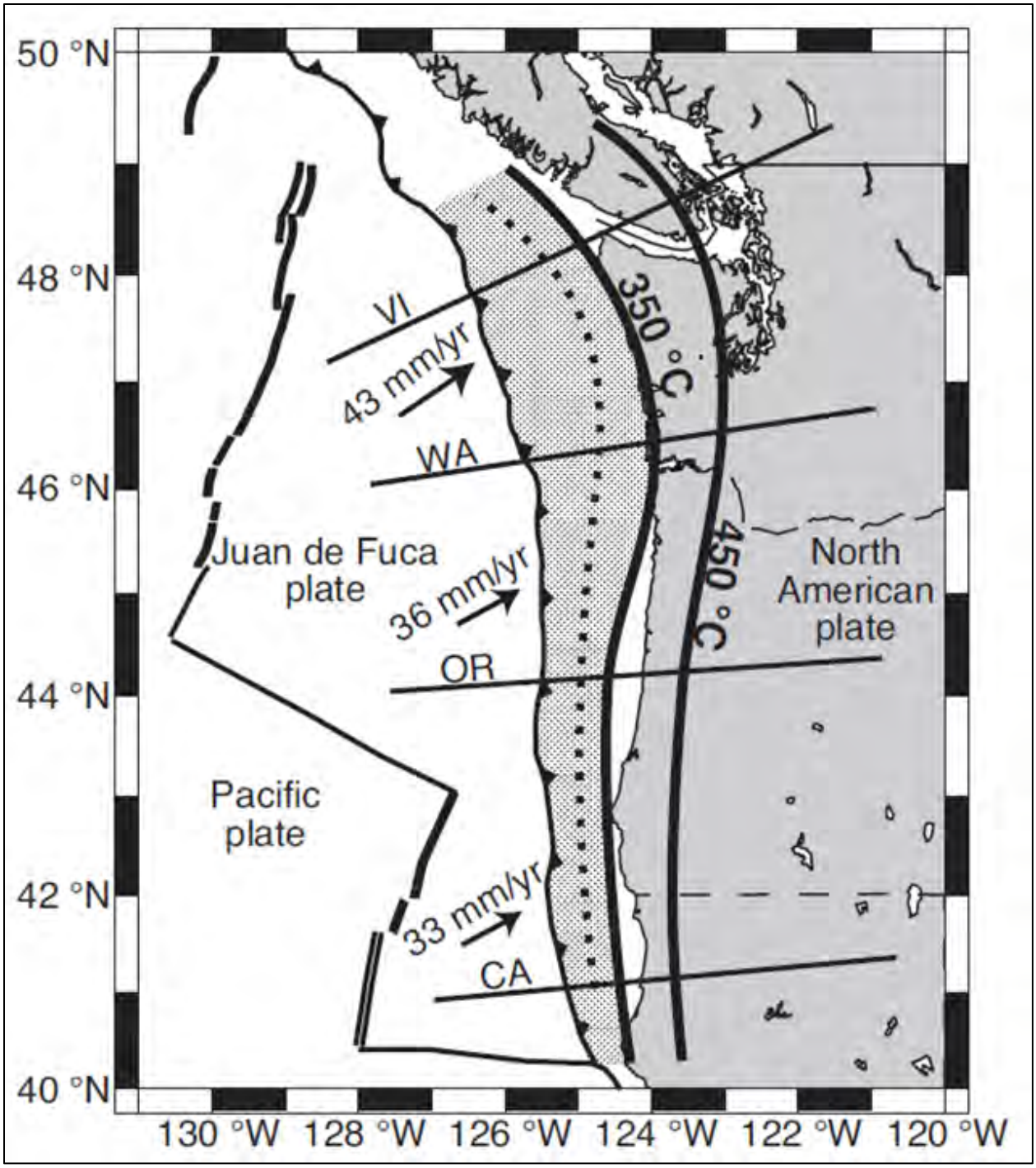


**Figure 8.13**. Alternative interpretation of the isotherms on the plate interface based on thermal modeling assuming circulation of fluids within the subducting slab (Cozzens and Spinelli 2012). The Hyndman (2013) location of the 350°C isotherm is shown by the dotted line and is seaward of this interpretation.

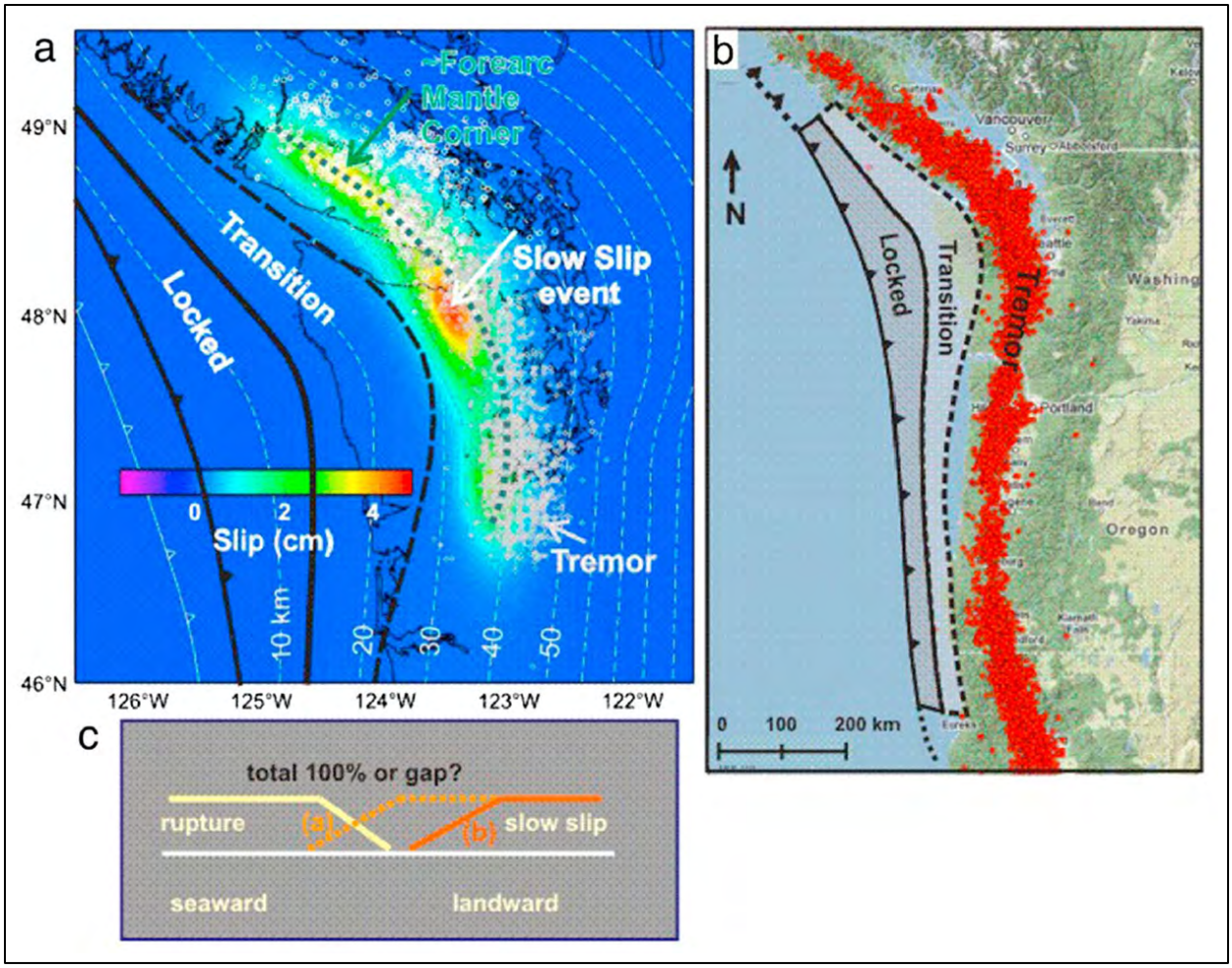


**Figure 8.14**. Maps from Hyndman (2013) showing the locked and transition zones of the plate interface defined from thermal and geodetic modeling in comparison to the location of ETS ("tremor") events shown in red. A 50- to 70-km-wide gap is noted between the updip location of ETS and the bottom of the locked zone based on thermal and geodetic data.

Researchers recently have explored the concept that great earthquakes anticipated on the CSZ plate interface can potentially rupture beyond the geodetically and thermally inferred locked zone to the depths of ETS or to the even deeper forearc mantle corner (FMC), which is the line of intersection of the forearc Moho with the interface. McCrory et al. (2014) have compiled and interpreted seismic velocity profiles along the CSZ based on active source experiments, 3-D tomographic models, and teleseismic arrays. Figure 8.16 shows the configuration of the FMC and its approximate location in map view based on the analysis of the various velocity profiles. The relationship between the FMC and the ETS events is not clear. Studies of other subduction zones by McCrory et al. suggest that the FMC may play a role in defining the downdip extent of seismogenic rupture during large interface events. Subduction zones evaluated are the Nankai trough, the Japan subduction zone (host of the 2011 $M_w$ 9.0 Tohoku-Oki earthquake), and the Sumatran subduction zone (host of the 2004 $M_w$ 9.1 Sumatra-Andaman earthquake).

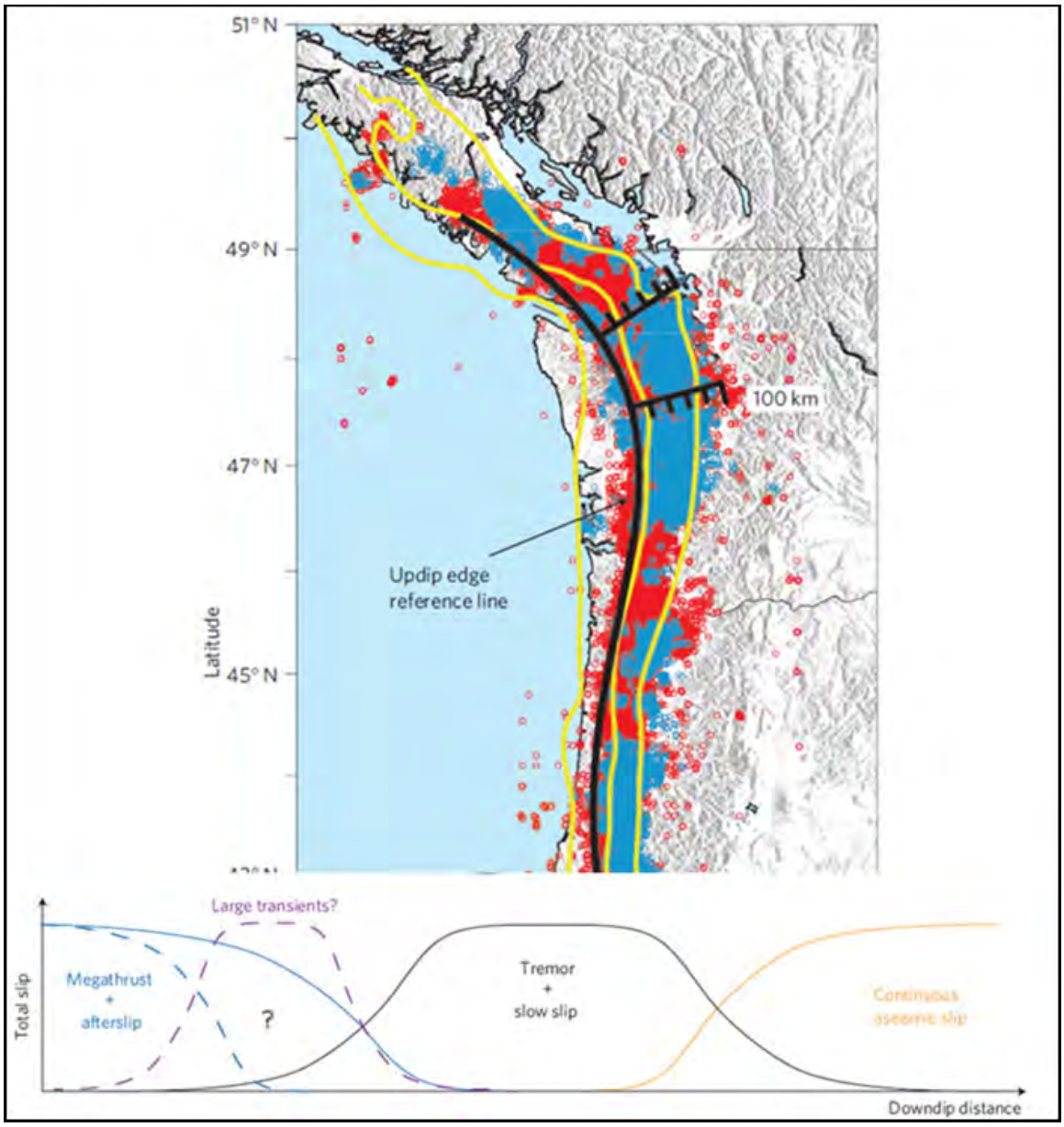


**Figure 8.15**. Map showing the location of ETS events and interpretation of their significance relative to the location of the seismogenic interface (Wech and Creager 2011). Note that the seismogenic interface ("megathrust + afterslip") zone is postulated to extend downdip to the top of the ETS events. The Hanford Site lies to the east of the limits of the figure.

Given the new data, models, and methods that have become available regarding the landward extent of the plate interface source, the TI Team considered the characterization given in the logic tree in the BC Hydro SSC model. The logic tree considered three potential locations for the landward-to-downdip extent of the seismogenic plate interface, which are labeled A, B, and C in Figure 8.17. At the time of developing the alternatives, the focus lay on the thermal models and the locations of the "coseismic transition zone." Regardless of the original constraints, the TI Team considered the degree to which the three alternatives capture the range of current interpretations for the location of the downdip limit of seismogenic rupture, based on all available data and interpretations. For example, the westernmost

alternative (A) lies at the approximate location of many of the thermal and geodetic models; the easternmost alternative (C) is the approximate location derived from models that conclude the seismogenic interface lies updip of the ETS events and is close to, but slightly updip of, the interpreted location of the FMC; and the central alternative (B) simply lies between the other two alternatives and generally represents the studies that have attempted to integrate all data types. The weights assigned to the alternatives in the BC Hydro study were as follows:

Location A [0.1]
Location B [0.7]
Location C [0.2].

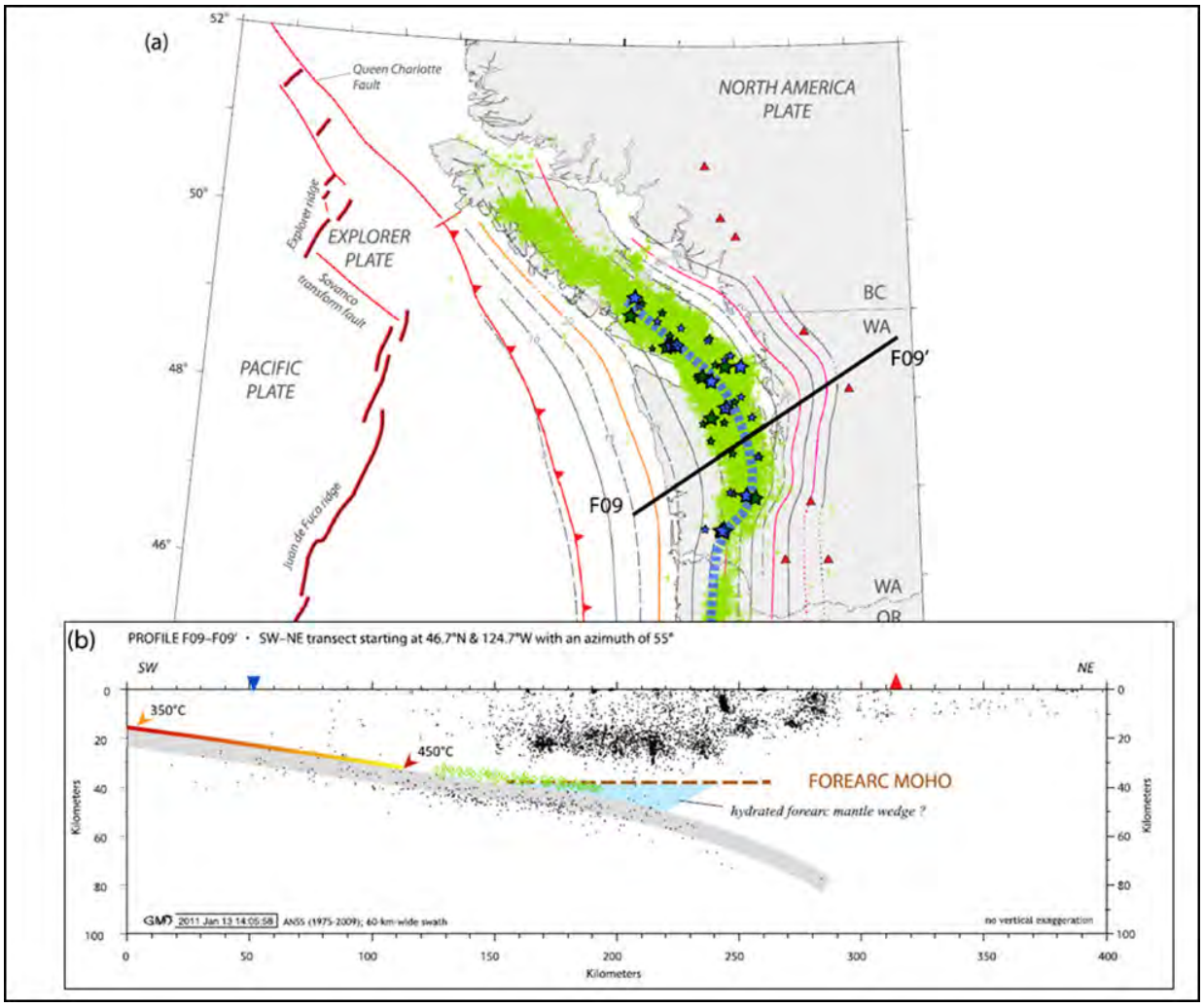


**Figure 8.16**. Interpreted location of forearc mantle corner (FMC) that lies at the intersection of the forearc Moho and the plate interface (McCrory et al 2014). The FMC lies at the location of the blue dashed line in map view (a), which also shows the data constraints (good-fair: large stars; poor: small stars). ETS events are shown as green dots. Interpreted locations of the 350° and 450°C isotherms at the top of the slab are also shown in cross section (b).

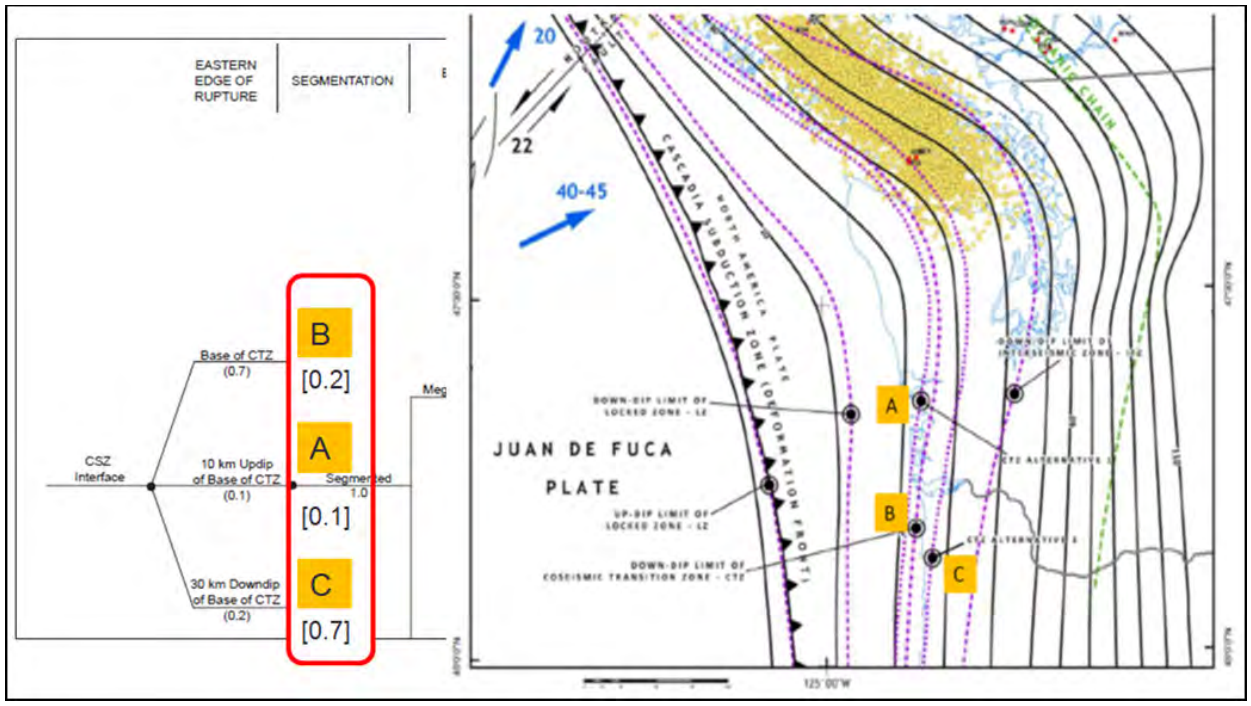


**Figure 8.17**. Interpretation of the eastern or downdip extent of the seismogenic plate interface in the BC Hydro study (BC Hydro 2012). The map shows the three alternative locations A, B, and C and associated pink dotted lines. ETS events in the northern part of the CSZ are shown by the yellow dots. The logic tree for the alternatives is also shown. Hanford Site lies to the east of the limits of the figure.

Based on consideration of the new information, the TI Team concluded that the three alternatives continue to provide a reasonable and defensible range of interpretations of the downdip extent of the interface. However, the TI Team also concluded that the relative weights assigned to the alternatives are not a representative description of current knowledge and uncertainties. Additional weight should be assigned to alternative C, which appears to be more consistent with interpretations that consider ETS events and the FMC. The assessment of weights for the three alternative locations is as follows:

| | |
|---|---|
| Location A | [0.1] |
| Location B | [0.2] |
| Location C | [0.7]. |

In addition to the location of the interface, the TI Team considered the new information related to the magnitude of Mmax and Mchar, as well as to the timing of paleoseismic earthquakes. For example, Witter et al. (2012) report on interpretations of the size of paleoseismic earthquakes based on the modeled slip of interface events associated with tsunami deposits. The implied magnitudes of the paleo-earthquakes are not well constrained, but lie within the range already included in the BC Hydro logic tree for Mchar and Mmax. No new primary data have been published related to the number and timing of paleoseismic events that would lead to the need to revise the recurrence rates given in the BC Hydro logic tree. Rather, the detailed statistical analyses of the paleoseismic data conducted for the BC Hydro project have now been published (Kulkarni et al. 2013). The TI Team concluded that the BC Hydro logic-tree elements related to Mchar, Mmax, and recurrence for the plate interface source do not require updating.

## 8.3 Seismic Source Zones

This section describes the seismic source zones characterized in the SSC model. The conceptual basis and criteria for identifying seismic sources generally, and for defining source zones specifically, are given in Section 8.1. This section (8.3) provides information regarding the elements of the SSC model that resulted from the TI Team's evaluation of available data, models, and methods and its integration process. This discussion is intended to show that the seismic source zones identified are technically defensible and that the center, body, and range of uncertainties included in the model are appropriate. First, the two types of source zones included in the model are discussed (Section 8.3.1). Then the various source zone characteristics and the methods used to assess them are described in Section 8.3.2. Finally, the specific seismic source zone characteristics in the SSC model for the four zones are described in Sections 8.3.3 and 8.3.4.

### 8.3.1 Two Types of Seismic Source Zones

As discussed in Section 8.1.4.2, all seismic sources are identified according to a set of criteria applied by the TI Team. Further, seismic source zones are an alternative to fault sources in the sense that fault sources are only called out in the SSC model if they exhibit a unique set of characteristics (i.e., differences in p[S], recurrence, Mmax, or future earthquake characteristics) that would suggest that they would localize seismicity differently from adjacent regions. Consistent with this definition and with current SSC practice (e.g., NRC 2012a), seismic source zones are assumed to have a p[S] = 1 throughout the zone and, unless indicated by source-specific data, the characteristics that define each source are assumed to be uniform throughout the zone. For example, the assessed style of faulting and Mmax distribution would apply to all parts of the zone.

The seismic source zones identified in the SSC model are listed in Table 8.2 and are shown in Figure 8.18.

**Table 8.2**. Seismic source zones included in the SSC model.

| Zone Name | Identifier |
|---|---|
| Yakima Fold and Thrust Belt Background | YFTB |
| Zone B | Zone B |
| Zone C | Zone C |
| Zone D | Zone D |

Two types of seismic source zones are identified: the YFTB source zone is a "background" zone to the fault sources of the YFTB zone, and Zones B, C, and D are source zones that do not include identified fault sources. The exceptions are the Arlington, Luna Butte, Laurel, and Maupin faults that exist within the YFTB zone and extend into the adjacent Zone D. However, the characteristics of these faults are defined within the YFTB zone and additional faults within Zone D have not been identified separately as fault sources. The YFTB zone is also the host zone to the Hanford Site.

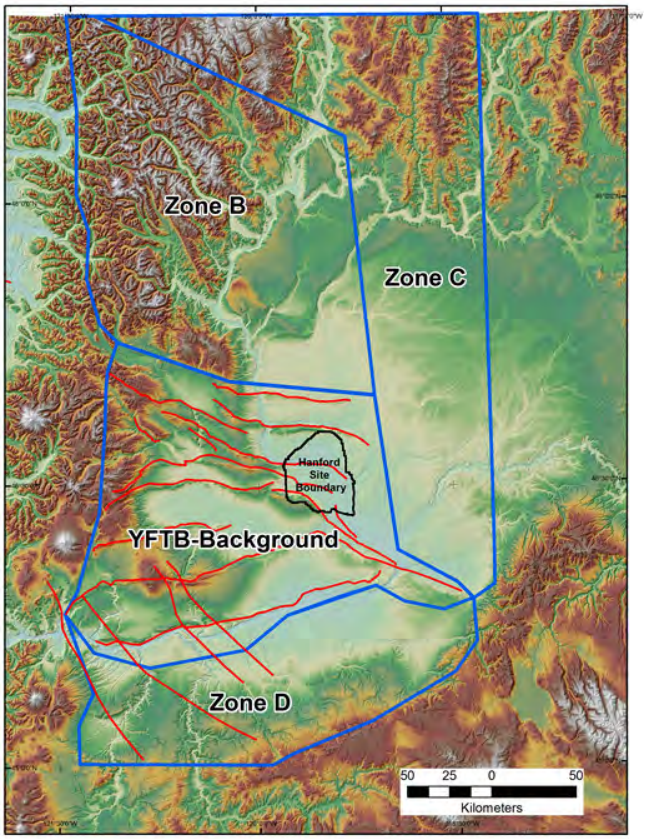


**Figure 8.18**. Map of the four seismic source zones in the SSC model. Fault sources are shown by the red lines.

The reason for the two types of source zones is the relative contribution that nearby sources make to the hazard at the site. Sensitivity analyses (V. Montaldo-Falero presentation at WS1 and WS3; Chapter 10.0) show that the fault sources contribute most to the site hazard, followed by the YFTB source zone, followed by the other source zones. This implies that identifying and characterizing the nearby faults is necessary and, in light of that characterization, the zone that includes those faults should be characterized differently from more distant zones. For example, the Mmax distribution for the YFTB zone is different from neighboring zones because the major faults, which, because of their extent, would localize larger earthquakes, are treated separately and the remaining parts of the zone would host shorter faults. Because of their distance from the site, individual faults within Zones B, C, and D are not specifically identified and characterized. Rather, the faults that exist within these source zones are modeled in the PSHA by "virtual faults" whose locations are random within each zone and whose characteristics are assessed in the SSC model.

### 8.3.2 Source Zone Characteristics for the SSC Model

This section describes the approach and methods used to characterize seismic source zones in the SSC model. The methods used are applicable to the data that are available for the characterization as well as the tectonic environment of the site region. For example, the characteristics of future earthquakes within the YFTB source zone, such as the style of faulting and orientation of ruptures, are assessed in light of the available geologic and seismologic data within that zone. If uncertainties exist, they are duly incorporated into the model.

The characterization of seismic source zones involves the consideration and incorporation of both epistemic uncertainties in logic trees as well as aleatory variabilities, expressed as relative frequencies. For example, aleatory assessments define the characteristics of future ruptures within the source zones, such as the relative frequency of future earthquakes having particular styles of faulting or geometries. The aleatory assessments are discussed in Sections 8.3.3 and 8.3.4 but, because they are aleatory and not epistemic, they are not shown in the logic trees.

#### 8.3.2.1 Source Boundary Locations

Source boundaries specify the 3-D location and geometry of a seismic source. For a source zone, the boundaries specify the lateral extent and thickness of the zone. As discussed in Section 8.1.1, source zone boundaries are defined by expected differences in earthquake recurrence rate, Mmax, future earthquake characteristics, or p[S]. In the context of source zones, differences in p[S] are not diagnostic because all source zones are assumed to be seismogenic. Differences in earthquake recurrence rate might be defined by distinct differences in the rate density (number of events per unit area) from one domain to another. Those differences might be accommodated either by drawing a source boundary that separates regions having different recurrence rate densities or through the use of a smoothing procedure that accounts for spatial variations in recurrence parameters. Differences in Mmax may be a function of whether or not fault sources have been defined within the source, the number and scale of known faults within the zone, or the size of the largest observed historical or instrumental earthquake. In addition to the observed seismicity record, differences in either recurrence rates or Mmax may also be inferred based on distinct seismotectonic boundaries and features.

Future earthquake characteristics include the seismogenic thickness, style of faulting, and geometry of ruptures. Differences in these characteristics spatially may provide the basis for drawing a source zone boundary. Defining differences in future earthquake characteristics necessitates the consideration of a wide variety of data sets. For example, spatial differences in seismogenic crustal thickness can be identified using earthquake hypocenter depths and by considering major tectonic boundaries. Likewise, expected differences in the geometries of future ruptures can be assessed based on consideration of earthquake focal mechanisms: structural geologic data, seismotectonic features, and geophysical data regarding the orientations of preexisting structures, and kinematic indicators of the orientation of the contemporary tectonic stress regime.

The preliminary SSC model for seismic source zones was based on the source zones defined in the Mid-Columbia PSHA (JBA et al. 2012). These source zones were rooted in a geodetic “block” model presented by McCaffrey et al. (2007). As part of the development of the SSC model for the Hanford PSHA, the Mid-Columbia source zone boundaries were modified based on a variety of new data and information, including revised geodetic models (e.g., McCaffrey et al. 2013), reanalysis of YFB fault geometries based on topographic analyses including newly acquired, high-resolution LiDAR imagery, new results from the QGS (Appendix E), the updated earthquake catalog developed for this project, and new data and analyses of potential field data (e.g., Blakely et al. 2013). The technical bases for the source zone boundaries for the YFTB source zone are given in Section 8.3.3 and for Zones B, C, and D in Section 8.3.4.

#### 8.3.2.2 Nature of Boundaries with Respect to the Propagation of Future Ruptures

In the hazard calculation procedure, finite fault ruptures nucleate on virtual faults within each source zone. As discussed in Section 8.3.2.6, the length and area of rupture for each earthquake are related to the magnitude of the earthquake being modeled. Earthquake ruptures that nucleate near a source zone boundary can either extend across the boundary (a "leaky" boundary) or be terminated at the boundary (a "strict" boundary), depending on the assessed nature of the boundary. In the SSC model, all source zone boundaries are assessed to be leaky to future ruptures. The basis for this assessment is that changes in tectonics, geology, and the seismicity across the zone boundaries are not sharply delineated. If the boundaries locally and sharply separated regions with distinctly different rupture strikes or styles of faulting, then weight could be given to strict zone boundaries.

#### 8.3.2.3 Seismogenic Crustal Thickness

The thickness of the seismogenic crust defines the depth extent of ruptures that release seismic energy important to ground motions. Seismogenic thickness is typically estimated based on consideration of the depths of earthquake hypocenters and, due to a lack of detailed knowledge of the processes that locally control the thickness at any given point, it is usually assumed that seismogenic thickness varies gradually spatially unless there is clear evidence otherwise. In the SSC model, the uncertainties in seismogenic crustal thickness are included in logic trees for each seismic source zone. Sensitivity analyses conducted using the preliminary SSC model showed only a small sensitivity to the seismogenic crustal thickness assessed for the YFTB source zone and the fault sources included within it, and no sensitivity to the thickness assessed for Zones B, C, and D.

The assessment of seismogenic crustal thickness is based on the focal depth distributions of well-recorded earthquakes, such that hypocentral depth can be determined with a high degree of confidence. To assist in the use of this information and to ensure high-resolution hypocenter locations, a substantial high-resolution earthquake relocation effort was conducted as part of this study, as summarized in Section 5.3 and presented in Appendix F.

Given a well-constrained focal depth distribution, physical considerations given by various researchers suggest that the base of the seismogenic zone is identified as lying near the deepest of the observed focal depths. For example, Scholz (1998) identifies the 300°C isotherm as corresponding to the onset of dislocation creep in quartz, which he interprets to control the seismic/aseismic transition zone. Tanaka (2004) and Tanaka and Ito (2002) compare high-quality thermal measurements and seismicity depth data to examine the concept that temperature is a fundamental parameter for determining the thickness of the seismogenic zone. Their gridded heat flow or geothermal gradient and $D_{90}$, the depth above which 90% of earthquakes occur, correlated well with each other. The evaluated temperatures for $D_{90}$ range between 250°C and 450°C, which falls within the typical range for defining the seismogenic zone (e.g., Fagereng and Toy 2011). The TI Team therefore concluded that the approach taken in the CEUS SSC project (NRC 2012a) of using $D_{90}$ to estimate the depth of the seismogenic crust was appropriate. Epistemic uncertainty associated with the seismogenic thickness is reflected in the logic tree and accounts for uncertainty in the assessment of $D_{90}$ as well as the degree to which $D_{90}$ provides a unique estimate of seismogenic thickness.

In the case of the YFTB source zone, the observed focal depth distribution of instrumental earthquakes shows that the numbers of earthquakes are dominated by small-magnitude events ($\mathbf{M} < 2$)

and a high number of events occurring in the upper 3 km (Figure 8.19). The TI Team was concerned that the large numbers of small-magnitude very shallow events could bias the assessment of $D_{90}$ toward shallower depths. However, sensitivity tests that placed limits on the number of earthquakes in the 1- to 3-km bins showed that their effect on the calculation of $D_{90}$ was very minor (less than 1 km). The distributions of seismogenic thickness for the YFTB source zone are given in Section 8.3.3 and for Zones B, C, and D they are given in Section 8.3.4.

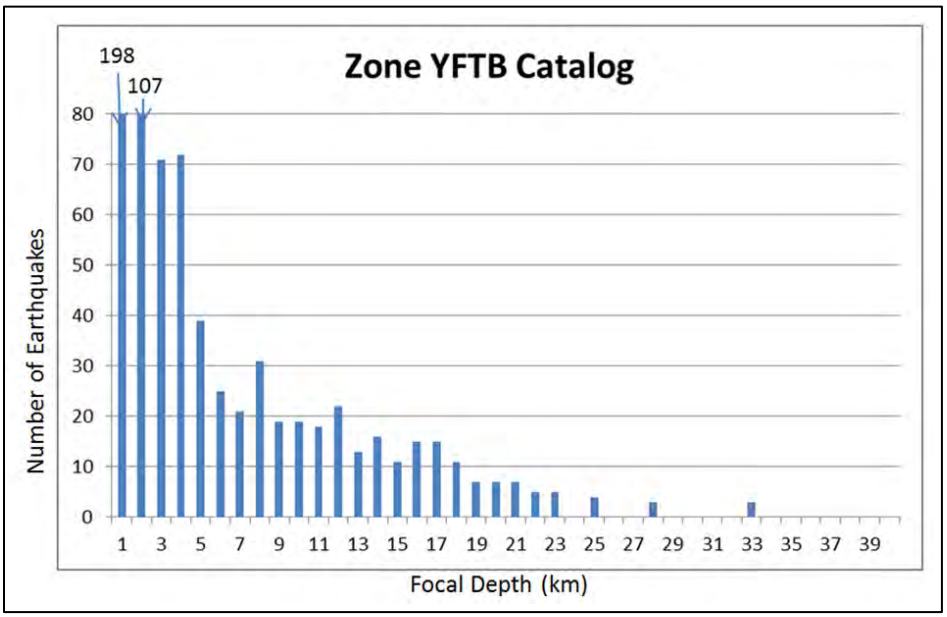


**Figure 8.19**. Focal depth distribution for all earthquakes within the YFTB source zone. Note the large numbers of very shallow earthquakes, which are mostly M < 3. Bins are 1 km wide.

#### 8.3.2.4 Depth Distribution and Ruptures of Future Earthquakes

The hazard calculations assume that future earthquakes will be associated with finite ruptures whose size is magnitude-dependent. The depth of nucleation (focal depth) of these earthquakes must be specified in the SSC model. The maximum depth is the depth of the seismogenic thickness, but the relative frequency of other focal depths must also be considered. This assessment could be especially important in a reverse-faulting regime in which the downdip dimension of future ruptures could be large relative to vertical faults. The depth distribution of hypocenters provides valuable information related to the relative frequency of focal depth, but the focal depth data in the Hanford region is dominated by small-magnitude (**M** < 3) earthquakes and most of these lie in the very shallow crust (Figure 8.19). Therefore, consideration must also be given to the observation that the depths of larger magnitude earthquakes commonly occur deeper within the seismogenic crust (e.g., Das and Scholz 1983; Mori and Abercrombie 1997).

Within the seismic source zones and along fault sources in the SSC model, the depth distribution of future moderate-to-large earthquake focal depths is defined by a combination of the focal depth distribution for small-magnitude earthquakes and magnitude-dependent models for the location of the hypocenter relative to the rupture for reverse faults. The focal depth distribution is a starting point for expressing the relative frequency of various nucleation depths of future earthquakes, provided that the observed distribution is judged to be representative of the future depths. The starting focal depth

distribution for the YFTB source zone and faults within that zone is given in Figure 8.19. As discussed in Section 8.3.2.3, the observed depth distribution has a large number of very shallow small-magnitude (**M** < 2) earthquakes. The TI Team considered whether the relative frequency of the observed depths would be representative of the expected relative frequency of moderate-to-large earthquakes. The decision was made to modify the observed distribution to lower the relative numbers of very shallow earthquakes because they are very small earthquakes and their large numbers were not judged by the TI Team to be representative of the relative frequency of nucleation of larger magnitude events. This interpretation is supported by the analysis of the shallow events within the CRB that suggests that these very small earthquakes are the result of a different process separate from the deeper crustal stress field, as reflected by swarm occurrence at very shallow depth within the basalts (see Section 8.1.4.3 and Section 6.2.3 in Appendix E). Figure 8.20 shows the focal depth distribution (expressed as the relative frequency or fraction of the total number of events) for the YFTB zone with **M** < 2 earthquakes removed, as well as the alternative depth distribution (labeled "assessed model") that the TI Team considered to be appropriate for use in expressing the relative frequency of the nucleation depths of future moderate-to-large earthquakes. Each earthquake is then associated with a rupture area that is magnitude-dependent, as described below.

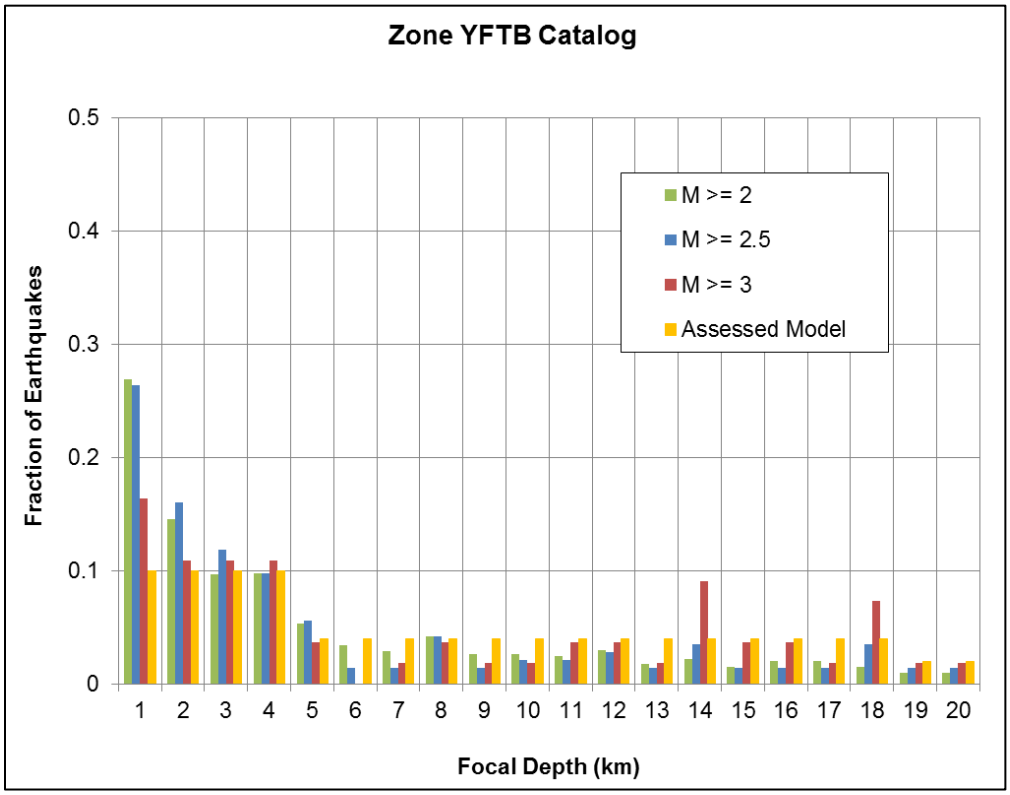


**Figure 8.20**. Focal depth distribution of observed earthquakes M ≥ 2 within the YFTB source zone. The assessed alternative focal depth distribution selected by the TI Team is shown in yellow. This distribution is used to model the nucleation depths of future moderate-to-large earthquakes within the YFTB source zone and for faults within that zone. Bins are 1 km wide.

Given the proposed alternative depth distribution and given the expected dominantly reverse style of faulting, the TI Team adopted an approach that would realistically model the downdip rupture of future earthquakes. The following procedure was followed to model future earthquake ruptures in the hazard calculations. For each magnitude, rupture area is calculated using the inverse of Hanks and Bakun (2008) (see Section 8.3.2.6). For the rupture length-to-width aspect ratio, the model for reverse faulting defined in Appendix B of Chiou and Youngs (2008) is used until the width reaches the maximum defined by the crustal thickness and the dip. For each assessed focal depth (defined in 1-km increments beginning at a depth of 1 km), the distribution for the location of the hypocenter with respect to the rupture for reverse faults defined in Appendix B of Chiou and Youngs (2008) defines a distribution for how to place the rupture on the hypocenter. If the rupture extends above the surface or below the seismogenic thickness, that case is discarded. Summing the weights for the remaining cases (product of the focal depth frequency and the probability of hypocenter location) and normalizing the results produces a distribution for distance to the top of the rupture ($Z_{TOR}$) that is a function of magnitude, dip, and thickness.

Examples of the $Z_{TOR}$ distributions are given in Figure 8.21 for two cases that are part of the suite of possibilities for fault sources within the YFTB source zone: shallow dip and large seismogenic thickness, and steep dip and small thickness. In both cases, the assessed focal depth distribution for the YFTB source zone is assumed. As can be seen in the figure, the shallow dip/large thickness case (upper panel) shows a range of distances for a full range of magnitudes (zero distance means that the fault ruptures the surface). This is because the very wide downdip widths allow for a range of ruptures that do not rupture the surface. In the steep dip, small thickness case, essentially all magnitudes larger than about **M**6 rupture the surface.

### 8.3.2.5 Style of Faulting, Strike, Dip of Future Ruptures

Future earthquakes within the source zones must be described according to the characteristics needed to model them in the GMC model. So, in addition to their depth and rupture area, their style of faulting (also called the sense of slip) and geometry must also be provided. In the case of source zones, these are descriptions that apply to the virtual faults that are modeled in the hazard calculations within each zone. Based on sensitivity analyses showing that the only source zone that makes a significant contribution to the hazard at the site is the YFTB source zone (V. Montaldo-Falero presentation at WS3; Chapter 10.0), most of the attention is given to that zone with regard to future earthquake characteristics.

The assessment of the characteristics of future ruptures comes from a consideration of the tectonic setting, characteristics of nearby fault sources, earthquake focal mechanisms, and other strain indicators including geodetic data. As discussed in Section 4.2, the contemporary tectonic setting in the YFB region is compressional with the major axis of maximum horizontal compression being approximately north-south. This is confirmed by the geologic kinematic indicators on the fault sources (Section 8.4.3.3 and Appendix E), earthquake focal mechanisms, and geodetic data. Available earthquake focal mechanisms in the Hanford Site region are shown in Figure 8.22 and, east of the Cascades, they show primarily reverse faulting with lesser amounts of strike slip. Inversion of the focal mechanisms was conducted for this project (see Section 6.2.1 in Appendix E) and shows that the axis of maximum horizontal compression is approximately north-south. This is generally consistent with the modeled north-northeast deformation field interpreted from geodetic data (Figure 8.23).

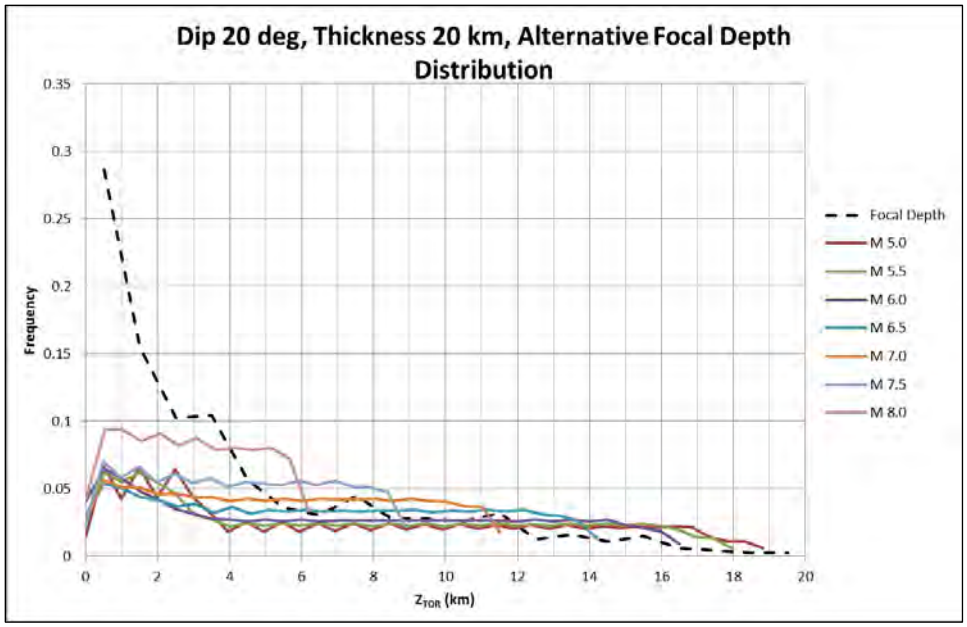


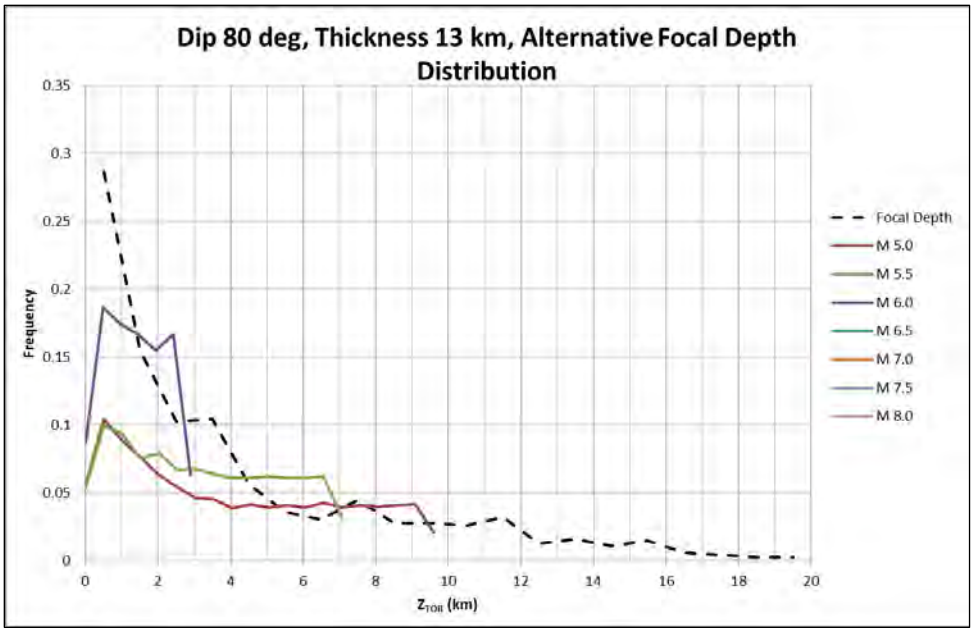


**Figure 8.21**. Examples of distributions of $Z_{TOR}$, distance to the top of rupture, for two assumed fault dips and seismogenic thicknesses and a range of magnitudes. Zero depth implies rupture to the surface. The assessed focal depth distribution used in both cases, dashed black line, is that for the YFTB source zone and shown in Figure 8.20.

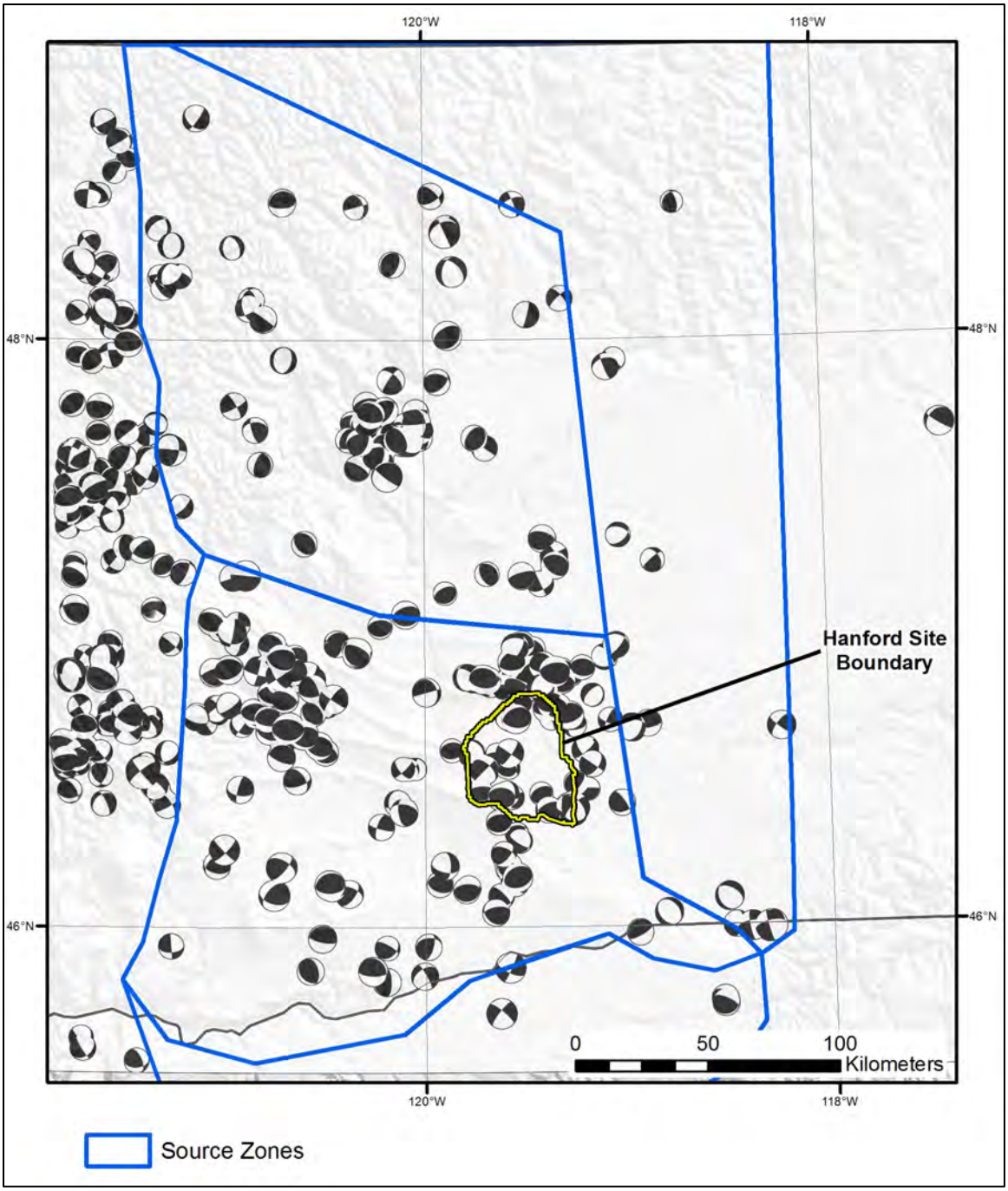


**Figure 8.22**. Earthquake focal mechanisms in the Hanford Site region. The Hanford Site is outlined in yellow and the seismic source zone boundaries are shown with blue lines for reference. Focal mechanisms are lower hemisphere projections with black indicating compression. Most focal mechanisms in the YFTB zone show reverse faulting with lesser amounts of strike slip. Earthquake magnitudes are generally $M \geq 3$.

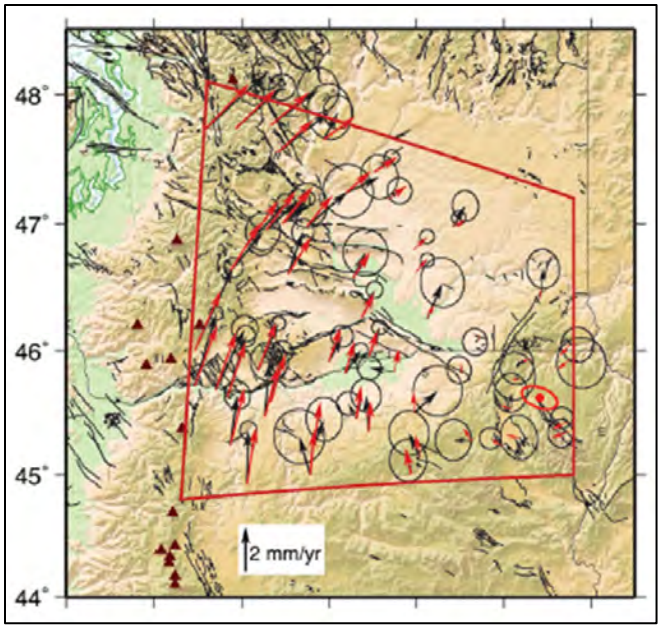


**Figure 8.23**. Observed (black) and predicted (red) GPS-derived velocities within the YFB relative to North America. Faults of the YFB are shown with black lines. Error ellipses are at 70% confidence level. (From McCaffrey 2013)

To take advantage of the focal mechanisms for purposes of characterizing future earthquake characteristics, analyses were conducted of 447 events within the region longitude -117.5 to -121.5, latitude 45.5 to 49°N. Using the definitions of styles of faulting based on rake angles, the numbers of earthquakes having particular styles of faulting are summarized below and shown in Figure 8.24. Definitions of various styles of faulting are from Aki and Richards (1980) and are consistent with the definitions used for the GMC models:

- 254 (57%) reverse events (rake of 90° ± 60°)
- 100 (22%) strike slip events
  - 50 (11%) left-lateral (rake of 0° ± 30°)
  - 50 (11%) right-lateral (rake of ± 180° ± 30°)
- 96 (21%) normal events (rake of -90° ± 60°).

As discussed in Section 8.3.3, the analysis of focal mechanisms provides a useful data set for making an aleatory assessment of the expected styles of faulting for the YFTB source zone.

In addition to styles of faulting, the analysis of focal mechanisms provides information regarding the strikes and dips of ruptures, which are also needed for the SSC model. The results of the analysis for the strikes of all earthquakes in the data set are shown in Figure 8.25, which shows strikes that are generally east-west, with a range in the northeast to southeast quadrants. The results for reverse-faulting earthquakes are also shown in Figure 8.25 and they are quite similar. As discussed in Section 8.3.3, these strikes are in accordance with the geometries of mapped faults and structural trends in the YFB region.

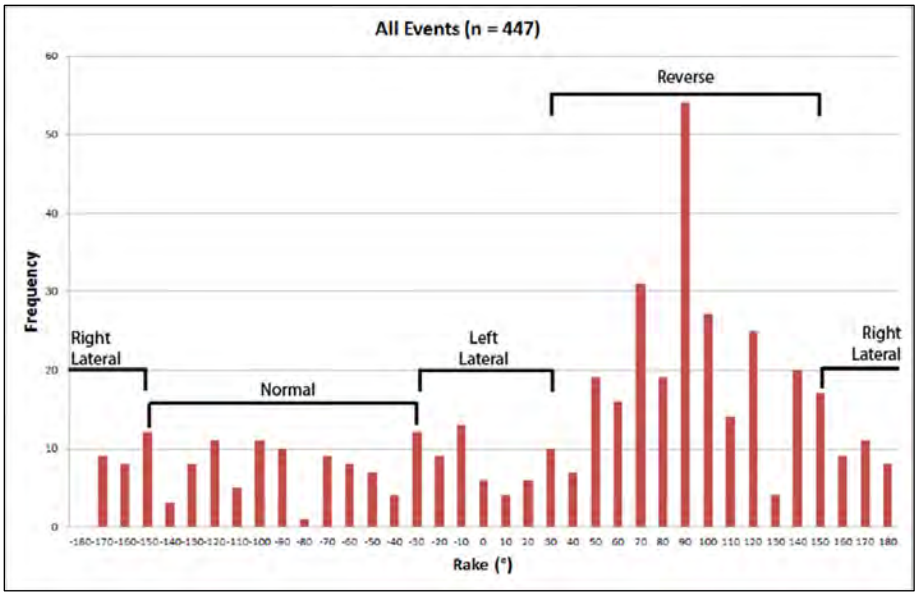


**Figure 8.24**. Rake angles for earthquake focal mechanisms in the YFB region. Ranges of rakes for a given style of faulting are from Aki and Richards (1980).

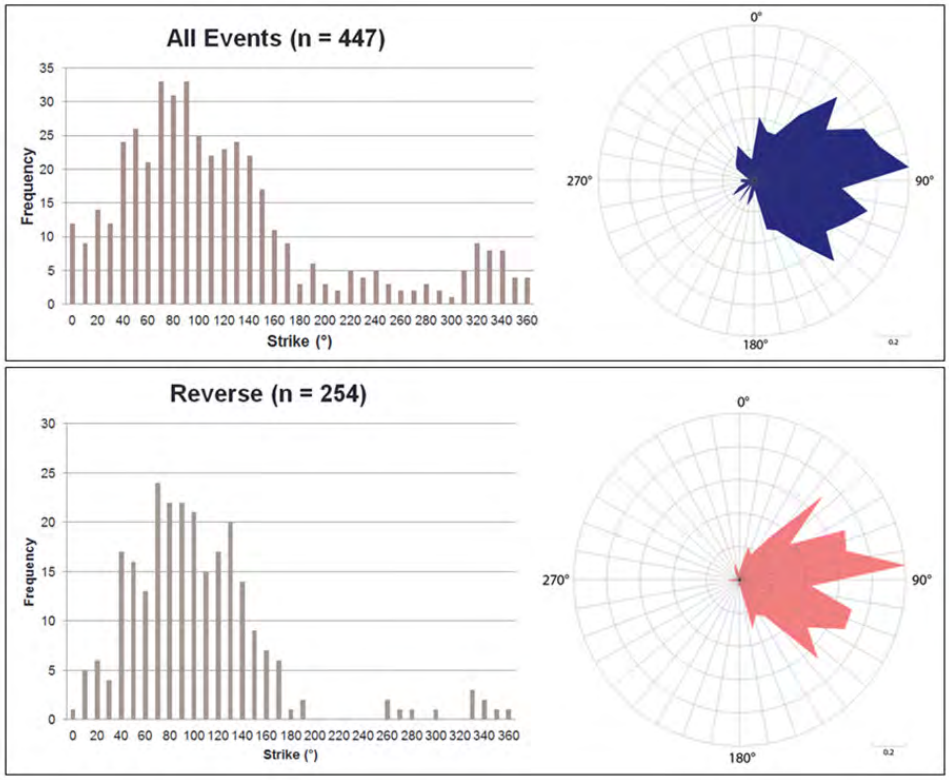


**Figure 8.25**. Distribution of strikes from the analysis of earthquake focal mechanisms, shown as a histogram and a rose diagram. The upper panel is for all earthquakes and the lower panel is for reverse events.

The dips of the earthquakes in the focal mechanism data set are shown in Figure 8.26 for all earthquakes and for reverse earthquakes. A broad range of dips is observed for all earthquakes and, as

can be seen by comparing both panels of the figure, the dips of reverse earthquakes dominate the dips for all events. Importantly, the larger data set includes a relatively large number of strike slip events and the steeper dips associated with these events contribute to the larger numbers in the dip range of 70 to 90°.

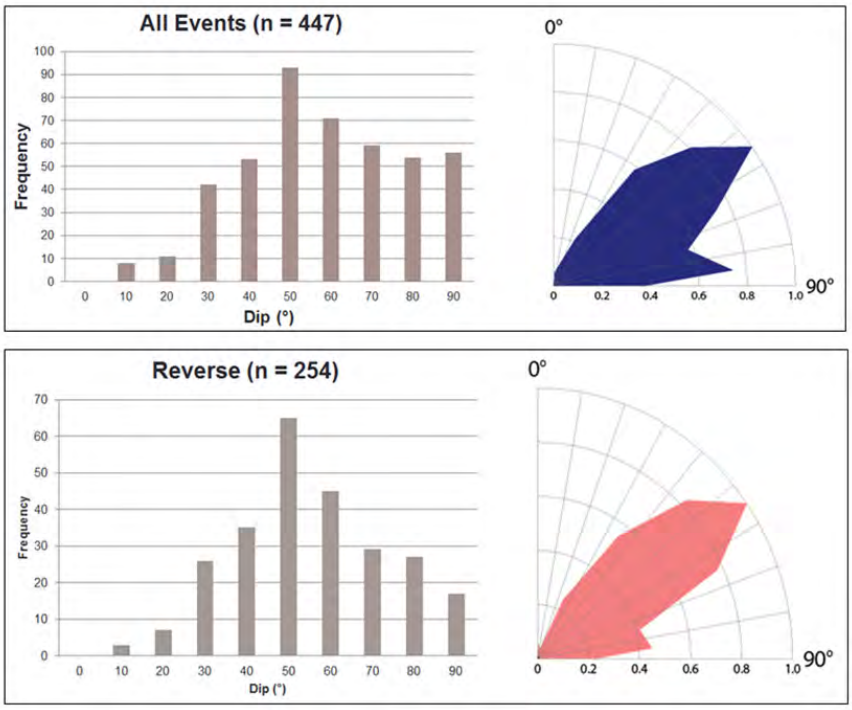


**Figure 8.26**. Distribution of fault dips from the analysis of earthquake focal mechanisms, shown as a histogram and a rose diagram. The upper panel is for all earthquakes and the lower panel is for reverse events.

As discussed in Section 8.3.3, these analyses of the earthquake focal mechanisms are coupled with geologic and tectonic considerations to arrive at aleatory distributions of the styles of faulting, strikes, and dips of future ruptures within the YFTB source zone. The distributions are aleatory and represent the relative frequency of different conditions that are all assessed to be possible within the source zone. As discussed in Section 8.3.4, more distant source zones—B, C, and D—are modeled more simply by their style of faulting and random geometries, because of their minor contribution to the hazard at the Hanford Site (see V. Montaldo-Falero presentation at WS3).

### 8.3.2.6 Rupture Area vs Magnitude Relationships for Hazard Analysis

Because future earthquake ruptures within the seismic source zones are modeled as finite faults, their dimensions of rupture must also be modeled and they are a function of magnitude. Hence, the recurrence curves for each seismic source zone will define the relative numbers of earthquakes having particular magnitudes and their associated rupture dimensions. The important assessment here is the relationship between rupture area and moment magnitude. Given a rupture area, the associated length and width are modeled for the hazard calculations as described in Section 8.3.2.4, which is appropriate for reverse-faulting earthquakes.

As discussed in detail in Section 8.4.3.8, alternative rupture area versus magnitude relationships have been proposed in the literature and were considered for application in this study. A common feature of these relationships is that they appear to be insensitive to the style of faulting, such that they can be used for all styles of faulting identified for the source zones in the SSC model. Section 8.4.3.8 discusses the selection of two alternative relationships for use in assessing the characteristic magnitudes (Mchar) for fault sources, the Hanks and Bakun (2008, "HB08") relationship and the Stirling et al. (2008, "S08") relationship. Both of these relationships are considered to be applicable for use in the SSC model for purposes of estimating Mchar. However, due to the minimal difference in their magnitude ranges of interest and, therefore, minor contribution to uncertainty, only the HB08 relationship is selected for use in the hazard calculations.

The magnitude dependency for rupture area A is given by the following relationships as given by Hanks and Bakun (2008):

$$\mathbf{M} = \log A + 3.98 \text{ for } A \leq 537 \text{ km}^2; \text{ and}$$

$$\mathbf{M} = 1.33 \log A + 3{:}07 \text{ for } A > 537 \text{ km}^2.$$

For use in the hazard calculations, a rupture area is needed for a given magnitude, so the inverse of the relationship is used.

### 8.3.2.7 Maximum Magnitudes

The assessment of maximum magnitudes (Mmax) for seismic source zones usually entails significant uncertainty. Approaches have been developed for use in stable continental regions (Johnston et al. 1994; NRC 2012a) that rely on a Bayesian procedure, but the YFB region does not qualify as a stable continental region, according to the criteria given by Johnston et al. (1994). A common approach to assessing Mmax is to consider the historical record and the largest observed earthquake within the seismic source zone of interest. In the case of the YFTB source, the largest observed earthquake is **M** 4.79 (expected magnitude in the project catalog, see Section 6.5) that occurred on November 17, 1918. This magnitude is judged by the TI Team to be too small to provide any meaningful constraint on the Mmax for the YFTB source zone. However, as discussed in Section 8.3.4, the 1872 Lake Chelan earthquake (**M** 6.5 – 7.0) that occurred within Zone B is judged to be sufficiently large to provide information related to Mmax for that source zone.

An important consideration in assessing Mmax for the source zones in the SSC model is the presence or absence of fault sources within the zone. Fault sources have substantial dimensions (both length and width) and, as a result, are capable of generating larger earthquakes that those parts of the crust lacking through-going faults. Based on this observation, an approach was developed for the YFTB source zone that accounts for the fact that fault sources within the zone have been "removed" and are treated separately in the SSC model. As a result, it is judged that the lower part of the distribution of Mmax for the fault sources should provide a reasonable upper constraint on the Mmax distribution for the YFTB source zone. This assumes that Mmax values much larger than the lower part of the Mmax distribution for faults would require through-going faults having dimensions comparable to those for the characterized fault sources.

As discussed in Section 8.4.3.8, the Mmax values for the fault sources are one-quarter magnitude unit larger than the Mchar values, which, themselves, have significant uncertainty. The combined uncertainty distribution for all fault sources in the SSC model is shown in Figure 8.27.

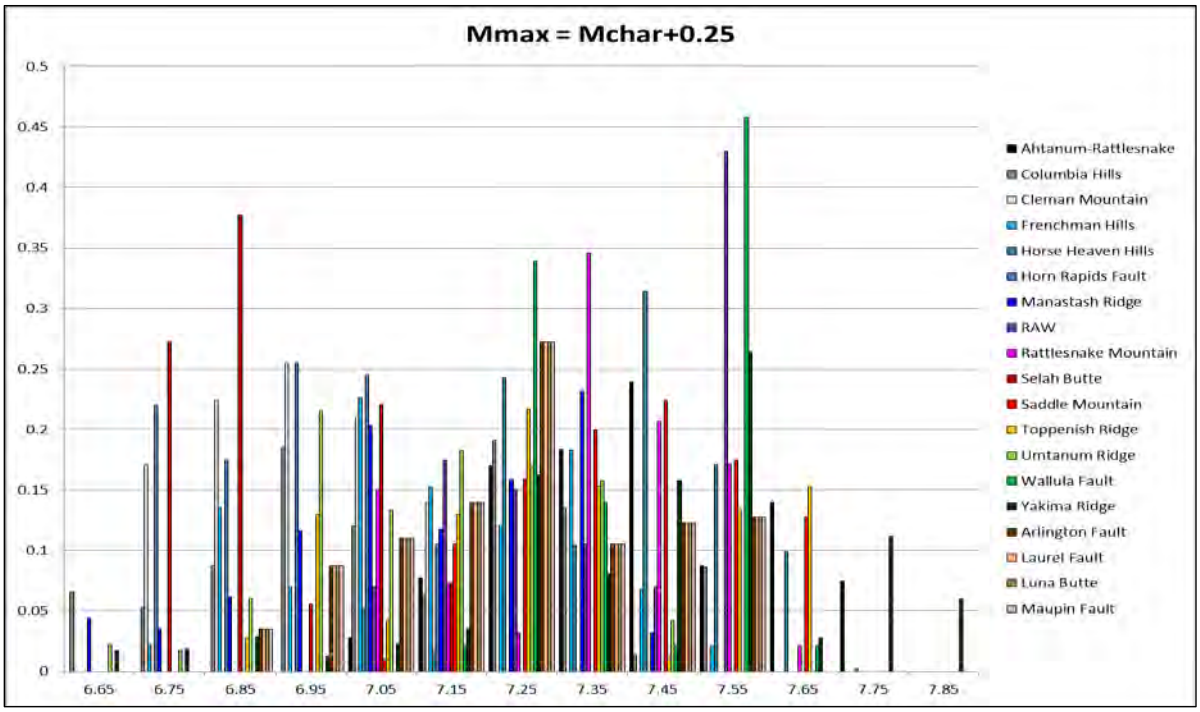


**Figure 8.27**. Probability distributions of Mmax for all fault sources in the SSC model.

Based on a consideration of the Mmax distribution for fault sources, an assessment of Mmax was made by the TI Team for the YFTB source zone, as described in Section 8.3.3. The same information was considered in assessing the Mmax for Zones B, C, and D, as well as the magnitude of the largest observed earthquake and the fact that fault sources have not been identified within those source zones.

### 8.3.2.8 Earthquake Recurrence

The assessment of earthquake recurrence within the seismic source zones entails the development of a catalog of earthquakes having a uniform size measure (moment magnitude), removal of dependent events through a declustering process, and correction of the catalog for incompleteness. As discussed in Chapter 6.0, for the Hanford PSHA a significant effort was devoted to developing a comprehensive crustal earthquake catalog that includes both historical and instrumental earthquakes (Section 6.2) and to converting all earthquakes from their native size measure to moment magnitude **M** (Section 6.5). These operations are associated with uncertainty and that uncertainty in magnitude for each earthquake is quantitatively addressed for purposes of recurrence calculations accounting for the bias that is introduced due to the exponential distribution of earthquake magnitudes in a recurrence curve (Section 6.5.4). The results are expressions of the expected magnitude E[M] for each earthquake in the catalog and corrected counts N* that account for this uncertainty and bias.

In addition, the earthquake catalog has been declustered to remove dependent earthquakes (foreshocks and aftershocks) using several declustering algorithms (Section 6.6). The resulting catalog of independent events is appropriate for use in recurrence calculations that are based on the assumption that

all earthquakes occur according to a Poisson process. Finally, an analysis of catalog completeness was conducted, which includes the assessment of the probability of detecting earthquakes as a function of time and magnitude in the region of the catalog (Section 6.7). The completeness analysis process used allows for full use of the historical and instrumental catalog.

Based on the methodologies discussed in Section 8.3.2.8, earthquake recurrence was calculated for the YFTB source zone (see Section 8.3.3) and Zones B, C, and D (see Section 8.3.4).

### 8.3.2.9 Spatial Variation of Recurrence

As discussed in Section 8.1.1, one of the criteria for defining seismic sources is differences in earthquake recurrence, which can be expressed as differences in the spatial density of earthquake occurrence defined by the pattern of observed earthquakes. If the observed pattern of spatial density variation is judged to be representative of the future distribution, the spatial pattern can be accounted for in the SSC model by either drawing seismic source boundaries or by spatial smoothing the recurrence parameters. Accordingly, the SSC model is based to a large extent on an assessment that spatial stationarity of seismicity will persist for time periods of interest for the Hanford PSHA (approximately the next 50 years). Stationarity in this sense does not mean that future locations and magnitudes of earthquakes will occur exactly where they have occurred in the past, based on the historical and instrumental record. Rather, the degree of spatial stationarity varies as a function of the type of data available to define the seismic source. Fault sources are based on geologic evidence of localized deformation from repeated large-magnitude earthquakes that occur in approximately the same location (i.e., the same fault) over geologic time periods. Uncertainties in the locations and sizes of these events are a function of the types of data available. Because the record that defines the fault sources spans a relatively long time period and records large-magnitude events, repeated events for these sources are expected to occur within a restricted location defined by the fault source.

On the other hand, patterns of seismicity within seismic source zones are defined from generally small- to moderate-magnitude earthquakes that have occurred during a relatively short (i.e., relative to the repeat times of large events) historical and instrumental record. Thus the locations of future earthquakes are not as tightly constrained by the locations of past earthquakes as they are for fault sources. Some recent studies within stable continental regions, such as the CEUS SSC study (NRC 2012a), have identified very large seismic source zones and have used “spatial smoothing” to express the spatial variation of recurrence rates. In the CEUS SSC study, b-values vary little across the study region and a-values vary at scales judged by the TI Team to reflect the belief that the observed record provides a spatial constraint on rate density variation. Likewise, in that smoothing approach, the recurrence calculation considers weighting of magnitudes in the recurrence rate calculations such that moderate events are assigned more weight than smaller events.

Spatial density models are used to define the future spatial density of earthquakes in the source zones when observed seismicity is used to define earthquake recurrence. The standard assumption is the location of future seismicity within a seismic source zone is spatially homogeneous with equal probability. Musson (2000) notes that this assumption is integral to an acceptable seismic hazard model and proposed that seismic hazard models be tested to verify that observed seismicity within particular source zones conforms to this assumption. Musson (2000) provides approaches for testing how well the observed seismicity pattern in a source zone conforms to the assumption of spatial homogeneity. He notes that a homogeneous pattern of seismicity does not need to necessarily be a uniform pattern, but may be random and not spatially clustered. If the seismicity within a source zone is not spatially

homogeneous, then an explanation should be provided for the inhomogeneity (perhaps it has a tectonic explanation), the zone should be subdivided into smaller zones that each are homogeneous, or spatial smoothing should be considered to account for the spatial variations.

The observed seismicity within the four seismic source zones in the SSC model is shown in Figure 8.28. Figure 8.28(a) shows that nearly all of the earthquakes are small in magnitude (M<4) and their epicenters are not uniformly spaced. Rather, the epicenters show local evidence of spatial clustering, which are termed swarms in this report. Examples include the swarm of seismicity near the southeastern boundary of the Hanford site (Wooded Island swarm) and the seismicity to the north of the site boundary in the Saddle Mountains area. High-resolution earthquake relocation analyses were conducted for this study (Appendix F) using sophisticated relocation techniques. One specific purpose of those studies was to evaluate whether or not the locations of earthquake hypocenters confirm the spatially clustered nature of seismicity. As discussed in the reports by Drs. Thurber and Waldhauser (Appendix F), the relocated earthquakes have a distinct spatially-clustered or swarm-like character. Further, their studies show that much of the seismicity occurs in the shallow parts of the crust (upper few kilometers) and there are no clearly-defined spatial correlations between the seismicity and known faults.

As noted by Musson (2000), even random distributions, which are homogeneous, show local evidence of spatial clusters. To test whether or not the seismicity within the four seismic sources is spatially homogeneous, the nearest-neighbor analysis given by Musson (2000) was applied to the four source zones. The locations of all epicenters are used in the analysis, and to assist in visualization, the epicenter locations for all magnitudes are shown in Figure 8.28(b). The nearest neighbor results indicated that the observed seismicity in Zone C can be considered consistent with a homogeneous distribution and that the distribution in Zone B is not consistent with a homogeneous distribution. The non-random spatial clustering within Zone B is clearly evident by visual inspection. In the cases of the YFTB zone and Zone D, the results were more equivocal and appeared to vary a bit based on which declustering algorithm was used to remove dependent events.

Given the results of these homogeneity tests, the TI Team also considered other key issues that are important in the consideration of spatial stationarity and whether or not spatial smoothing of recurrence parameters was appropriate for the seismic source zones. An important consideration is the fact that although the spatial distribution of observed events is based on small-magnitude earthquakes, the spatial smoothing of recurrence parameters would be used in the hazard analysis to describe the spatial variation of moderate-to-large-magnitude earthquakes. It was decided that spatial smoothing should be conducted using only the larger $\mathbf{M} > 3$ earthquakes to avoid possible spatial swarms of very small events in the CRBs. Zone B has hosted larger magnitude earthquakes and the significant spatial swarm in the central part of the zone was also the approximate location of the 1872 earthquake. Note that the cluster in that location is still present even after the catalog has been declustered to remove foreshocks and aftershocks. Another important consideration is which recurrence parameters are subject to smoothing. The TI Team decided to allow for smoothing of the equivalent number of events, N*, but to consider b-values to be uniform (with appropriate uncertainty) throughout each source zone. This assessment is consistent with the assessments of b-values for the source zones in the CEUS SSC project (NRC 2012a). In that study, the source zones are very large relative to the size of the Hanford PSHA sources (by more than a factor of 10), yet very little variation in b-values was assessed. This is also consistent with the constant b-values assessed for seismic source zones in the U.S. National Seismic Hazard maps (Petersen et al. 2008). Given the relatively small dimensions of the Hanford seismic source zones and the absence of tectonic mechanisms that might suggest that spatial variations in b-values might be appropriate (e.g., active volcanic-related seismicity), the TI Team assessed the b-values within each source zone to be uniform.

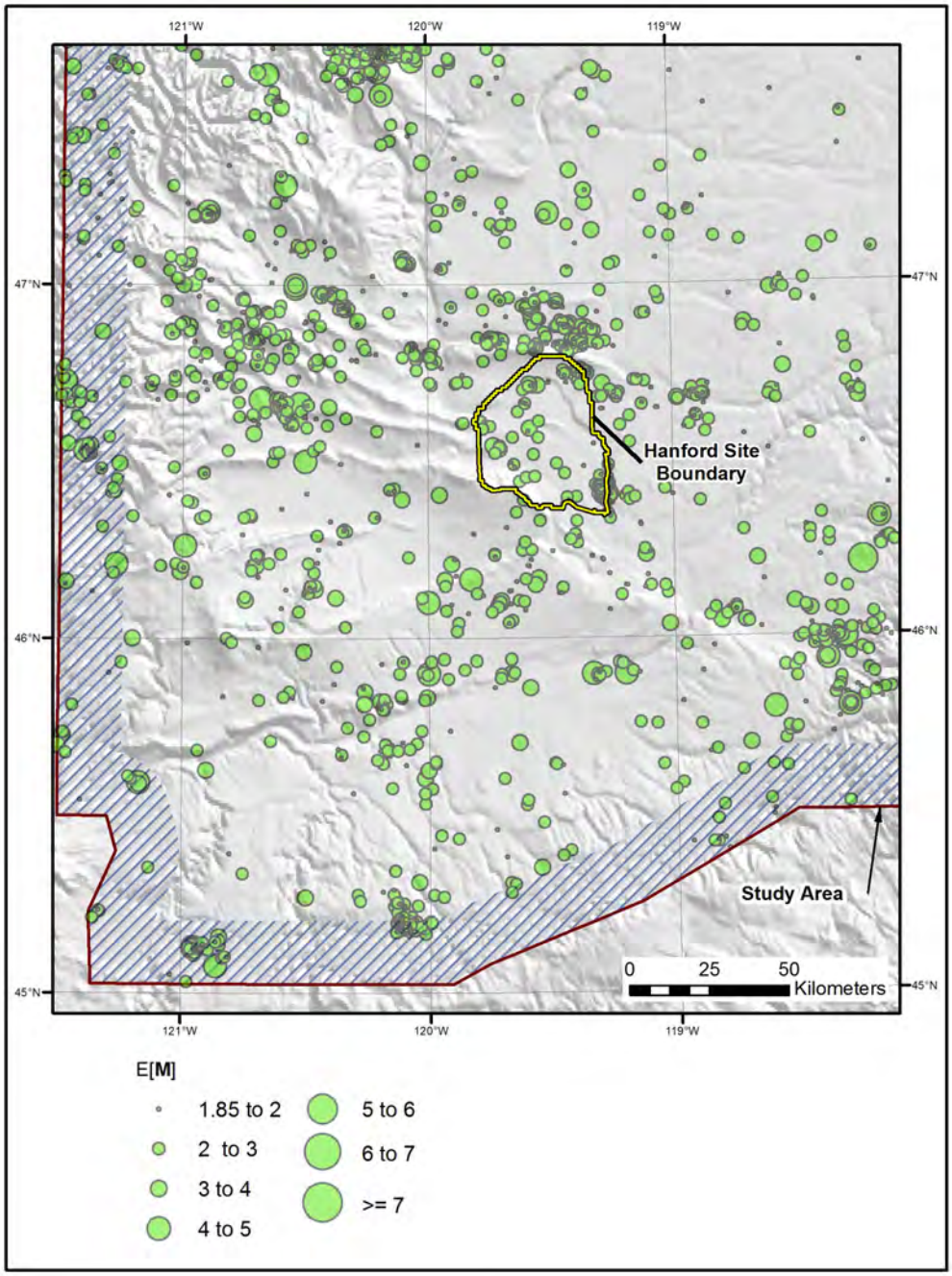


(a)

**Figure 8.28**. Seismicity from the crustal earthquake catalog in the vicinity of the YFB. Upper panel (a) indicates the magnitude of earthquakes and shows the spatial clustering (swarms) of many of the smaller magnitude (M<4) earlthquakes, such as the Wooded Island swarm near the southeastern boundary of the Hanford site boundary. Magnitude values used in the plots are E[M] values (see Section 6.5.2). Lower panel (b) shows the spatial pattern of earthquake epicenters relative to the seismic source zones. To assist in seeing spatial patterns, all epicenters are shown with the same symbol regardless of their magnitudes. Alternative approaches to characterizing the spatial distribution of recurrence parameters (i.e., spatial smoothing versus uniform distributions) are assessed for the SSC model by conducting a nearest-neighbor spatial analysis of these epicenter locations.

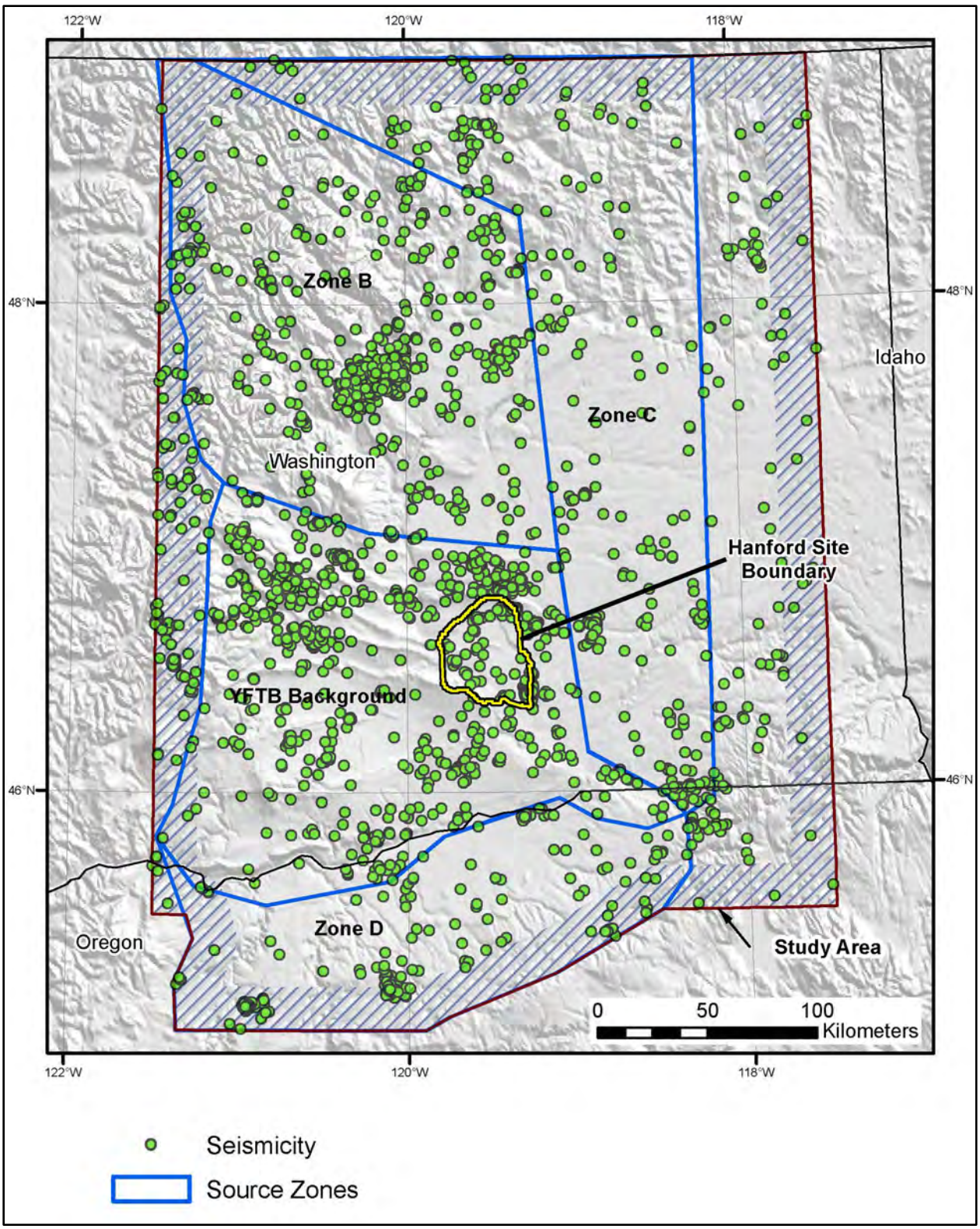


(b)

**Figure 8.28**. (contd)

In light of the various issues defined above, the TI Team decided to conduct spatial smoothing for Zones B, YFTB, and D. In the case of YFTB and D, the smoothing approach is weighted as an alternative to a uniform distribution, as discussed in Sections 8.3.3 and 8.3.4. The approach taken for spatial smoothing is the approach recommended by Stock and Smith (2002) as a preferred approach to the fixed smoothing kernel approach because it uses an adaptive kernel (Silverman 1986). In this approach, the kernel size is adjusted throughout the study region, decreasing in size in areas of higher data density and increasing in size in areas of sparse data. An initial kernel bandwidth (h) equal to 15 km was selected for these source zones by testing values of h from 5 to 100 km, in 5-km increments and log-likelihood according to the procedure given by Silverman (1986). The adaptive kernel method was then used to define the final spatial density for the hazard calculations.

## 8.3.3 Yakima Fold and Thrust Belt Background Source Zone

This section describes the characteristics and the technical basis for assessments used in the SSC model for the YFTB background source zone. Note that the term "YFTB" is used exclusively in this document to indicate the source zone, and the term "YFB" or Yakima Fold Belt is used to describe the tectonic region or domain. The characteristics and methods used by the TI Team to define the zone are explained in Section 8.3.1 and 8.3.2.

### 8.3.3.1. Source Zone Geometry

The geometry of the YFTB background source zone represents a modification to Zone A of JBA et al. (2012) in that it repositions the western boundary of Zone A to include all of the faults of the YFB and extends the area to the southeast to include the Wallula fault (Figure 8.29). The revised boundaries reflect changes in seismicity rates and spatial patterns as interpreted from current geologic, seismologic, and tectonic data. The rationale for the revised boundaries is given below.

The eastern boundary of the YFTB source zone defines the eastern limit of folding and reverse faulting associated with the YFB fault sources (Figure 8.29), as well as a distinct decrease in observed seismicity rates from the YFB to the east (Figure 8.28). It follows the edge of the craton, as shown in Figure 8.30 (Reidel 2002). This boundary is supported by well logs (1-10 Darcell, 1 Hanna, and 1 Kirkpatrick), which show that distinctly different lithologies are present in well logs that penetrate the YFB (Figure 8.31; Reidel 2002). The Darcell borehole lies near the $^{87}Sr/^{86}Sr$ (Sri) = 0.706 isopleth, which has been postulated to delineate the western margin of North American crystalline basement (Armstrong et al. 1977; Burchfiel et al. 1992).

Coinciding with the craton edge are the northwest-trending Ice Harbor dikes (Figure 8.32). The eastern boundary of YFTB follows the Ice Harbor dikes as they cut through the western part of the Pasco gravity low of Blakely et al. (2013) (Figure 8.29 and Figure 8.32). Published magnetic and gravity models of Blakely et al. (2013) explain a gravity low to the east of the dikes by a distinct change in lithology from the pre-Tertiary basement of oceanic assemblages to the west (underlying the YFTB) to the Precambrian metasedimentary basement to the east (craton), despite a decrease in depth to basement east of the dikes.

The eastern boundary adopted by the TI Team lies west of the postulated location for the 1936 Milton-Freewater earthquake, as reflected by an epicentral location on the eastern side of the Hite fault (WCC 1980b) near Waitsburg, Washington, instead of Milton-Freewater, Oregon (Figure 8.32). In

addition, reanalysis of the 1936 earthquake by WCC (1980b) locates its epicenter near the intersection of the Hite-Wallula faults. The 1936 event is postulated to be either oblique (right-lateral/reverse) on N30°E fault or oblique (left-lateral/reverse) on a N40°W-striking fault. The former would suggest slip on the Hite fault, whereas the latter would suggest slip on the Wallula fault, but in a sense opposite to geologic evidence (most observations support right-lateral movement). For the SSC model, the TI Team concluded that the preferred solution is on the Hite fault, with a N30°E orientation. This strike is on trend with the April 8, 1979 (E[**M]** 4.05) well-located earthquake to the northeast, suggesting that both occurred on the Hite fault (WCC 1980b; see Section 4.4 for additional details). The fault planes from these focal mechanisms are inconsistent with those of the YFB faults, thus supporting the conclusion that the 1936 and 1979 earthquakes lie to the east of the eastern boundary for the YFTB source zone.

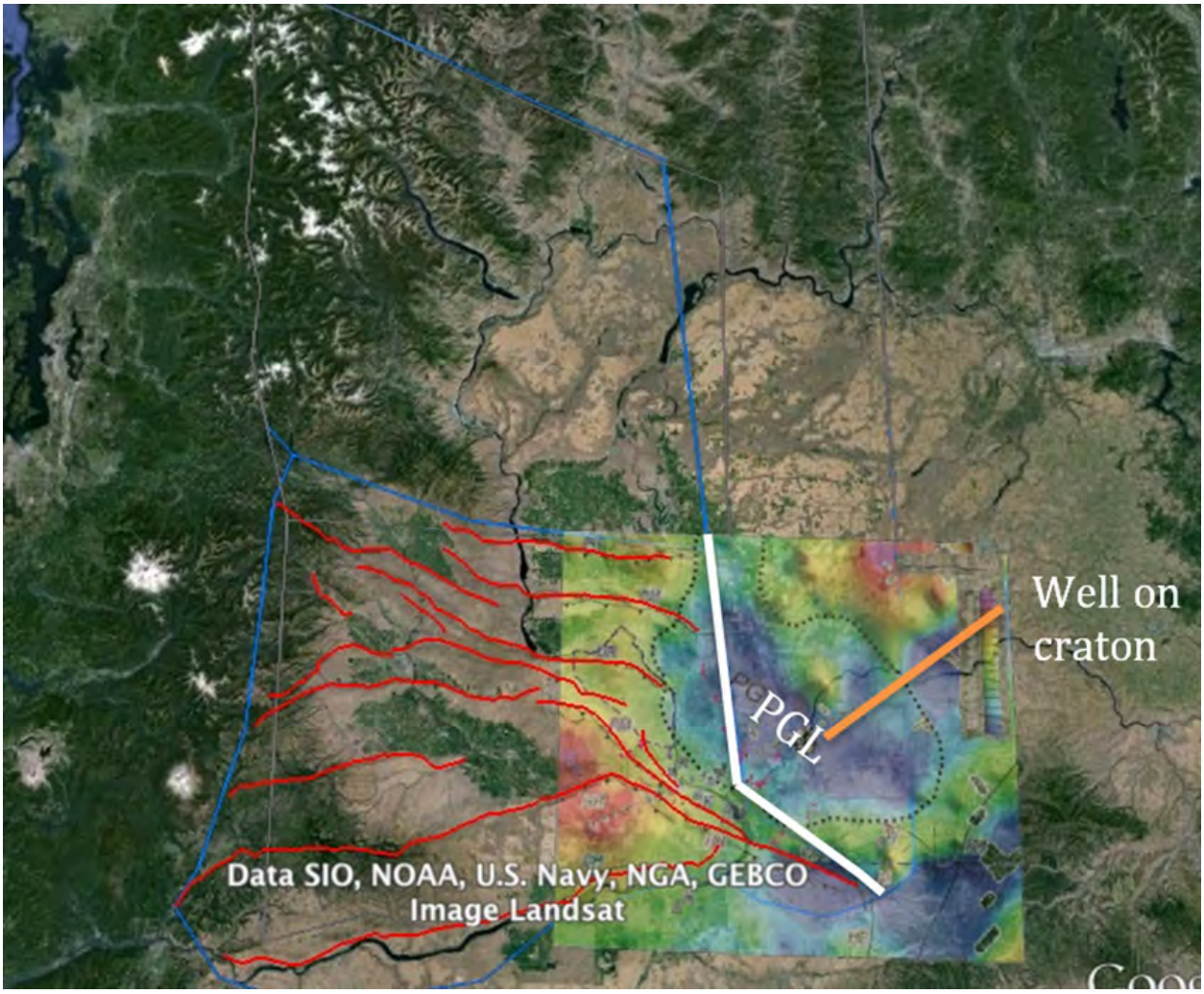


**Figure 8.29**. Location of the YFTB eastern boundary (white line) with Zone C. The boundary follows the eastern extent of the fault sources, the edge of the craton (see Figure 8.30), and the strike of exposed dikes of the Ice Harbor Member of the CRBG. The boundary continues to southeast, following the Pasco gravity low (PGL), and terminates at the end of the RAW and Wallula faults.

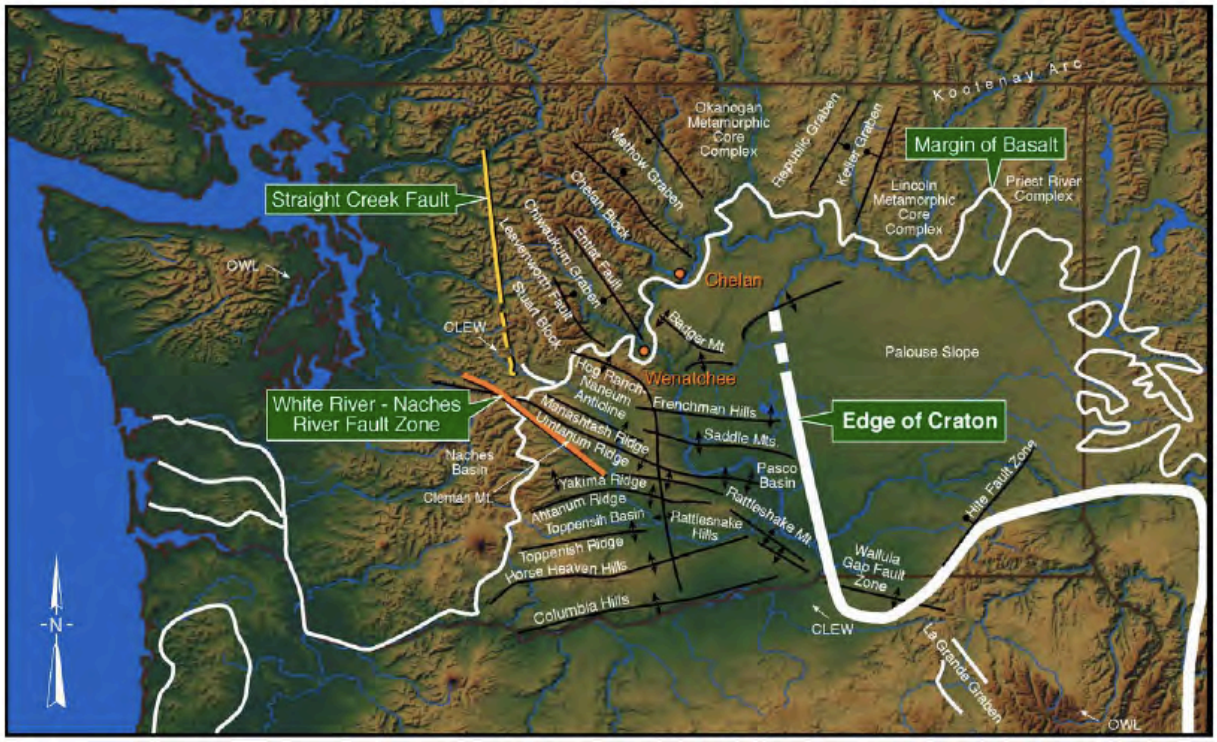


**Figure 8.30**. Edge of craton as defined by $^{87}Sr/^{86}Sr$ (Sri) = 0.706 isopleth (figure from Reidel 2002).

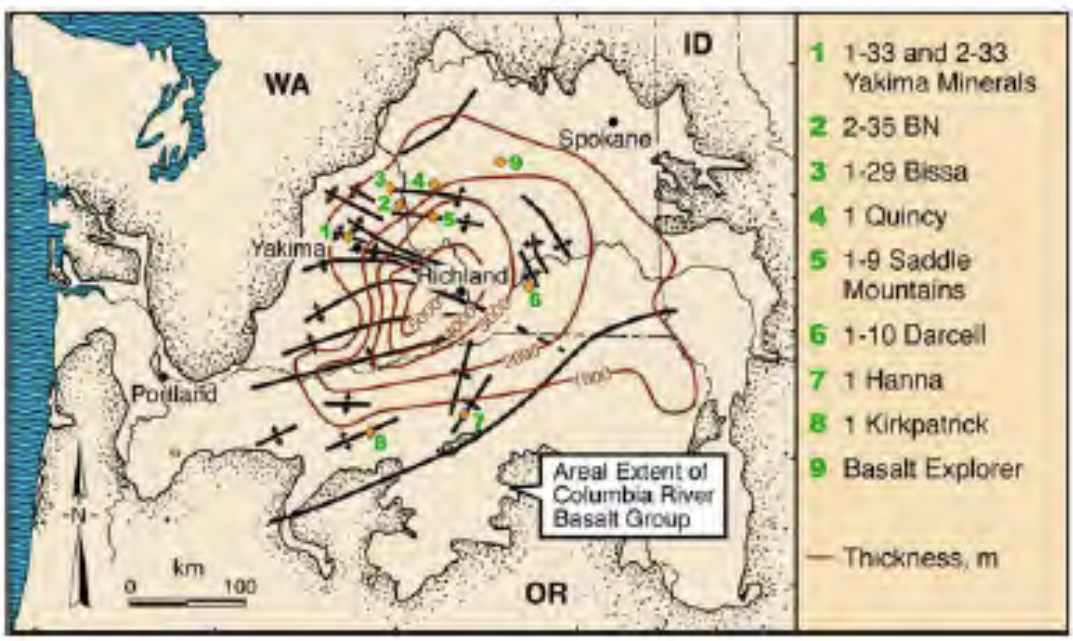


**Figure 8.31**. Location of deep boreholes that penetrated basement rocks in the Hanford study area (from Reidel 2002).

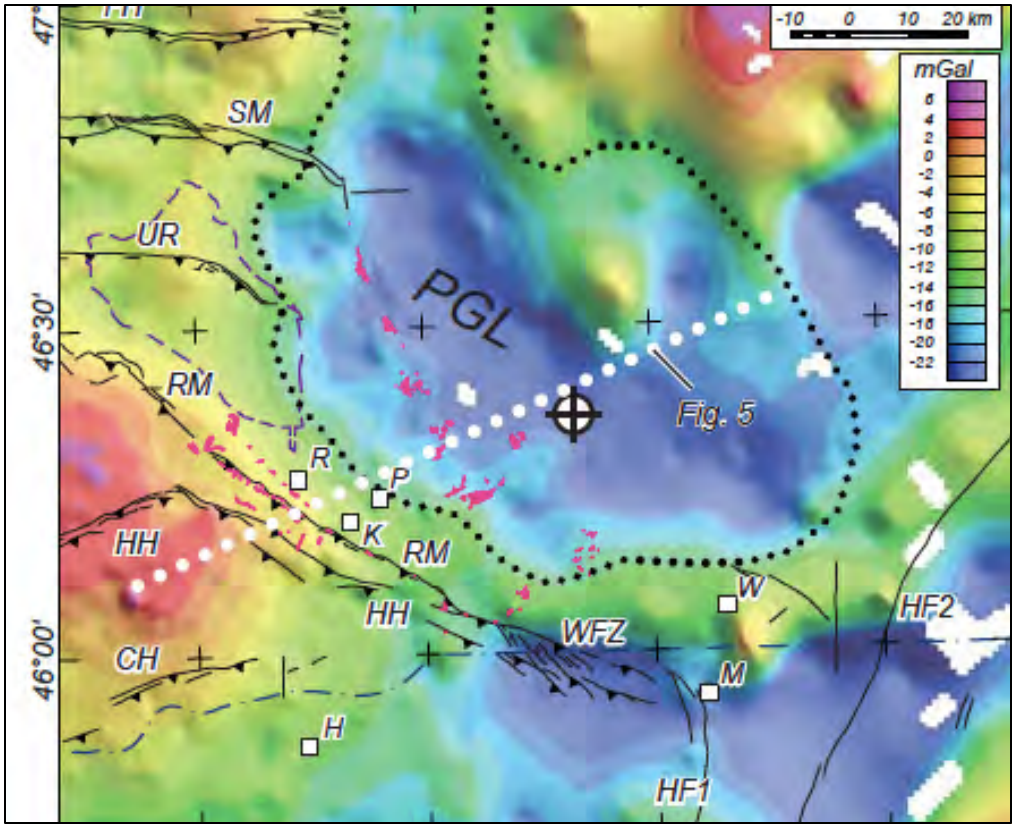


**Figure 8.32**. Location of Ice Harbor dikes, cross-sectional model of Blakely et al. (2013) (dotted white line), and the Darcell-10 well within the Pasco gravity low (PGL). Ice Harbor dikes (scattered red units) follow the trend of the craton edge and the eastward termination of the YFTB fault sources (black lines). (HF1 and HF2 are branches of the Hite fault; W = Waitsburg, Washington; M = Milton-Freewater, Oregon; WFZ = Wallula fault zone; other abbreviations are as defined by Blakely et al. [2013]) (From Blakely et al. 2013)

The YFTB source zone's southern boundary is located south of the Columbia Hills and includes a collection of north-northwest faults, such as the Arlington, Luna Butte, and other fault systems, which are discussed in more detail in Section 8.4.1.2 (Figure 8.33). The rationale for positioning the boundary is 1) a decrease in seismicity rate to the south (Figure 8.28), 2) distinctly different lithology and tectonic style of the Blue Mountains to the south and east, and 3) a gravity high that separates two adjacent gravity lows, one of which defines the southwestern edge of the Pasco gravity low (Figure 8.32). The Arlington fault was included in YFTB source zone based on its similarity in Mmax and in depth and rate of seismicity. JBA et al. (2012) lists the Arlington fault as having a right-lateral offset, similar to the style of faulting for the Wallula and La Grande faults. According to JBA et al. (2012), the Arlington and Luna Butte faults constitute north-northwest-striking, dominantly dextral strike slip fault zones that cut through the Columbia Hills anticline, and include normal and strike slip faults as well as anticlines. The southern boundary is also positioned close to a tectonic block boundary, as postulated by McCaffrey et al. (2007).

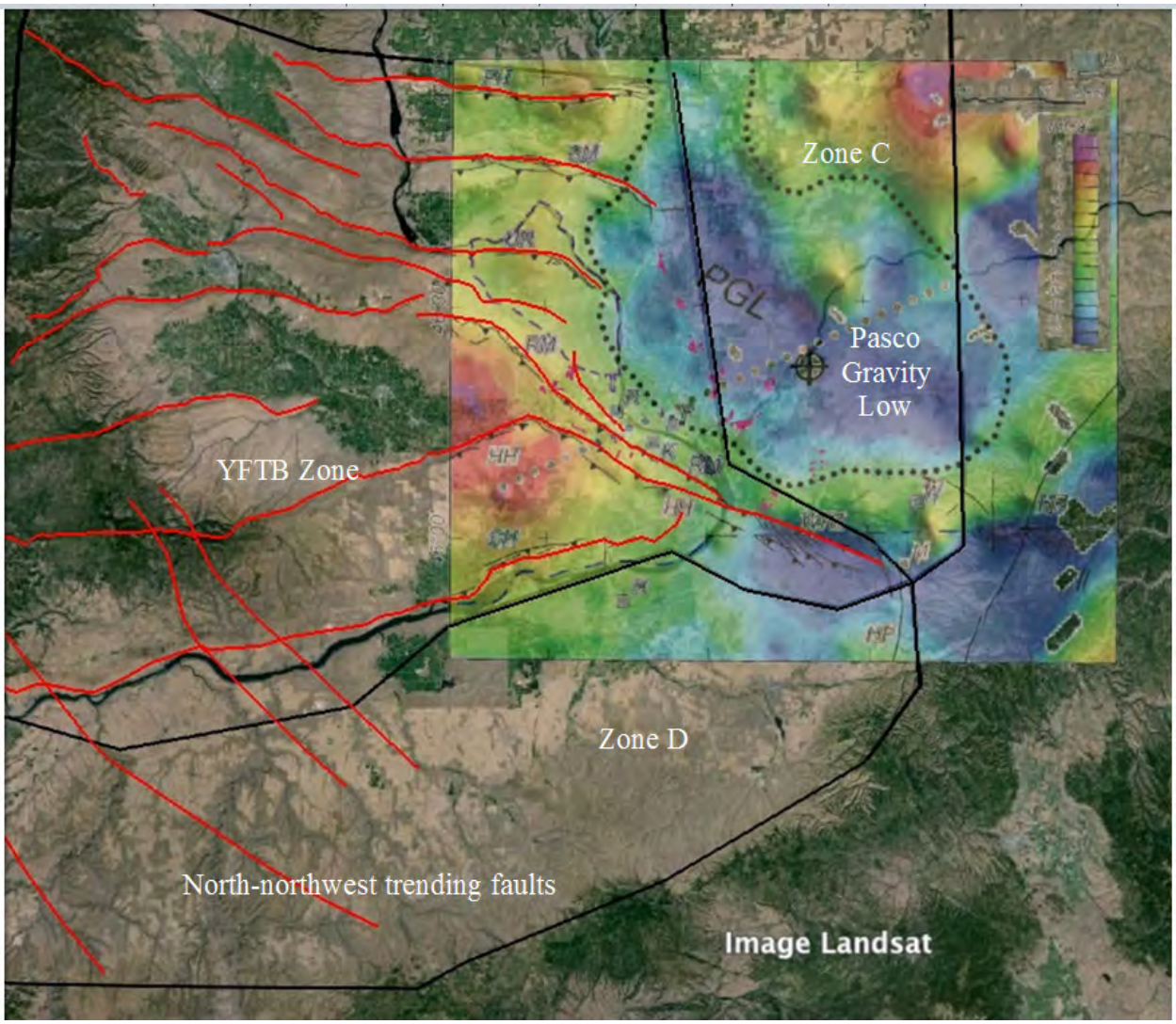


**Figure 8.33**. Location of southern boundary of YFTB source zone with Zones C and D.

The YFTB western boundary is positioned to include the westernmost topographic expression of the YFB faults and its boundary with the Cascades tectonic province to the west, the southwestern end of the Arlington fault, and the western edge of Manastash Ridge (Figure 8.34).

The YFTB northern boundary corresponds to the boundary between WenaS and WenaN−EWashS in the McCaffrey et al. (2007) "block" model and the boundary between Zones A and B in the JBA et al. (2012) model. This boundary reflects a change in seismicity rate (Figure 8.28) and depth of seismicity. The maximum depth of seismicity under YFTB is ~20 km, whereas in Zone B to the north it is ~15 km. As discussed for the JBA (2012) model, the WenaS and YFTB blocks of McCaffrey et al. (2007) were combined in Zone A after a comparison of seismicity rates normalized by area showed them to be very similar (see Figure 4-20 in JBA et al. 2012).

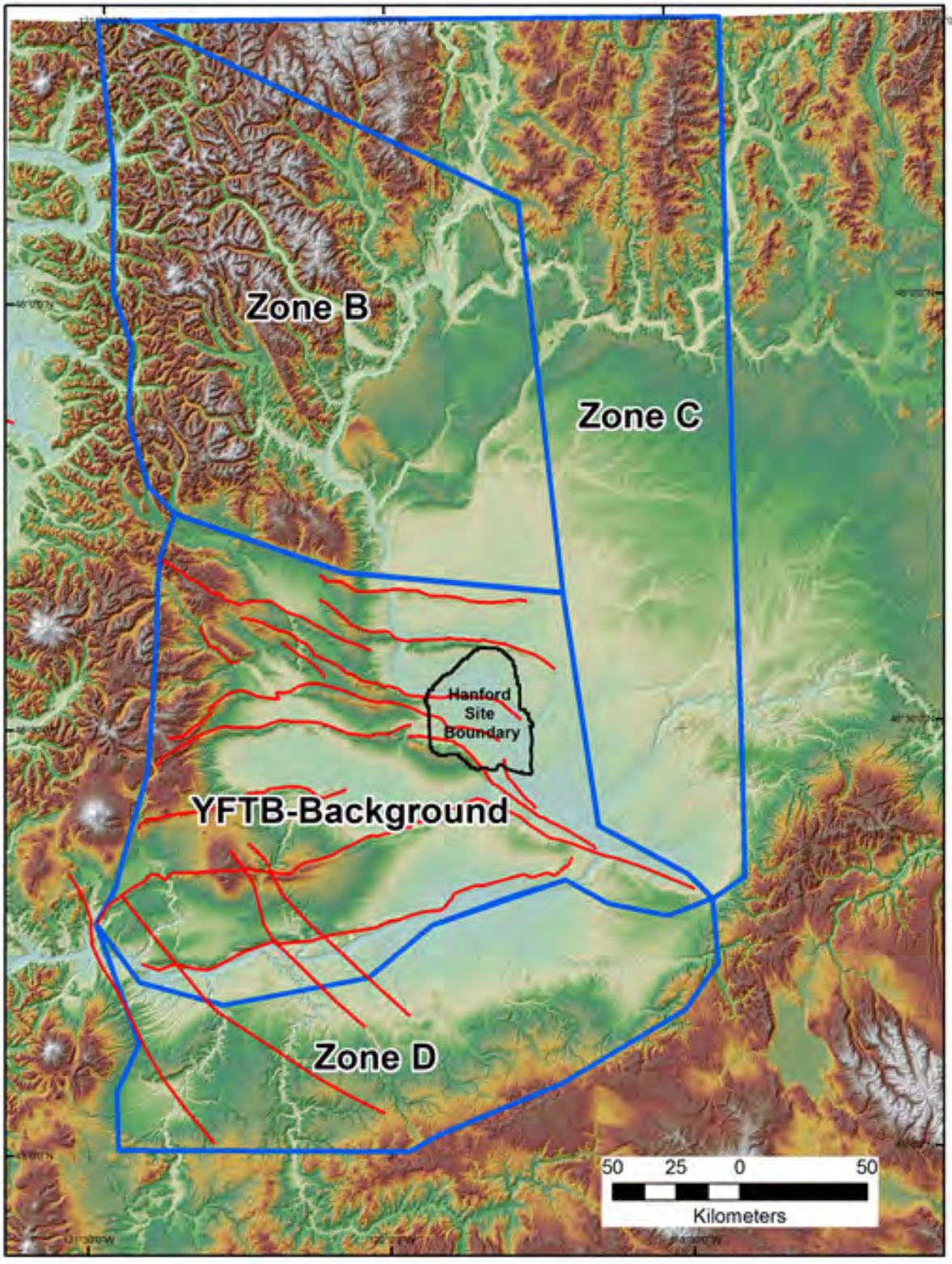


**Figure 8.34**. YFTB western boundary encompasses the extent of the fault sources (red lines) and separates the YFTB source zone from the Cascade tectonic province to the west.

As can be seen in Figure 8.28, a grouping of small-magnitude earthquakes are observed in the vicinity of the junction of the YFTB, D, and C zones. It should be noted that these earthquakes are mostly small-magnitude events and their locations were not used directly to define the locations of the source zone boundaries. Rather, the technical bases for the boundaries are described in this section of the report and include a variety of seismologic, geophysical, and geologic criteria. This includes the location and focal mechanism characteristics of the moderate-magnitude 1936 and 1979 earthquakes. Given the smallmagnitudes of the earthquakes in the grouping and the relatively large number of earthquakes already included in the recurrence calculations for the YFTB source, the inclusion of these events within the YFTB source zone (moving the source boundary slightly to include them) would not be expected to lead to a significant change in the recurrence rate.

### 8.3.3.2. Properties of Boundaries to Future Earthquakes

As discussed in Section 8.3.2.2, all source zone boundaries in the SSC model are assumed to be leaky, such that ruptures beginning within a source zone can propagate into adjacent source zones. The basis for this assessment is that observed changes in tectonics, geology, and seismicity across the zone boundaries are not sharply delineated, but rather smoothly varying.

### 8.3.3.3. Seismogenic Thickness and Focal Depth Distribution

Seismogenic thickness for the YFTB source zone was determined using the $D_{90}$ value, the depth above which 90% of earthquakes occur, as determined from the Hanford PSHA earthquake catalog developed for this project (see Section 8.3.2.4). The rationale for using the $D_{90}$ value is outlined in Section 8.3.2.3. Based on the depth distribution shown in Figure 8.35, the seismogenic thickness for the YFTB source zone was estimated to be 16 km, with appropriate uncertainty. The assessment of the seismogenic thickness for the YFTB source is expressed in the logic tree by the following: 13 km [0.2], 16 km [0.5], and 20 km [0.4].

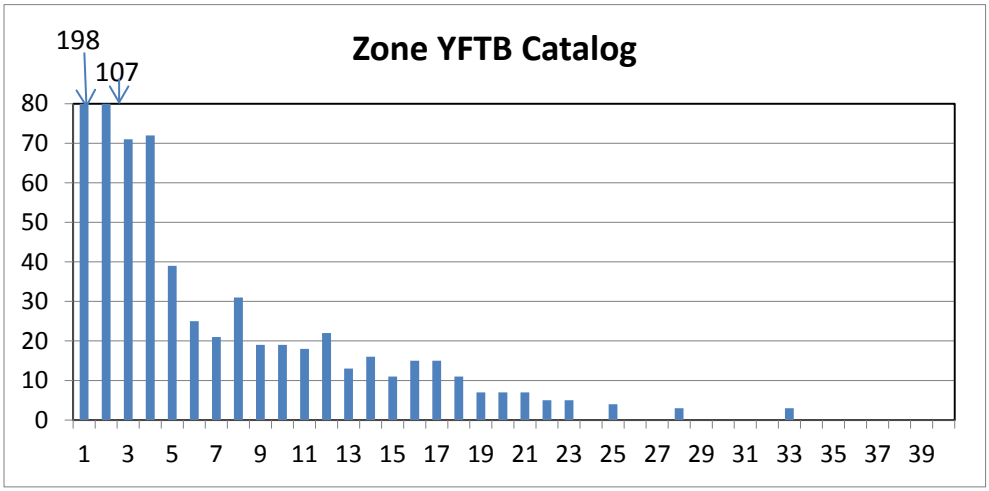


**Figure 8.35**. Focal depth distribution for all earthquakes within the YFTB source zone. Note the large numbers of very shallow earthquakes, which are mostly M < 3.

#### 8.3.3.4. Earthquake Recurrence

Earthquake recurrence for the SSC model was estimated for source zones using a truncated exponential model (Cornell and Van Marke 1969) of observed seismicity from a new catalog compiled from a variety of existing earthquake catalogs sources. Declustering, magnitude conversions, completeness corrections, and other aspects of creating the Hanford PSHA catalog are discussed in detail in Sections 8.3.2.8 and Chapter 6.0. Earthquake recurrence for the YFTB source zone is characterized by a Poisson process and, after declustering the catalog, all earthquakes are assumed to be independent events. As discussed in Section 8.3.2.8, uncertainties in the magnitude assessed for each earthquake in the catalog is propagated into the uncertainty in recurrence parameter estimates for both a- and b-values, with weights assigned by computing their relative likelihoods. Spatial variation in recurrence is an epistemic uncertainty that was included in the logic tree as discussed below in Section 8.3.3.6. For the hazard calculations, earthquakes are represented by finite ruptures having a particular orientation, downdip geometry, and style of faulting. The rupture size is a function of the earthquake magnitude. The location of these ruptures is modeled as random within the YFTB source zone, and the relative frequency is defined by a spatial density model, as discussed in Section 8.3.2.9.

The assessment of recurrence for the YFTB source zone is a function of whether or not some of the seismicity within the YFTB source zone is assigned to the fault sources or is assessed to not be associated with the fault sources (see discussion in Section 8.4.3.9.1 in the context of recurrence models for the fault sources). The “capture zones” for the seismicity attributed to the faults (Figure 8.93 in Section 8.4.3.8) are the polygons developed from the structural analyses (see Section 8.4), because these are the surface manifestation of deformation along the fault down to the base of the seismogenic crust. Alternatives for whether observed seismicity is attributed to the fault sources or to the YFTB source zone are included in the logic tree in Figure 8.4. If the seismicity is assessed to be associated with fault sources, the seismicity within the polygon capture areas is removed from the YFTB source zone recurrence calculation.

The weights associated with these alternatives are as follows:

| | |
|---|---|
| Observed seismicity is associated with fault sources | [0.2] |
| Observed seismicity is not associated with fault sources | [0.8] |

The resulting recurrence curve for the YFTB source zone with its associated uncertainty distribution is given in Figure 8.36. As discussed in Section 6.0, the calculation of earthquake recurrence is done assuming an exponential distribution of magnitudes, incorporating the uncertainties in magnitudes, and correcting for the bias in counts due to the exponential distribution. Based on the maximum likelihood approach used, the uncertainties in rates for each magnitude bin are a function of the counts within each bin. Those uncertainties are shown in Figure 8.36 by the error bars associated with the mean counts shown by the solid dotted line. As can be seen, the uncertainties increase with increasing magnitudes and decreasing counts of earthquakes. In the case of all the Hanford source zones, there are no observed earthquakes in the largest magnitude bins near the maximum magnitude and very few earthquakes in the larger magnitude bins. Because the maximum likelihood approach to recurrence calculation accounts for the numbers of events within each bin (Weichert 1980), the recurrence curve is not very sensitive to the counts in the largest magnitude bins. This explains why the recurrence curves are either above or below the mean counts in the largest observed magnitude bins.

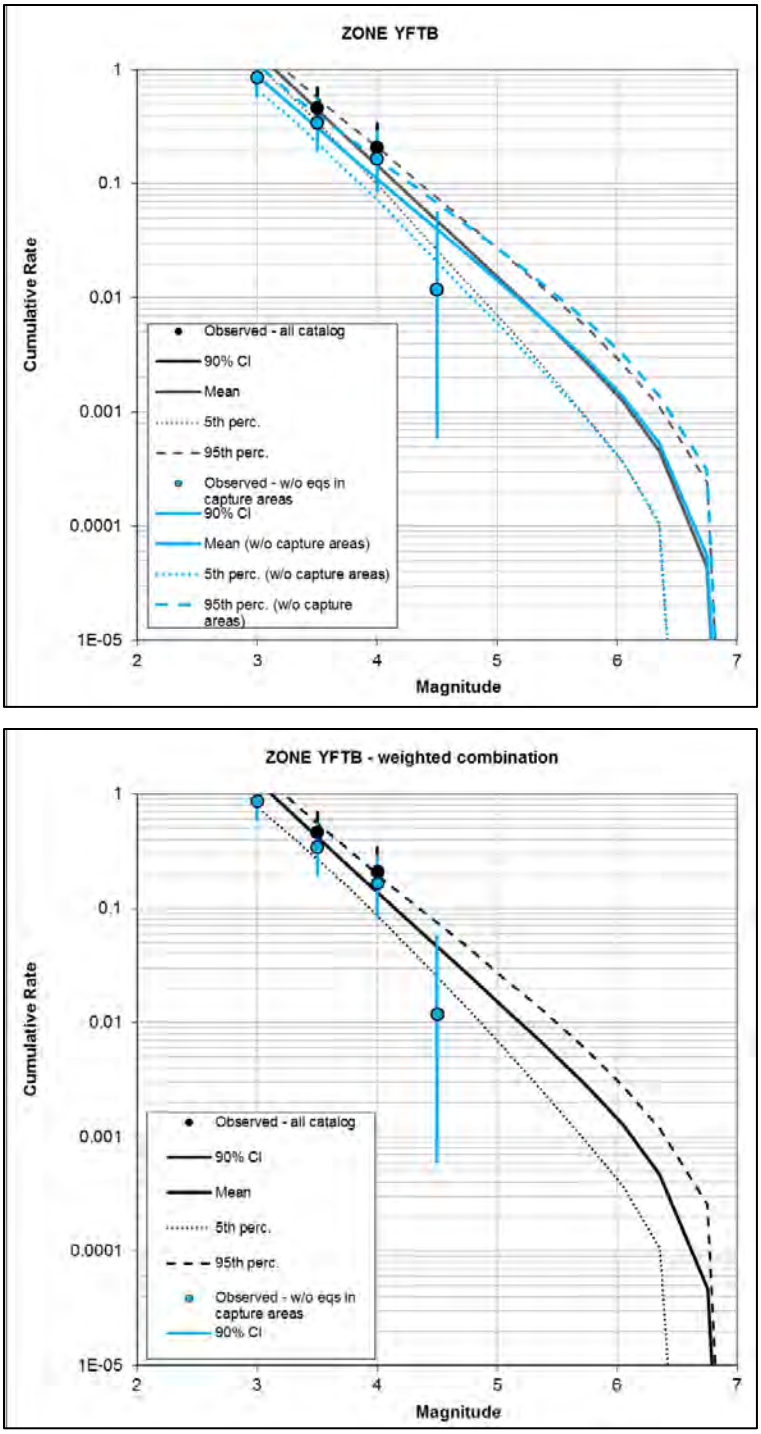


**Figure 8.36**. YFTB source zone recurrence curves. Magnitudes are E[**M**]. The upper panel shows the recurrence curve for the YFTB source zone (with and without capture zones), showing 90% confidence interval (CI). Black and blue dots show the rates with and without the earthquakes that would be associated with the capture areas, respectively. The lower panel shows the recurrence curve that results from the weighted combination of the models that remove the earthquakes within the capture areas [0.2] or that do not remove the earthquakes within the capture areas [0.8].

#### 8.3.3.5. Maximum Magnitude (Mmax)

The Mmax approach for YFTB is different than the other source zones because the fault sources within it are characterized separately and the remaining areas of the zone do not include significant faults. The YFTB Mmax distribution has an upper tail that overlaps with the lower part of the Mmax distributions for the faults within the zone (see Section 8.3.2.7). In the case of the YFTB source, the largest observed earthquake was the M 4.79 earthquake that occurred on November 17, 1918. This magnitude was judged by the TI Team to be too small to constrain the Mmax for the YFTB source zone. As a result, the Team made the assessment that the lower part of the Mmax distribution for the fault sources provides a reasonable upper constraint on the Mmax distribution for the YFTB source zone (Figure 8.29). The maximum magnitude distribution for the YFTB source zone in the logic tree is 6.5 [0.3], 6.75 [0.4], and 7.0 [0.3].

#### 8.3.3.6. Spatial Distribution of Recurrence Parameters

As discussed in Section 8.3.2.9, the YFTB source zone was characterized by the future spatial distribution of recurrence parameters using either a uniform or spatially smoothed distribution. Statistical tests were conducted to assess whether or not observed seismicity was spatially homogeneous using the nearest-neighbor tests described by Musson (2002). Musson makes note of the fact that a homogeneous pattern of seismicity does not need to necessarily be a uniform pattern, but may be random and show local spatial clusters. In the case of the YFTB zone, these tests were equivocal and appeared to vary with whichever declustering algorithm was used to remove dependent events. Based on these tests, the TI Team decided that spatial smoothing should be conducted using only the larger ($M > 3$) earthquakes to avoid bias due to possible spatial clusters of very small events in the CRBs. It was also decided to allow for smoothing of the equivalent number of events, N*, but to consider b-values to be uniform (with appropriate uncertainty) throughout each source zone. For the YFTB source zone, the smoothing approach is weighted as an alternative to a uniform distribution, (uniform [0.8]; smoothing [0.2]). The adaptive kernel approach taken for spatial smoothing is described in Section 8.3.2.9.

#### 8.3.3.7. Properties of Future Earthquake Ruptures

The style of faulting, strike, and dip of ruptures within the YFTB source zone are based on the analysis of well-determined focal mechanisms, as discussed in Section 8.3.5, and other sources of geologic and tectonic information briefly discussed below. Focal mechanisms of 447 earthquakes were distributed as follows (Figure 8.37):

- 254 (57%) reverse events (rake of 90° ± 60°)
- 96 (21%) normal events (rake of -90° ± 60°)
- 100 (22%) strike slip events
- 50 (11%) left-lateral (rake of 0° ± 30°)
- 50 (11%) right-lateral (rake of ± 180° ± 30°).

In general, these focal mechanisms indicate primarily reverse faulting with lesser amounts of strike slip.

In addition to the focal mechanism analysis, the TI Team considered the orientations of basement structures and styles of faulting proposed in previously published studies (e.g., Catchings and Mooney 1988; Montgomery 2008; Blakely et al. 2011, 2013; Jarchow et al. 1994). McCaffrey et al. (2007, 2013)

note that the current tectonic setting is best described as a roughly north-south compression, which is in agreement with the results of the focal mechanism analysis (Section 6.2.1 in Appendix E) and kinematic indicators from geologic mapping of the fault sources.

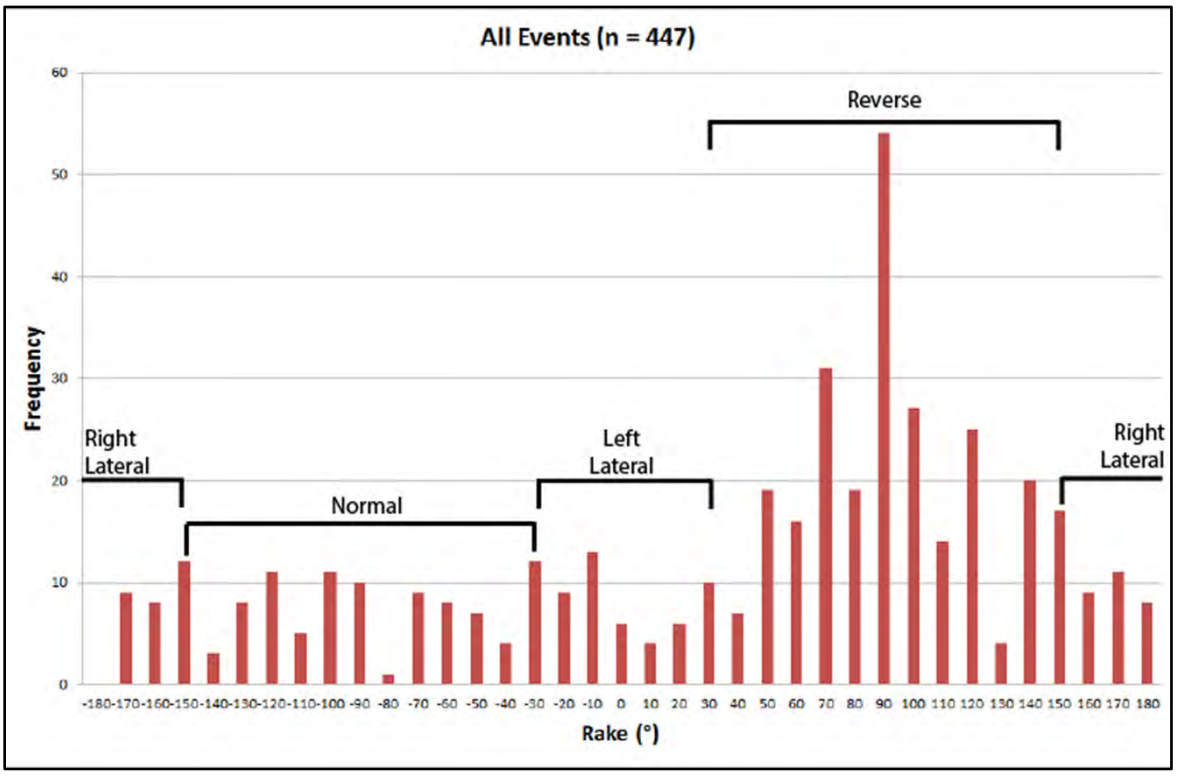


**Figure 8.37**. Rake angles for earthquake focal mechanisms in the YFB region. The ranges of rakes for a given style of faulting are from Aki and Richards (1980).

Based on these available data, the style of faulting of future ruptures within the YFTB is defined by the following aleatory (relative frequency) distribution:

- reverse (60%)
- normal (20%)
- strike slip (20%).

Similarly, the aleatory distributions of strike were determined from a combination of the focal mechanism analysis and the orientations of basement structures:

- reverse
  - 40º (20%)
  - 90º (60%)
  - 140º (20%)
- normal
  - 10º (20%)
  - 90º (60%)
  - 140º (20%)

- strike slip
  - 60º (50%)
  - 150º (50%).

The dip of ruptures is dependent on the style of faulting and is based on the SSC TI Team's analysis of focal mechanisms as well as published compilations of the geometry of coseismic ruptures (e.g., Sibson and Xie 1998). Because the ruptures are not tied to any identified geologic structures, the dip direction is assumed to be random:

- reverse
  - 30º (20%)
  - 50º (60%)
  - 70º (20%)
- normal
  - 40º (20%)
  - 60º (60%)
  - 80º (20%)
- strike slip
  - 70º (40%)
  - 90º (60%)

### 8.3.4 Source Zones B, C, and D

This section describes the characterization of Zones B, C, and D, which are shown in Figure 8.18. Unlike the YFTB background source zone, Zones B, C, and D do not include fault sources, as discussed in Section 8.3.1.

#### 8.3.4.1 Source Zone Geometry

The locations of the boundaries for source Zones B and C were adopted directly from JBA et al. (2012), with modifications affecting the YFTB as described in Section 8.3.3.1. In addition to these source zones, the TI Team added a fourth source zone, Zone D, to the hazard analysis to test the sensitivity of the hazard calculations to their presence and to other geologic structures south of the Columbia Hills and north of the Blue Mountains. The southern boundary for Zone D follows the trend of the Blue Mountains, which demarks the boundary of the YFTB source zone with a different geologic and physiographic province. The zone was extended to capture the area around a series of north-northwest fault systems mapped in the western part of the zone. With the exception of the group of north-northwest oriented faults characterized as part of the YFB region (e.g., Arlington, Laurel, Lune Butte, and Maupin faults), the current state of knowledge about other mapped faults in the zone does not allow them to be characterized separately, as was done with fault sources in the YFTB source zone. The western boundary of Zone D, like the western boundaries of the YFTB zone and Zone B, follows the trend of the Cascade tectonic province boundary.

#### 8.3.4.2 Properties of Boundaries to Future Earthquakes

As discussed in Section 8.3.2.2, source zone boundaries in the SSC model are assumed to be leaky. That is, fault ruptures that originate near a source zone boundary can extend beyond the boundary and are not terminated at the boundary.

#### 8.3.4.3 Seismogenic Thickness and Focal Depth Distribution

In the SSC model, seismogenic thickness is estimated based on the depth distributions of earthquake hypocenters and is assumed to smoothly vary spatially across the zone. As discussed in Section 8.3.2.2, the assessment of seismogenic thickness is assessed based on consideration of the $D_{90}$ values. The uncertainties in seismogenic crustal thickness are included in logic trees for each seismic source zone.

Depth distributions for source Zones B, C, and D are summarized in Table 8.3.

**Table 8.3**. Summary of percentile ($D_{85}$, $D_{90}$, $D_{95}$) of earthquake hypocenter depth distributions. Numbers are depth in kilometers.

| | Entire Region | B | C | D | YFTB |
|---|---|---|---|---|---|
| $D_{85}$ | 9.96 | 8.36 | 10.78 | 19.50 | 12.44 |
| $D_{90}$ | 12.87 | 10.16 | 15.92 | 20.30 | 15.54 |
| $D_{95}$ | 16.75 | 12.63 | 19.48 | 23.60 | 19.47 |

Based on the analysis of earthquake hypocenters, the TI Team defined the seismogenic thicknesses and associated uncertainties for each source zone, as shown in Table 8.4. To ensure correlation between the seismogenic thickness of the various source zones for the hazard calculations, the thicknesses are described as thin, moderate, and thick, with corresponding weights as listed in Table 8.4. It is assumed that all zones are perfectly correlated such that a "thin" seismogenic thickness for one zone in the hazard calculation would imply that the other zones are modeled as thin also for that particular hazard run.

**Table 8.4**. Depth distributions and weights of source Zones B, C, and D in the SSC model.

| | Descriptor | Zone B | Zone C | Zone D |
|---|---|---|---|---|
| Seismogenic Thickness | Thin | 10 km [0.2] | 13 km [0.2] | 15 km [0.2] |
| | Moderate | 12 km [0.5] | 16 km [0.5] | 20 km [0.5] |
| | Thick | 15 km [0.3] | 20 km [0.3] | 24 km [0.3] |

#### 8.3.4.4 Earthquake Recurrence

Earthquake recurrence is calculated for Zones B, C, and D in the same manner as for the YFTB zone and the source-specific recurrence curves are described in this section. That is, the assessment of earthquake recurrence within source Zones B, C, and D was derived from the Hanford PSHA catalog, the development of which is described in detail in Chapter 6.0 and Sections 8.3.2.8. This catalog consists of both historical and observed earthquakes having a uniform size measure (moment magnitude), in which dependent events have been removed through a declustering process, and a completeness correction has been applied. The resulting catalog of independent events assumes that all earthquakes occur according to a Poisson process. Recurrence curves for Zones B, C, and D are shown in Figure 8.38, Figure 8.39, and Figure 8.40, respectively. A comparison of all seismic source zones is shown in Figure 8.41.

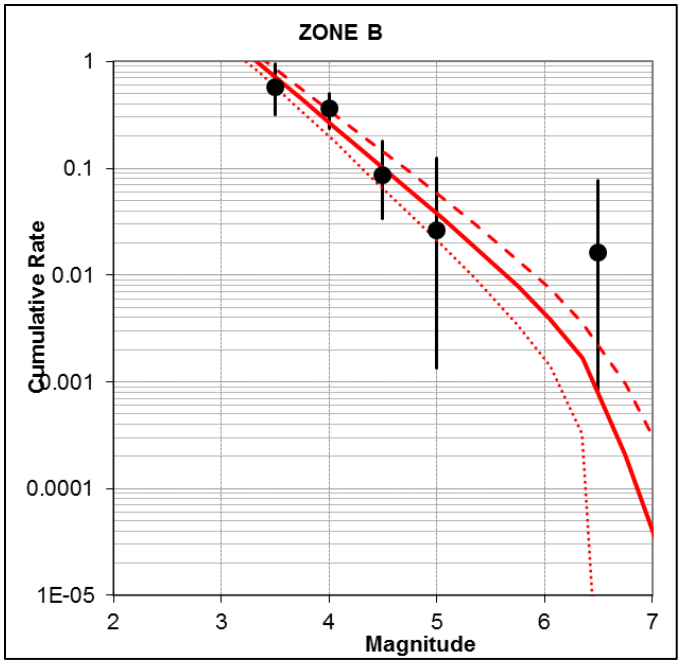


**Figure 8.38**. Earthquake recurrence curve (cumulative rate versus magnitude) for Zone B. Black dots = all observed earthquakes in the catalog; solid line = mean; dotted line = 5th percentile; dashed line = 95th percentile.

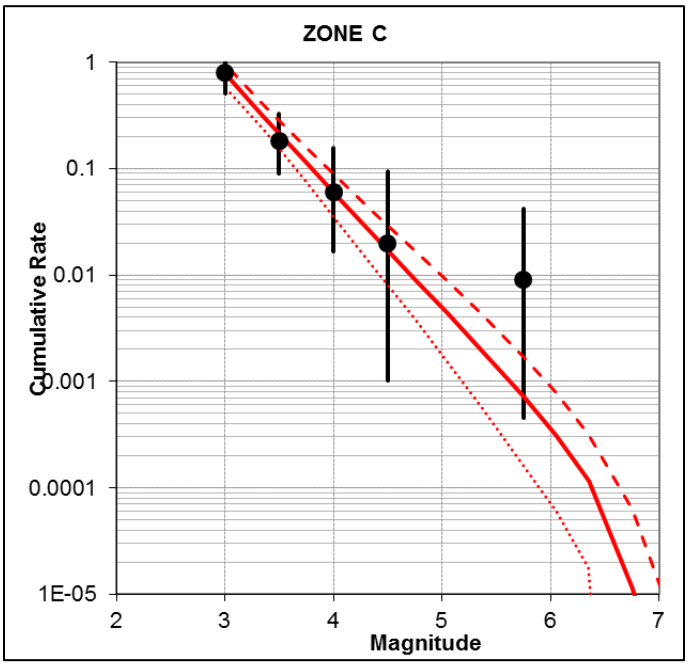


**Figure 8.39**. Earthquake recurrence curve (cumulative rate versus magnitude) for Zone C. Black dots = all observed earthquakes in catalog; solid line = mean; dotted line = 5th percentile; dashed line = 95th percentile.

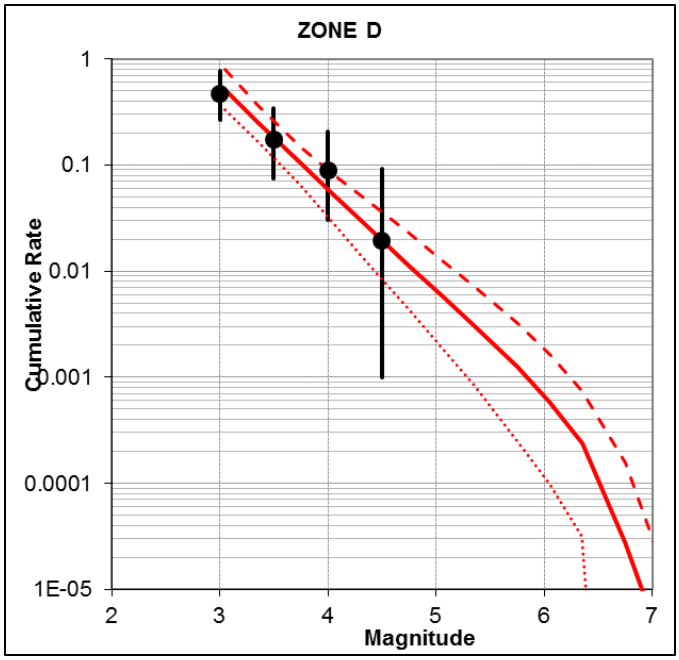


**Figure 8.40**. Earthquake recurrence curve (cumulative rate versus magnitude) for Zone D. Black dots = all observed earthquakes in catalog; solid line = mean; dotted line = 5th percentile; dashed line = 95th percentile.

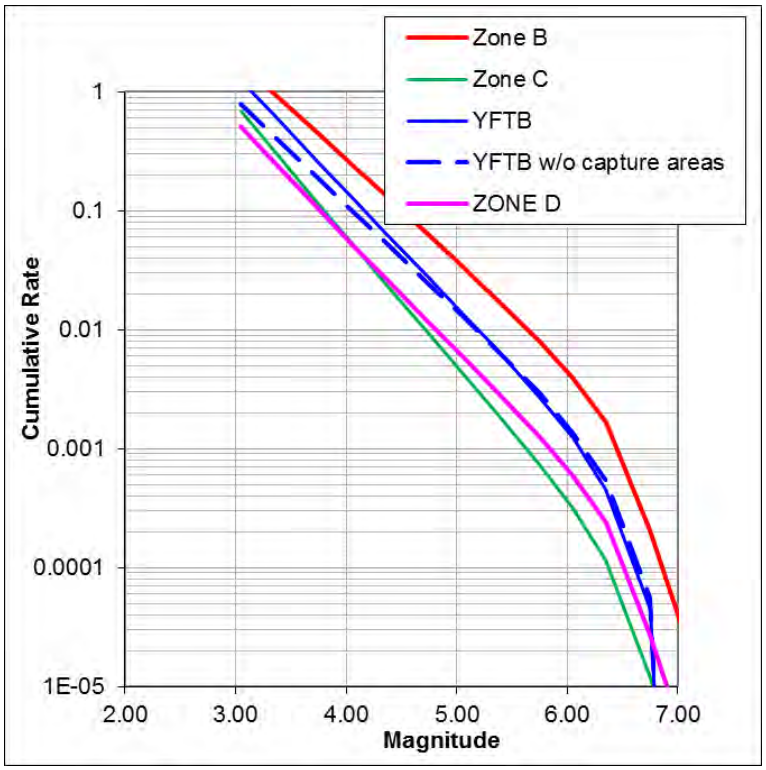


**Figure 8.41**. Comparison of recurrence curves (cumulative rate of earthquakes versus magnitude) for all source zones. The recurrence curve for the YFTB zone (blue) shows the rates assuming the earthquakes in the fault capture areas are removed (dashed line) or not removed (solid line).

#### 8.3.4.5 Spatial Distribution of Recurrence Parameters

Spatial density models are used to define the future spatial density of earthquakes in the seismic source zones when observed seismicity is used to define earthquake recurrence, as discussed in Section 8.3.2.9. Using tests described by Musson (2002), source Zones B, C and D were examined for how well the observed seismicity conformed to the assumption of spatial homogeneity. The observed seismicity within the four seismic source zones in the SSC model is shown in Figure 8.2842.

Based on the nearest-neighbor analysis given by Musson (2000) the seismicity in Zone C was determined to be consistent with a homogeneous distribution, but the distribution in Zone B is not and the nearest-neighbor results for Zone D were equivocal. The non-random spatial clustering within Zone B is clearly evident by visual inspection. Given the results of these homogeneity tests, the TI Team decided to adopt spatial smoothing for Zones B and D, using only the larger M > 3 earthquakes to avoid possible spatial clusters of very small events in the CRBs (see discussion in Section 8.3.2.9). Zone B has hosted larger magnitude earthquakes and the significant spatial cluster in the central part of the zone is the approximate location of the 1872 Lake Chelan earthquake. Note that the seismicity in that location is still present even after the catalog has been declustered to remove foreshocks and aftershocks. The TI Team decided to allow for smoothing of the equivalent number of events, N*, but to consider b-values to be uniform (with appropriate uncertainty) throughout each source zone. In the case of Zone D, the smoothing approach is weighted as an alternative to a uniform distribution, as tabulated below. The approach taken for spatial smoothing is detailed in Section 8.3.2.9.

| | Smoothing | Uniform |
|---|---|---|
| Zone B | [1.0] | |
| Zone C | | [1.0] |
| Zone D | [0.2 | [0.8] |

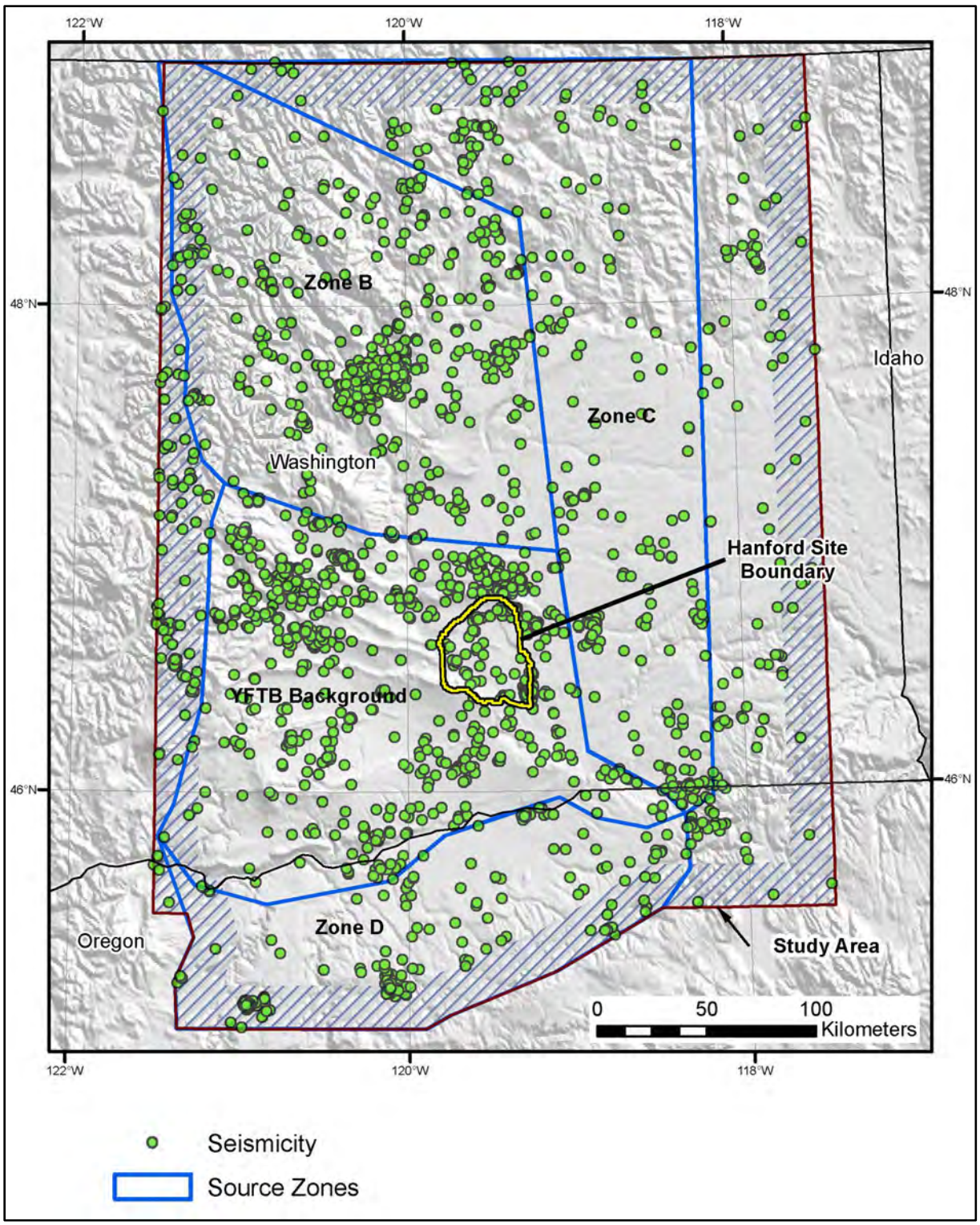


**Figure 8.42**. Seismicity from the project crustal earthquake catalog in the vicinity of the seismic source zones. Tests of spatial homogeneity were conducted using the nearest-neighbor analysis given by Musson (2000) using these epicenter locations. Spatial clustering of seismicity is clearly evident within Zone B in the Lake Chelan region and is also seen in the western and southern part of Zone D.

#### 8.3.4.6 Maximum Magnitude (Mmax)

Estimates of Mmax for Zones B, C, and D were made in light of the largest observed magnitudes within each source zone and consideration of the possible presence of faults that might have significant dimensions. Magnitude estimates for the 1872 Lake Chelan earthquake are M 6.5 to 7.0 at the 95th confidence level (Bakun et al. 2002). This magnitude is significantly large enough that the TI Team felt it could help provide some constraint on the Mmax for Zone B. The Milton-Freewater earthquake in Zone C is estimated at M 6.1 (WCC 1980b). As discussed in Section 8.3.2.7, unlike the YFTB source zone, faults that may exist within Zones B, C, and D are not explicitly modeled for the hazard analysis. Thus all seismicity in these areas is attributed to the seismic source zones. This implies that the Mmax distribution should allow for magnitudes that may be as large as those assessed for the YFB fault sources (Figure 8.27). Although the available data suggest differences in the rate of occurrence of earthquakes within each of the three source zones, the TI Team's assessment is that there is no technical basis for defining differences in their Mmax distributions. This is because the fundamental constraint on the Mmax estimates is the presence or absence of fault sources. Within the YFTB source zone, the fault sources are characterized specifically; however, within Zones B, D, and D, fault sources are not identified. Differences in the seismogenic thickness estimates for the various source zones and possible differences in the tectonic characteristics of the crust (i.e., within or outside of the continental craton) do not lead to differences in Mmax distributions, because these characteristics do not provide direct input to the Mmax assessment process for the source zones. This is because the approach of assessing Mmax based on constraints on the maximum rupture dimensions (length and area), which is used for the fault sources, is not used for the sources zones because of a lack of constraints on those dimensions. Likewise, the manner in which the tectonic nature of the crust (cratonic or not) affects the Mmax is not known. The distribution of Mmax and its respective weights are 6.5 [0.2], 6.75 [0.5], 7.0 [0.2], 7.25 [0.09], 7.5 [0.01].

#### 8.3.4.7 Properties of Future Earthquake Ruptures

As discussed in Section 8.3.2.5, sensitivity analyses (V. Montaldo-Falero presentation at WS2) (PNNL 2013b) show that the contribution of Zones B, C, and D to the site hazard is very low, thus justifying a simple approach to characterizing the properties of future earthquake ruptures within these zones. The style of faulting of future ruptures within Zones B, C, and D is defined by the following aleatory distribution: reverse (60%) and strike slip (40%). This is based on consideration of earthquake focal mechanisms within these zones and the regional tectonic regime. Because of the lack of hazard significance to the Hanford Site, the strike of future ruptures is defined by a uniform (i.e., 100%, 0−360°) random aleatory distribution and dips are assumed to be vertical.

## 8.4 Fault Sources

Twenty fault sources are included in the SSC model (Figure 8.43). They consist of the faults associated with the YFB as well as the Seattle fault. For purposes of assessing the slip rates and recurrence, some of the faults have also been identified according to individual segments, as listed in Table 8.5.

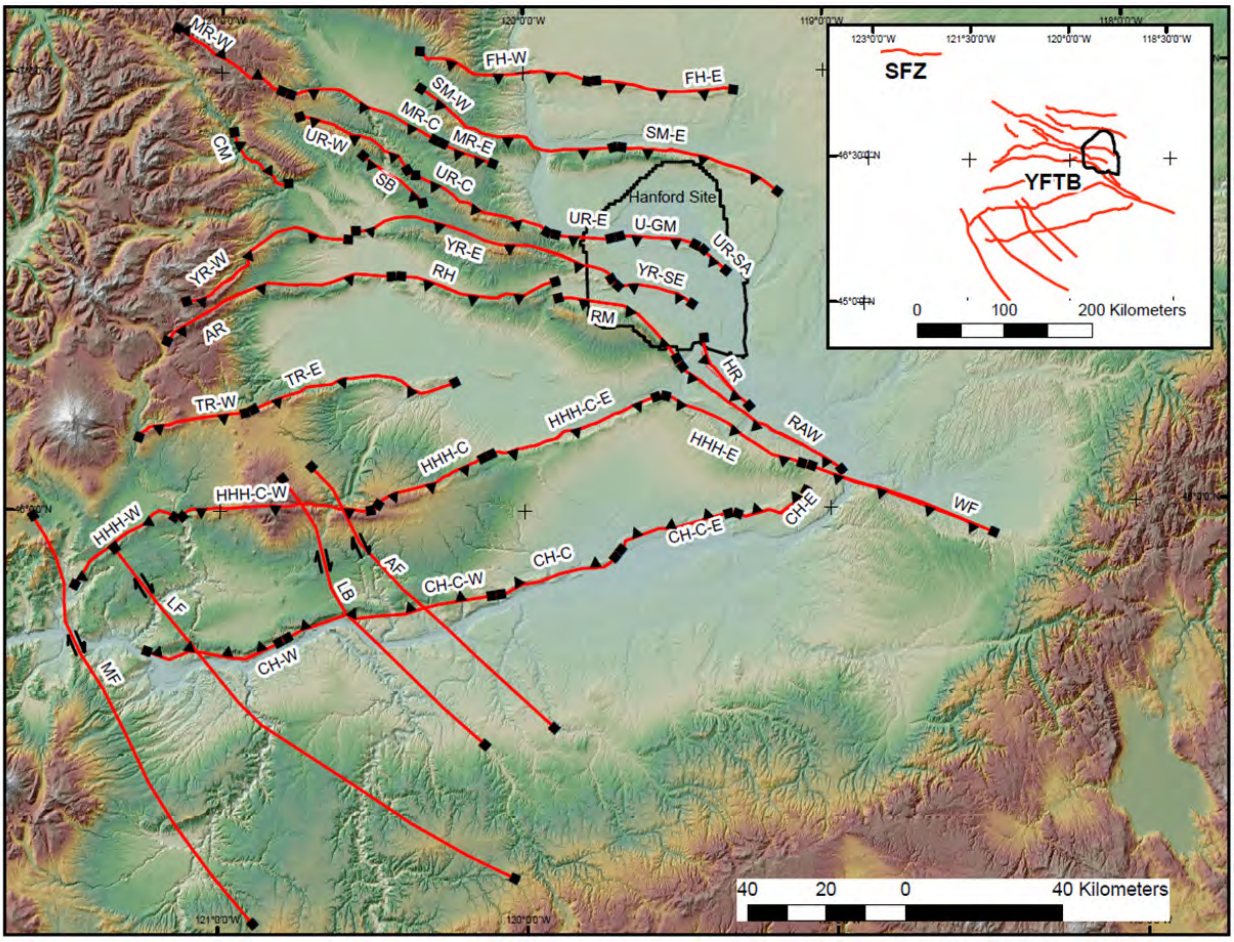


**Figure 8.43**. Fault sources and fault segments. Teeth are shown on the hanging wall of the faults and squares define the segment boundaries. Acronyms for fault sources are given in Table 8.5. The insert shows the location of the Seattle fault relative to the Hanford Site and to other fault sources.

**Table 8.5**. Fault sources including fault segments.

| Fault Source | Abbreviation |
|---|---|
| Ahtanum Ridge | AR |
| Arlington | AF |
| Cleman Mountain | CM |
| Columbia Hills | CH |
| Columbia Hills-Central-East | CH-C-E |
| Columbia Hills-East | CH-E |
| Columbia Hills-West | CH-W |
| Columbia Hills-Central | CH-C |
| Columbia Hills-Central-West | CH-C-W |
| Frenchman Hills | FH |
| Horn Rapids Fault | HR |

**Table 8.5**. (contd)

| Fault Source | Abbreviation |
|---|---|
| Horse Heaven Hills | HHH |
| Horse Heaven Hills-Central | HHH-C |
| Horse Heaven Hills-Central-East | HHH-C-E |
| Horse Heaven Hills-Central-West | HHH-C-W |
| Horse Heaven Hills-West | HHH-W |
| Laurel | LF |
| Luna Butte | LB |
| Manastash Ridge | MR |
| Manastash Ridge-Central | MR-C |
| Manastash Ridge-East | MR-E |
| Manastash Ridge-West | MR-W |
| Maupin | MF |
| Rattles of the Rattlesnake-Wallula Alignment | RAW |
| Rattlesnake Hills | RH |
| Rattlesnake Mountain | RM |
| Saddle Mountains | SM |
| Saddle Mountains-East | SM-E |
| Saddle Mountains-West | SM-W |
| Seattle Fault | SFZ |
| Selah Butte | SB |
| Toppenish Ridge | TR |
| Toppenish Ridge-East | TR-E |
| Toppenish Ridge-West | TR-W |
| Umtanum Ridge | UR |
| Umtanum Ridge-Southeast Anticline | UR-SA |
| Umtanum Ridge-Gable Mountain | UR-GM |
| Umtanum Ridge-Central | UR-C |
| Umtanum Ridge-East | UR-E |
| Umtanum Ridge-West | UR-W |
| Wallula Fault | WF |
| Yakima Ridge | YR |
| Yakima Ridge-East | YR-E |
| Yakima Ridge-West | YR-W |
| Yakima Ridge-Southeast | YR-SE |

The Seattle fault, which lies at a distance of greater than 200 km from the Hanford Site boundary (Figure 8.43), is a known Quaternary fault in the Puget Lowlands region and is assessed to have the highest slip rate of faults in that region. Sensitivity analyses conducted as part of this study showed that the Seattle fault contributes slightly (about 1%) to hazard for areas of the Hanford Site (V. Montaldo-

Falero presentation at WS3 and Chapter 10.0); therefore, the fault was included in the final source model for completeness. The SSC parameters for the Seattle fault follow the characterization outlined in the BC Hydro seismic source model (BC Hydro 2012) (Figure 8.44).

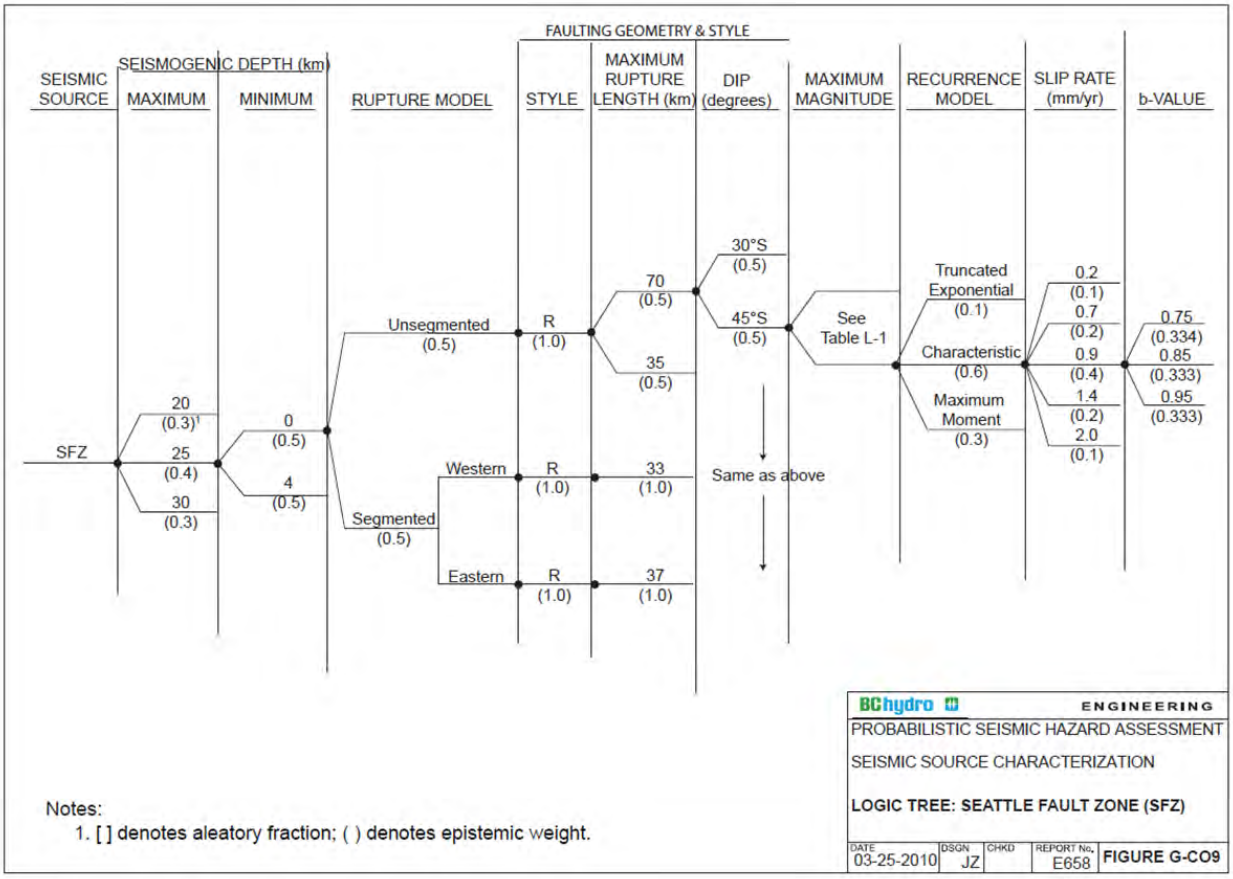


**Figure 8.44**. Logic tree for the Seattle fault zone as given in the BC Hydro (2012) SSC model.

The following sections describe criteria used to assess the seismogenic probability of the other faults included in the model (Section 8.4.1), approaches used to assess segmentation and future rupture lengths (Section 8.4.2), and fault characteristics (location, geometry, sense of slip, recurrence, magnitude, and magnitude frequency distributions) (Section 8.4.3).

### 8.4.1 Seismogenic Probability

In the Hanford PSHA, a seismogenic fault is defined as being all of the following:

- actively involved in the contemporary tectonic environment;
- capable of generating moderate-to-large (M > 5) earthquakes; and
- a localizer of moderate-to-large earthquakes as a fault source in the PSHA.

These attributes give rise to the types of criteria that are useful in identifying seismogenic faults as well as the manner in which seismogenic faults are included in the hazard analysis. Faults that are not identified as being seismogenic are represented by virtual faults within source zones, which are defined

by random locations with given rupture orientations, styles of faulting, dips, depths, and magnitude-dependent rupture dimensions (see Section 8.3.2). In this sense, all seismic source zones are assumed to be seismogenic. However, any individual mapped fault is either seismogenic or not seismogenic from the standpoint of the PSHA; the uncertainty in this assessment is expressed as the "seismogenic probability," or p[S]. A fault assessed to have a p[S] > 0 is modeled in the PSHA as a localizer of future seismicity and the fault source is characterized by fault-specific attributes that define the style of faulting, three-dimensional geometry, characteristic earthquake magnitude Mchar, maximum magnitude Mmax, and earthquake recurrence.

The assessment of p[S] for any particular fault is a judgment made by the TI Team in light of the available data. A number of criteria were used to make the assessment and these range from being very diagnostic criteria to less diagnostic. The ability to apply these criteria is a function of the types and quality of the data available. Criteria for assessing p[S] that were considered by the TI Team range from more diagnostic (top of the list) to less diagnostic (bottom of the list) are as follows:

- *causal* association with a **M** > 5 historical earthquake
- geologic evidence for coseismic displacement(s) during late Quaternary to Holocene
- geologic evidence for Quaternary displacement
- geologic evidence for displacements that are consistent with the contemporary tectonic environment, but inconsistent with previous environments
- *spatial* association with **M** > 5 earthquake.

#### 8.4.1.1 Yakima Fold Belt Faults

As discussed in Sections 4.1 and 4.2, faulting and associated folding of the YFB is an ongoing process within the contemporary tectonic regime. Detailed analysis of modern structural and topographic relief in the YFB shows that this relief entirely post-dates the CRB eruptions (Section 8.4.3.2, Appendix E). Fifteen fault sources within the YFB that have been defined based on topographic and structural relief that is shown to post-date the CRBG are assigned a p[S] = 1 because they are all assessed to be part of contemporary tectonic processes and have sufficient dimensions to generate M ≥ 5 earthquakes.

Paleoseismic evidence for late Quaternary to Holocene faulting is available for several of these folds (Ahtanum Ridge, Manastash Ridge, Rattlesnake Mountain, RAW, Saddle Mountains, Toppenish Ridge, Umtanum Mountain-Gable Mountain, Wallula fault) (Section 8.4.3.7; Section 7.5 of Appendix E) (Figure 8.45). Summaries of key observations and conclusions from sites where Quaternary faulting is observed or suspected are provided by Bjornstad et al. (2012) and Barnett and Sherrod (In Review). Preliminary observations and conclusions from the geomorphic analyses and preliminary mapping of fluvial terraces in the Yakima Canyon also suggest modest late Quaternary deformation associated with Manastash, Umtanum, and Yakima Ridges and Selah Butte (Section 7.0 of Appendix E).

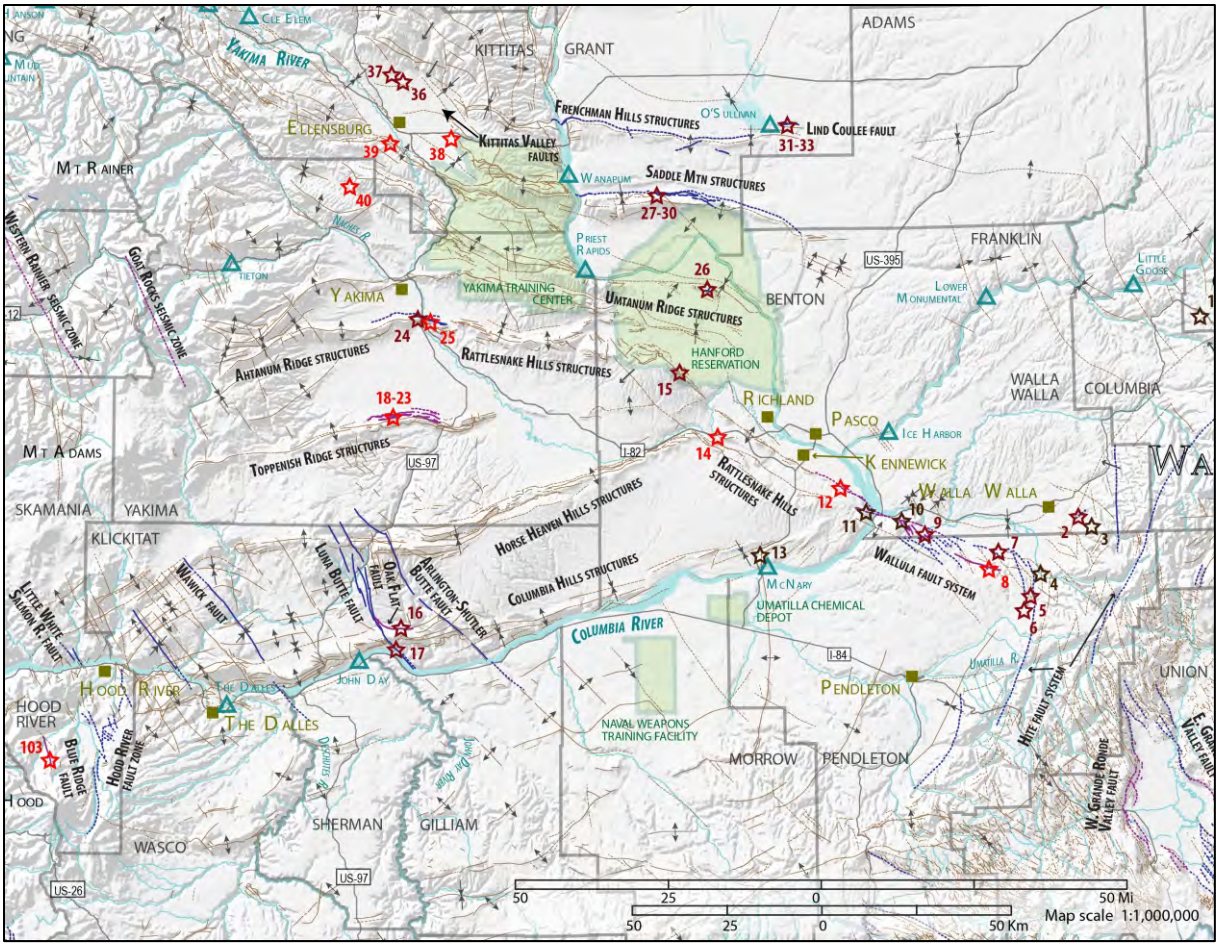


**Figure 8.45**. Map showing Quaternary faults and locations of paleoseismic studies in the YFB (modified from Barnett and Sherrod [In Review]). See Appendix E.4 for descriptions of paleoseismic observations.

### 8.4.1.2 Arlington, Luna Butte, Laurel, and Maupin Faults

Four additional faults are identified as having a seismogenic probability (p[S]) of greater than zero, but less than 1.0. These four faults—the Arlington, Luna Butte, Laurel, and Maupin faults—are part of a sequence of northwest-trending faults that developed concurrently with YFB structures. Geologic information used to assess the p[S] for these faults and related recurrence and magnitude parameters when the faults are included as seismogenic sources are described below.

Northwest-trending, dominantly strike slip faults are prominent features in the southwestern part of the YFB (Figure 8.46). Conjugate northeast-trending sinistral faults are also present, but they are shorter and less numerous. The abundance and regional extent of the northwest-trending faults (some are >100 km) distinguish this part of the province (Anderson et al. 2013). The structures, which were initially recognized by several early workers including Bentley and Anderson (1979), Bentley et al. (1980), Myers et al. (1979), Newcomb (1970), the U.S. Army Corps of Engineers (USACE 1983), and Anderson (1987), are the focus of a recent paper by Anderson et al. (2013). As noted in the recent summary paper, the consensus within the technical community is that these faults are generally considered to be wrench faults based on distinctive characteristics, including 1) conjugate en echelon faults, 2) genetically related en

echelon folds, 3) reversal of apparent dip-slip displacement along strike, 4) lengths of tens of kilometers to more than 80 km, and 5) seismicity with focal mechanism solutions indicating right-lateral strike slip and oblique slip movement.

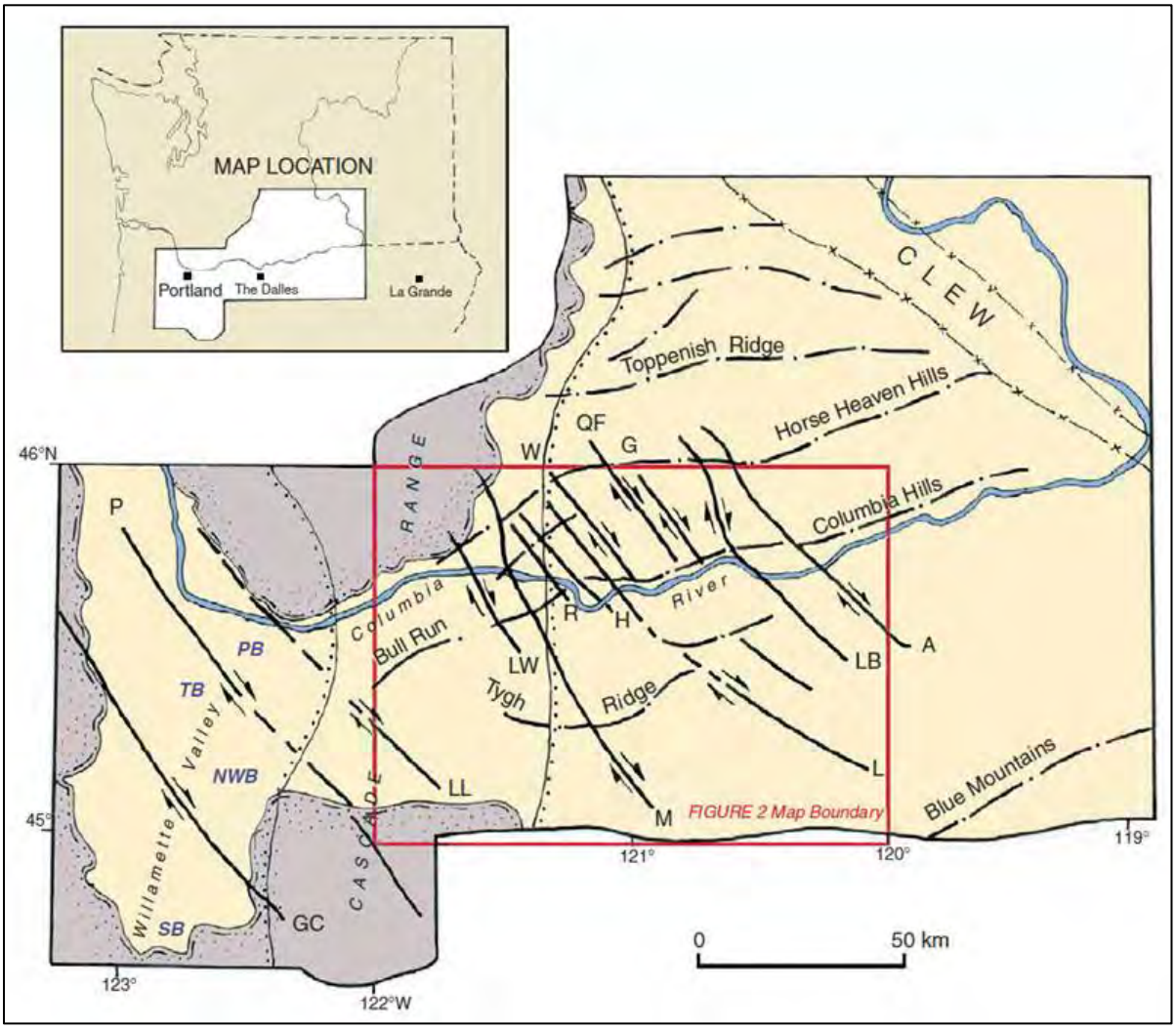


**Figure 8.46**. Generalized tectonic map derived from Tolan and Reidel (1989) emphasizing regional northwest-trending, right-lateral, strike slip fault zones. Willamette Valley basins (from north to south): PB − Portland basin; TB − Tualatin basin; NWB − northern Willamette basin; SB − Stayton basin. Yakima folds are shown with dot-dash pattern. CLEW − Cle Elum–Wallula structural alignment. Fault zones (from east to west A − Arlington; LB − Luna Butte; G − Goldendale; QF − Quiney Flat; W − Warwick; L − Laurel; H − Horse Thief Lake; R − Rowena; M − Maupin; LW − Little White Salmon; LL − Lacamas Lake–Sandy River; P − Portland Hills–Clackamas River; GC − Gales Creek–Mount Angel. Red rectangle indicates the outline of the map shown in Figure 8.38 (from Anderson et al. 2013).

Anderson (1987) concludes that these strike slip faults were recurrently active during the uplift of the Yakima folds, and that they serve as tear faults within the ridges in many instances, but also extend out of the uplifts into adjacent basins. Anderson et al. (2013) speculate that it is probable that many of these faults are basement structures that are episodically reactivated and they have undergone cycles of

emergence, burial by flood deposits, and reemergence. Eruptive events in the Simcoe backarc volcanic field appear to be aligned along some of these strike slip faults.

Anderson (1987) and Anderson et al. (2013) make the following observations regarding the relationship between the YFB uplifts and the northwest-trending faults:

- Strike slip faulting was active early in the history of the YFB uplifts, at least by emplacement of CRBG lavas, but after the YFB uplift spacing had been established.
- Strike slip deformation appears to have been simultaneous within the YFB uplifts and synclinal basins, but the pattern and magnitude of deformation differ significantly between the uplifts and basins.
- YFB uplifts have been segmented and displaced many kilometers by the strike slip faults, but displacements within the adjacent basins is an order of magnitude less. Deformation within the basins appears to be more immature and lacking in connection.
- In some cases the northwest-trending faults accommodate a change in the vergence of thrust faults associated with the uplifts.

Evidence for deformation associated with the northwest-trending strike slip faults within the present tectonic regime as outlined by Anderson et al. (2013) includes the following:

- The eastern three or four faults cross the Simcoe Mountain volcanic field (Luna Butte fault) or transect canyon-filling sequences originating there (Laurel and Arlington faults).
- The Goldendale and Quincy Flats faults also cross the field and the Warwick fault displaces a thick canyon-filling sequence within Klickitat Valley basin.
- All of these faults have displaced or folded Pliocene-age Simcoe units to varying degrees, but whether Pleistocene Simcoe volcanic units are involved is unknown.
- An interbedded canyon-filling lava flow (7.5 ± 0.7 Ma) is right-laterally offset 250–350 m by the Laurel fault south of the Columbia Hills anticline, yielding a long-term slip rate of 0.03–0.05 mm/yr.
- Small thrust faults associated with the Luna Butte fault have displaced glacial Lake Missoula flood deposits. The faults are kinematically compatible with localized transpressional structures developed in CRBG units nearby.

In a study of the John Day Lock and Dam near The Dalles, Oregon, the USACE (1983) summarized previous studies (e.g., unpublished consulting reports from Shannon and Wilson and Foundation Sciences) that have bracketed the age of latest movement of the Arlington-Shutler Buttes lineament (ASBL; referred to as the Arlington fault by Anderson et al. 2013) as between 1 and 4 Ma based on the relationship of the timing of folding of the Columbia Hills anticline and Simcoe volcanic stratigraphy. The USACE report states that the Warwick fault has been bracketed between 4.3 and 1.5 Ma, and that stratigraphic relationships indicate that other faults (Arlington-Shutler Buttes, Goldendale, and Laurel faults) have not had substantial movement since 0.9 Ma. The USACE (1983) report notes, however, that strike slip and normal faults splaying from the trend of the ASBL cut deposits that are between 2 Ma and 200 ka.

Parts of two of the faults, the Arlington-Shutler Butte and Luna Butte faults, are rated as Class A structures in the USGS Quaternary Fault and Fold Database (Personius and Lidke 2003d, e; Lidke et al.

2003) (Figure 8.47a). Although no scarps in Quaternary deposits have been identified along these faults, the Class A designation was assigned based on reported geomorphic expression of possible middle to late Quaternary activity (Pezzopane 1993). Dr. Pezzopane indicated that his initial assessment relied in part on the results of USACE reports (personal communication, January 21, 2014). Based on a lineament analysis and field checking, the USACE (1983) reported possible geomorphic evidence of recent activity along only one fault, the Oak Flat fault (associated with the ASBL).

Four strike slip faults out of more than 35 dextral faults with mean strike directions of 320° are regional in extent and cross two or more ridge uplifts within the study region (Figure 8.46). These include (from east to west) the Arlington (94 km), Luna Butte (89 km), Laurel (134 km), and Maupin (122 km) faults. Given the length of these faults and the observation that they extend beyond the limits of a single uplift, they were evaluated as potential seismogenic fault sources that could generate earthquakes larger than the size of the YFTB background zone.

Two possible conceptual models were considered in the assessment of the seismogenic probability of these faults. One model assumes the faults are independent reactivated basement faults (i.e., seismogenic). We give this model a weight of [0.4]. The second model assumes the faults are tear faults or secondary features associated with deformation of the folds (i.e., nonseismogenic). The nonseismogenic model is considered more likely with a weight of [0.6] based on the following:

1. The highest spatial density of faults is observed in the hanging wall of the Horse Heaven Hills fault source (between Horse Heaven Hills and Columbia Hills). Many faults are clearly constrained to lie in the hanging wall block.
2. Based on review of the 10-m DEM, there is no apparent displacement of the Yakima fold ridgelines or Simcoe volcanics across these faults.
3. The most significant long-term offsets (3.7 to 8 km) are observed shifts in the positions of the folds. The amount of the offsets between folds is at least an order-of-magnitude less and is more discontinuous.
4. Although shown as relatively continuous faults by Anderson et al. (2013), some of the longer faults do not appear to be as continuous based on tectonic maps and lineament analysis presented by the USACE (1983). Examination of the hillshade map from the 10-m DEM supports the USACE (1983) conclusion that the faults are not geomorphically well expressed along their mapped lengths.
5. The USACE (1983) report suggests that the Arlington-Shutler Butte fault connects with the Service anticline structure through an east-west trending sinuous thrust fault. This suggests that evidence of post-CRBG faulting south of the Columbia Hills anticline could also be secondary hanging wall deformation features.

There is little information about the slip rate of these faults, but the lack of Quaternary fault scarps and the absence of lineaments along the mapped trend of the fault as imaged in hillshade maps from the 10-m DEM indicate that the rate is low. Previous seismic hazard studies (e.g., Geomatrix [1995] Oregon Department of Transportation study; JBA et al. 2012) have assigned slip rates ranging from 0.01 to 0.1 mm/yr to the Arlington-Shutler Butte and Luna Butte faults. This range of slip rate is consistent with the limited longer-term slip-rate data available for faults away from the uplift areas (e.g., the 0.03–0.05 mm/yr rate estimated for the Laurel fault as described above). Based on these observations, the following slip-rate distribution is assigned to each of the four fault sources: 0.01 mm/yr [0.4], 0.05 mm/yr [0.5], 0.1 mm/yr [0.1].

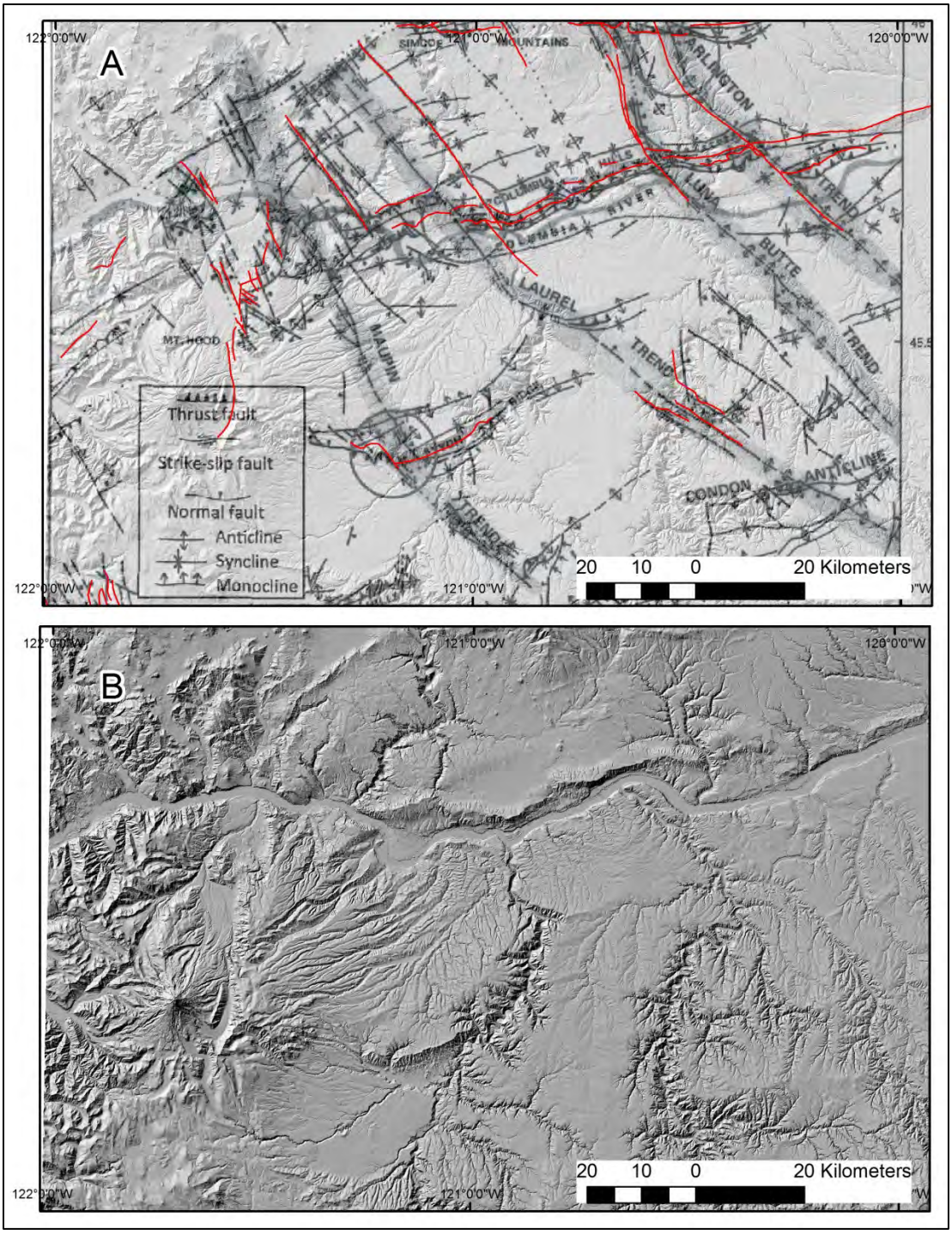


**Figure 8.47**. a) Map showing regional northwest- trending faults (Anderson et al. 2013) superimposed on a hillshade map derived from the 10-m DEM. Red faults show the extent of the Arlington-Shutler and Luna Butte faults that were designated as Class A faults in the USGS Quaternary Fault and Fold Database (Lidke et al. 2003). b) An uninterpreted hillshade map derived from the 10-m DEM.

Although the faults are shown as continuous features at a regional scale, detailed mapping shows more discontinuous fault traces (Figure 8.48). Based on the geometric discontinuities, stepovers, and bends and complexities due to intersections with the Yakima ridges, the rupture lengths used to estimate magnitudes of characteristic earthquakes of these sources are 35 km [0.5] and 50 km [0.5].

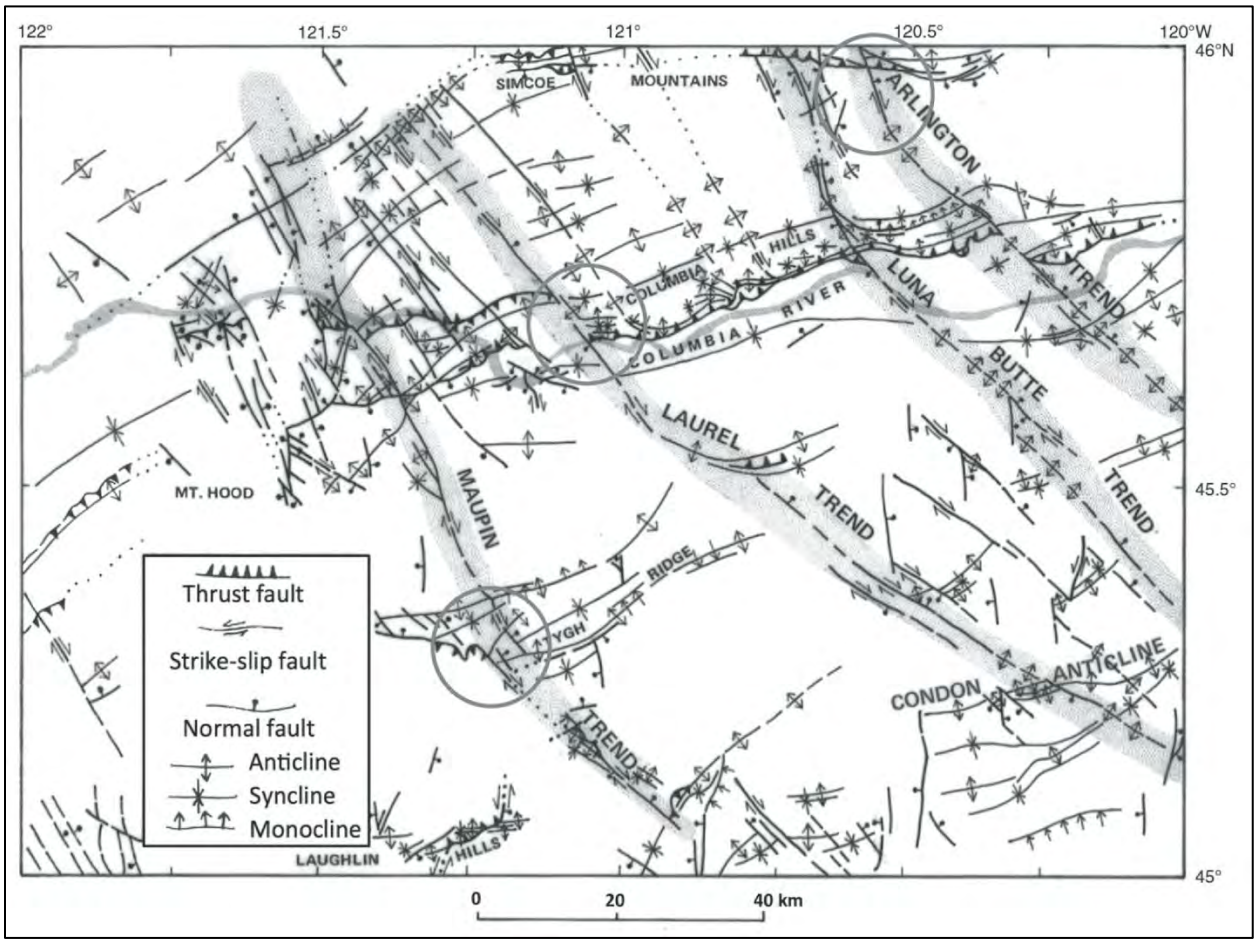


**Figure 8.48**. Tectonic map of part of the southwest Columbia Plateau. Map area includes The Dalles 1 × 2 degree (1:250,000 scale) quadrangle. Regional location is shown in Figure 8.46. Named faults with gray shading are regional trends. Circles indicate three areas where reversals of vergence occur in Yakima Fold Belt uplifts at intersections with regional northwest-trending, right-lateral, strike slip faults. These circled areas are, from north to south, the Horse Heaven Hills, Columbia Hills, and Tygh Ridge. (From Anderson et al. 2013, modified from Swanson et al. 1979, 1981)

### 8.4.2 Approaches to Segmentation and Future Ruptures

Fault sources in the SSC model are characterized as being capable of generating a range of magnitudes up to a fault-specific Mmax. Studies of historical surface ruptures show that moderate-to-large-magnitude earthquakes occur on preexisting faults, and that the dimensions of rupture are correlated with earthquake magnitude. Further, paleoseismic studies of faults have provided estimates of the lengths of prehistoric ruptures and the amount of displacement associated with those ruptures at multiple locations along the fault length. These studies and comparisons with historical rupture characteristics

(e.g., Wesnousky 2008) have allowed estimates to be made of potential future rupture segments that could occur on a fault of interest. Estimates of such potential rupture segments can allow estimates to be made of the magnitudes of future earthquakes associated with the segments (e.g., Wells and Coppersmith 1995). Accordingly, geologic information related to possible segmentation of the faults in the YFB were reviewed and assessed for purposes of evaluating the earthquake magnitudes that faults are capable of generating (Section 8.4.3.8).

Most studies of fault segmentation have been focused on "behavioral" evidence for segmentation (e.g., differences in the timing of the most recent earthquake along strike, slip-rate differences) or "geometric" evidence (e.g., discontinuities in the mapped fault trace, cross structures). There is general consensus that behavioral segments are more definitive of future ruptures than geometric segmentation evidence (e.g., McCalpin 1996), but both types of information are often used to develop a segmentation model for a fault of interest.

As is discussed in Section 8.4.3.2, the structural relief of the YFB faults has been measured along the lengths of faults based on analysis of the topographic relief. Ridge profiles drawn along the highest points along the crest of each fold (Figure 8.49) define distinctive slip gradient shapes that tend to have most relief in the central part and gradients that taper toward the ends. Multiple detailed cross sections drawn normal to the strike of the faults show the topographic expression of each fold and these, in turn, are defined as polygons in map view, as shown in Figure 8.50. Note the distinctive shape to the ridge profiles between the points shown in Figure 8.49, whose locations lie at the ends of the polygons in map view. This distinctive shape is very similar to the shapes of displacement distributions for observed coseismic surface ruptures (Wesnousky 2008; Petersen et al. 2011; Biasi et al. 2011). The repeated occurrence of such displacement distributions along the same section of a fault would lead to cumulative structural relief and slip rates that are also higher in the central section and taper toward the ends (e.g., Schwartz and Coppersmith 1984). As is discussed in Section 8.4.3.6, the structural relief associated with the YFB faults is assessed to provide a confident basis for assessing the slip rate of segments along the fault. Likewise, the TI Team assessed spatial pattern of structural relief along the faults and determined that it provides information regarding the segmentation of the fault sources.

In addition to the variation in structural relief along strike and the overall shape of the relief polygons, other information was considered in the identification of possible segments along the fault sources. For Toppenish Ridge and Ahtanum-Rattlesnake Hills, the geomorphic expression of late Quaternary faulting provides an indication of the lengths of segments. For all of the faults, evidence included significant discontinuities (multiple kilometers) in the surface trace, large stepovers in the surface trace, changes in vergence along the fault strike (suggesting changes in the dip of faults at depth), large changes in fault strike, sudden changes in fault dip (as evidenced by changes in the width of the topographic polygon), and cross structures (such as basement features or strike slip faults). In some cases, geologic evidence for continuity or discontinuity of stratigraphy across the fault projection provided evidence. For example, as discussed in Section 7.4.1.2 of Appendix E, geologic mapping in the area between Rattlesnake Mountain and Red Mountain shows no evidence of a discontinuity or displacement in CRB units, thus lending strong support to a segmentation point between Rattlesnake Mountain and RAW-Rattles.

Based on consideration of the various lines of evidence, the TI Team identified segmentation points along the lengths of the fault sources, as shown in Figure 8.51.

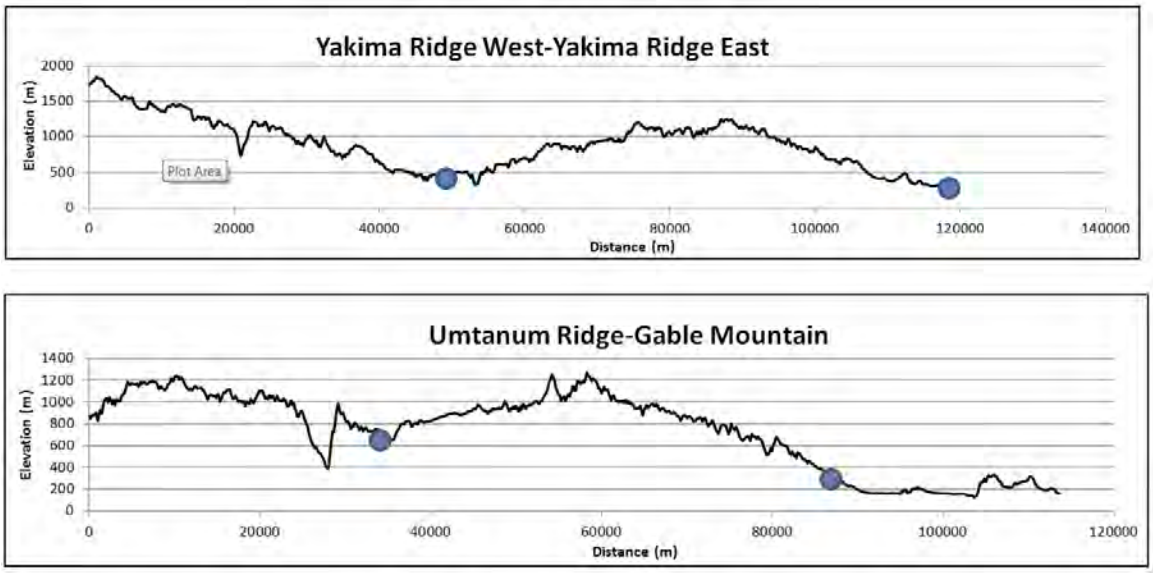


**Figure 8.49**. Examples of ridge profiles drawn along the axis of the highest points of the folds associated with the Yakima Ridge and Umtanum Ridge-Gable Mountain faults. Distinctive slip gradients seen in the ridge profiles and corresponding topographic relief polygons (Figure 8.50) are shown between the blue dots.

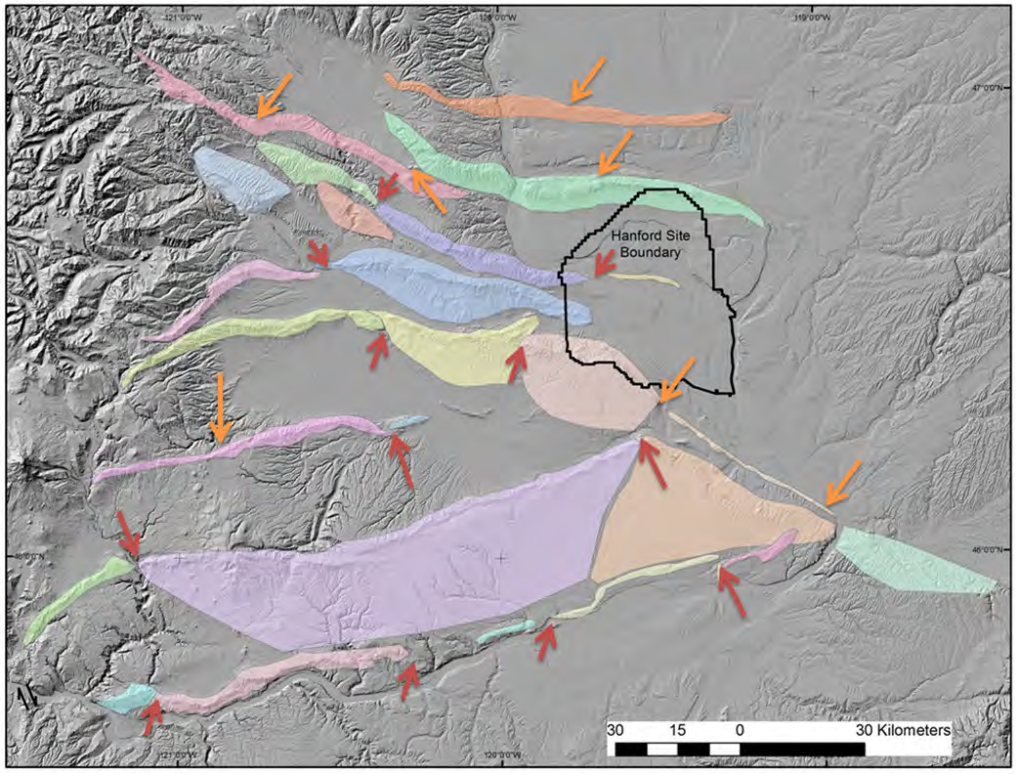


**Figure 8.50**. Polygons defined by the topographic relief associated with each of the folds in the YFB region. The process involved in the development of the polygons is discussed in Section 8.4.3.2. Red arrows are topographic discontinuities and stepovers derived from the polygon analysis; and orange arrows are indications of segmentation based on changes in structural relief, ridge profile amplitude, or fault discontinuities from geologic mapping.

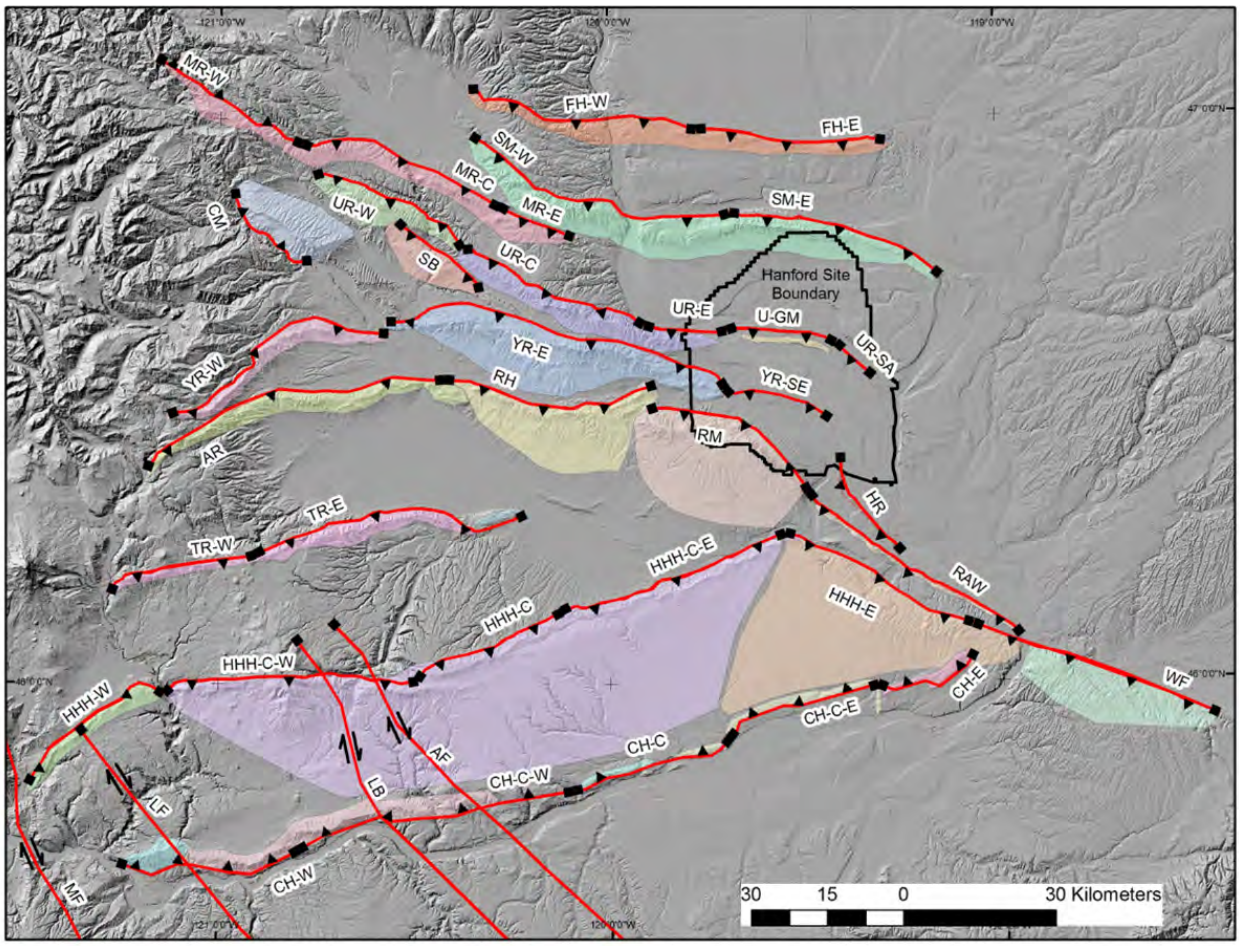


**Figure 8.51**. Segmentation points, shown with black squares, identified by the TI Team based on consideration of a variety of geologic indicators, including variations in structural relief. The strike slip Arlington, Luna Butte, Maupin, and Laurel faults do not show significant topographic relief.

The identified segments are important in the characterization of the fault sources in the SSC model. Slip rates, which are based on structural relief, fault dip, style of faulting, and start time, are defined for each fault segment (Section 8.4.3.6). This is consistent with studies of long-term slip rates along faults showing that they reflect the repeat of coseismic slip distributions during multiple earthquakes (e.g., Hecker et al. 2013; Simoes et al. 2014). The combination of slip rate and fault segment downdip geometry defines the seismic moment rate that is used in the recurrence calculation for fault sources. Based on consideration of the segmentation of the various faults and the potential for rupturing one or more segments, characteristic earthquake ruptures associated with Mchar are identified for each fault source (Section 8.4.3.8) as well as Mmax. Although the segmentation points are important, the TI Team did not conclude that they would invariably be a barrier to rupture. Therefore, the hazard calculations allow for ruptures to propagate across segmentation points along a fault of interest. However, the seismic moment rates of individual segments are maintained (or "balanced") throughout the full range of ruptures that are modeled to occur, based on the recurrence relationships (Section 8.4.3.9). It should be noted that all of the coseismic rupture scenarios considered in the SSC model involve the rupture of parts of, or the entire length of, individual faults of the YFB. Although the simultaneous occurrence of ruptures of

multiple fault sources is not precluded due to random chance, there are no coseismic rupture scenarios that specifically entail the "linkage" of multiple fault sources. The bases for this assessment are given in Section 8.4.3.8.

## 8.4.3 Fault Characteristics Included in the SSC Model

This section provides a description of the fault characteristics that are included in the logic trees for the SSC model, whose overall structure was described in Section 8.1.5. All of the logic trees are discussed as are the methods that are used to characterize the fault sources. In some cases, fault-specific data sets are available for particular sources, such as the availability of Quaternary slip-rate data or paleoseismic evidence that is available for only a few faults. In those cases, reference is made to the particular sections of the report where a detailed description is provided.

The fault sources within the SSC model are characterized using three logic trees that provide a full expression of the knowledge and uncertainties regarding important fault source characteristics. Three of the logic trees are common to all fault sources, and a fourth tree relates to the Rattlesnake Mountain fault source. As discussed in Section 8.4.2, the YFB faults display differences in the geometry and structural relief along their lengths and segmentation points were identified along their lengths. Because many of the SSC geometric and behavioral characteristics are a function of their structural aspects, the faults are characterized in the SSC model on a segment-by-segment basis along their lengths. The SSC model also provides assessments of the manner in which future earthquake ruptures could involve more than one segment.

The first logic tree for the fault sources is shown in Figure 8.52. It includes the characteristics that define the 3-D geometry, style of faulting, and net- slip rate for each fault segment. The first two nodes of the tree are common for all fault segments, and the subsequent parts of the tree are fault segment-specific, as indicated by the vertical line and listing of each fault segment. The seismogenic thickness that is assessed for all fault sources in the model is comparable to the seismogenic thickness assessed for the YFTB source zone. As discussed in Section 8.3.2.3, the estimate is based on consideration of the focal depths of earthquakes within the zone. As given in Section 8.3.3, the logic-tree branches for seismogenic thickness and their associated weights are as follows:

| Seismogenic Thickness | |
|---|---|
| 13 km | [0.2] |
| 16 km | [0.5] |
| 20 km | [0.3]. |

The second node of the logic tree is an assessment that has a direct influence on the dip of faults. As discussed in Section 8.4.3.4, estimates of fault dip come from the geometric consideration of the width of the topographic relief that defines each fault segment and seismogenic thickness. To express the uncertainty in fault dip, a range of estimates of the width of the topographic expression at the surface is considered. The range includes the maximum width of the topographic polygons (which defines the shallowest fault dips at depth) to 60% of the observed topographic polygons (which defines the steepest fault dips at depth) for each segment. The alternative branches and their weights are as follows:

Basis for Fault Dip

| | |
|---|---|
| Maximum polygon width | [0.2] |
| Average polygon width | [0.5] |
| 60% of average polygon width | [0.3]. |

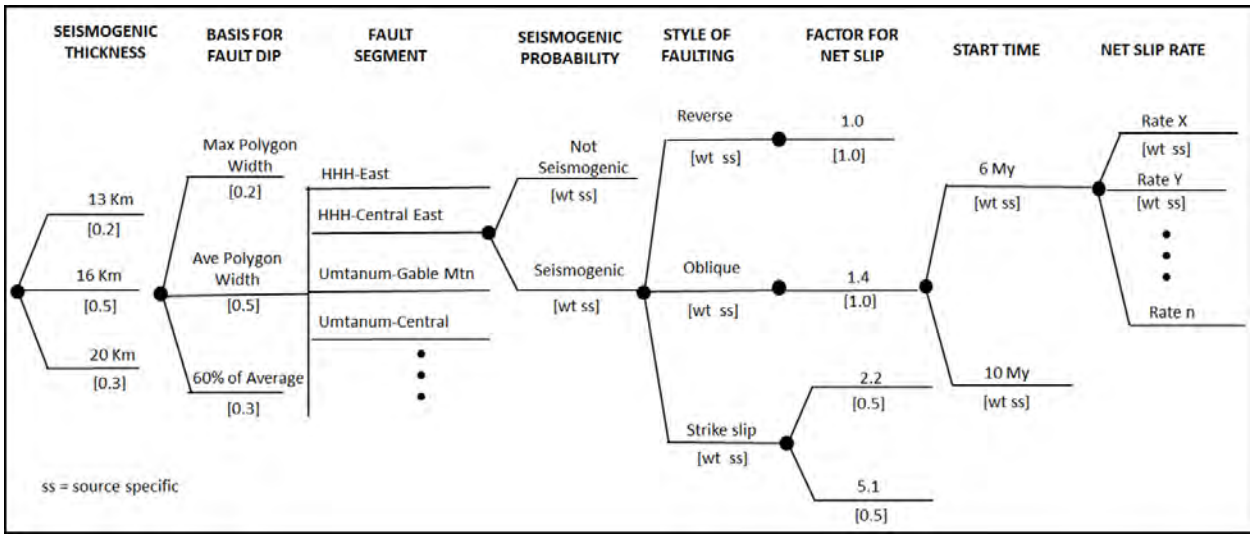


**Figure 8.52**. Logic tree that defines the elements important to fault segment geometry, style of faulting, and slip rate.

The first fault source-specific assessment is the seismogenic probability, which expresses whether or not the fault is included in the SSC model. As discussed in Section 8.4.1, all of the YFB faults are assessed to have a seismogenic probability of 1.0, except the strike slip Arlington, Luna Butte, Laurel, and Maupin faults, which are assessed to have a p[S] = 0.4. All subsequent assessments in the SSC model assume that the fault is seismogenic.

The next node of the logic tree is the style of faulting (often also called the sense of slip). As discussed in Section 8.4.3.3, the assessment of the style of faulting is fault-specific and is based on consideration of local geologic evidence as well as more regional data regarding the tectonic stress regime and other strain indicators. The assessments of the style of faulting for each fault source are given in Table 8.6.

**Table 8.6**. Style of faulting for the fault sources in the SSC model.

| | Style of Faulting | | |
|---|---|---|---|
| Fault Segment | Reverse | Oblique | Strike Slip |
| A-RH: Ahtanum segment | 0.5 | 0.5 | |
| A-RH: Rattlesnake Hills segment | 0.9 | 0.1 | |
| Arlington | | | 1.0 |
| Cleman Mtn | 0.3 | 0.7 | |
| Columbia Hills-all segments | 1.0 | | |
| Frenchman Hills-all segments | 1.0 | | |
| Horn Rapids Fault | 0.6 | 0.4 | |

**Table 8.6**. (contd)

| Fault Segment | Style of Faulting | | |
|---|---|---|---|
| | Reverse | Oblique | Strike Slip |
| Horse Heaven Hills-East | 0.8 | 0.2 | |
| HHH-all other segments | 1.0 | | |
| Laurel | | | 1.0 |
| Luna Butte | | | 1.0 |
| Manastash-all segments | 0.9 | 0.1 | |
| Maupin | | | 1.0 |
| Rattlesnake Mtn | 0.9 | 0.1 | |
| RAW | 0.4 | 0.6 | |
| Saddle Mtn-all segments | 1.0 | | |
| Selah Butte | 0.3 | 0.7 | |
| Toppenish Ridge-all segments | 0.9 | 0.1 | |
| Umtanum Ridge-all segments | 0.9 | 0.1 | |
| Wallula fault | 0.3 | 0.6 | 0.1 |
| Yakima Ridge-all segments | 0.9 | 0.1 | |

For purposes of the hazard analysis, the correlations in the defined style of faulting among the various segments of a given fault must be specified. The cases where all segments of a given fault have the same style of faulting are indicated in Table 8.6 by the term "all segments." For the other cases, the correlations and the weights assigned by the TI Team based on consideration of the available geologic evidence are as follows:

<u>Ahtanum-Rattlesnake Hills</u>
Both segments are reverse [0.5]
Only RH segment is reverse [0.4]
Both segments are oblique [0.1]

<u>Horse Heaven Hills</u>
All segments are reverse [0.8]
HHH-East is oblique; others are reverse [0.2].

Given the style of faulting, the next node of the logic tree expresses the factor by which the dip slip is multiplied to arrive at the net-slip rate. As discussed in Section 8.4.3.3, the vertical component of slip on each fault is derived from the structural relief; the vertical component is then translated into dip slip based on the fault dip; and the dip slip is used with the net-slip factors to arrive at net slip. The net-slip factors are based on the components of lateral to dip slip that are commonly used for defining reverse, oblique, and strike slip faulting states. In the case of strike slip faulting, two alternative cases are considered: one based on a 2:1 lateral to dip slip ratio and the other based on a 5:1 ratio. The alternative net-slip factors and their associated weights are as follows:

Factor for Net Slip: Strike Slip
2.2 [0.5]
5.5 [0.5].

The next node of the logic tree is the start time for calculating the slip rates for the fault sources. As discussed in Section 8.4.3.5, the start time establishes the period in geologic time over which the deformation associated with each YFB fault occurred and can be used to define the contemporary slip rate. Uncertainties in the start time translate into uncertainties in the slip rate for each fault. The start time for each fault applies to all segments of a fault source. The assessments of start time for the fault sources are given in Table 8.7.

**Table 8.7**. Start times and weights for calculating slip rate for fault segments.

| | Start Time for Slip Rate | |
|---|---|---|
| Fault Segment[(a)] | 6 Myr | 10 Myr |
| Ahtanum-Rattlesnake Hills | 0.4 | 0.6 |
| Cleman Mtn | 0.4 | 0.6 |
| Columbia Hills | 0.4 | 0.6 |
| Frenchman Hills | 0.4 | 0.6 |
| Horn Rapids Fault | 0.3 | 0.7 |
| Horse Heaven Hills | 0.3 | 0.7 |
| Manastash | 0.4 | 0.6 |
| Rattlesnake Mtn | 0.3 | 0.7 |
| RAW | 0.3 | 0.7 |
| Saddle Mtn | 0.4 | 0.6 |
| Selah Butte | 0.4 | 0.6 |
| Toppenish Ridge | 0.4 | 0.6 |
| Umtanum Ridge | 0.4 | 0.6 |
| Wallula fault | 0.3 | 0.7 |
| Yakima Ridge | 0.4 | 0.6 |

(a) The assessments shown are applicable for all segments of the fault named.

In addition to the fault-specific assessment of the start time, the hazard analysis also requires that the correlation among start times of the faults be specified. Based on consideration of the available evidence, the TI Team provided the following assessment of correlations:

Start Time Correlations
All faults have start time of 10 Myr [0.6]
Only HR, HHH, RM, RAW, and WF have a start time of 10 Myr [0.1]
All faults have start time of 6 Myr [0.3].

The assessment of seismogenic probability is source-specific and subsequent nodes of the tree are dependent on the fault segment being seismogenic. The style of faulting is also source-specific, duly accounting for a variety of geologic and seismologic data, and the factor for calculating net slip is a function of the particular style of faulting. The final assessment in the tree is the start time for calculating

net-slip rate, and each combination of net slip and start time leads to a distribution of segment-specific net-slip rates, as shown at the end of the logic tree. These net-slip rates for each fault source are given in Section 8.4.3.6.1 and they are used as input to the logic tree related to earthquake recurrence rates.

As discussed in Section 8.4.3.6.2, the Rattlesnake Mountain fault has documented evidence for Quaternary deformation and Quaternary slip rates have also been assessed for this fault source, which are combined in the logic tree with the long-term slip rates presented as weighted alternatives. The logic tree for the Rattlesnake Mountain fault slip rates is given in Figure 8.53.

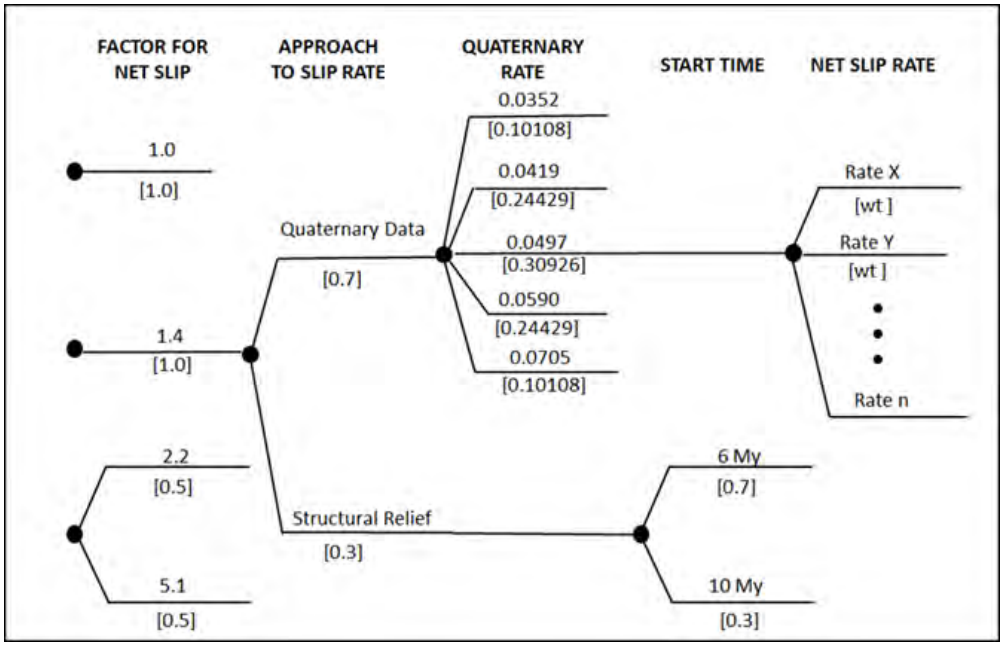


**Figure 8.53**. Logic tree defining the alternative approaches to assessing the slip rate for the Rattlesnake Mountain fault source. Quaternary slip rates shown are vertical separation rates.

The use of Quaternary data to assess slip rate is given higher weight [0.7] than the use of structural relief and the long-term deformation of the CRB [0.3]. This is because the available Quaternary data are well-resolved and provide good estimates of the vertical separation across the fault zone (see discussion in Section 8.4.3.6.2). Also, given high-quality data, the Quaternary time period is generally considered to be representative of the contemporary tectonic regime. As discussed in Section 8.4.3.6.2, a distribution of the Quaternary vertical separation rate is given for the Rattlesnake Mountain fault based on the consideration of the uncertainties in the separation and the age of the Quaternary units. Given the vertical separation rate distribution, the net-sliprate distribution is calculated in the same manner as the long-term rates taking into account the fault dip and style of faulting factors.

As discussed in Section 8.4.3.6.2 and Section 7.0 of Appendix E, the assessed Quaternary and the long-term net slip rates on the Rattlesnake Mountain fault are very similar; the Quaternary rate is slightly lower than the long-term rate. Appendix E also discusses the evidence for Quaternary vertical rates on parts of Manastash and Umtanum Ridges, based on the Quaternary studies. The Quaternary rate (post 1.1 Ma) on Manastash Ridge is essentially the same as the long-term post-CRB rate (0.03 – 0.06 mm/yr). On Umtanum Ridge, the Quaternary vertical rate (post 16 Ma) of about 0.024 m/kyr is somewhat less than the long-term post-CRB rate (0.04 – 0.07 mm/yr), but the terrace correlations and age data are very

preliminary and more mapping and dating are planned as part of federally funded research. Given the state of knowledge at the present time, the TI Team decided to include the Quaternary rates as weighted alternatives to the long-term rates for the Rattlesnake Mountain fault source, but to not specifically include the Quaternary rates for Umtanum Ridge or Manastash Ridge in the logic trees for those fault sources. Based on the current state of knowledge, this decision would have no impact on the hazard contribution from the Umtanum Ridge or Manastash Ridge fault sources.

The net-sliprate distributions for all YFB fault sources are given in Section 8.4.3.6.1 and the slip rates for the strike slip Arlington, Luna Butte, Laurel, and Maupin faults are given in Section 8.4.1.2. As a check on the assessed slip rates and to provide additional insights, the derived long-term slip rates are used to calculate shortening rates along various transects across the YFB and these are compared with rates derived from geodetic data (Section 8.4.3.6.3). Within the uncertainties, the shortening rates from geologic slip rate compare reasonably well to the shortening rates from geodetic data.

The next logic tree, shown in Figure 8.54, provides the nodes for assessing the characteristic magnitudes, Mchar, for each fault source. Given the available data for the YFB faults, all of the assessments in the Mchar logic tree are related to the expected dimensions of rupture (length, width, and area) and the magnitudes associated with those dimensions. Unlike the slip rates, which are assessed for each fault segment, the assessment of Mchar is for the entire fault. Likewise, the characteristic ruptures and the associated magnitudes can occur along any part of the fault in the hazard analysis.

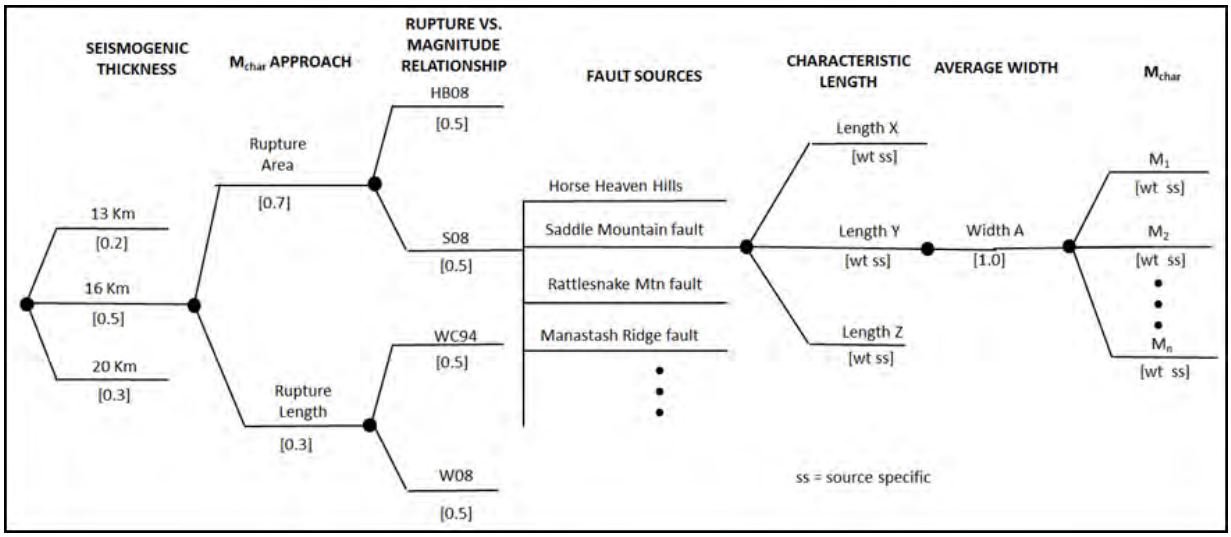


**Figure 8.54**. Logic tree for characteristic magnitudes, Mchar, for fault sources.

The first two nodes of the Mchar logic tree are common to all fault sources. An important constraint on the dimensions of rupture is the seismogenic thickness, which is the same assessment that was developed for the YFTB source zone (Section 8.3.3). In combination with the assessed fault dip, the seismogenic thickness defines the downdip width associated with characteristic ruptures.

The next two nodes of the logic tree involve assessments regarding approaches to calculating Mchar given a rupture dimension (see discussion in Section 8.4.3.9). The first node is an assessment of the relative weight assigned to alternative approaches to calculating Mchar: use of rupture area or use of rupture length. The rupture area approach is given higher weight [0.7] than the rupture length approach

[0.3] because, although both dimensions are empirically correlated with earthquake magnitude, rupture area is more closely associated with seismic moment. Further, rupture area versus magnitude relationships are not sensitive to the style of faulting and therefore uncertainty in style of faulting does not add uncertainty to the magnitude estimates.

Given either a rupture area approach or a rupture length approach, two alternative relationships are considered in each case. As discussed in Section 8.4.3.9, the approaches identified are considered to be appropriate for the tectonic environment and styles of faulting present for the YFB fault sources. Because there is little technical basis to identify a preferred alternative, they are assigned equal weight.

Given the global assessment of seismogenic thickness and the assessment of Mchar approaches in the first part of the logic tree, the remainder of the tree is fault-specific, as indicated by the vertical bar. As discussed in Section 8.4.3.9, the assessment of characteristic rupture lengths is based on the TI Team's consideration of the segmentation of each fault source and the lengths of various segments along the fault. The lengths of alternative characteristic rupture lengths and their weights are given in Table 8.8.

**Table 8.8**. Assessed potential characteristic rupture lengths for fault sources and their relative weights.

| | Characteristic Rupture Length | |
|---|---|---|
| Fault Source | Length (km) | Weight |
| Ahtanum Ridge-Rattlesnake Hills | 45 | 0.5 |
| | 60 | 0.5 |
| Arlington | 35 | 0.5 |
| | 50 | 0.5 |
| Cleman Mountain | 23 | 1.0 |
| Columbia Hills | 20 | 0.3 |
| | 35 | 0.5 |
| | 50 | 0.2 |
| Frenchman Hills | 27 | 0.4 |
| | 37 | 0.4 |
| | 45 | 0.2 |
| Horn Rapids Fault | 24 | 1.0 |
| Horse Heaven Hills | 35 | 0.3 |
| | 45 | 0.6 |
| | 50 | 0.1 |
| Laurel | 35 | 0.5 |
| | 50 | 0.5 |
| Luna Butte | 35 | 0.5 |
| | 50 | 0.5 |
| Manastash Ridge | 20 | 0.2 |
| | 35 | 0.5 |
| | 40 | 0.3 |
| Maupin | 35 | 0.5 |
| | 50 | 0.5 |
| Rattlesnake Mountain | 38 | 1.0 |

**Table 8.8**. (contd)

| Fault Source | Characteristic Rupture Length | |
|---|---|---|
| | Length (km) | Weight |
| RAW | 50 | 1.0 |
| Saddle Mountains | 45 | 0.5 |
| | 55 | 0.5 |
| Selah Butte | 22 | 1.0 |
| Toppenish Ridge | 30 | 0.4 |
| | 55 | 0.6 |
| Umtanum-Gable | 20 | 0.1 |
| | 30 | 0.5 |
| | 40 | 0.4 |
| Wallula Fault | 50 | 1.0 |
| Yakima Ridge | 20 | 0.1 |
| | 50 | 0.5 |
| | 70 | 0.4 |

The next node of the logic tree involves the calculation of an average downdip width for the fault source for use in the calculation of rupture area. The width is a weighted average across the lengths of various segments and the downdip widths of each fault segment, which, in turn, are a function of the ranges of dip and seismogenic thickness for each segment.

Given the weighted alternative Mchar approaches and fault-specific assessments of characteristic rupture lengths and widths, a distribution of Mchar was calculated for each fault source. The Mchar distributions for each fault are given in Section 8.4.3.8 and a summary figure of all Mchar distributions is given in Figure 8.55.

The next logic tree includes assessments related to earthquake recurrence for the fault segments (Figure 8.56). As discussed previously in this section, fault slip rates are assessed in a fault-segment-specific manner from the assessment of structural relief. Given the geometry of the segment and associated downdip width, the slip rates are then translated into seismic moment rates for each segment. The length-weighted average seismic moment rate can then be calculated for the entire fault source and, together with a magnitude frequency distribution (Section 8.4.3.0), earthquake recurrence can be developed for each fault source. It should be noted that the fault recurrence rate describes the rate of various magnitudes occurring on the fault source and the hazard calculations allow for the ruptures associated with those magnitudes to occur anywhere along the entire fault. However, the seismic moment rates for each fault segment are maintained.

The first node of the recurrence logic tree is global for all fault sources and is not fault-specific. This is the temporal model scale factor that accounts for the non-Poissonian behavior of a renewal process (see discussion in Section 8.4.3.10). The temporal model scale factor is multiplied by the Poisson recurrence rate for each fault source to arrive at an equivalent Poisson rate that accounts for the uncertainties associated with a strain accumulation and release process. As discussed in Section 8.4.3.10, a Brownian Passage Time (BPT) model is adopted that requires input related to the mean recurrence times,

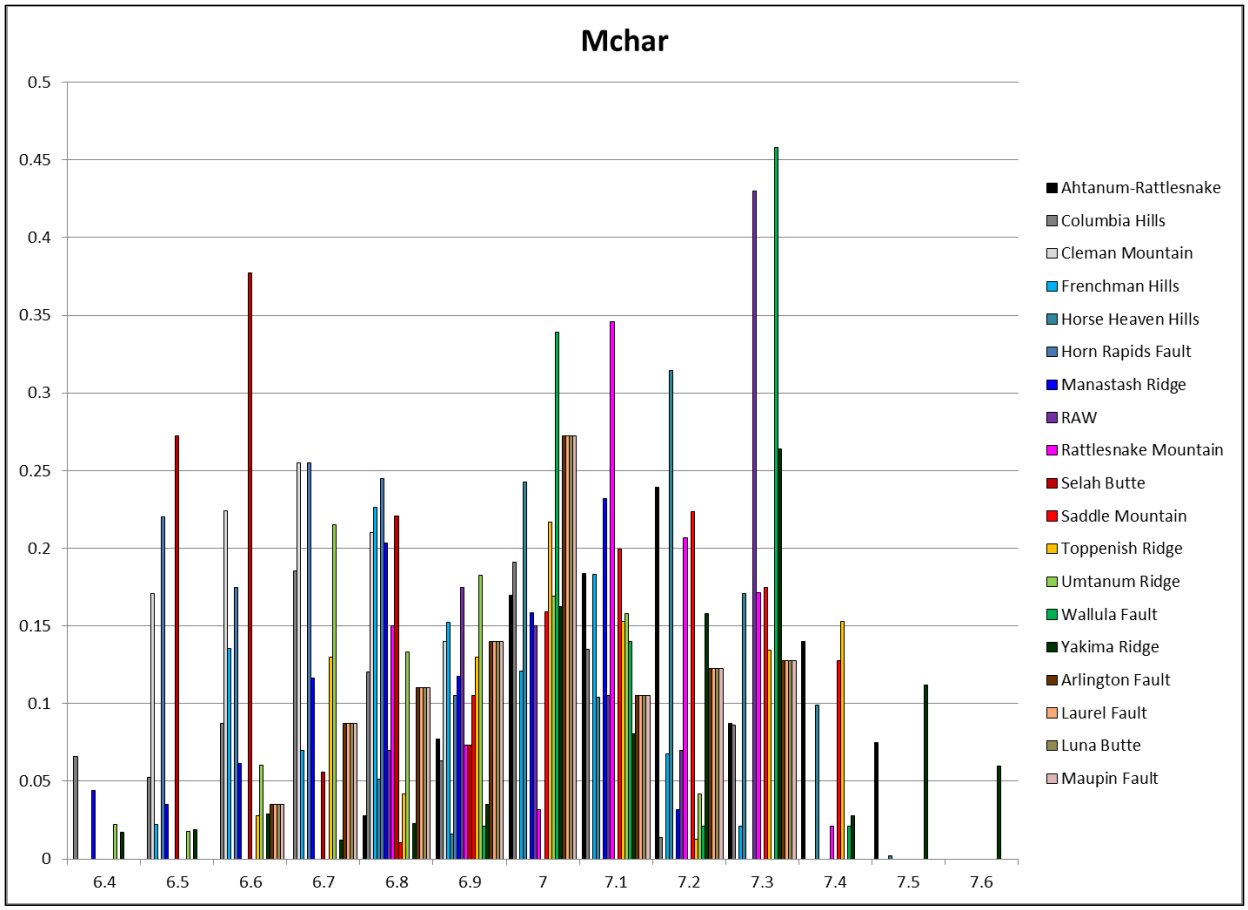


**Figure 8.55**. Summary of the Mchar distributions for all fault sources. Individual Mchar distributions for each fault are given in Section 8.4.3.8.

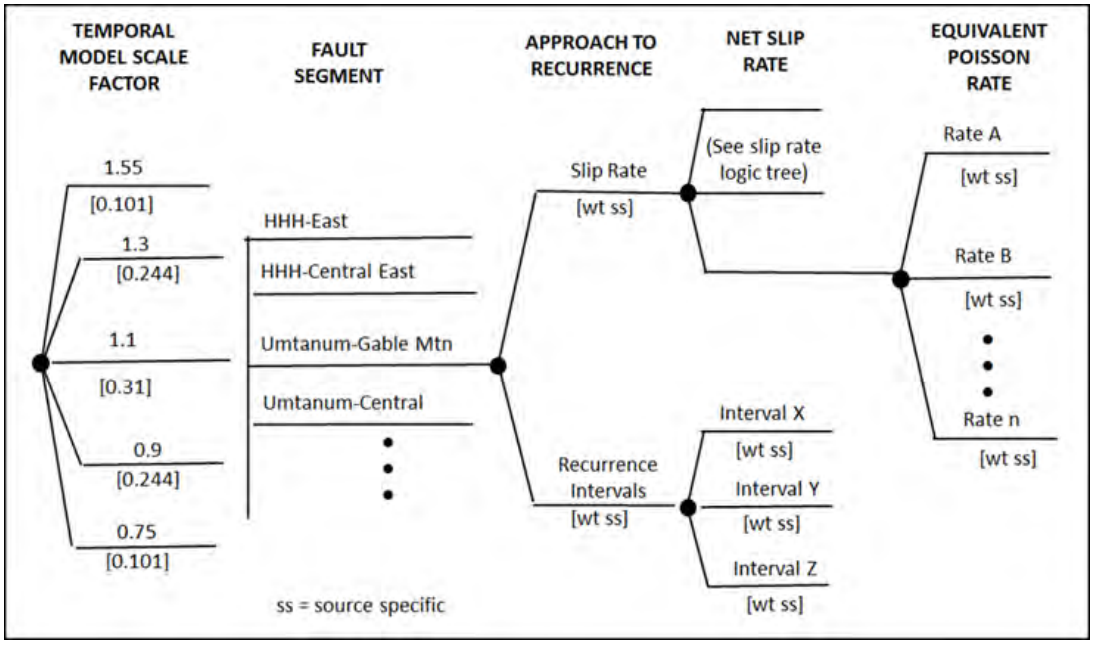


**Figure 8.56**. Logic tree for the recurrence characteristics of fault segments.

uncertainty in the mean recurrence times ($\alpha$, alpha), and the time that has elapsed since the most recent earthquake. Mean recurrence is derived from the range of slip rates, and a distribution of values of alpha was developed based on data appropriate for non-plate boundary faults. For nearly all of the fault sources, the large uncertainties in both alpha and elapsed time lead to a broad range in the temporal model scale factor. The renewal process is assessed to apply to the characteristic part of the recurrence distribution and not to the exponential part, which expresses the recurrence of smaller magnitudes (Section 8.4.3.10).

The next parts of the logic tree are fault-specific, as indicated by the vertical line. For all of the fault sources, data are available for assessing slip rates and the associated uncertainties. For three of the fault sources (Ahtanum-Rattlesnake Hills, Toppenish Ridge, and RAW faults), paleoseismic information is also available that can be used to assess recurrence intervals. For those faults, the relative weights to be given to the slip rate and the recurrence interval approaches to earthquake recurrence were assessed. As discussed in Section 8.4.3.7, the relative weights assigned to the alternative approaches are a function of the quality and uncertainties associated with the data available for each fault. As also discussed in that section, the assessment of recurrence using paleoseismic data regarding the number and timing of earthquakes is highly uncertain and that uncertainty is included in the calculational procedure used. The procedure is based on assessments of the number and timing of paleo-earthquakes, sampling the uncertainties in both of those assessments through multiple simulations, and arriving at a range of recurrence intervals for use in the hazard calculations. The range of uncertainties in recurrence intervals is shown as weighted alternative recurrence interval branches in the logic tree (Figure 8.56). The logic-tree node showing the range of net-slip rates is the output from the logic tree leading to net-slip rate (Figure 8.52).

In both the slip rate and recurrence interval approaches, the resulting recurrence rates are calculated using the common Poisson assumptions and the characteristic earthquake magnitude frequency distribution (see discussion in Section 8.4.3.9.3). These rates are then multiplied by the temporal model scale factors to arrive at equivalent Poisson rates that account for the physical process of a renewal model. Recurrence curves for each of the fault sources that incorporates all elements of the logic tree are given in Section 8.4.3.11.

### 8.4.3.1 Location

The fault sources identified in this study are expressed as predominantly reverse and reverse-oblique fault-related folds that are responsible for uplift of the YFB. Topographic data were analyzed in conjunction with geologic maps, a 3-D hydrogeologic model of the Columbia Plateau (Burns et al. 2011), and structure contour maps on the top of basalt (Myers et al. 1979) to evaluate the locations of the YFB structures. The locations of the fault sources are shown in Figure 8.57. The majority of these faults have been relatively well understood and mapped for many years (Reidel 1984; Anderson 1987; Reidel et al. 1994); however, the exact locations and extents of many faults have been revised as part of this study, particularly those that are blind or buried. While secondary faulting in basalt is commonplace in outcrops throughout the YFB, it is rare that the primary thrust or reverse fault is observable in the field. This is particularly true in areas affected by major erosion and deposition from Pleistocene flooding in the proximity of the Hanford Site and along the RAW structure.

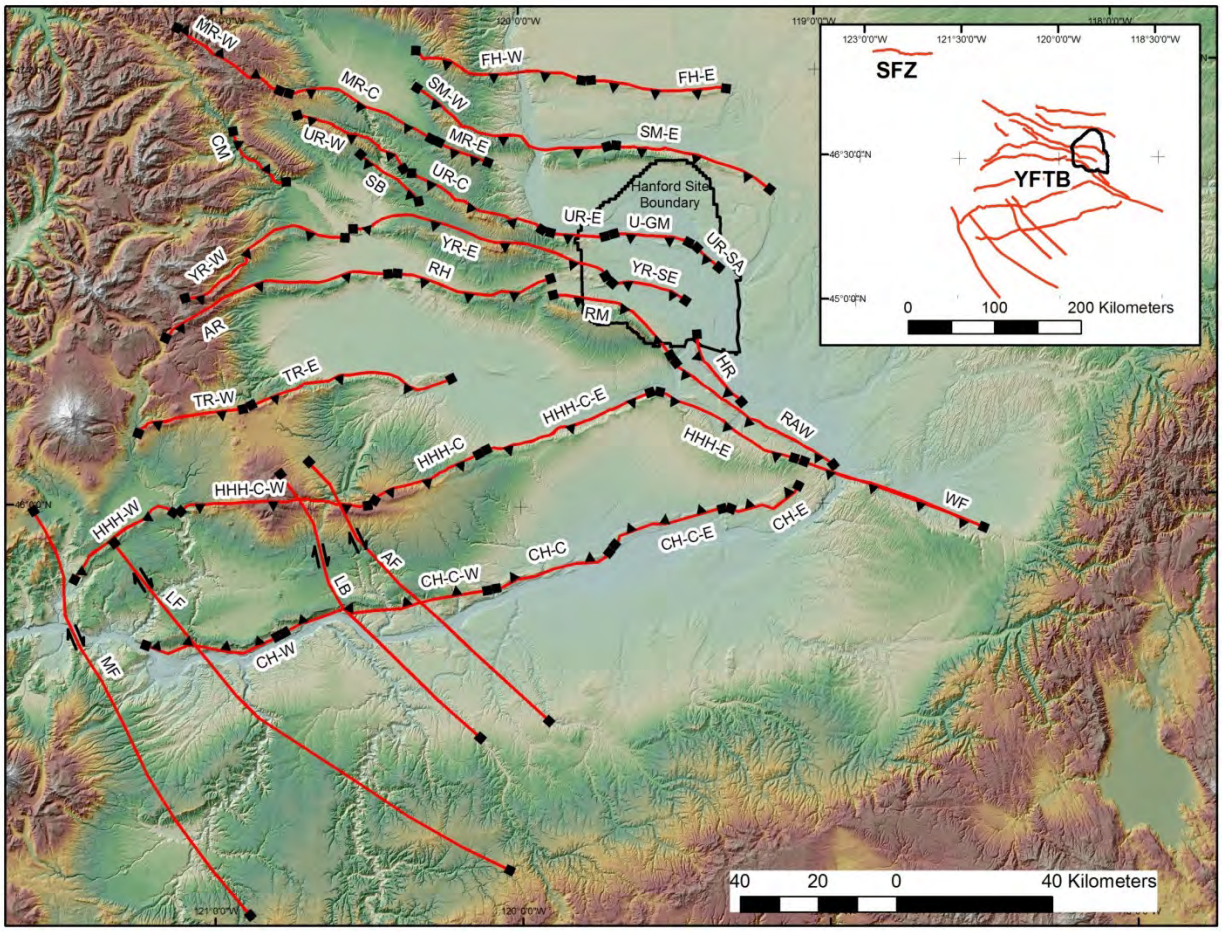


**Figure 8.57**. Map showing locations of fault sources in the study area. The fault source labels are listed in Table 8.5.

The fault sources in this study are the primary seismogenic faults that control the uplift of the CRB. The locations of the fault sources were identified by appropriate methods depending on the available information, and the structural and geomorphic setting. The YFB includes major east-west to northwest-southeast trending ridges with pronounced topographic expression, lower amplitude folds near the Hanford Site with poor topographic expression, and steeply dipping northwest striking faults in the southwest YFB.

The major east-west and northwest-southeast striking faults of the YFB that are responsible for the uplift of large anticlines with hundreds of meters of vertical relief are highlighted in Figure 8.58. These faults are a result of north-south compression resulting in uplifted CRB units that are very resistant to erosion and therefore are well preserved in most locations. The faults and associated folds have been mapped in detail by Walsh (1986), Reidel and Fecht (1994), and Schuster (1994) and compiled into a digital 100K GIS-based geologic map (Figure 8.59). These faults are predominantly south-dipping with exceptions at Columbia Hills, Selah Butte, and Cleman Mountain, which dip to the north. The folds are very large and often trend for tens of kilometers, and therefore hanging wall faulting and folding are commonly superimposed on the limbs of the folds. The fault sources of interest in this study are associated with the uplift of the ridges and are positioned at the base of the frontal escarpments, usually observed as a change of slope in the topography. The folds vary in width from broad thrust sheets to

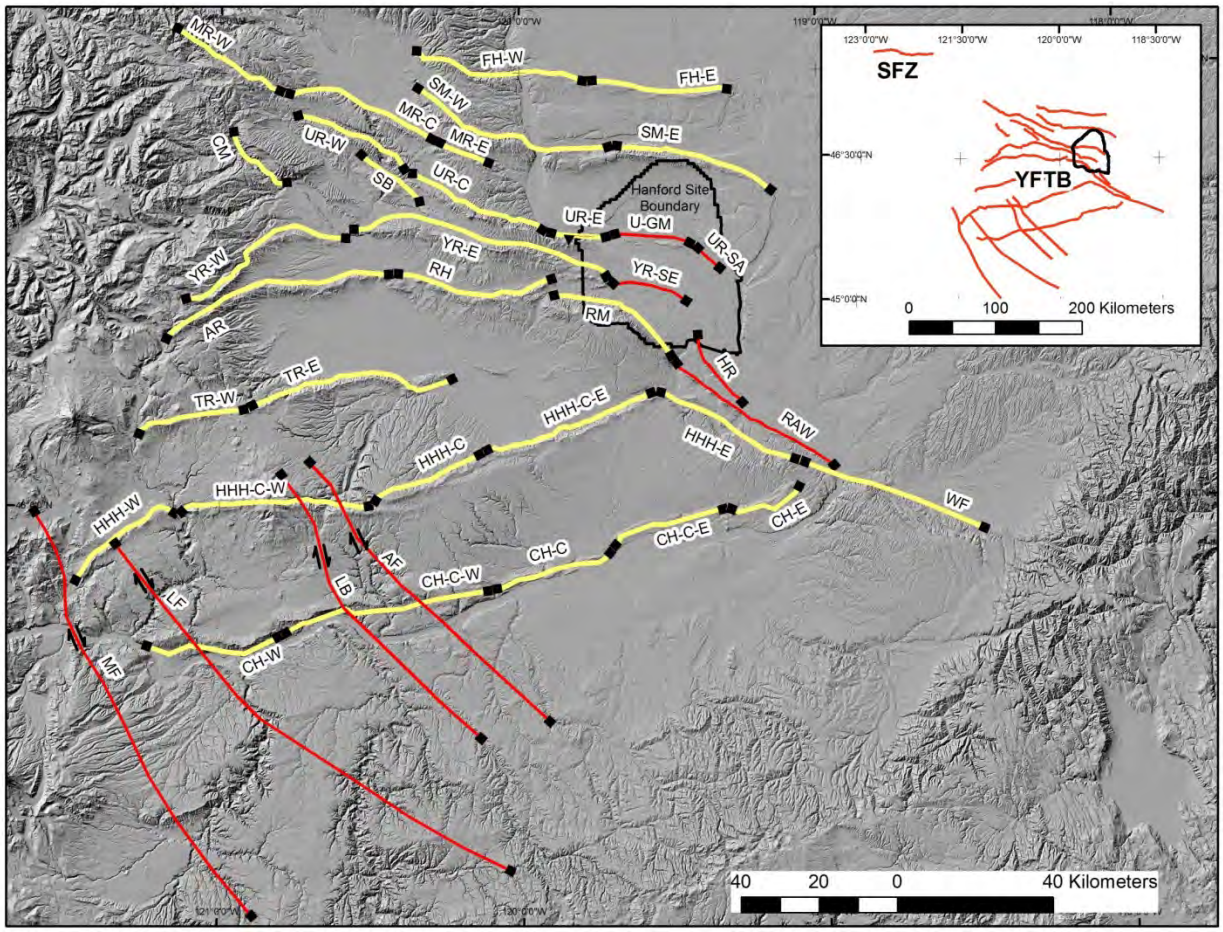


**Figure 8.58**. Map of fault sources in the study area. The yellow-highlighted faults are associated with the uplift of major anticlines and ridges.

narrow ridges. The existing mapping along with the topographic analysis performed as part of this study were used to document the vergence of each structure, which allowed for accurate locations of faults. In many cases, such as at Horse Heaven Hills and Rattlesnake Mountain, the seismogenic fault is close to the surface and buried by loess or alluvial deposits. In other cases, such as at Yakima Ridge, the fault is thought to be blind due to the absence of a major escarpment on a relatively symmetric fold. In both cases, it is not possible to observe the fault directly in the field, but the location of the fault is inferred based on the geometry of the folding. The idea of using the topography as a constraint for fault geometry is further discussed in Sections 8.4.3.2 and 8.4.3.4.

Some of the fault sources are not well expressed in the topography and therefore are more difficult to locate. The faults with less topographic expression typically occur in the area of Pleistocene flood erosion and deposition. These fault sources are highlighted in Figure 8.60. The eastern extensions of Umtanum Ridge and Yakima Ridge are located within the Hanford Site boundary. The eastern portions of both ridges were highly eroded during Pleistocene flooding and subsequently buried by flood deposits. The remnants of this portion of Umtanum Ridge can be observed in the topography as Gable Butte and Gable Mountain, whereas the extension of Yakima Ridge has no geomorphic expression. Borehole compilations from the past several decades have resulted in a 10-m resolution structure contour map of the top of basalt in this area (Thorne et al. 2014). The high resolution of the structure contour map

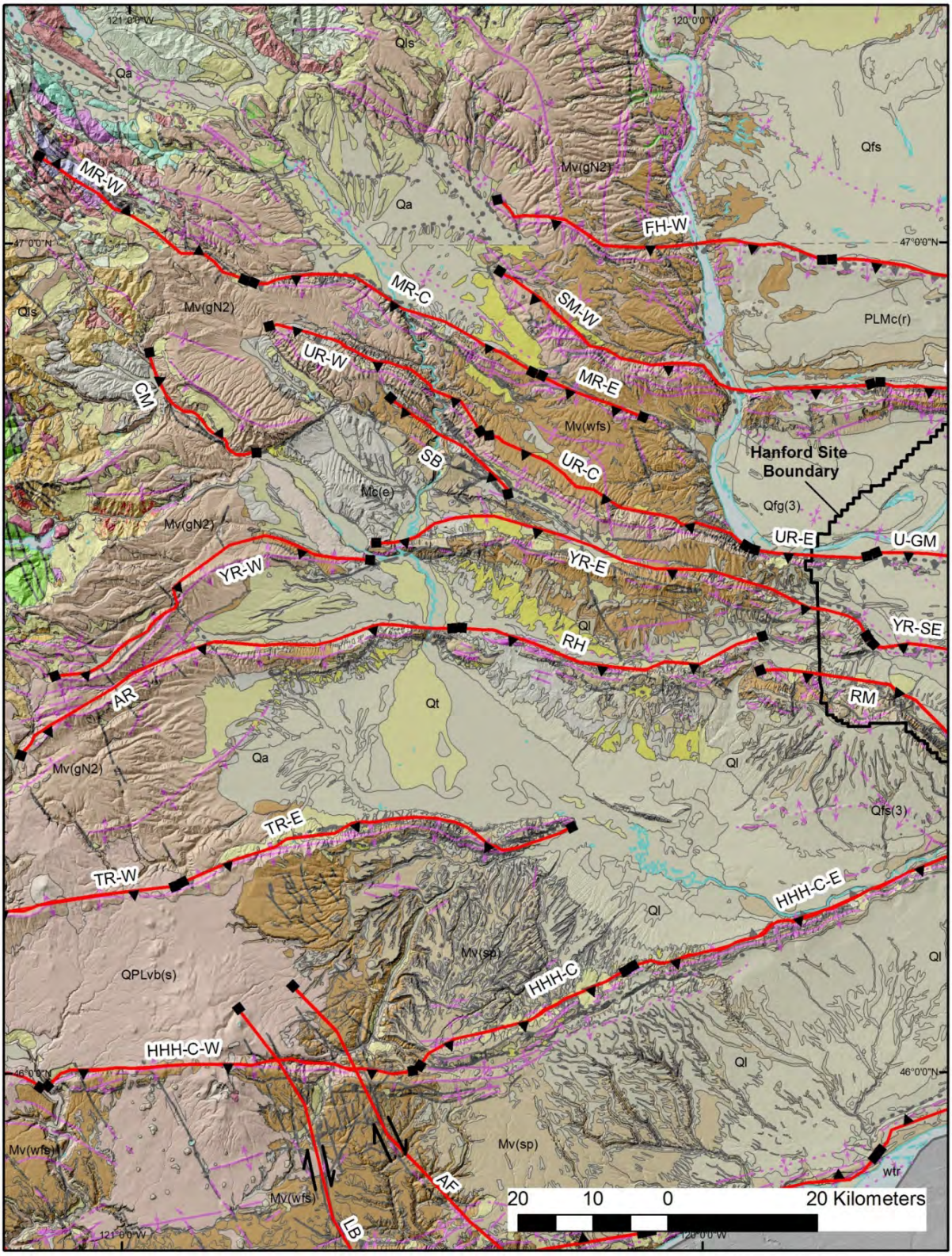


**Figure 8.59**. Geologic map with fault sources showing the compilation of previous mapping efforts in the study area. Secondary hanging wall deformation in the form of folds and minor faults is frequently mapped along the limbs of major folds (modified from Schuster 2000).

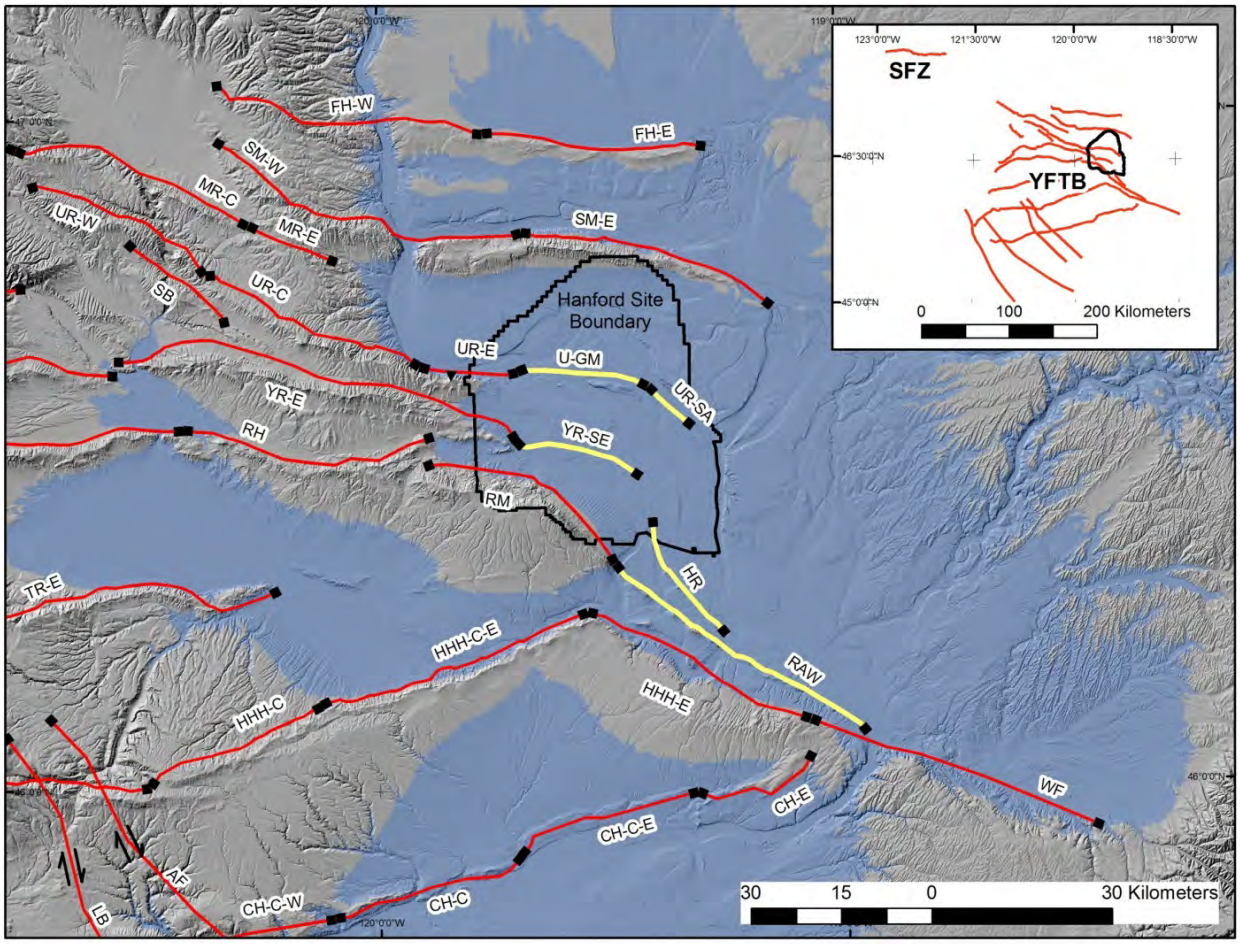


**Figure 8.60**. Map of fault sources in the study area. The yellow-highlighted faults indicate fault sources lacking geomorphic expression. The blue shading indicates the high-water elevation during Pleistocene flooding of 365 m above msl.

highlights the anticlines in the subsurface. Previous studies have investigated portions of the subsurface extension of Umtanum Ridge (NRC 1982; Geomatrix 1996), but this study relocated the fault source slightly given new, higher-resolution data. Further, prior studies have not focused specifically on the location of a fault source related to the extension of Yakima Ridge. Figure 8.61 shows a map of the Hanford Site with the 10-m DEM on the left panel and the subsurface structure contours from Fecht et al. (1992) on the right panel. The anticlines are continuous in the subsurface for several kilometers. The extension of Umtanum Ridge is subdivided into two fault source segments, U-GM and UR-SA, because of a distinct change in orientation and structural relief—information that is not apparent based on topography alone. The extension of Yakima Ridge, YR-SE, is approximately 20 km long with modest amounts of structural relief. Continuity along its length suggests that it is a single segment.

South of the Hanford Site are the Horn Rapids and RAW fault sources that also were highly eroded by Pleistocene flooding. These two faults are predominantly reverse faults with an oblique component, and they both dip to the southwest. The RAW fault is topographically expressed as a linear set of doubly plunging anticlines within the CRB that have been highly eroded by flooding. Many past studies have identified secondary faulting exposed in the hanging wall (e.g., the fault at Finley quarry, as discussed in Section 8.4.3.7.3); however, no studies have identified and studied the main fault that is buried by flood

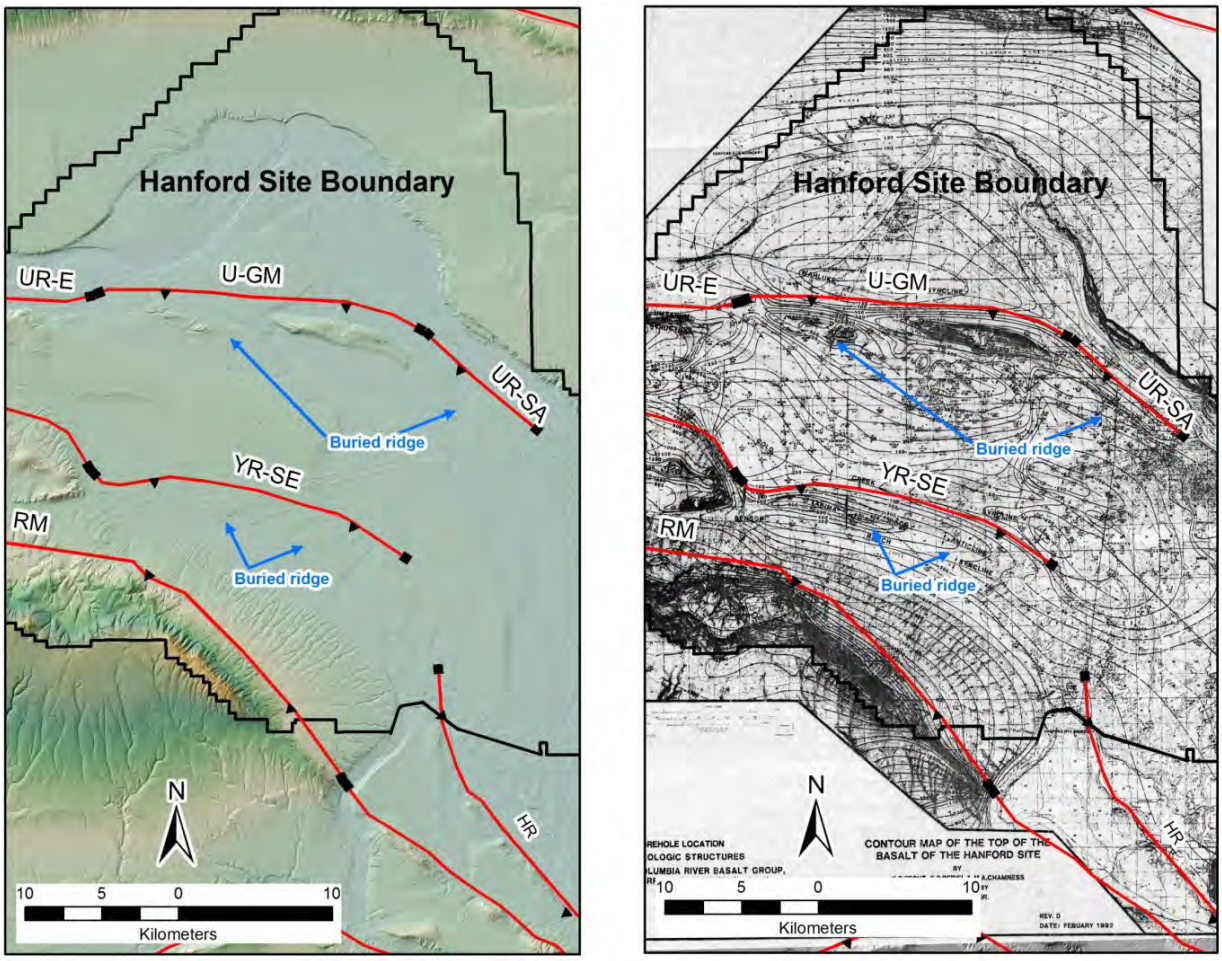


**Figure 8.61**. Map showing the Umtanum-Gable Mountain (U-GM) Southeast Anticline (UR-SA) and Yakima Ridge-Southeast (YR-SE) structures. The left panel shows the lack of topographic expression from Pleistocene flood erosion and burial. The right panel shows the CRB structure contour map by Fecht et al. (1992) that highlights the subsurface extent of the anticlinal ridges.

deposits and loess. The Horn Rapids fault is positioned to the northeast of the RAW fault and strikes subparallel to it. The Horn Rapids fault is geomorphically less pronounced than the RAW fault but can be observed as an uplifted hanging wall with some relief change in near the fault. To correctly locate the seismogenic faults, structure contour maps of the top of basalt from Myers et al. (1979) were used. The structure contour map is shown in Figure 8.62 with fault sources positioned at the vertical separation indicated by the contours.

In the southwest portion of the study area there are four steeply dipping northwest striking fault sources (highlighted in Figure 8.63). The Maupin, Laurel, Luna Butte, and Arlington faults, which are located 90 to 160 km from the Hanford Site, have commonly been mapped as wrench faults that formed contemporaneously with the YFB (Anderson and Tolan 1986; Reidel et al. 1989). While portions of these structures have been incorporated into nearby hazard analyses (JBA et al. 2012), more recent work by Anderson et al. (2013) suggests these fault zones should be refined based on topographic lineaments in bedrock and drainages along with linear uplifted folds in the CRB (Figure 8.64; see discussion in Section 8.4.1.2).

The most distant fault source from the Hanford Site is the Seattle fault, located approximately 200 km northwest of the Hanford Site (Figure 8.57). The Seattle fault zone is a 4- to 7-km-wide fault zone in the Cascade Range foothills to the Puget Lowlands. The location of the fault zone is derived from Johnson et al. (2004) and its fault source characteristics are given in Section 8.4.1.2.

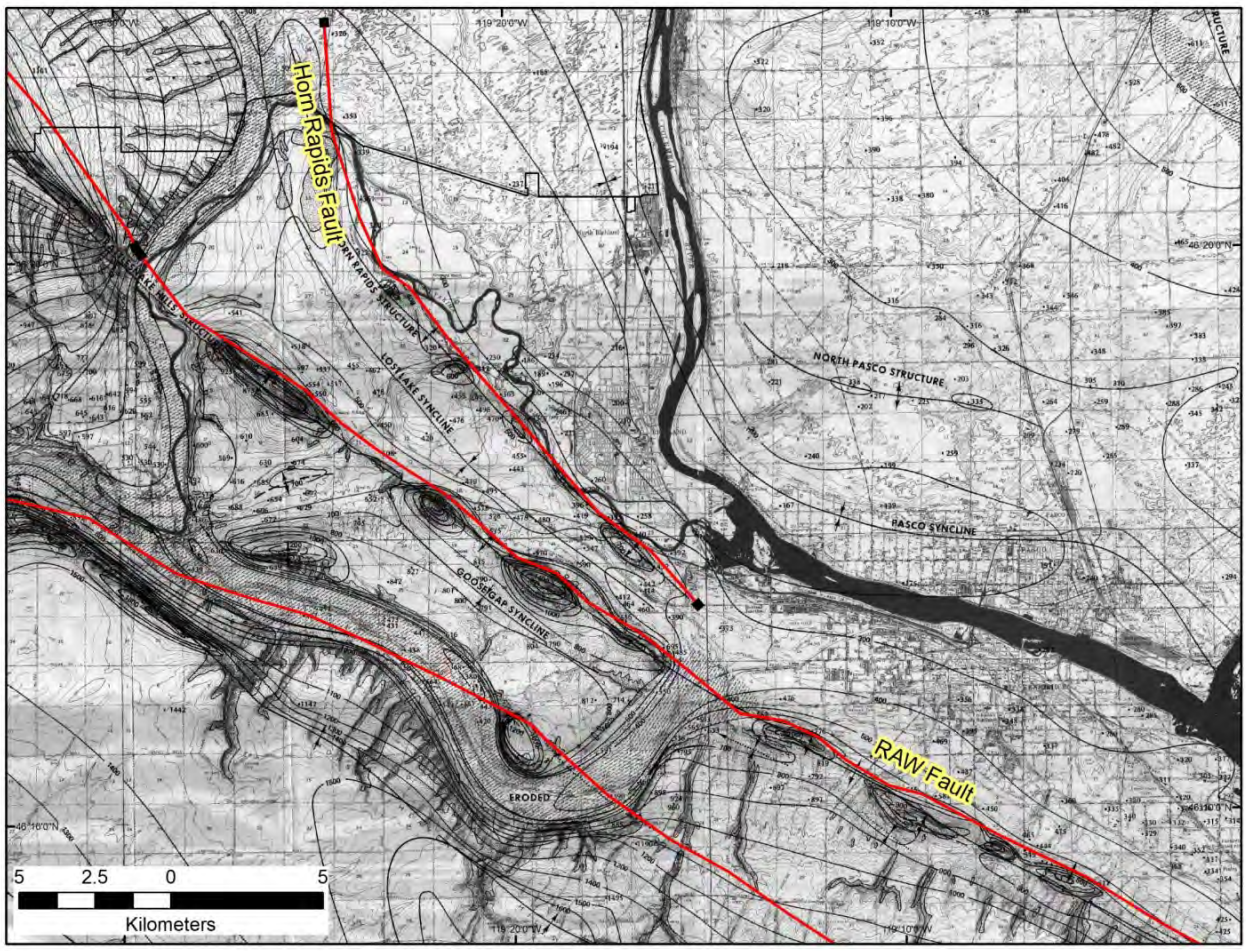


**Figure 8.62**. Map showing the Horn Rapids fault and RAW-Rattles structure over a top-of-CRB structure contour map by Myers et al. (1979).

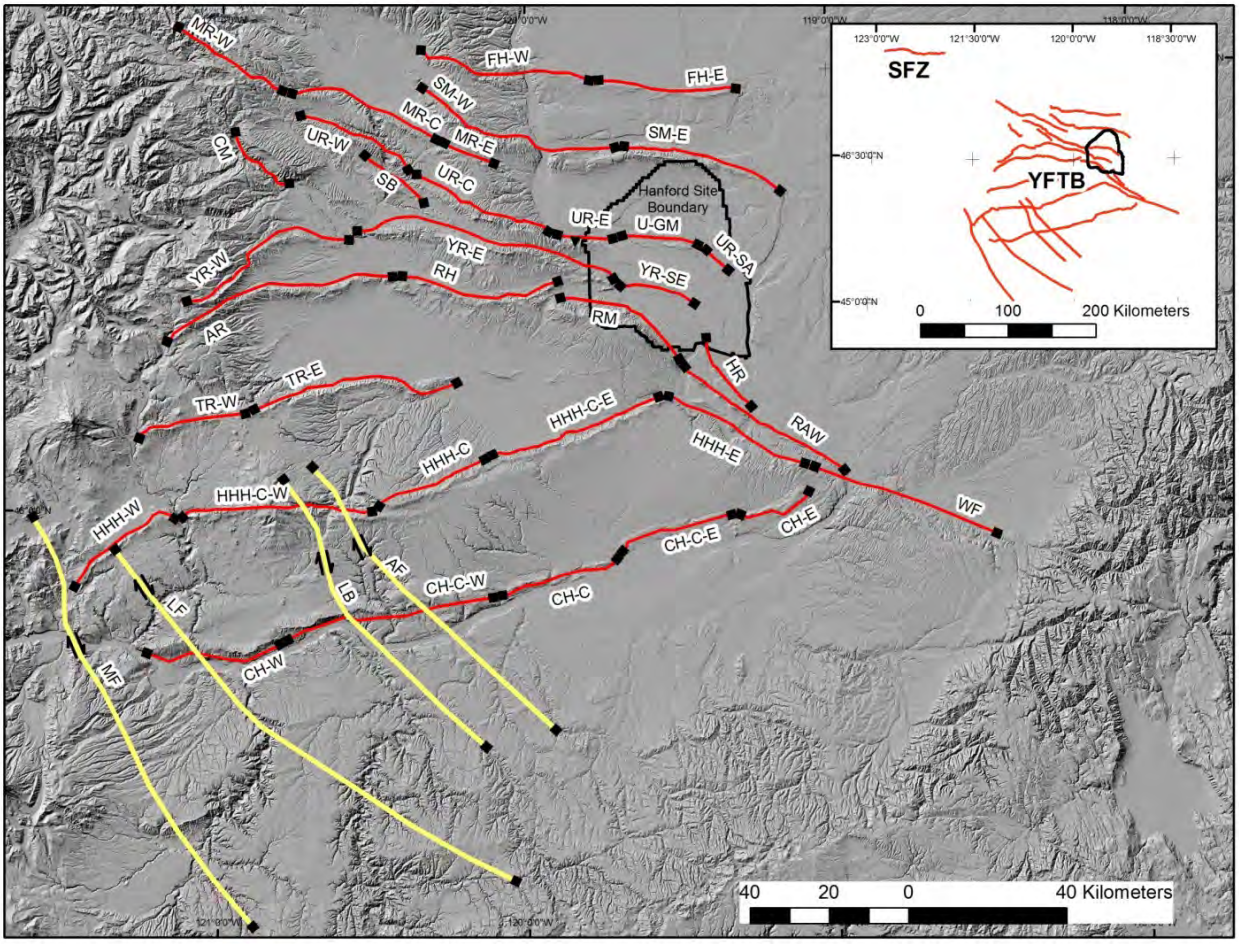


**Figure 8.63**. Map of fault sources in the study area. The yellow-highlighted faults indicate the northwest striking faults.

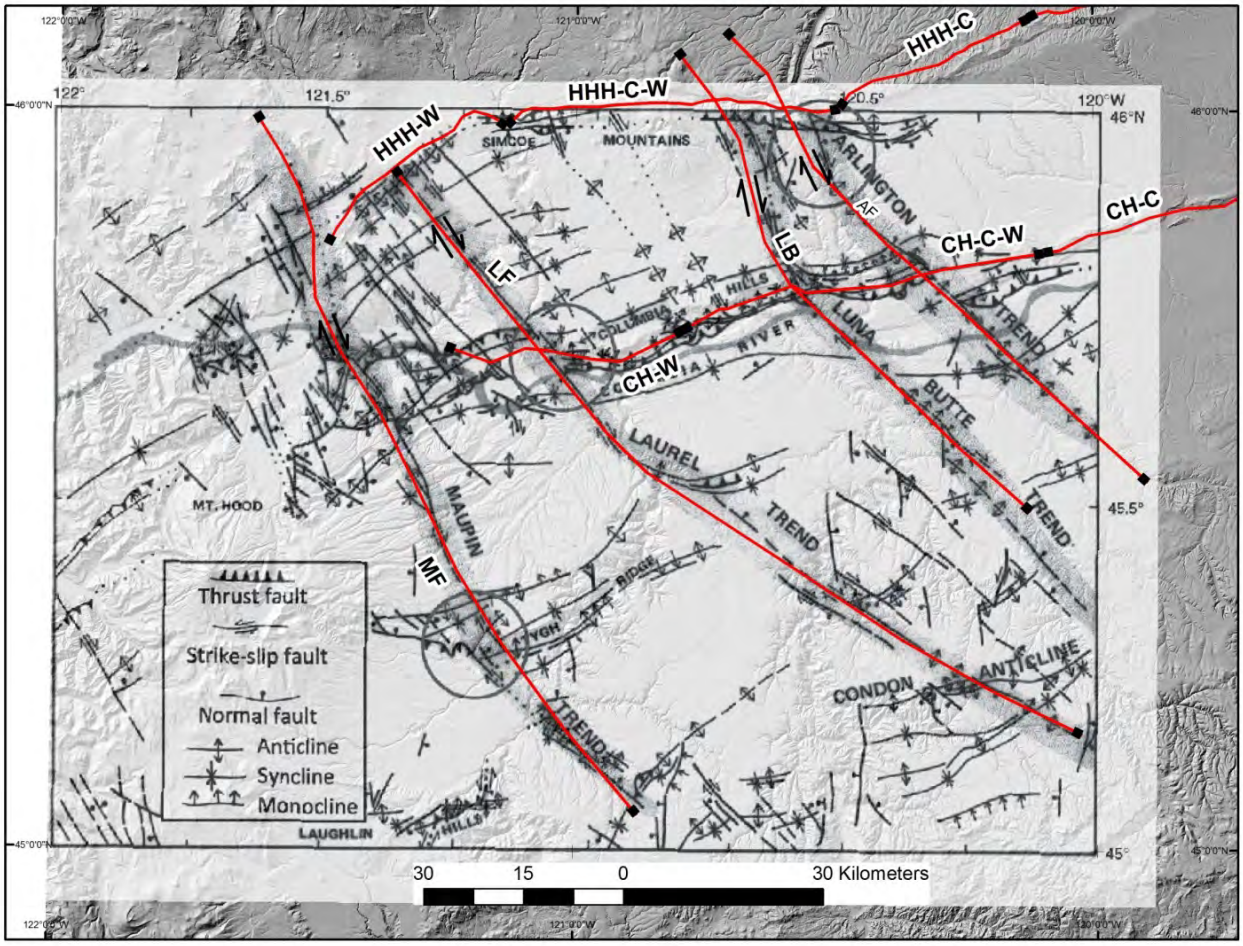


**Figure 8.64**. Map of northwest striking fault sources in the southwest portion of the study area. The published map from Anderson et al. (2013) shows the details of the fault zones within the CRB.

### 8.4.3.2 Structural Relief

Structural relief is a measure of the total vertical distance between stratigraphically equivalent points at the crest of an anticline and the trough of an adjacent syncline and therefore provides crucial information about the uplift history of a structure over the time period represented by the stratigraphic constraints. A lack of paleoseismic information in the YFB makes it difficult to characterize recent slip rates along individual faults. If good structural relief information is gathered for specific faults, it can be used to calculate long-term slip rates and to better understand the tectonic history of the study area. The topographic expression of the YFB is very pronounced and well expressed, especially where major anticlines have been uplifted and preserved above the Pleistocene flood levels. The major ridges are composed of CRB that range in age from 15 Ma to 6 Ma and preserve a long history of uplift in the form of asymmetric anticlines and broad thrust sheets. If the ridges and valleys have not been significantly eroded, the topographic relief can be used as an approximation of structural relief. To evaluate whether topographic relief could be used as a proxy for structural relief for faults and to better understand the underlying fault geometries of the YFB, the Quaternary Studies Team performed a detailed topographic analysis.

A 10-m−resolution DEM was used in an ArcGIS environment to evaluate the amplitude and wavelength of the YFB structures. Individual folds were investigated by analyzing multiple topographic profiles perpendicular to the fold axis. The extent of the fold was mapped along each profile to determine the width of the fold at a given location. The width is defined as the topographic expression of the fold limbs in profile view, from the front of the forelimb to the synformal hinge in the backlimb. A similar process was applied for neighboring profiles to map the changes in the fold width along the trend of the structure. Once the width of the structure was mapped along the extent of the fold, a polygon was drawn to capture the extent of the structure's topographic expression (Figure 8.65). Topographic polygons were constructed for each structure within the YFB for faults with topographic expression Figure 8.66). In addition to looking at profiles perpendicular to the fold axes, ridge profiles were created parallel to the folds along the highest elevation of the ridgeline (Figure 8.49). When used in conjunction with regional geologic maps and knowledge of the geomorphology, ridge profiles aided in identifying potential characteristic rupture segments, further discussed in Section 8.4.3.8. The structural relief would eventually be measured along each of these newly defined fault segments.

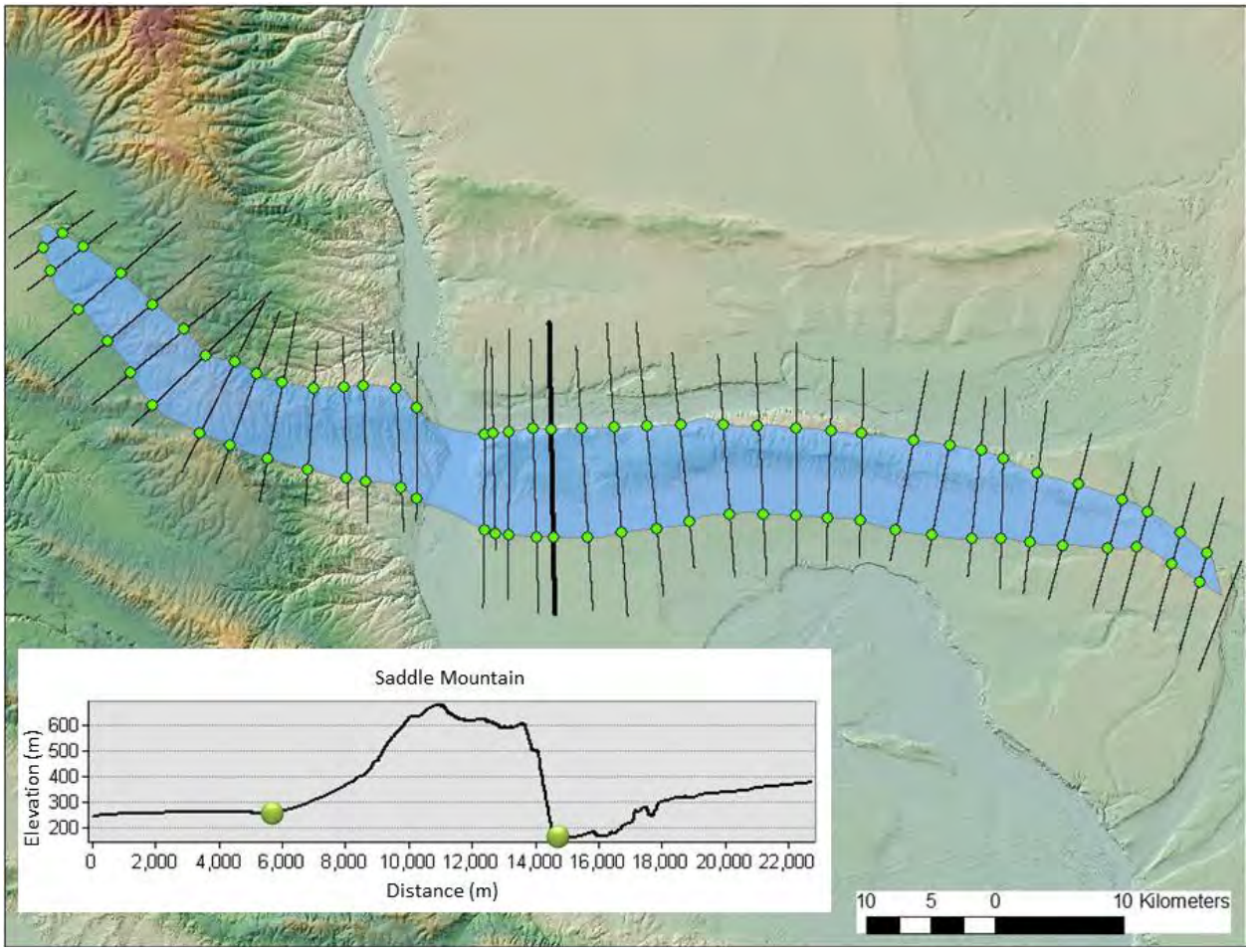


**Figure 8.65**. Example of a topographic polygon from Saddle Mountains. Topographic profiles were extracted from the 10-m DEM in ArcGIS to map the extent of topographic expression (green dots) across Yakima folds. The polygons provide constraints on areas of uplift for a given fault source.

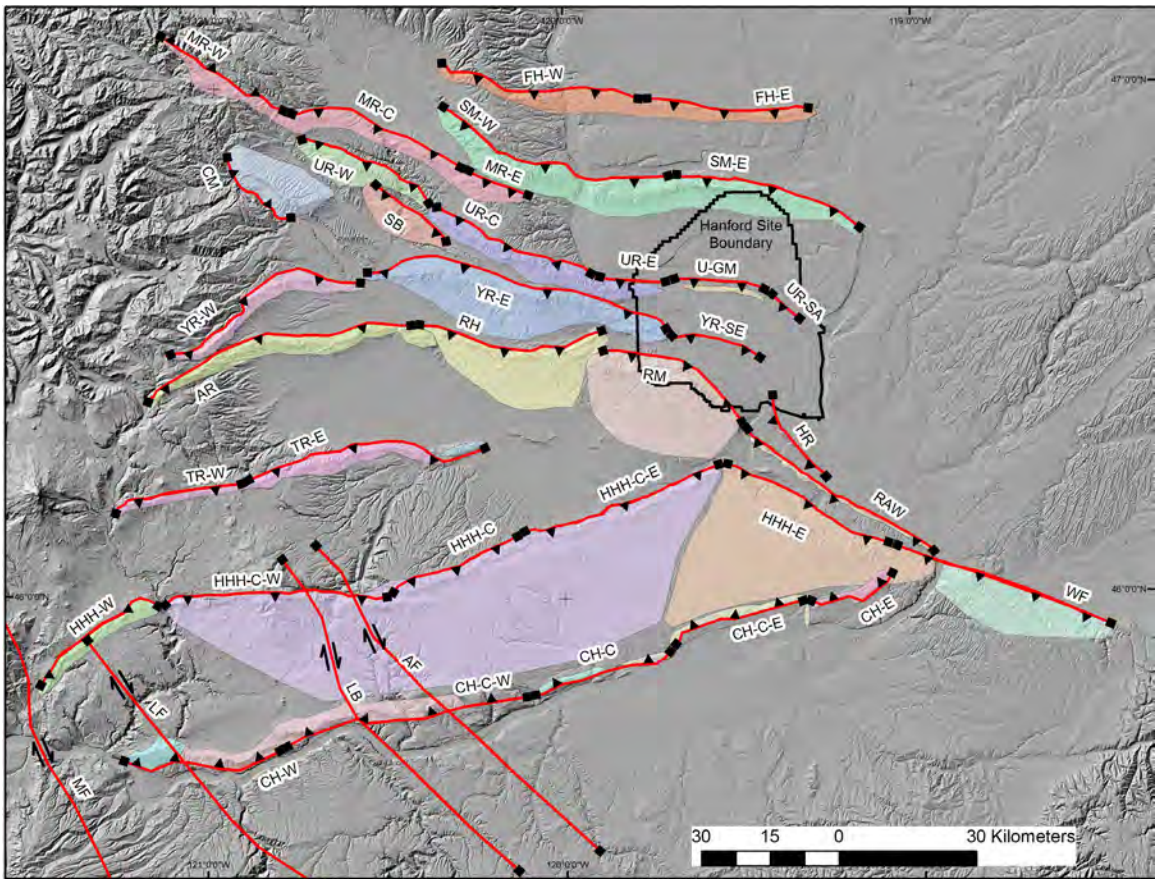


**Figure 8.66**. Map of the topographic polygons constructed using the 10-m DEM. The colored polygons show the extent of topographic expression of folds in the YFB. The topographic polygons provide guidance in determining the location, geometry, and segmentation of the fault sources shown in red.

To determine whether the topographic relief identified during the analysis could be used as a proxy for structural relief, the Burns et al. (2011) 3-D model (hereafter referred to as the Burns et al. model) was used. The regional Burns et al. model is constrained by regional well data that can be viewed with a web tool by extracting cross sections within the YFB. The cross sections include the three major CRB units along with overburden thickness. Cross sections can be extracted across major structures and the vertical separation between units can be directly measured (Figure 8.67). Because of the absence of good well data on the peaks and flanks of ridges, the model is well suited for measurements within valleys and basins, but not well constrained across the folds with high relief. A major observation using the Burns et al. model was that the structural relief observed in the model-derived cross sections was very similar to that measured in the topography, confirming the hypothesis made during the topographic analysis that topographic relief is essentially equivalent to structural relief. In the model documentation, Burns et al. (2011) discuss a statistical evaluation of the fit of the modeled surfaces to the data. The SSC TI Team performed an independent check of the 3-D model against well data to assess whether the first-order stratigraphic and structural relationships were rendered accurately enough to perform a comparison of structural relief to the topographic relief. Based on this analysis and comparison, it was found that the accuracy of the Burns et al. model decreases with depth, but generally is sufficient for making regional, long-wavelength, comparisons of the structural relief on the Saddle Mountains and Wanapum units of the CRB with topography. For details of the analysis see Section 5.1 of Appendix E.

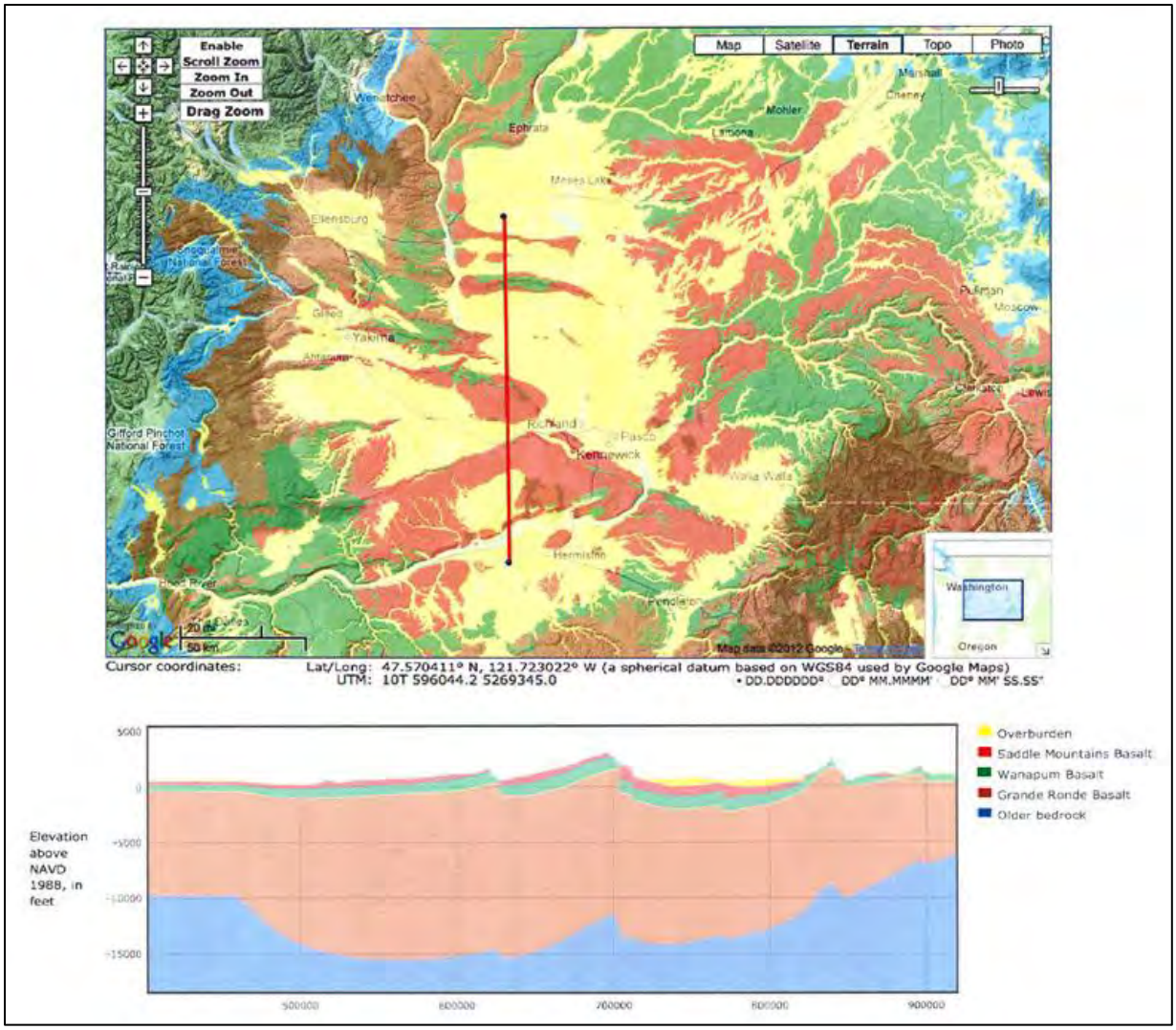


**Figure 8.67**. Example of a cross section extracted from the Burns et al. (2011) model from the online web tool. The model is well constrained from a regional borehole compilation and helped to provide information regarding structural relief. The colors in the cross section represent different rock formations in the basement and CRB.

The analysis of the Burns et al. model using observations from the topographic analysis resulted in four major conclusions about the hypothesis that topographic relief could be used to measure structural relief. The conclusions are as follows:

- Multiple field observations from QGS field studies (see Section 7.0 in Appendix E) along prominent Yakima folds suggest modern topographic relief is comparable to structural relief.
- Evaluation of regional borehole data and the Burns et al. model suggests modern topography is comparable to structural relief.
- Where flood erosion has disrupted modern topography, borehole data and/or structure contour maps should be used to measure structural relief rather than the 10-m DEM.

- The Burns et al. model lacks accuracy on the flanks and peaks of the major ridges because of the lack of boreholes in these locations. Therefore, the subsurface information should be used in the valleys and basins to measure structural relief, but the 10-m DEM is more appropriate to use when measuring structural relief across the major folds.

With the use of the topographic polygons as guides for defining segmentation (Section 8.4.3.8), the structural relief was measured in several locations along each fault segment. To measure the structural relief, several topographic profiles were extracted perpendicular to the fault using the 10-m DEM. For each profile, a base level was established to account for the regional elevation gradient. The relief was measured at the fold axis from the base level to the peak of the ridge. An example of this measurement is shown for the central segment of Horse Heaven Hills in Figure 8.68. Depending on the length of a fault source, anywhere from 4 to 10 topographic profiles were evaluated per segment. After sufficient measurements were taken along a given fault segment, the average (mean) value of the structural relief was used for the characterization of the fault source. This method worked well across the major folds west of the Columbia River where the structures were not affected by Pleistocene flooding and the CRB was well preserved. In areas where erosion or deposition from flood events made it difficult to rely on the topography alone, top-of-basalt structure contour maps were used in conjunction with geologic maps and local borehole data.

In the footwalls of the Wallula and Saddle Mountains faults, the CRB units have been significantly eroded by Pleistocene flooding. To accurately measure structural relief, the units near the crest of the fold must correlate with the units across the reverse fault in the footwall. If the footwall was deeply incised or buried, the topographic relief would necessarily be indicative of the structural relief. To add more information to the topographic profiles in these cases, the 1:100,000 scale Washington State Geologic Map was used in conjunction with local borehole data to further constrain vertical separation across the fault. An example of this circumstance is observed on the northern side of the Saddle Mountains. The local borehole and geologic data were added to the topographic data to further constrain the structural relief seen in Figure 8.69 and Figure 8.70. Profile 1 in Figure 8.70 shows a pronounced trough from a major Pleistocene flood channel in the footwall of the Saddle Mountains. If the topography alone were relied on to measure structural relief in this case, the measurement to the valley floor would result in an overestimation of the true structural relief identified as 325 m in this location. Along the northeastern side of the Wallula fault, burial due to Pleistocene flood deposition has created a similar complication. To more accurately measure structural relief at this location, local well data were used to correlate vertical separation of units across the fault. In this case the structural relief measured in the borehole horizons was similar to that measured in the topographic relief. In areas to the north of Wallula Gap near the Hanford Site, structures in the direct path of Pleistocene floods have little to no topographic expression. In these circumstances the structural relief was constrained entirely using subsurface data.

Structural contour maps of the top of the Saddle Mountains Basalt cover a large area of the Hanford Site (Myers et al. 1979). Fecht et al. (1992) and Thorne et al. (2014) provide detailed information about the subsurface geometry and relief of buried structures (Figure 8.71). The main fault sources that were altered by the Pleistocene floods include the eastern portions of the Yakima and Umtanum Ridges, Horn Rapids, and the RAW-Rattles structure. In these locations, topographic profiles were extracted from the structure contour maps in the same manner described using the 10-m DEM. Further discussion of creating topographic profiles from the structural contour maps can be found in Section 5.2.3 of Appendix E.

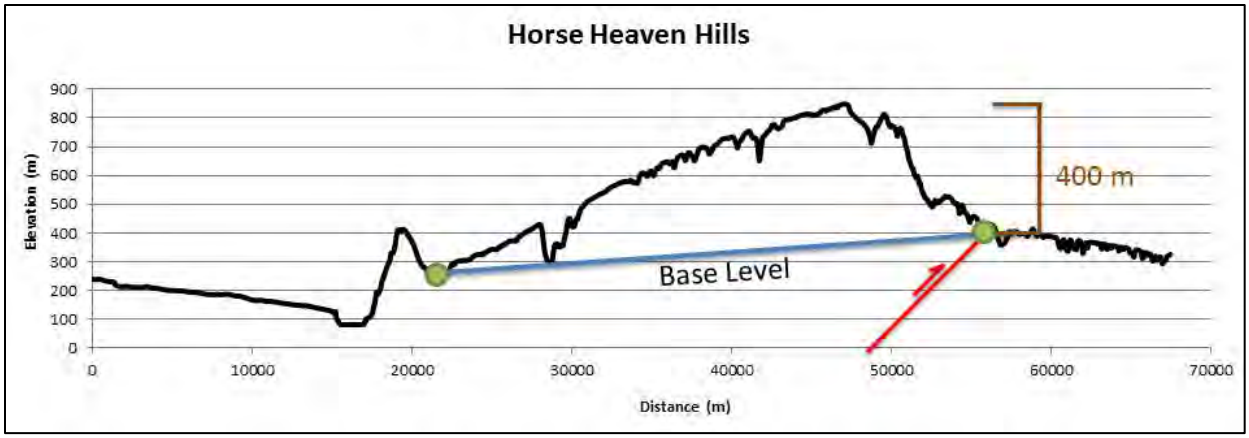


**Figure 8.68**. Topographic profile across the central segment of Horse Heaven Hills (HHH-C). A base level was established for every measurement to account for regional elevation gradients. The fault location is accurate and the fault geometry is schematic. The measurement of structural relief was taken from the frontal thrust to the peak of the ridge.

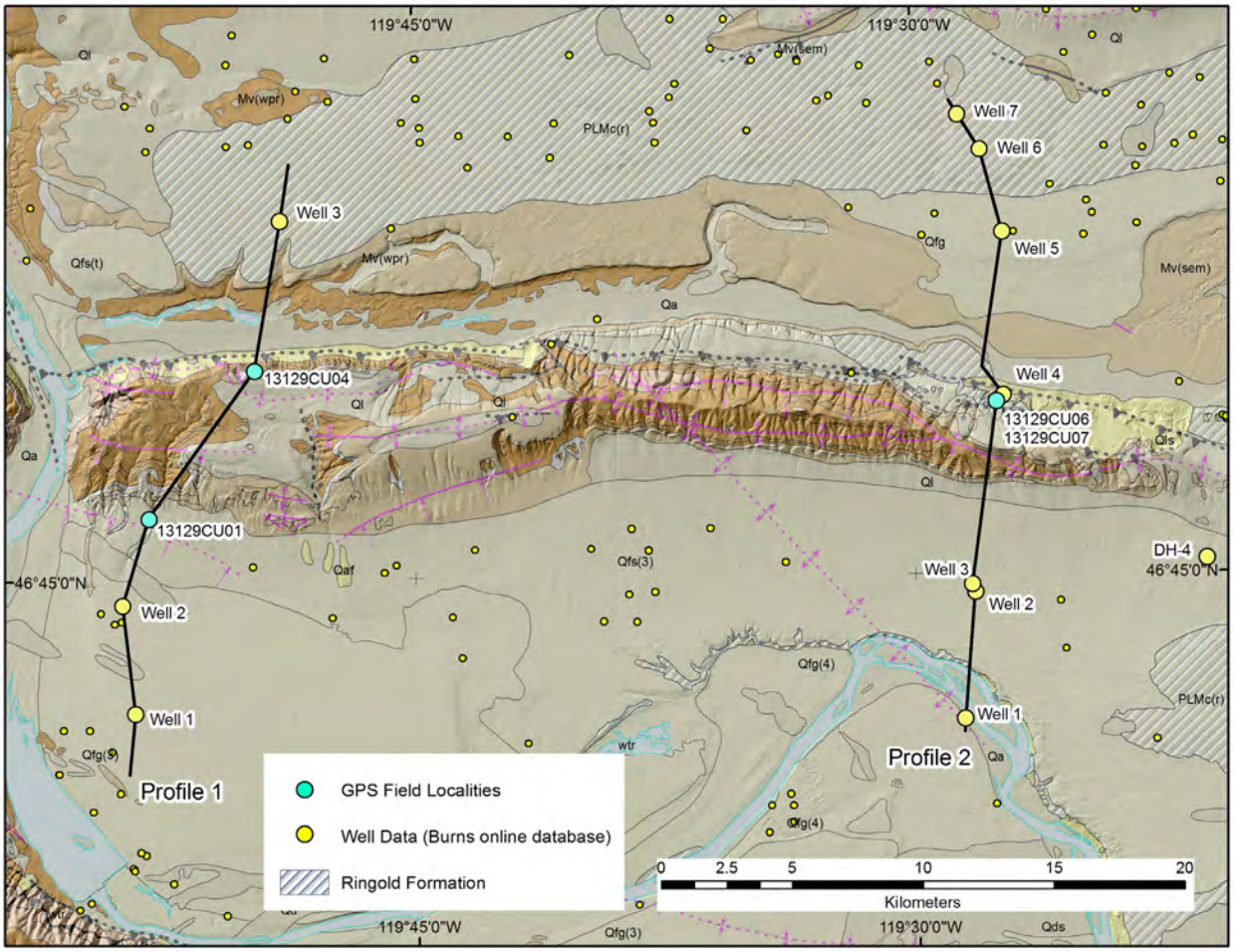


**Figure 8.69**. Geologic map of the Saddle Mountains showing the locations of well data used to provide constraints in determining the structural relief. The locations of Profiles 1 and 2, along with the well data intersected by the profiles, are shown.

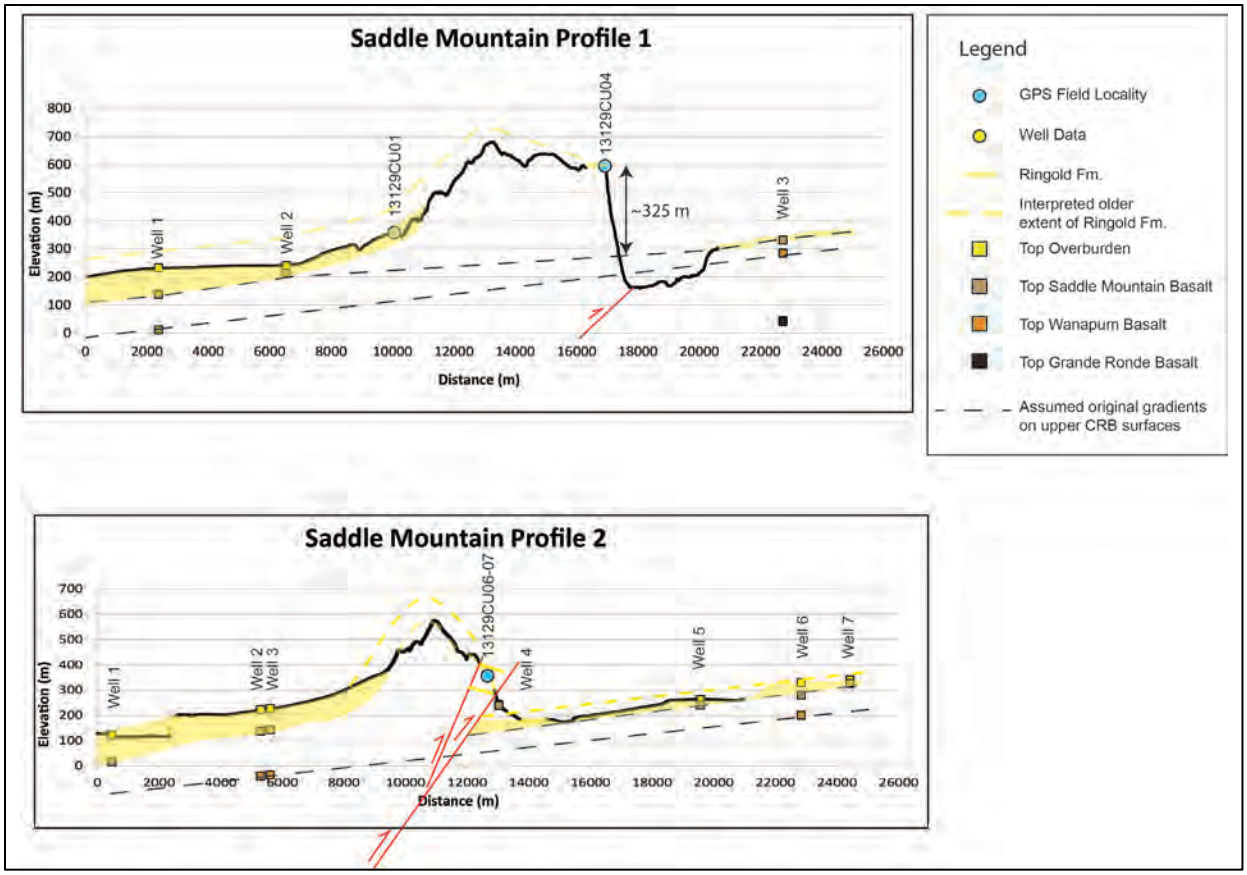


**Figure 8.70**. Topographic profiles across the Saddle Mountains. The depths of major CRB units from well log data are shown. Profile 1 shows the structural relief measurement that takes into account a regional elevation gradient.

Structural relief information was tabulated for each fault segment within the YFB. The average (mean) value for each fault segment is used in the characterization of the fault sources and represents the average total vertical component of slip. Results of the structural relief analysis are provided in Table 8.9 and Figure 8.72. The results of this analysis were used in conjunction with the downdip geometry of each structure to calculate the total dip slip along each fault source. The dip slip value was then used to calculate a net slip value, depending on the sense of slip along a given fault as described in Section 8.4.3.3. The implications of using the structural relief to determine the net slip along each fault within the YFB provides an accurate measurement to then calculate a long-term average slip rate, are further discussed in Section 8.4.3.6.1.

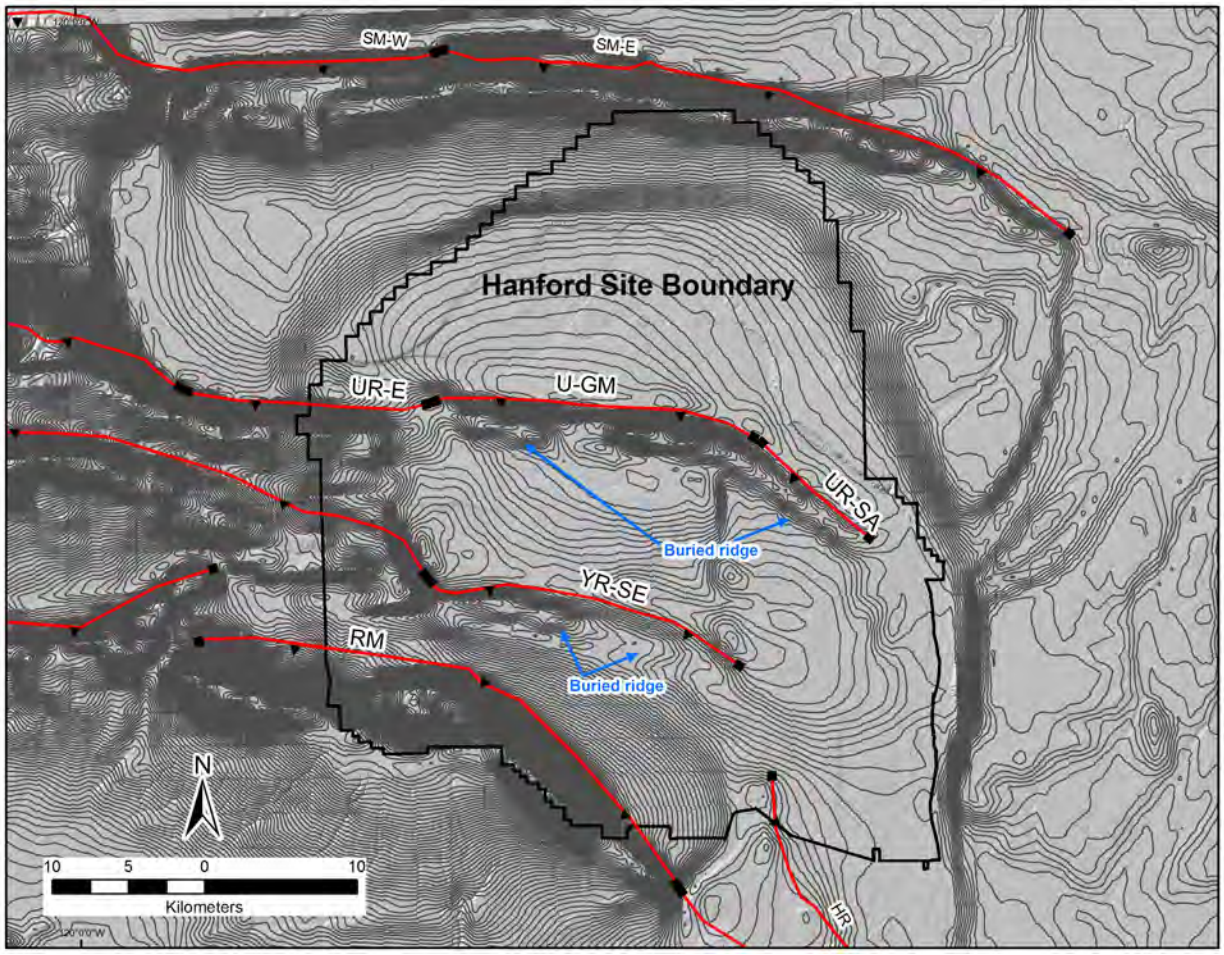


**Figure 8.71**. Top-of-basalt structure contour map of the Hanford Site. The fault sources are shown in red and the background is a hillshade derived from a 10-m DEM. The structure contour map is constrained by geologic mapping and borehole data and was compiled by Thorne et al. (2014).

**Table 8.9**. Mean structural relief measurements for fault sources in the YFB.

| Fault Source | Fault Source Acronym | Mean Structural Relief (m) |
|---|---|---|
| Ahtanum Ridge | AR | 330 |
| Cleman Mountain | CM | 650 |
| Columbia Hills-Central-East | CH-C-E | 55 |
| Columbia Hills-East | CH-E | 105 |
| Columbia Hills-West | CH-W | 375 |
| Columbia Hills-Central | CH-C | 135 |
| Columbia Hills-Central-West | CH-C-W | 230 |
| Frenchman Hills-East | FH-E | 155 |
| Frenchman Hills-West | FH-W | 155 |
| Horn Rapids Fault | HR | 90 |
| Horse Heaven Hills-Central | HHH-C | 485 |
| Horse Heaven Hills-Central-East | HHH-C-E | 415 |
| Horse Heaven Hills-Central-West | HHH-C-W | 575 |
| Horse Heaven Hills-East | HHH-E | 205 |
| Horse Heaven Hills-West | HHH-W | 270 |
| Manastash Ridge-Central | MR-C | 300 |
| Manastash Ridge-East | MR-E | 145 |
| Manastash Ridge-West | MR-W | 415 |
| Rattles | RAW | 130 |
| Rattlesnake Hills | RH | 335 |
| Rattlesnake Mountain | RM | 619 |
| Saddle Mountains-East | SM-E | 320 |
| Saddle Mountains-West | SM-W | 335 |
| Selah Butte | SB | 460 |
| Toppenish Ridge-East | TR-E | 300 |
| Toppenish Ridge-West | TR-W | 310 |
| Umtanum Ridge-Central | UR-C | 360 |
| Umtanum Ridge-East | UR-E | 250 |
| Umtanum Ridge-Southeast Anticline | UR-SA | 90 |
| Umtanum Ridge-West | UR-W | 400 |
| Umtanum-Gable Mountain | U-GM | 160 |
| Wallula Fault | WF | 250 |
| Yakima Ridge-East | YR-E | 325 |
| Yakima Ridge-West | YR-W | 250 |
| Yakima Ridge-Southeast | YR-SE | 65 |

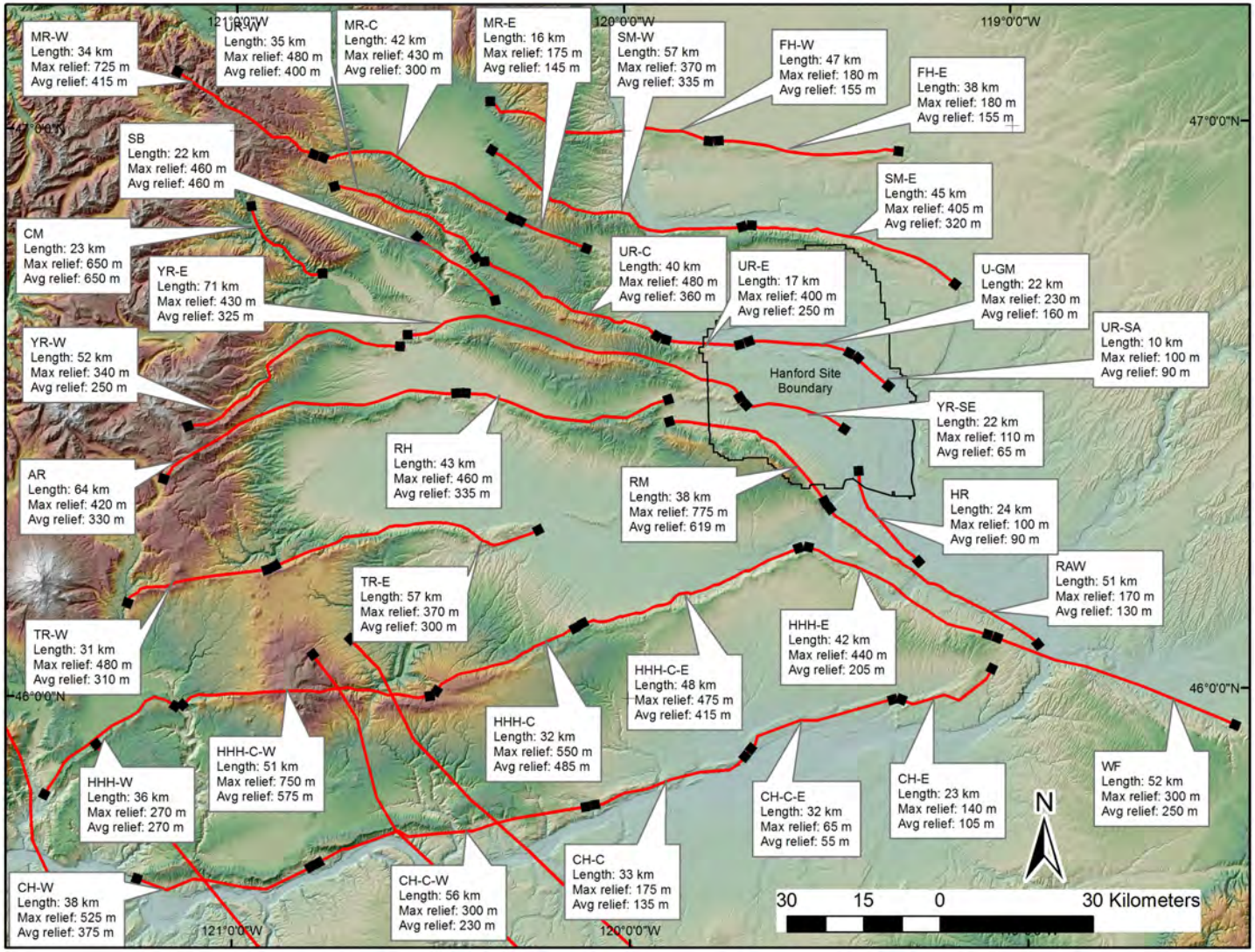


**Figure 8.72**. Map showing the results of the structural relief analysis. The average relief is the value used in the fault characterization model; however, the maximum relief and length are also labeled for additional information.

#### 8.4.3.3 Sense of Slip, Factors for Net Slip

The YFB comprises predominantly reverse faults that have uplifted basement rocks and overlying CRB for the past 6 to 10 Myr. From a tectonic perspective, the YFB may not be considered a classic fold and thrust belt due to its orientation being perpendicular to, and its location being far from, the plate margin. Further, the orientation of the structures is a fanning morphology of subparallel faults opposed to parallel stacking thrust sheets that gives rise to high topography. Regardless, the faults within the YFB have produced large-scale fault-related anticlines that have hundreds of meters of vertical relief (see Figure 8.72), indicating that overall, the fold belt is in a compressional environment with predominantly reverse movement accommodating north-south shortening.

Assessing the style of faulting within the YFB for individual fault sources is challenging due to the lack of paleoseismic data and site-specific kinematic indicators. While local kinematic data are often unavailable, the sense of slip was determined for fault sources based primarily on regional evidence from geologic mapping and topographic data. The Washington State Geologic Map, compiled from mapping done by Walsh (1986), Reidel and Fecht (1994), and Schuster (1994), suggests that the major faults in the YFB are reverse faults as shown in Figure 8.59. This mapping in conjunction with observations of major compressional structures made during the QGS (Appendix E) and topographic analysis as part of this study provides strong evidence for reverse motion along the YFB faults. The style of faulting was assessed on a segment-by-segment basis for each fault source so that it can be used to provide assessment of net-slip rate for each fault segment. Table 8.10 presents the weights assessed by the SSC TI Team for the style of faulting for all of the fault sources in the SSC model. The locations of the fault sources along with the weights given for the style of faulting in the YFB are displayed in Figure 8.73.

**Table 8.10**. Style of faulting for the fault sources in the SSC model.

| | Style of Faulting | | |
|---|---|---|---|
| Fault Segment | Reverse | Oblique | Strike Slip |
| A-RH: Ahtanum segment | 0.5 | 0.5 | |
| A-RH: Rattlesnake Hills segment | 0.9 | 0.1 | |
| Arlington | | | 1.0 |
| Cleman Mtn | 0.3 | 0.7 | |
| Columbia Hills-all segments | 1.0 | | |
| Frenchman Hills-all segments | 1.0 | | |
| Horn Rapids Fault | 0.6 | 0.4 | |
| Horse Heaven Hills-East | 0.8 | 0.2 | |
| HHH-all other segments | 1.0 | | |
| Laurel | | | 1.0 |
| Luna Butte | | | 1.0 |
| Manastash-all segments | 0.9 | 0.1 | |
| Maupin | | | 1.0 |
| Rattlesnake Mtn | 0.9 | 0.1 | |
| RAW | 0.4 | 0.6 | |
| Saddle Mtn-all segments | 1.0 | | |
| Selah Butte | 0.3 | 0.7 | |
| Toppenish Ridge-all segments | 0.9 | 0.1 | |
| Umtanum Ridge-all segments | 0.9 | 0.1 | |
| Wallula fault | 0.3 | 0.6 | 0.1 |
| Yakima Ridge-all segments | 0.9 | 0.1 | |

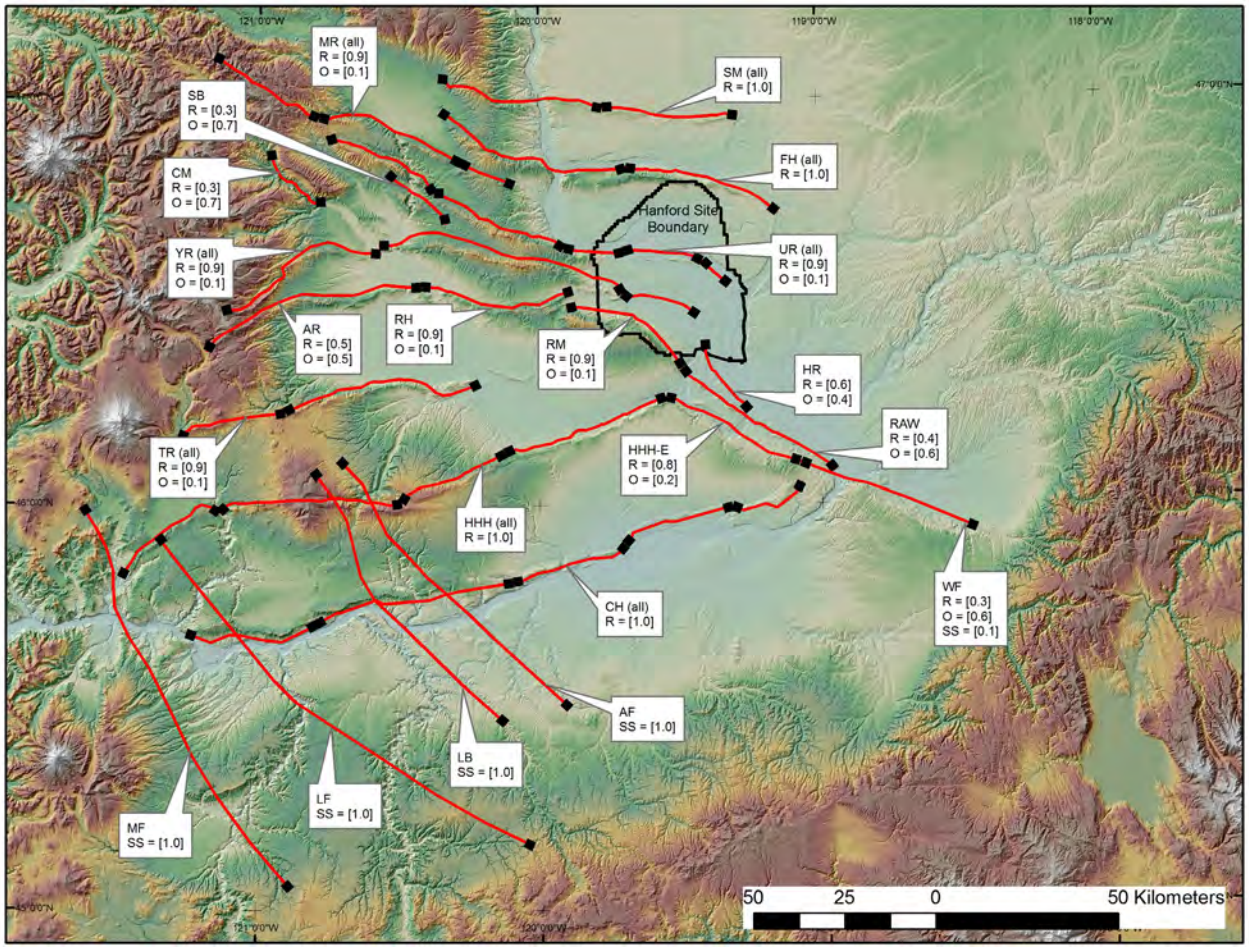


**Figure 8.73**. Locations of fault sources along with weights given for style of faulting in the YFB. R = reverse, O = oblique, SS = strike slip. Note that in many situations the same weight was given for all or many of the segments comprising a single fault source. Where the label reads "all" the same weights are applied to the remainder of the fault trace until a new label is present.

Given the strong evidence of reverse displacement, four of the major faults in the YFB, including Saddle Mountains, Frenchman Hills, Horse Heaven Hills (all but HHH-E segment), and Columbia Hills, were given a weight of [1.0] for reverse faulting. Saddle Mountains and Frenchman Hills have been mapped by many geologists as continuous, asymmetric anticlines uplifted on an underlying fault (Reidel 1984; Schuster et al. 1997; West 1997). The presence of normal faulting in the hanging wall with strikes parallel to the fold axis is consistent with secondary faulting in a shortening, pure dip-slip environment. The most classic example of a pure thrust fault within the YFB can be found along the east-west segments of Horse Heaven Hills. The very long (~40 km) backlimb of this fault in conjunction with a shallow dip suggests pure dip-slip displacement. The Columbia Hills sit at the back edge of the Horse Heaven Hills and form a series of linear, segmented anticlines formed on north-dipping backthrust faults.

Several folds in the YFB are predominantly formed by reverse faulting where a small oblique component cannot be precluded. The faults associated with Rattlesnake Mountain, Rattlesnake Hills, Manastash Ridge, Toppenish Ridge, Umtanum Ridge, and Yakima Ridge were given a weight of [0.9] for reverse faulting and [0.1] for oblique faulting. Complexity in the hanging wall of some folds such as

cross-faulting and stepovers were used as indicators for oblique components of slip. Another factor that was considered as evidence of oblique slip on the reverse folds was the width of the folds. The fold width was evaluated in the topographic analysis when assessing structural relief as described in Section 8.4.3.2. Ridges with narrow widths, such as Toppenish Ridge, Yakima Ridge, and Umtanum Ridge, were interpreted in this study to have steeper dipping faults than those with broader, wider ridges, such as the western segments of Horse Heaven Hills and Saddle Mountains. The rationale for using topographic width to calculate dip is described in Section 8.4.3.4. A steeper dipping fault in a compressional environment creates a circumstance where oblique slip is possible and therefore was factored into the weighting. In the case of Ahtanum Ridge, the ridge narrows drastically from the neighboring Rattlesnake Hills segment and is mapped as a zone of primarily reverse faults that are offset by cross faults, suggesting more oblique slip than the faults described in the beginning of this paragraph. For this reason, the Ahtanum segment was assigned a weight of [0.5] for reverse faulting and [0.5] for oblique faulting. Additional consideration for oblique slip occurring within a predominantly reverse-faulting environment included small-magnitude earthquake focal mechanisms, which suggest a mix of reverse-faulting and strike slip faulting events (Section 6.0 of Appendix E). These events suggest that an oblique component of slip is being accommodated within the seismogenic crust and it cannot be precluded that, to some degree, oblique slip may be occurring within the zones of major YFB structures. The range of styles of faulting and their respective weights given in the SSC model provide for the range of uncertainties that exist, given the available geologic and seismologic evidence.

The Rattlesnake Mountain fault has generated 619 m of structural relief, a very high amount relative to other fault sources measured in the YFB. This observation, along with the mapping of three major thrust faults within the CRB at the range front by Reidel (In Press), suggests that the Rattlesnake Mountain fault is predominantly a reverse fault. Studies by Blakely et al. (2014) postulate significant strike slip movement has occurred along the Wallula fault and has transferred up to 250 m of right-lateral movement along the Rattlesnake Mountain fault. Field investigations performed as part of this study investigated the Quaternary deposits overlying the CRB at the range-front escarpment and determined there was no evidence for lateral displacement along the frontal thrust system and no evidence of lateral slip that could be transferred between the RAW fault and the Rattlesnake Mountain fault (Section 7.3 of Appendix E). The epistemic uncertainty associated with field observations allows for an oblique component of movement to have been missed to some degree in the field; therefore, a weight of [0.1] is given for oblique slip.

The HHH-E fault changes orientation from the western segments of the Horse Heaven Hills fault while maintaining nearly identical thrust sheet morphology to the neighboring HHH-C-E segment. The fault is interpreted to be primarily a thrust fault. Structural complexities in the hanging wall of this fault suggest an increase in fold amplitude from northwest to southeast, suggesting there might be evidence of a slip gradient along this fault, or some evidence for oblique slip. To account for this observation, the weights assigned to HHH-E segment for style of faulting are [0.8] for reverse slip and [0.2] for oblique slip.

The Horn Rapids, Wallula, and RAW faults are located southwest of Rattlesnake Mountain. The Horn Rapids fault was included in this study based on analysis of top-of-basalt structure contour maps during the topographic analysis described in Section 8.4.3.1. The vertical separation observed across the Horn Rapids fault indicates primarily reverse movement. The fault dips to the west-southwest, changing orientations from northwest to north striking along its trace. Given the geometry of the fault and the location outboard of the Rattlesnake Mountain fault, a major reverse fault, and RAW, an oblique-reverse

fault, it is interpreted that the Horn Rapids fault may accommodate some oblique slip. Therefore, the weight for the style of faulting for Horn Rapids is [0.6] for reverse slip and [0.4] for oblique slip.

The style of faulting along the RAW and Wallula faults has been debated for many years. Both faults have major vertical relief associated with them. Structures along the RAW fault include several doubly plunging anticlines along a linear fault interpreted as a single segment. The structural relief averaged across the anticlines and synclines is 130 m as discussed in Section 8.4.3.2. Studies documented along the RAW structure include the analysis of hanging wall deformation at Finley quarry by Farooqui and Thoms (1980), Sherrod et al. (In Review), and Appendix E, which suggest there may be some strike slip movement being accommodated in secondary faulting. Further, the slight en echelon arrangement of the long axes of the isolated folds between Wallula Gap and Red Mountain are cited as evidence of limited strike slip within this domain (Appendix N, Energy Northwest 1998; Mann and Meyer 1993). However, more recent geologic mapping shows southwest-dipping thrust or reverse faults underlying these folds (Reidel and Fecht 1994; Schuster et al. 1997). Reidel and Tolan (1994) present arguments for little or no strike slip along the RAW structure. Studies along this structure have been evaluated in great detail as part of this study and are described in Section 5.2 of this report and Section 7.4 of Appendix E. The interpretation of the style of faulting along the RAW fault takes into account all of these studies that suggest evidence of oblique movement in a compressional environment. Therefore, weights assigned to the RAW fault are [0.4] for reverse slip and [0.6] for oblique slip.

The Wallula fault has greater vertical separation than the RAW fault, with 250 m of measured structural relief. Studies along the fault trace by Bingham et al. (1970), Gardner (1981), and Mann and Meyer (1993) have resulted in various interpretations from reverse to strike slip faulting. Details of the various studies are described in Section 7.5 of Appendix E. As part of the QGS, the Quaternary Studies Team reviewed previous licensing documents and reports, examined hillshade and slope maps from high-resolution LiDAR data, and visited selected localities along the Wallula fault zone. Past studies indicated that there may be evidence of strike slip faulting in cross faults within the hanging wall of the anticline associated with Wallula fault. To take into account the possibility of oblique and some strike slip movement being accommodated along this fault, the style of faulting has been weighted as [0.3] reverse slip, [0.6] oblique slip, and [0.1] strike slip.

The Selah Butte and Cleman Mountain faults are located in the northwestern portion of the study area between Yakima Ridge and Umtanum Ridge. Both faults have relatively short trace lengths, around 20 km, and high structural relief, 460 to 660 m, respectively. Selah Butte dips to the southwest directly parallel and south of Umtanum Ridge at the Yakima River. Cleman Mountain dips to the northeast and strikes parallel to Umtanum Ridge as well. Both faults locally indicate evidence of reverse faulting through tight folding of CRB units. However, given the regional tectonic scale, location of these structures, along with the short trace lengths and proximity to major Yakima folds, these structures are interpreted as accommodating oblique-reverse movement between Umtanum and Yakima Ridges. Therefore, the weights assigned to these two structures are [0.7] for oblique slip and [0.3] for reverse slip.

The northwest striking faults in the southwest corner of the YFB include the Maupin, Laurel, Luna Butte, and Arlington faults. These faults were recently studied by Anderson et al. (2013) and identified as steeply dipping strike slip faults within the CRB. A detailed map over a 100-m hillshade is provided in Figure 8.64. These faults have been described as wrench faults that formed contemporaneously with the YFB (Anderson and Tolan 1986; Reidel et al. 1989), but contrast in structural style due to forming far from the pole of rotation. The weights assigned to these faults are [1.0] for strike slip.

Figure 8.74 shows a diagram of the process used to calculate net slip, the total amount of slip occurring on a fault that takes into account the style of faulting. With the assumption described in Section 8.4.3.2 that topographic relief can be used as a proxy for structural relief, the structural relief value was used with the fault dip to calculate the total amount of dip slip along each fault source. To account for the three styles of faulting, slip factors were developed for this study (Table 8.11). The factors are based on reasonable assumptions for different types of faulting. For reverse faults, the dip slip is equal to the net slip and therefore has a factor of 1.0. For faults with an oblique slip, a 1:1 ratio of lateral to dip slip is assumed, which results in a factor of 1.4. For faults with strike slip, 2:1 and 5:1 lateral to dip slip ratios are assumed, resulting in slip factors of 2.2 and 5.1, respectively.

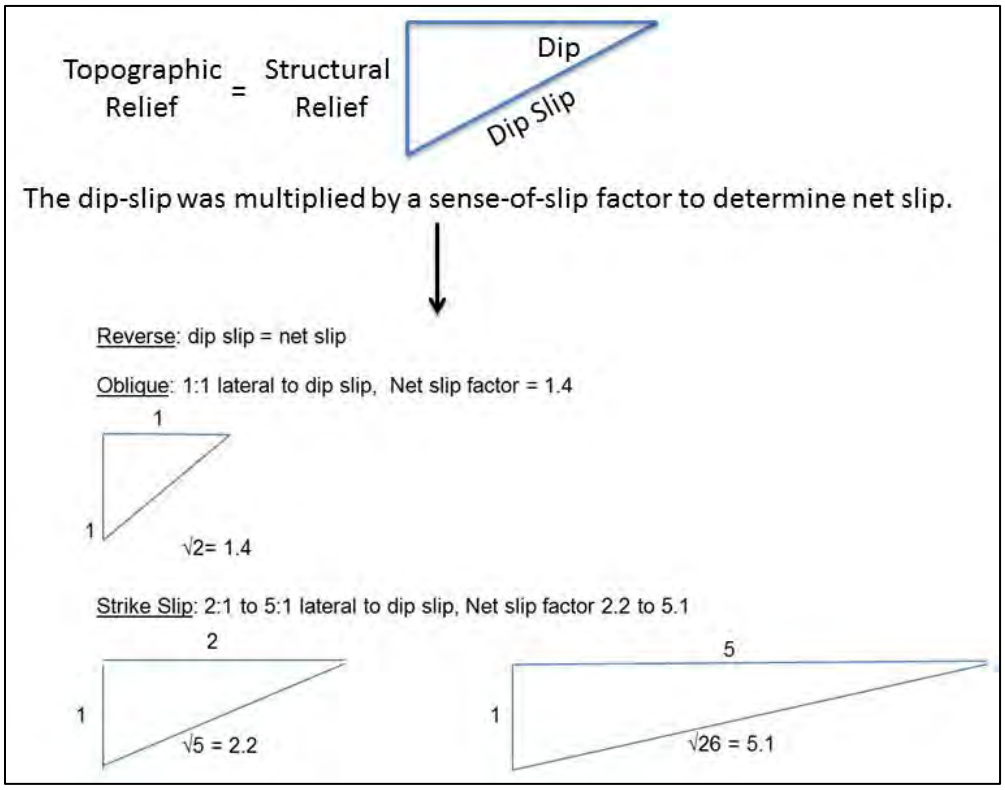


**Figure 8.74**. A diagram of the procedure used to calculate dip slip and net slip for fault sources. The net-slip factor varies for each style of faulting. The net slip was used to calculate long-term slip rates.

**Table 8.11**. Factors for multiplying the dip slip to arrive at the net slip.

| Sense | Slip Factor | Weight |
|---|---|---|
| Reverse | 1.0 | [1.0] |
| Oblique | 1.4 | [1.0] |
| Strike Slip | 2.2 | [0.5] |
| | 5.1 | [0.5] |

To calculate net slip for each fault source, the dip slip value was multiplied by the net-slip factor. Because many of the fault sources are assigned weights for various styles of faulting, these faults have a range of associated net slip values that increase from reverse to strike slip.

#### 8.4.3.4 Fault Dip

The dip angle of thrust or reverse faults beneath YFB anticlines was derived using a simple model to relate the fault geometry to the plan dimensions of the folds. The model assumes that the anticlines have developed in the hanging walls of blind or emergent thrust faults. The faults are assumed to extend from where they are mapped at the surface (or, if the fault is blind, from beneath the synformal hinge at the base of the forelimb of the anticline), and dip in the same direction as the backlimb of the anticline. Because the majority of the Yakima folds are asymmetric, north-vergent anticlines, the associated underlying thrust or reverse faults dip south.

The key geometric assumption of the model is that the faults terminate downward at the base of the seismogenic crust vertically beneath the synformal hinge at the base of the fold backlimb (Figure 8.75). For the faults that lie within the YFTB source zone, the SSC TI Team adopted 13 km, 16 km, and 20 km as alternative models for the seismogenic thickness (see Sections 8.3.2 and 8.3.3 for discussion). With these assumptions, the fault dip ($\theta$) is given by the following:

$$\Theta = \tan^{-1} (\text{seismogenic thickness/fold wavelength}).$$

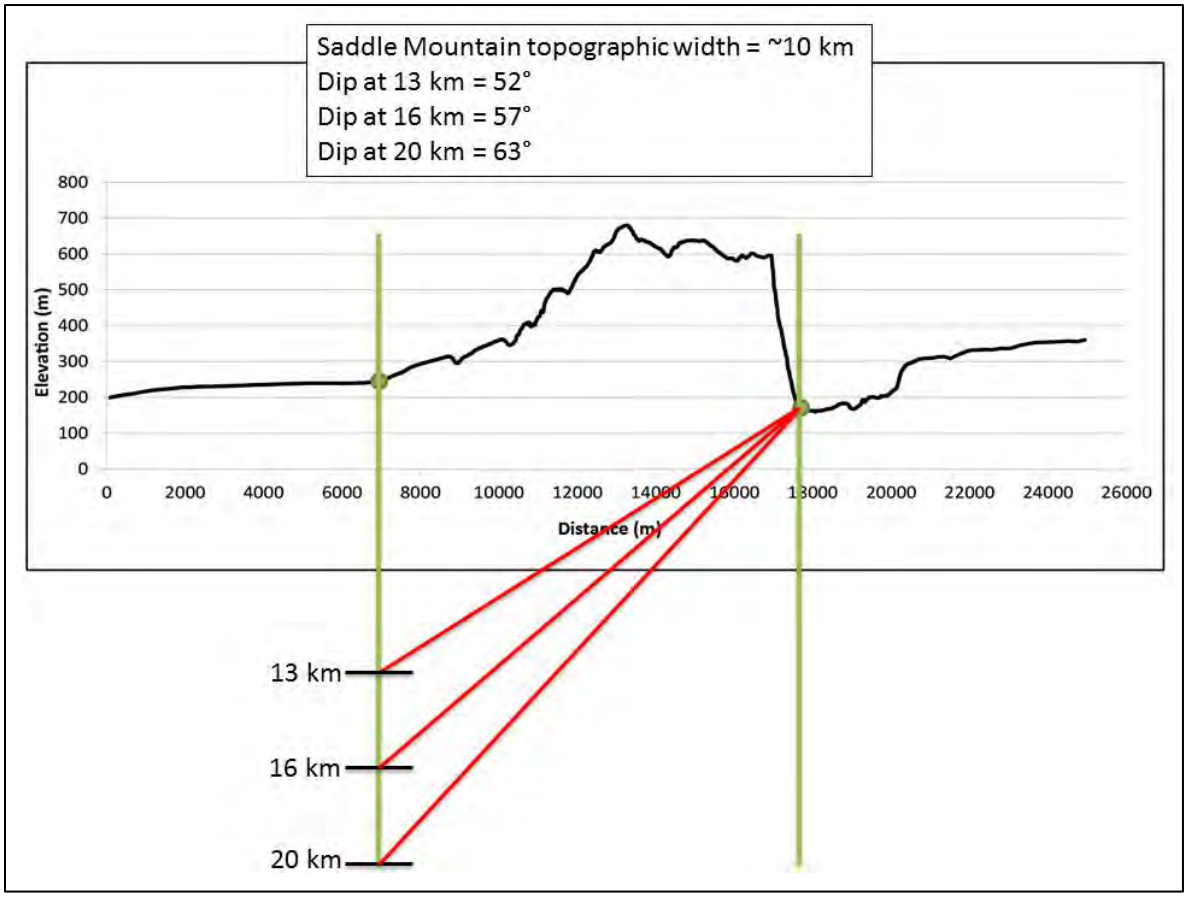


**Figure 8.75**. Example showing projection of alternative dips given the geometry of the fold and alternative seismogenic depths.

This model for deriving fault dip is informed by an analysis of the Syrian Arc fold belt in Israel for the Shivta nuclear power plant site characterization by William Lettis & Associates, Inc. (WLA 2000). Like the Yakima folds, the Syrian Arc structures are wide, gentle, asymmetric anticlines with local structural relief varying from about 500 m to 1100 m, and with relatively long backlimbs ranging from about 10 km to 28 km in width. As discussed in detail by WLA (2000), classes of kinematic models that assume folds grow by propagation of kink bands (e.g., Suppe and Medwedeff 1990) cannot credibly replicate the geometry of such folds for the following reasons:

- Kink-band models generally assume that the dip of the backlimb of the fold is equivalent to the dip of the underlying thrust fault. Because the backlimbs of the Syrian Arc anticlines and some of the Yakima folds are very low (less than 30°, and in some cases less than 10°), the models require very low-angle faults. This geometry is not plausible because very low-angle faults that root from the base of the seismogenic crust do not climb rapidly enough to reach the surface within the vicinity of the forelimb of the fold, contrary to mapping of emergent thrust faults along or within the forelimbs of most Yakima folds (e.g., Schuster 2005).
- This class of models assumes that the fold backlimb grows as a kink band above a propagating fault at depth, such that the width of the backlimb is approximately equivalent to total fault slip. Given the dimensions of the Yakima folds, this implies that thrust faults underlying individual anticlines have accommodated between several kilometers and tens of kilometers of slip, and an approximately equivalent amount of horizontal shortening. Because these structures have primarily grown as fault-propagation folds, the shortening would necessarily be concentrated in the forelimb of the fold. Such shortening is not observed, however; in most cases, the forelimbs of the anticlines are simple low-strain homoclines or monoclines. The forelimbs locally are faulted where the thrust fault has ruptured to the surface, but the total shortening represented by the folding and fault offset is not equivalent to the width of the fold backlimb.

As an alternative to kink-band folding, WLA (2000) used an elastic dislocation model to test the hypothesis that the geometries of the Syrian Arc folds can be reproduced by slip above a simple, planar fault with a moderate-to-steep dip (Figure 8.76). The numerical modeling software used in the analysis, DIS3D, assumed that the crust behaves like a linear elastic material. Individual faults were modeled as a dislocation with finite displacement in an elastic half-space. The slip on the dislocation deforms the elastic medium, and the resulting displacements, strains, and elastic stresses are calculated analytically using elastic field equations (see discussion in the DIS3D User's Manual by Erickson [1987]).

WLA (2000) used a forward-modeling approach to find a combination of dip angle and total slip on individual faults that replicated the observed fold geometry and structural relief across the Syrian Arc fold belt. The starting model assumed that the downdip termination of the fault is located vertically beneath the synformal hinge at the base of the backlimb of the hanging wall anticline, which is identical to the key assumption adopted by the Team for deriving the dip angle of thrust faults beneath the Yakima folds. The reverse slip adopted for the starting model was based on the amount of slip required to generate the observed structural relief; given the initial fault dip, the slip is a trigonometric function of fault dip and maximum structural relief. From these starting parameters, the fault dip and total fault slip were progressively varied to find a best-fit combination that replicated the amplitude and wavelength of the Syrian Arc folds (WLA 2000).

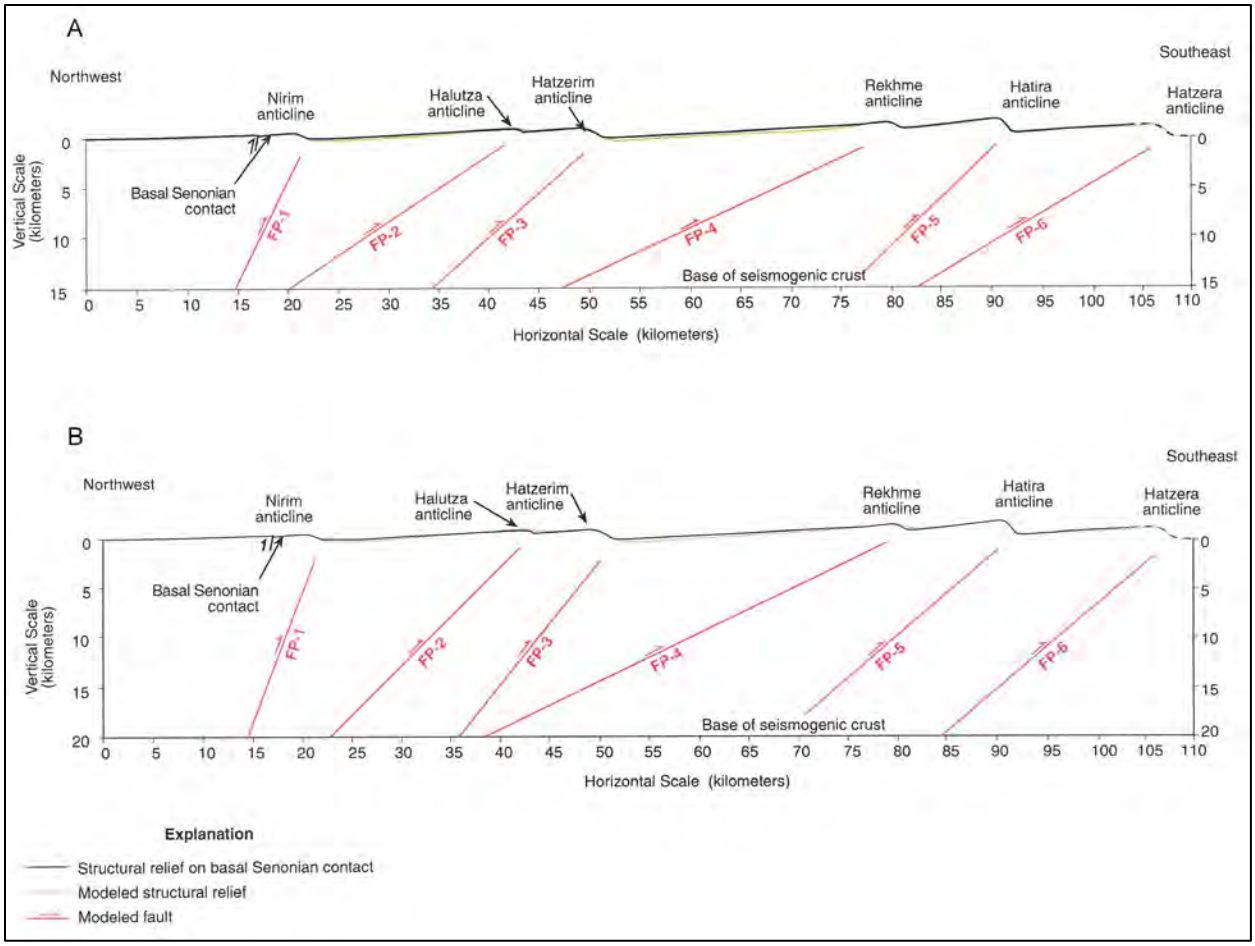


**Figure 8.76**. Results of elastic dislocation modeling from WLA (2000) showing best-fit planar thrust faults to generate the wavelength and amplitude of anticlines in the Syrian Arc fold belt, Negev Desert, Israel. (A) Fault models assuming a 15-km-thick brittle-elastic seismogenic crust. (B) Fault models assuming a 20-km-thick brittle-elastic seismogenic crust. Note that the dips of faults are steeper for the 20-km crust than the 15-km crust.

Based on the elastic modeling, WLA (2000) found that that the downdip extent of the thrust faults must be sufficient to underlie the entire backlimb of the respective overlying anticlines, which supports the starting model assumption that the fault terminates against the base of the seismogenic crust directly below the base of the fold backlimb. The elastic models generally predict less steeply dipping thrust faults than kinematic kink-fold models, which infer that the causative fault terminates downward against a detachment vertically beneath a point located somewhere between the base of the backlimb and the crest of the fold. For elastic thicknesses ranging between 15 km and 20 km, the long-wavelength Syrian Arc folds could be reasonably reproduced by slip on planar faults with dips ranging from about 25° to 69°. Variations in fault dip between the starting model and final best-fit model ranged between +16° to -23° for the full range of elastic thicknesses evaluated (WLA 2000).

Because the dip of faults in the best-fit Shivta elastic models generally varied from the starting assumptions, the TI Team developed three alternative geometries for the Hanford SSC model to capture uncertainty in fault dip (Figure 8.77):

- **Geometry 1**: The fault dip was derived with the assumptions described above, and by using the average width or wavelength of the Yakima folds measured along trend to define the base of the backlimb. This is equivalent to the average width of the polygon that characterizes the plan dimensions of the fold, which is described in Appendix E of this Hanford PSHA document.
- **Geometry 2**: The fault dip was derived from the maximum width of the polygon that characterizes the plan fold dimensions. For a given thickness of seismogenic crust, the fault dip angle derived from the maximum polygon width will be less than the dip based on average polygon width.
- **Geometry 3**: The fault dip was derived from 60% of the average width of the polygon that characterizes the plan fold dimensions. For a given thickness of seismogenic crust, the dip angle derived in this manner will be greater than the dip based on average polygon width.

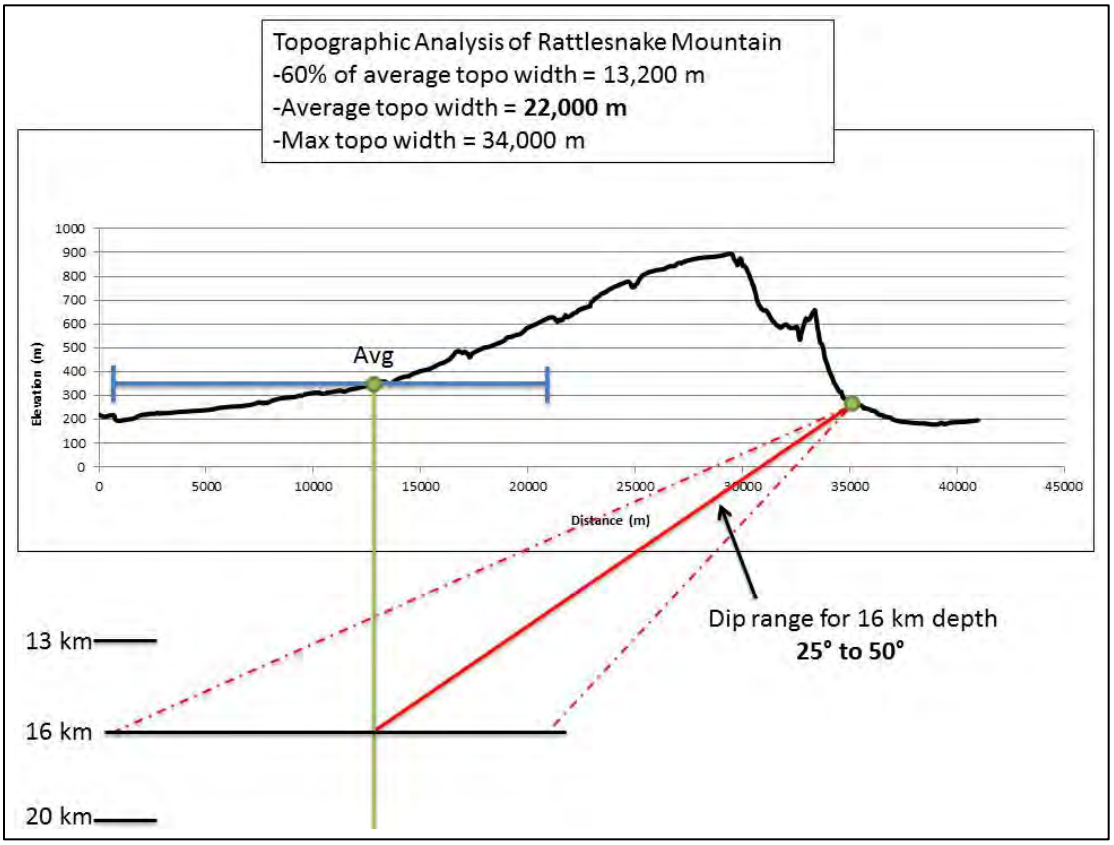


**Figure 8.77**. Example showing alternative geometries used to capture epistemic uncertainty in fault dip.

The TI Team assigns the highest weight [0.5] to Geometry 1 (dip angle based on average polygon width), because the Shivta elastic modeling results generally support the assumption that thrust fault width is scaled to the length of the backlimb of the fold (WLA 2000). Slightly higher weight is given to Geometry 3 than Geometry 2 [0.3 and 0.2, respectively], because the Shivta modeling shows that a steeper fault dip tends to produce a slight concavity in the fold backlimb, which is expressed in topographic profiles across several of the Yakima folds (see Appendix E).

#### 8.4.3.5 Start Time

Values for long-term average slip rate that are used to characterize fault sources in the SSC model are derived from the magnitude of fault dip, vertical slip required to generate the structural/topographic relief on the CRB in the YFB, style of faulting, and the period of time over which regional shortening has occurred. Based on the regional tectonic history and analysis of fold deformation history of individual folds such as the Saddle Mountains (Appendix E), the Team assumes that the total post-CRB (specifically, post-10.5 Ma Elephant Mountain Member) structural relief reflects growth of the folds at a steady rate during the late Cenozoic. With this assumption, a key variable for deriving long-term average slip rates for the model is when the modern tectonic setting of western Washington was established and the Yakima folds began growing at their present rates.

As shown by Reidel et al. (1983) and Reidel (1984), systematic thinning of CRB flows over the crest of Rattlesnake Mountain anticline and Saddle Mountains anticline provide evidence for uplift and growth of at least these two YFB structures during middle Miocene. By assuming that the differential thickness of the flows over the folds relative to thickness in the adjacent synclines is equivalent to tectonic uplift, Reidel et al. (1983) and Reidel (1984) plotted the incremental growth rate as a function of time. The results indicate a reduction of growth rate during deposition of Saddle Mountains Basalt flows relative to uplift rate during deposition of Wanapum Basalt flows. Reidel et al. (1983) projected a long-term average growth rate of about 0.06 mm/yr during Saddle Mountains Basalt time (14.5 Ma to 10.5 Ma) forward to the present and showed that it could account for the modern structural relief on Elephant Mountain Member at Rattlesnake Mountain and Saddle Mountains anticlines. These results suggest relatively steady rates of uplift for the folds from mid-Miocene to present, consistent with the conclusion of Wells and McCaffrey (2013) that the long-term average clockwise rotation rate of crustal blocks in the Pacific Northwest during the past 16 Ma, as determined from paleomagnetic data, is similar to the secular rotation rate of these blocks from modeling of GPS data.

In detail, data bearing on the mid-Miocene uplift of Rattlesnake Mountain suggest that fold growth varied during deposition of the Saddle Mountains flows and may have been lower than the post-10.5 Ma uplift rate. From data tabulated in Barnett et al. (2007), Figure 8.78 shows the differential thicknesses of Saddle Mountains flows over the crest Rattlesnake Mountain relative to the flow thicknesses documented in borehole DB-13 in the Cold Creek syncline on the Hanford Site to the north (Table 8.12). Following the approach of Reidel et al. (1983), the differential thicknesses of Saddle Mountains Basalt flows in Figure 8.78 are used to plot the uplift rate of Rattlesnake Mountain during deposition of the Saddle Mountains Basalt in Figure 8.79. The maximum long-term average growth rate between deposition of the top of the Wanapum Basalt (i.e., the 14.5 Ma Priest Rapids flows) and the deposition of the 10.5 Elephant Mountain Member of the Saddle Mountains Basalt is about 0.03 mm/yr (Figure 8.79). This rate is a maximum because the top of the Elephant Mountain Member is eroded from the crest of Rattlesnake Mountain, thus contributing an unknown component of (non-tectonic) thinning across the fold relative to the Hanford Site. The data indicate that the incremental growth rate of Rattlesnake Mountain was higher during deposition of the Umatilla, Ezquatsel, and Pomona flows (about 0.04 mm/yr between 14.5 Ma and 12 Ma) than during deposition of the Elephant Mountain flows (about 0.02 mm/yr maximum between 12 Ma and 10.5 Ma). Plots of uplift rate for Rattlesnake Mountain and Saddle Mountains anticlines in Reidel et al. (1983) show similar relationships.

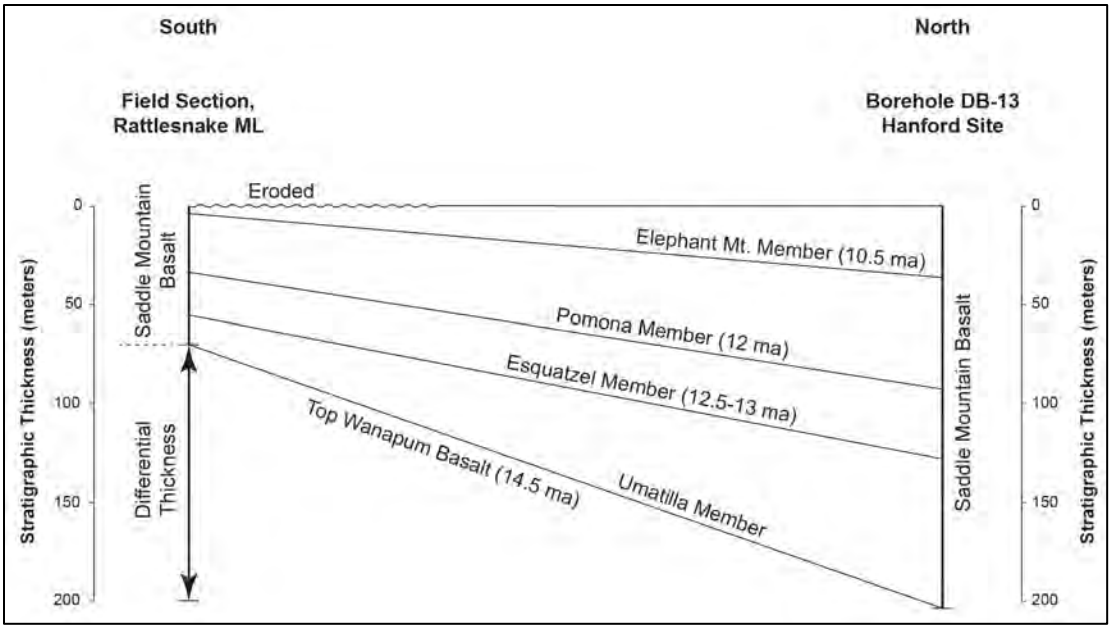


**Figure 8.78**. Differential thickness of the Saddle Mountains Basalt flows between the crest of Rattlesnake Mountain anticline and Borehole DB-13 on the Hanford Site to the north. (Data from Barnett et al. 2007; see Table 8.12)

**Table 8.12**. Thickness of individual members of the Saddle Mountains Basalt, Rattlesnake Mountain, and Hanford Site. (Data from Barnett et al. (2007) used in Figure 8.78 and Figure 8.79.)

| Saddle Mountains Basalt Member | Age | Thickness In Borehole DB-13 | | Rattlesnake Mountain Field Section | |
|---|---|---|---|---|---|
| | | ft | m | ft | m |
| Elephant Mountain | 10.5 Ma | 121 | 37 | 10 | 3 |
| Pomona | 12 Ma | 184 | 56 | 102 | 31 |
| Esquatzel | 12–13 Ma | 118 | 36 | 72 | 22 |
| Umatilla | > 13 Ma | 247 | 75 | 45 | 14 |
| Total | | 670 | 204 | 229 | 70 |

In contrast, the long-term average late Cenozoic uplift rate of Rattlesnake Mountain derived from the present structural relief on the Elephant Mountain Member is about 0.06 mm/yr (619 m since 10.5 Ma), which is a factor of two to three higher than the mid-Miocene growth rate during deposition of the Saddle Mountains Basalt flows. The 0.06 mm/yr estimate of the long-term late Cenozoic rate is a minimum, because the increase in uplift rate that occurred after eruption of the Saddle Mountains Basalt to generate the present structural relief could have happened much later than 10.5 Ma.

Given these observations, the TI Team adopts two end-member dates in the SSC model for onset of the long-term average late Cenozoic shortening rates in eastern Washington: 10 Ma and 6 Ma. This assessment primarily is based on the following lines of evidence:

1. The modern structural and topographic relief of the Yakima folds in the Hanford region and central Columbia Basin is primarily expressed in the 10.5 Ma Elephant Mountain Member of the CRB (Reidel et al. 1994). Because this stratigraphic unit represents an originally sub-horizontal datum

across a large area of the YFB (particularly the eastern Yakima belt and the Hanford Site), the present structural relief has developed since 10.5 Ma.

2. Major tectonic events in the Pacific Northwest consistent with the onset of large-scale rotation of lithospheric blocks in Cascadia forearc and shortening in eastern Washington—such as changes in large-scale plate motions that increased the obliquity of oceanic plate motions relative to North America and transferred dextral shear to the interior of the Cordillera—primarily occurred between 10 Ma and 6 Ma.
3. Stratigraphic and structural relationships in the eastern YFB show that growth of the folds was occurring during deposition of the late Miocene to Pliocene Ringold Formation.

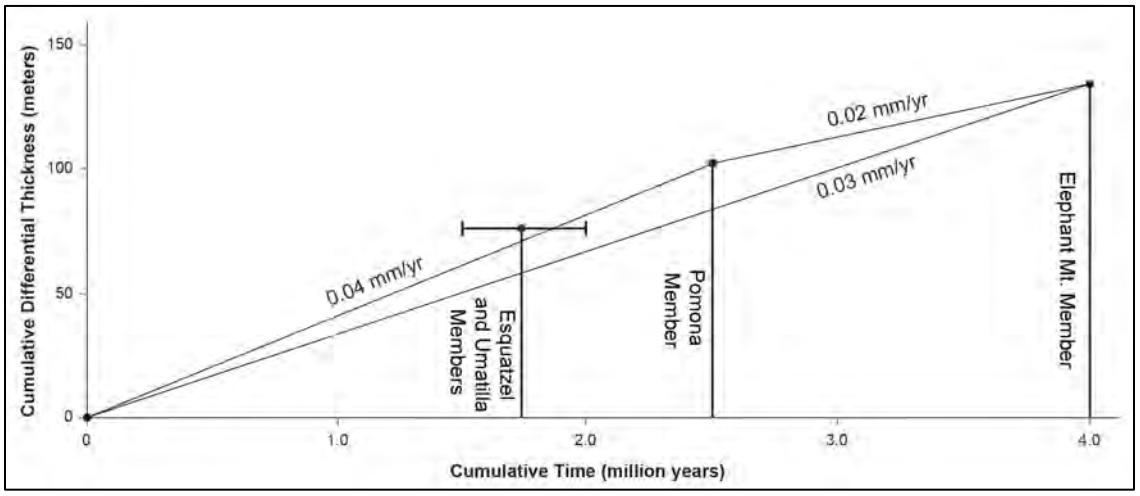


**Figure 8.79**. Miocene growth rate of Rattlesnake Mountain from plotting differential thickness of the Saddle Mountains Basalt blows as a function of time (see Figure 8.78 for data).

The older bounding age of 10 Ma assumes that current deformation rates were established very shortly after deposition of Elephant Mountain basalt; i.e, that the uplift rates of the Yakima folds have been steady during the past 10 Ma. A 10 Ma onset time is broadly consistent with the interpretation of Barrash et al. (1983) that the orientation of the maximum compressive stress $\sigma_1$ in the Columbia Plateau changed from northwest-southeast to north-south at about 10 Ma +/- 2 Ma, and the interpretation of Robin and Hoover (1982) that north-directed shortening in the Blue Mountains south of the YFB began after about 10 Ma. Zoback et al. (1981) further noted that the direction of extension in the northern Basin and Range rotated clockwise to its current northwest-southeast orientation at about 10 Ma. The modern northwest-southeast direction of extension in the Basin and Range being linked to the current pattern of block translations and clockwise rotations in the Pacific Northwest (Section 4.2) suggests that the modern tectonic framework in the western United States, and consequently in eastern Washington, was established about 10 Ma.

The younger bounding age of 6 Ma assumes that regional rotation and translation of rigid crustal blocks in the Pacific Northwest backarc region began when Pacific-North American plate motion stepped eastward into the interior of the western Cordillera. Detailed reconstruction of interactions between the Pacific Plate and North America by Atwater and Stock (1998) indicate that Pacific-North American motion became more oblique at about 7.8 Ma, which presumably increased shear tractions along the western margin of North America. The opening of the Gulf of California and transfer of Baja California

to the Pacific Plate followed at about 6 Ma (Oskin et al. 2001), reflecting eastward propagation of plate boundary deformation into the North American continental lithosphere. At about this time or slightly later, northwest dextral shear was established in the southern Walker Lane belt (Faulds and Henry 2008), which separated the Sierran microplate from the rest of the Cordillera and transferred plate motion into the northern Basin and Range. Based on these relationships, the TI Team infers that the modern tectonic setting in the western Cordillera dates to no later than 6 Ma, thus establishing an upper bound for the onset of the modern tectonic setting in eastern Washington.

Stratigraphic relationships at the Saddle Mountains north of the Hanford Site further suggest that north-south shortening, accommodated by uplift and folding of the CRB, was occurring in late Miocene time. The 10.5 Ma Elephant Mountain Member of the CRB is overlain by the late Miocene-Pliocene Ringold Formation, a widespread fluvial and lacustrine deposit in the greater Hanford region. As summarized by Gustafson (2011), stratigraphic relationships indicate that the base of the Ringold Formation is 8.5 Ma in age or younger, and the Ringold Formation contains late Miocene to Pliocene fauna ranging in age from about 5 Ma to 3.1 Ma, so the unit spans much of late Neogene time. Observations cited in Appendix 2.5N of the Energy Northwest Final Safety Analysis Report Observations cited in Appendix 2.5N of the Energy Northwest Final Safety Analysis Report (1998) indicate that bedding dips gradually decrease upsection within the Ringold Formation, suggesting that regional deformation and folding was occurring during the late Miocene while the Ringold was being deposited.

Observations during field reconnaissance for the present study reveal a modest angular unconformity between the Ringold Formation and the Elephant Mountain basalt on the backlimb of the Saddle Mountains anticline, and possible thinning of the Ringold Formation across the crest of the fold (see Appendix E), suggesting that folding began prior to, and/or was coeval with, local deposition of the Ringold Formation. Similar relationships are shown in a series of cross sections across the Gable Mountain structure developed by Bjornstad et al. (2010) from correlation of borehole data. Specifically, these cross sections indicate uplift, folding was occurring, and incision of the CRB units beneath the Hanford Site prior to deposition of basal Ringold Formation strata between about 8.5 Ma and 5 Ma.

To summarize, proponent models of regional tectonics in eastern Washington, analyses of the direction and distribution of Pacific-North American plate motion since late Neogene time, and stratigraphic and structural relations in the Hanford area are consistent with uplift and folding of the 10.5 Ma Elephant Mountain Member of the CRB between about 10 Ma and 6 Ma. Given the stratigraphic and structural relations in the Hanford region indicating that uplift, folding, and incision of the Elephant Mountain Member occurred before deposition of the basal Ringold Formation (Bjornstad et al. 2010), as well as proponent models for progressive growth of the Yakima folds during eruption and deposition of the Saddle Mountains flows of the CRB (Reidel et al. 1983; Reidel 1984), the Team assigns slightly higher weights to the older 10 Ma date for the start time of deformation.

In addition, the Team recognizes studies that infer a preexisting structural high or highs were present in the Horse Heaven Hills and Wallula Gap areas that controlled the distribution of the Pomona (approx. 12 Ma), Elephant Mountain (approx. 10.4 Ma), and Ice Harbor (approx. 8.5 Ma) Members of the CRB (Gardner et al. 1981). It is possible that uplift and folding of the YFB structures began earlier in the south with the onset of rotation in eastern Oregon, and propagated from south to north in eastern Washington over time. To capture this possibility in the source model, the Team assigns slightly higher weights to the 10-Myr start time for structures in the southern YFB than those in the north, as shown in Table 8.13.

**Table 8.13**. Start times and weights for calculating slip rate for fault segments.

| Fault Segment[(a)] | Start Time for Slip Rate | |
|---|---|---|
| | 6 Myr | 10 Myr |
| Ahtanum-Rattlesnake Hills | 0.4 | 0.6 |
| Cleman Mountain | 0.4 | 0.6 |
| Columbia Hills | 0.4 | 0.6 |
| Frenchman Hills | 0.4 | 0.6 |
| Horn Rapids Fault | 0.3 | 0.7 |
| Horse Heaven Hills | 0.3 | 0.7 |
| Manastash | 0.4 | 0.6 |
| Rattlesnake Mountain | 0.3 | 0.7 |
| RAW | 0.3 | 0.7 |
| Saddle Mountains | 0.4 | 0.6 |
| Selah Butte | 0.4 | 0.6 |
| Toppenish Ridge | 0.4 | 0.6 |
| Umtanum Ridge | 0.4 | 0.6 |
| Wallula Fault | 0.3 | 0.7 |
| Yakima Ridge | 0.4 | 0.6 |

(a) The assessments shown are applicable for all segments of the fault named.

#### 8.4.3.6 Net-Slip Rates

The net slip discussed in Section 8.4.3.3 is the total amount of slip that has occurred on a fault given the style of faulting represented by a net-slip factor. The net slip was derived from the dip slip, which was based on the dip of the fault plane and amount of structural relief accommodated on the plane. The net-slip value relies on the style of faulting; therefore each fault segment has up to four net-slip values because there are four possible net-slip factors (1 for reverse, 1.4 for oblique, 2.2 and 5.1 for strike slip). Further, the net slip is calculated for each of the three dip ranges based on the topographic width: the average width, maximum width, and 60% of the width as discussed in Section 8.4.3.4. Lastly, also discussed in Section 8.4.3.4, there are three possible seismogenic depths: 13 km [0.2], 16 km [0.5], and 20 km [0.3]. In the end, there are nine total net-slip values per fault type and their associated weights for a given fault source segment. Together these net-slip values and their associated weights cover a defensible range of epistemic uncertainty built into the fault source characterization portion of the model.

To calculate a rate from the amount of net slip, it is divided by a time period over which deformation occurred. Section 8.4.3.5 describes the rationale behind the two end-member start times of CRB deformation at 10 Ma and 6 Ma. The result of this calculation is a long-term slip rate for each fault segment. Taking into account the two starting times and the three options of dip, there are six net-slip rates calculated for each seismogenic depth. Given that there are three seismogenic depths in the model, a total of 18 net-slip rates are calculated for each fault type for each fault segment. The average net-slip rate for the entire fault is calculated as a length-average of all segments of the fault. The resulting net-slip rates are the fault-specific, long-term average slip rates for the YFB faults.

#### 8.4.3.6.1 Quaternary Slip Rates

Quaternary slip-rate information is available for three fault sources: Rattlesnake Mountain, Manastash, and Umtanum faults. As described below, only Quaternary slip-rate data for the Rattlesnake Mountain are directly included in the source characterization logic tree. Data for the Manastash and Umtanum faults are viewed as more preliminary and thus, were not explicitly included in the source model.

Prior to this study, a range of Quaternary vertical separation rates (~0.02 to 0.17 mm/yr) had been estimated for the Manastash fault based on mapping and dating of Quaternary fluvial and alluvial fan deposits of varying ages near and west of the mouth of Yakima Canyon (Ladinsky 2012; Ladinsky and Kelsey 2012). Additional mapping of fluvial terraces within Yakima Canyon (Amos and Sorsby 2013 [Appendix E.2]) and cosmogenic ($^{26}Al/^{10}Be$) dating of three samples from these terraces (Bierman 2014 [Appendix E.3]) provide new information to evaluate previous estimated rates for the Manastash fault as well as to estimate the Quaternary rate for the Umtanum fault.

A discussion of information regarding differential rates of Quaternary uplift and incision across the Manastash and Umtanum structures synthesized from previous work (e.g., Bentley 1977; Waitt 1979; Ladinsky 2012; Ladinsky and Kelsey 2012), and the preliminary mapping and dating of fluvial terraces and reconnaissance field observations of the Quaternary Studies Team in the Yakima Canyon, is provided in Section 9.0 of Appendix E. The range in the estimated rate of vertical stratigraphic separation across the Manastash and Umtanum faults based on the available data related to Quaternary uplift and incision as summarized in Table 9.1 of Appendix E is consistent with the range in estimated post-CRB vertical separation rate (Section 8.4.3.6). Mapping and dating of the Yakima River fluvial terraces is ongoing and due to the preliminary nature of both the dating results and terrace correlations, these results are used primarily as a check on the long-term post-CRB rates inferred from the structural analysis described above in Sections 8.4.3.2 and 8.4.3.6.

Quaternary studies related to the Rattlesnake Mountain fault that were conducted as part of this study yielded information about the Quaternary rate of vertical separation that is explicitly included in the assessment of the recurrence for this fault. Based on field observations and desktop studies (see Section 7.3.3 of Appendix E) the most suitable Quaternary deposit to use for evaluating total vertical stratigraphic separation across the entire Rattlesnake Mountain fault zone (including both the range-front fault and the gas field anticline) is a broad coalescing alluvial fan (bajada) (map unit Qaf4). The age of the Qaf4 fan is estimated to be middle Pleistocene (>380–800 ka) based on comparison of the degree of soil profile development and clast weathering of this unit relative to nearby flood gravel deposits in the Badger Coulee area that have been dated using both thorium/uranium analysis of pedogenic carbonate rinds and magnetic polarity data (Baker et al. 1991; Appendix E, Tables 4.3 and 7.1). The large extent of the Qaf4 fans suggest a long period of deposition, possibly throughout much of the marine oxygen isotope stage (MIS) 16, MIS 14, and MIS 12 glaciations and transitional periods to intervening interglacial periods (Figure 8.80). It is assumed that the final abandonment and initiation of soil profile development likely occurred toward the latter part of this time period. Subsequent stages are characterized by more extreme interglacial periods (e.g., MIS 11 and MIS 9) when conditions are judged to be less favorable for extensive fan deposition.

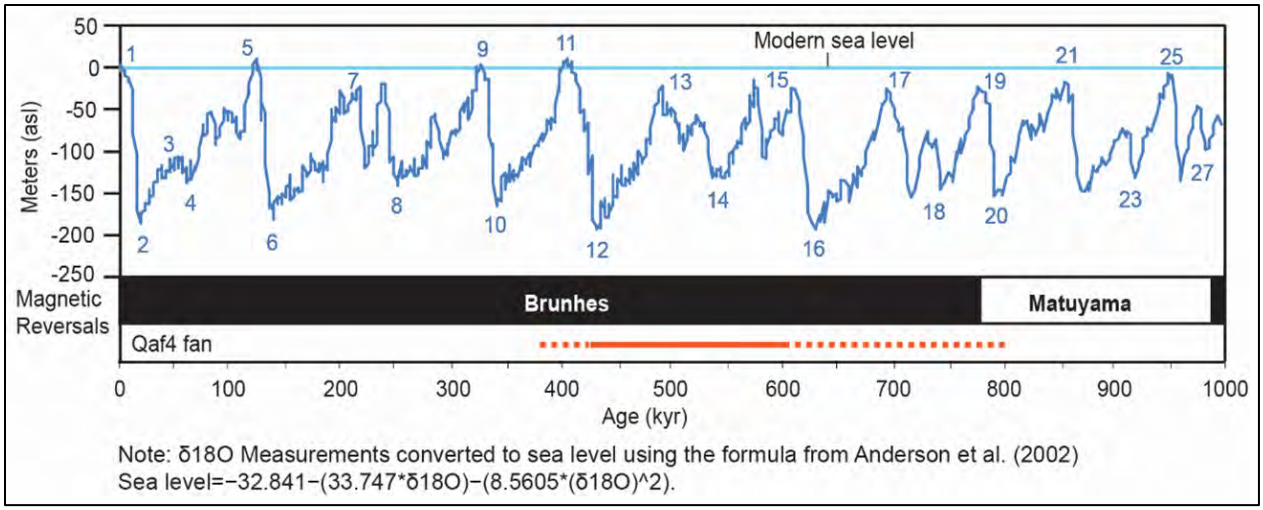


**Figure 8.80**. Sea-level curve (based on data from Lisiecki and Raymo 2005) relative to magnetic reversals. Periods of sea-level highstands (odd numbers) correlate to interglacial periods and lowstands (even numbers) correlate to glacial periods. The red bar represents the estimated age of the Qaf4 fan; the solid portion represents the preferred age of abandonment and beginning of soil profile development.

Based on these observations and the best estimated values from the thorium/uranium analyses used for calibration, a preferred age of between 425 and 600 ka is used to calculate a post-Qaf4 vertical separation rate.

Total cumulative vertical stratigraphic separation across both the range-front and gas field structures estimated from the reconstructed projections range from 20 ± 3 m at Profile 4 to 30 ± 3 m at Profile 3 (see Appendix E, Plate 2), with an average value of approximately 25 m. Profiles 2 and 3, which span the central part of the emergent range-front fault, show similar cumulative offsets of 29–30 m.

A cumulative distribution function (CDF) for a Quaternary vertical stratigraphic separation rate is estimated from the combined probability distributions for age and displacement of the Qaf4 fan surface. Based on the preferred ages and displacements outlined above a trapezoidal form was used to develop both probability distributions based on the following:

| | | | |
|---|---|---|---|
| Age: | minimum 380 ka | preferred 425–600 ka | maximum 800 ka |
| Displacement: | minimum 22 m | preferred 25–30 m | maximum 33 m |

The results range from a minimum vertical stratigraphic separation rate of 0.03 mm/yr to a maximum of 0.09 mm/yr (Figure 8.81). The Miller and Rice (1983) methodology used to define a set of discrete approximations that represent the CDF yields the following five-point distribution:

| Weight | Vertical stratigraphic separation rate (mm/yr) or (m/kyr) |
|---|---|
| 0.10108 | 0.035 |
| 0.24429 | 0.042 |
| 0.30926 | 0.050 |
| 0.24429 | 0.059 |
| 0.10108 | 0.070. |

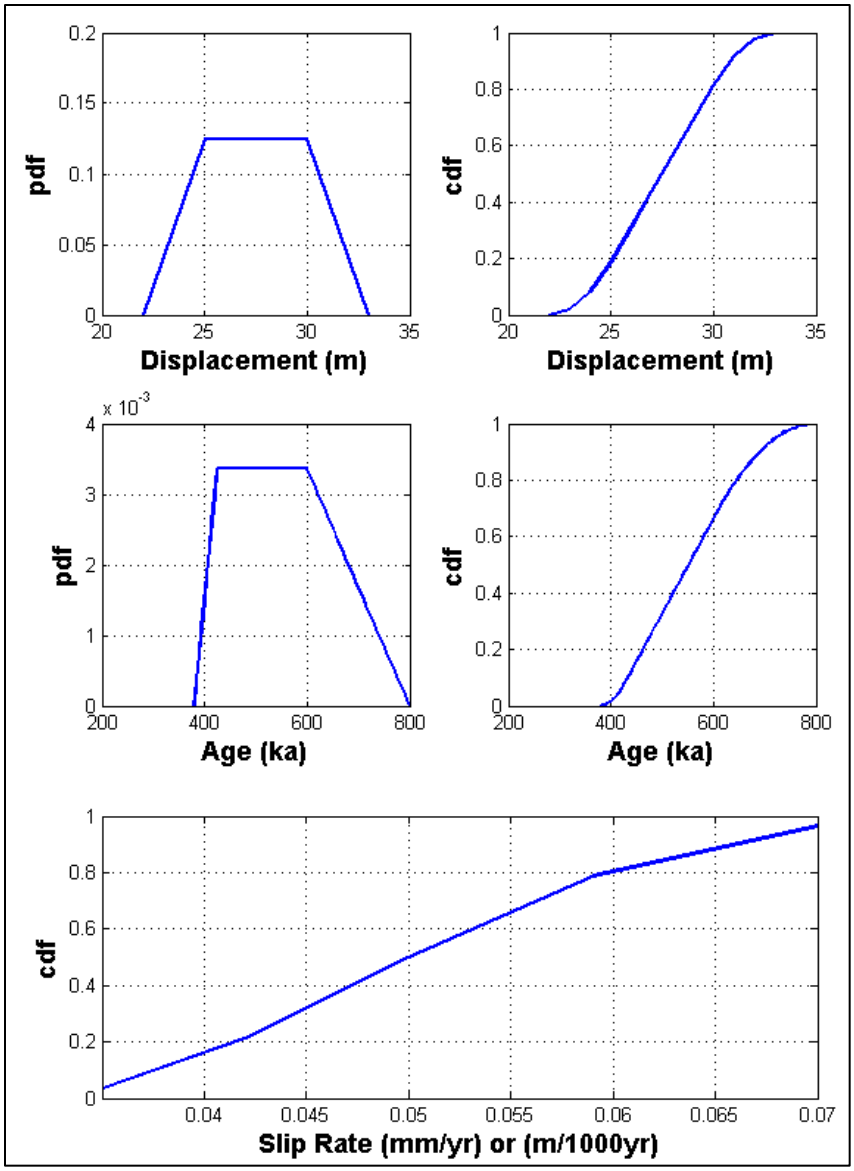


**Figure 8.81**. Displacement and cumulative probability plots for age and displacement data used to estimate a Quaternary vertical stratigraphic separation rate for the Rattlesnake Mountain fault source.

The average Quaternary (post-Qaf4 fan) rate can be compared to long-term average post-CRB vertical separation rates based on the structural analysis and start times described in Sections 8.4.3.2, 8.4.3.5, and 8.4.3.6. Based on the general location of the study area relative to the crestal profile of the entire Rattlesnake Mountain fold, it is reasonable to assume that the cumulative vertical separation of the Qaf4 fan in the central part of the study area is representative of the average post-middle Pleistocene separation (Figure 8.82). The Quaternary slip-rate distribution outlined above is similar to but slightly lower than the long-term vertical separation rate based on post-CRB topography (618 m/6–10 Myr = 0.06–0.1 m/kyr) and the estimated rate (0.06 m/kyr) from the beginning of Saddle Mountains Basalt time based on thinning of basalt flows across the structure (Reidel et al. 1983).

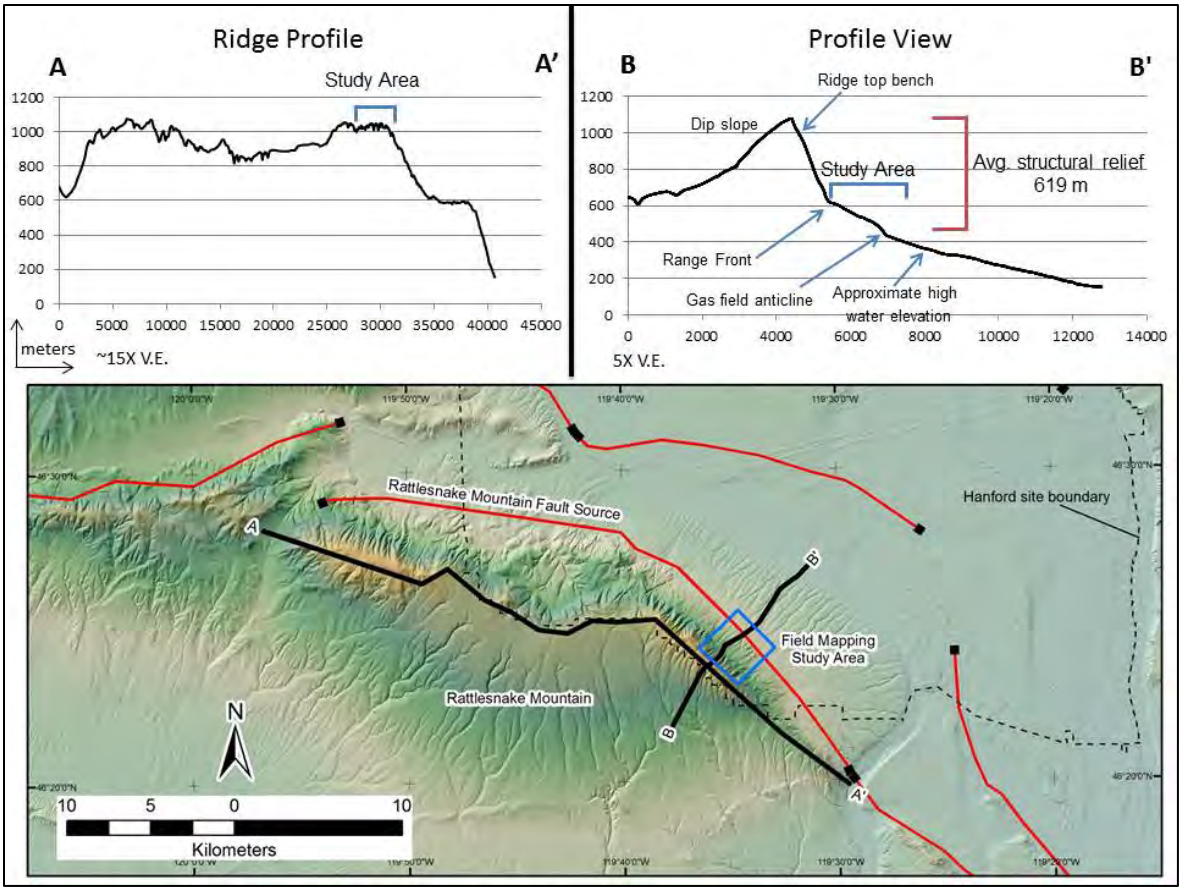


**Figure 8.82**. Map and topographic profiles showing the position of the study area relative to the Rattlesnake Mountain anticlinal ridge.

Evidence of no measurable lateral offset of geomorphic features, combined with the evidence for vertical separation across a surface scarp at the range front and fold deformation on the gas field that is consistent with the presence of a blind thrust or reverse fault, demonstrates that the uplift of Rattlesnake Mountain in the Quaternary has been accommodated primarily by reverse slip on a fault that includes both emergent and blind splays that likely merge at depth (Appendix E, Section 7.3.3.1). As discussed in Section 8.4.3.3, a small component of lateral slip is not precluded by these observations, and because the orientation of the Rattlesnake Mountain fault is favorable for some lateral slip, as suggested by the analysis of small-magnitude earthquake focal mechanism data (see Appendix E, Section 6.0), oblique slip is given some weight [0.1]; based on the geologic evidence, reverse slip is given the majority of the weight [0.9].

#### 8.4.3.6.2 Long-Term Rates

The long-term (post-CRB) slip rates estimated from the structural analyses provide information about fault sources that allow for fault-specific characterization in the absence of good Quaternary slip-rate information. For individual faults the long-term rates range from hundredths up to tenths of millimeters per year. Figure 8.83 presents the CDF results for the long-term slip rates for each fault source. The CDF is a slip-rate probability function that takes into account all factors in the logic tree that contribute to slip rate as well as their relative weights. These factors include topographic width, fault dip, seismogenic

depth, structural relief, and style of faulting as described in previous sections. The fault segments that make up the entire fault source are plotted together with the combined distribution for the entire fault in the figures.

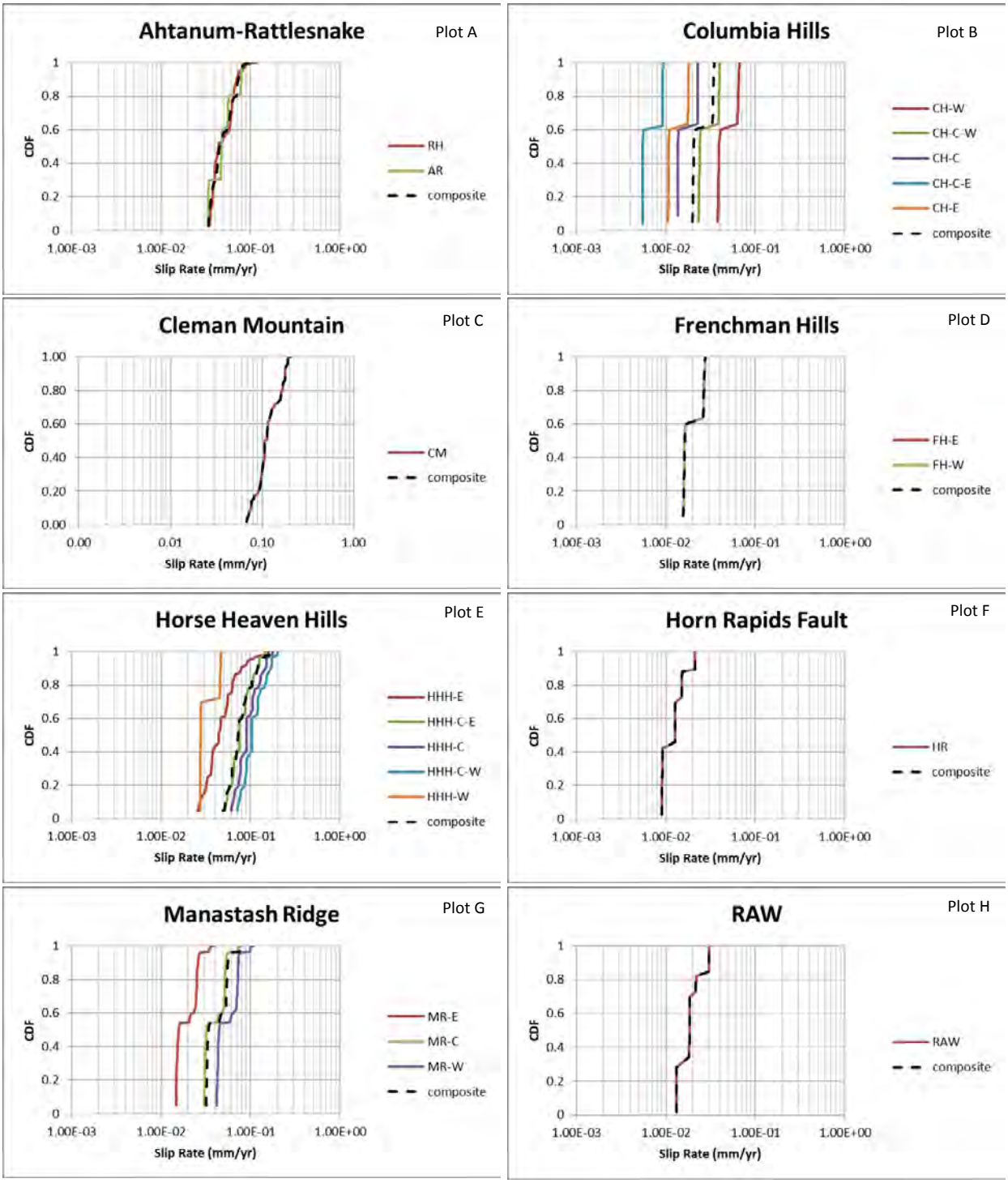


**Figure 8.83.** Cumulative distribution functions of slip rates for each fault segment. Each plot shows the rates for each fault segment plotted with the combined distributions for the entire fault for comparison.

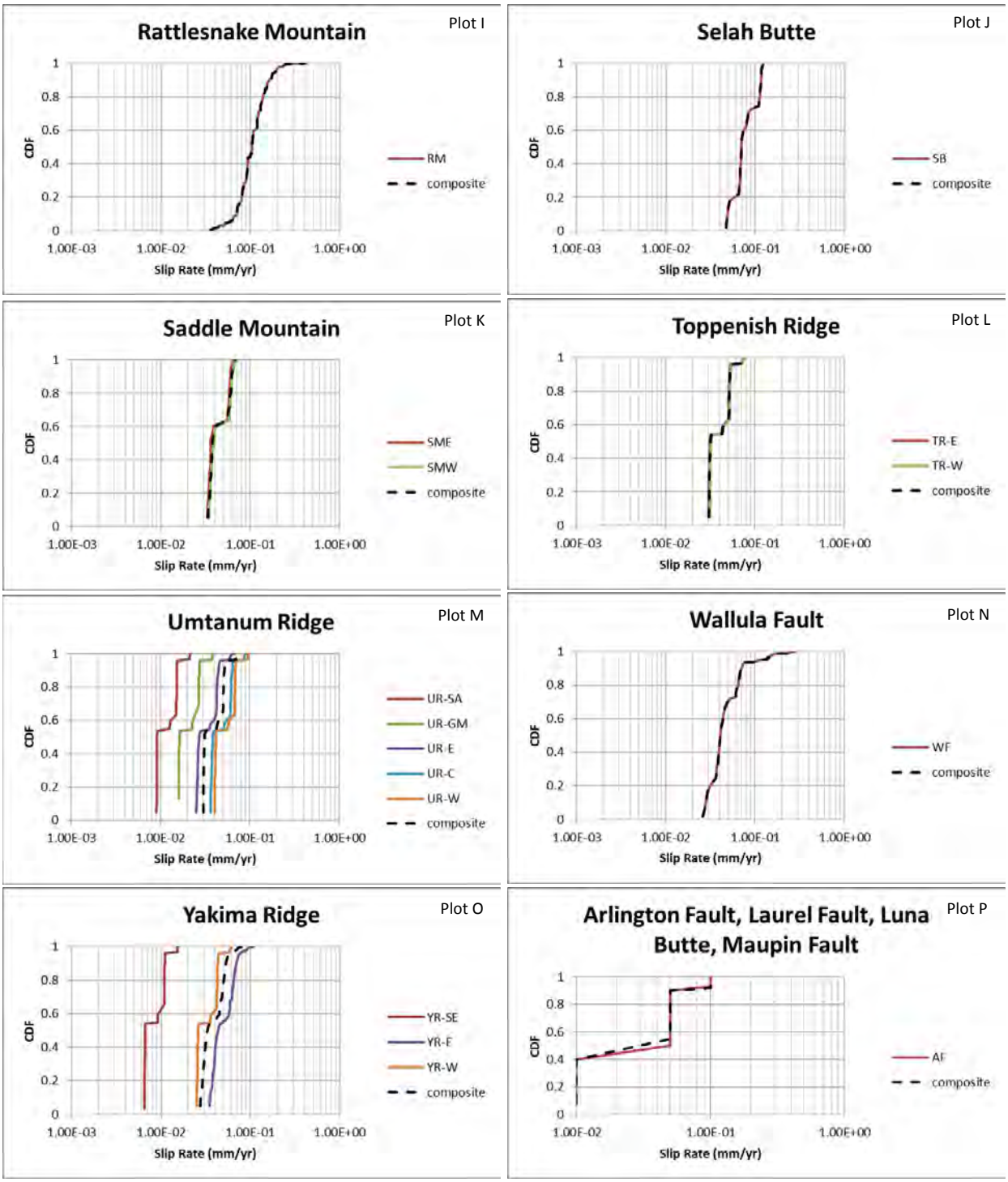


**Figure 8.83**. (contd)

### *8.4.3.6.2.1 Faults Near the Hanford Site*

Major faults closest to the Hanford Site that are summarized below include Saddle Mountains to the north, Rattlesnake Mountain, Horse Heaven Hills, and Wallula fault to the southwest, and Umtanum Ridge and Yakima Ridge to the west-northwest.

The long-term slip-rate CDF for Rattlesnake Mountain is shown in Plot I in Figure 8.83. The slip rates for Rattlesnake Mountain range from 0.03 to 0.4 mm/yr, centering on 0.1 mm/yr at a 50% probability. Rattlesnake Mountain is one of the few fault sources for which Quaternary slip-rate information is available. Section 8.4.3.6.1 describes the data available to determine Quaternary slip rates. The long-term rates bracket the minimum and maximum Quaternary slip rates, but the average long-term rates are somewhat higher than the Quaternary rates.

Plot E in Figure 8.83 shows the plots for the five segments of the Horse Heaven Hills fault source. The slip rate varies slightly for each fault segment due to different amounts of structural relief being accommodated along each segment. All of the fault segments are assessed to be reverse faults with the exception of HHH-E, which also has a small weight for oblique slip. The HHH-E segment has a similar slope until the 95% CDF where the slope flattens and slip rates increase due to the higher net-slip factor for oblique slip given the same amount of dip slip.

The long-term slip-rate CDFs for Umtanum and Yakima Ridges are shown in Plots M and O, respectively. These faults provide good examples of slip gradients occurring on a single fault source. The shapes of the slip probability functions are nearly identical for all segments, but the slip rate varies depending on the amount of structural relief measured along the segment. For Umtanum Ridge, UR-W has a maximum slip rate that is an order of magnitude higher than the minimum slip rate on UR-SA.

#### *8.4.3.6.2.2. Wallula Fault*

The long-term slip-rate CDF for the Wallula fault is shown in Plot N. As discussed in Section 8.4.3.3, all three styles of faulting were considered and assigned some weight for the Wallula fault. The long-term slip rates developed as part of this study indicate a range of approximately 0.03 to 0.3 mm/yr as observed in Plot N. The Wallula fault has vertical separation across a major escarpment as observed in the geologic maps and local borehole data. However, it has been the topic of discussion and recent studies suggest a large component of strike slip faulting. A discussion of past and recent studies of the fault zone is provided in Section 7.5 of Appendix E. Recent studies by Blakely et al. (2013) have drawn conclusions relevant to the long-term slip rate of the Wallula fault zone and therefore are discussed here.

Blakely et al. (2013) use a combination of magnetic, gravity, and geologic data to develop a tectonic model for the Wallula fault zone. They estimate the amount of offset, representing right-lateral horizontal displacement along the Wallula fault zone, by correlating individual linear magnetic anomalies seen on the north side of the fault zone with those on the south side, across a >10-km-wide zone. The authors acknowledge that the use of “piercing points,” or geologic features, for estimating offset are reliable if unique lithologies or structures are identifiable across a fault. However, they note that the Ice Harbor Member is not exposed or mapped south of the Wallula fault zone. They acknowledge that piercing points derived from regional-scale magnetic maps are more subject to interpretation and uncertainty than observed geologic evidence.

According to the assumptions made in their model (e.g., that magnetic lineations observed south of the Wallula fault zone represent the continuation of dike swarms exposed on the north side) and one pair of “piercing points” interpreted from magnetic anomalies straddling the fault zone, Blakely et al. (2013) postulate that the Wallula fault zone has experienced right-lateral offset across the entire zone of 6.9 km, or an average of 0.8 mm/yr since 8.5 Ma (age of dike intrusion) (Figure 8.84). However, five pairs of piercing points associated with single-dike anomalies that intersect the northern strand of the Wallula

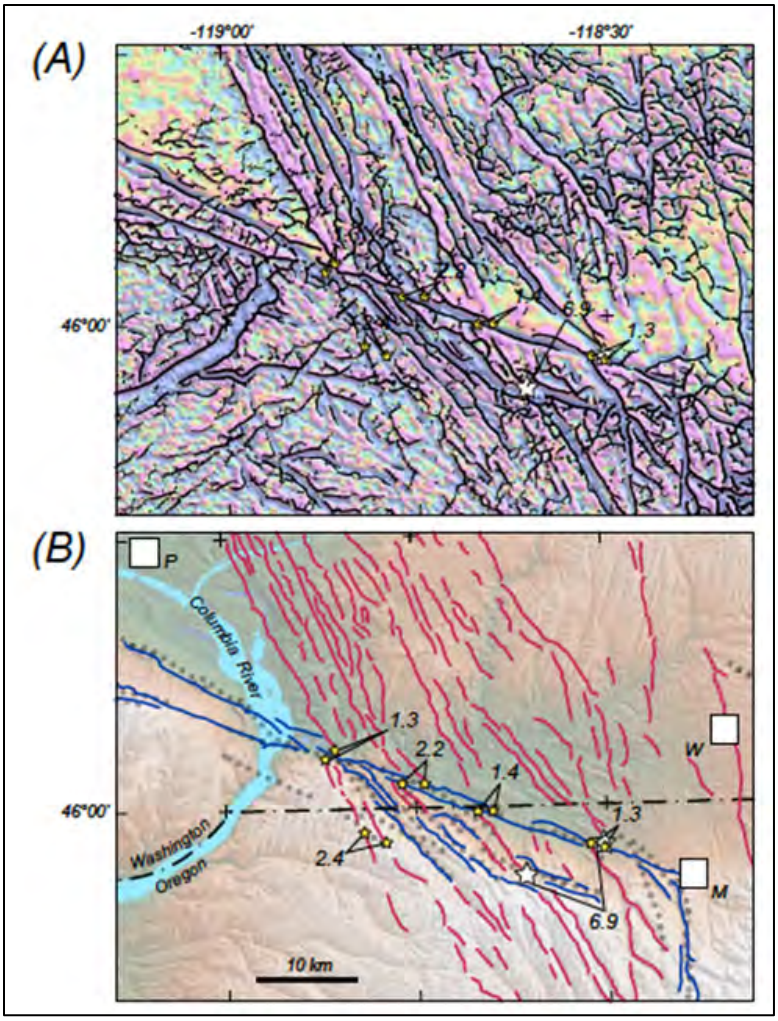


**Figure 8.84**. Lineations identified from aeromagnetic data filtered to emphasize shallow magnetic sources. Black lines in panel (A) are magnetic lineations calculated using an automated method of Phillips et al. (2007). Yellow dots in panel (B) indicate offsets of individual anomalies identified in (A) and numbers are in kilometers. Average offsets of lineations are 1.72 km. White stars indicate an offset interpreted to represent cumulative displacement of the entire fault zone (6.9 km). (From Blakely et al. 2013)

fault zone indicate right-lateral offsets (from west to east) of 1.3, 2.4, 2.2, 1.4, and 1.3 km, with an average of 1.72 km. The basis for accepting the maximum offset expressed by one pair of piercing points as opposed to using the average of individual offsets is unclear and not well established. Although the interpretation of 6.9 km since 8.5 Ma is not impossible, it rests on the assumption that this single pair of piercing points is correctly identified as representing the cumulative displacement across the entire fault zone. Blakely et al. note that the recent reanalysis of geodetic data by McCaffrey et al. (2013) "…recently reduced this estimate to less than 1 mm/y (McCaffrey et al. 2013), roughly consistent with the 0.8 mm/y right-lateral slip…" However, as discussed in Section 8.4.3.6.3, McCaffrey et al. (2013) conclude that the shortening rate decreases to the east across the YFB region and at 119° W longitude (approximately the north end of the RAW fault), geodetic shortening cannot be resolved from zero. Thus, the Blakely et al. estimate of 0.8 mm/yr is not consistent with a shortening rate that cannot be resolved from zero.

A second line of evidence for right-lateral displacement along the Olympic-Wallowa lineament (OWL) as noted by Blakely et al. (2013) is its interpreted offsets of seven stream drainages along a mapped scarp on the northeastern slope of Rattlesnake Mountain, approximately 70 km west of the Wallula fault zone (see Figure 10 in Blakely et al. 2013). Stream offsets along the scarp are interpreted to average about 250 m individually, as calculated from aerial photographs. The authors note, however, that apparent horizontal displacement may result from "consistent deflection of each stream in a right-lateral sense by alluvial fans developed where each stream debouches from the up-thrown side of the fault scarp onto the surface of the downthrown side" (Blakely et al. 2013). No estimate of the slip rate is provided, given that the interpretation of stream offsets is correct. However, as discussed in Sections 8.4.3.3, 8.4.3.6.2, and Appendix E, detailed geologic and geomorphic studies conducted at Rattlesnake Mountain for this project show that the 250-m offsets are not technically defensible and there is no evidence for significant amounts of strike slip. Thus, the offsets interpreted from the imagery do not provide support for the estimates derived from the magnetic data. Other data and interpretations regarding the potential for strike slip and reverse faulting on Rattlesnake Mountain, RAW fault, and the Wallula fault are discussed in Section 7.0 of Appendix E.

As can be seen in the slip-rate CDF for the Wallula fault in Figure 8.83, the net-slip rate for the Wallula fault source spans a range from 0.03 to 0.3 mm/yr based on interpretations of structural relief, style of faulting, and consideration of Quaternary deformation (see Section 8.4.3.6.2). Rates on the order of low tenths of millimeters per year are consistent with the postulated offsets in Blakely et al. (2013) of about 1.7 km of the 8.5 Ma dikes (0.2 mm/yr). However, a rate as high as 0.8 mm/yr, which results from postulating the 6.9-km offset of the anomalies, is not considered to be technically defensible by the TI Team and such rates are therefore not included in the range of slip rates for the Wallula fault.

#### 8.4.3.6.3 Comparison with Shortening Rates

The long-term average shortening rates derived from fault slip rates in the SSC model were compared with secular strain rates in the YFB determined by McCaffrey et al. (2013) from analysis of GPS data. The comparison provides insights into the degree to which the long-term geologic record of deformation is consistent with the very short geodetic record.

As discussed in Section 4.2, McCaffrey et al. (2013) modeled deformation in the YFB as distributed quasi-ductile shortening driven by impingement of the rigid eastern Oregon block from the south. Using a subset of 55 GPS stations in eastern Washington and northern Oregon that generally encompass the YFB, McCaffrey et al. (2013) decomposed the local velocity field associated with these stations into two components: 1) rigid motion of the entire 55-station network, which does not contribute to shortening or slip on faults; and 2) uniform horizontal strain within the network, which is presumably accommodated by shortening and fault slip. The rigid motion of the 55-station network is described by clockwise rotation of 0.35°/Myr about a pole in northeastern Oregon that is southeast of and on trend with the OWL (McCaffrey et al. 2013). The uniform strain rate in the YFB is characterized by a maximum shortening rate of about -6.8 ns/yr directed toward about N56°E (ns = nanostrain, or $10^{-9}$ strain) (McCaffrey et al. 2013).

From this uniform horizontal strain rate, McCaffrey et al. (2013) further derived the resolved component of the strain rate along several longitudinal (north-south) traverses through the YFB. Their results indicate the following:

- The strain rate along 119°W longitude is -0.5 ns/yr ± 1.6 ns/yr, which is nominally contractional but not resolvable from zero (or a very low extensional strain rate) within uncertainty. This north-south traverse primarily crosses the OWL in the eastern YFB.
- The strain rate along 120°W longitude (central YFB) is -1.3 ns/yr ± 1.1 ns/yr, indicating a component of north-south shortening that is just barely resolved within uncertainty. The strain rate is equivalent to an integrated shortening rate of about 0.2 mm/yr ± 0.15 mm/yr along a 142-km-long north-south traverse that crosses the Columbia Hills, Horse Heaven Hills, Rattlesnake Mountain, Saddle Mountains, and the Frenchman Hills.
- The strain rate along 121°W longitude (western YFB and eastern Cascades foothills) is -4.1 ns/yr ± 1.0 ns/yr, indicating a component of north-south shortening that is resolved within uncertainty. The strain rate is equivalent to an integrated shortening rate of about 0.7 mm/yr ± 0.2 mm/yr along a 177-km-long north-south traverse that crosses the western ends of the Columbia Hills, Horse Heaven Hills, Toppenish Ridge, Yakima Ridge, Umtanum Ridge, and Manastash Ridge.

To compare these shortening rates derived from GPS data to long-term average rates predicted by the source model, the TI Team calculated the integrated component of north-south shortening along the same three longitudinal traverses (119°W, 120°W, 121°W) used by McCaffrey et al. (2013). The analysis consisted of the following steps:

1. The Team first derived the total net slip on a given fault by calculating the reverse component of slip from the fault dip and structural relief, and then multiplying the reverse slip component by the slip ratio *N* for a given style of faulting (reverse, oblique, or strike slip) in the source model. For this analysis, values of fault dip were derived for a 16-km-thick seismogenic crust.
2. The Team then derived the rake angle for the slip vector on the fault as a function of *N*. For pure reverse dip slip, $N = 1$ and the associated rake is 90°. For other models that assume oblique or strike slip faulting (i.e., N>1), the rake of the slip vector in the plane of the fault is given by:

$$\text{Rake } (\theta) = 90° - [\cos^{-1} (1/N)]$$

3. Given the strike and dip of the fault and the rake angle $\theta$, the Team derived the trend (azimuth) and plunge angle of the net-slip vector in the plane of the fault using an Excel spreadsheet prepared by Eric Nelson of the Colorado School of Mines that uses standard trigonometric functions to calculate relationships among strike, dip, rake, trend, and plunge (Nelson 2014) (http://serc.carleton.edu/NAGTWorkshops/structure/computer_resources.html).
4. The trend of the slip vector derived using these relationships is the azimuth of maximum shortening associated with slip on the fault.
5. The Team calculated the amount of the horizontal shortening ($S_H$) in the direction of the trend of the net slip vector via the following trigonometric relationship:

$$S_H = \text{(amount of net slip) x cosine (plunge angle of net-slip vector)}$$

6. To find the amount of horizontal shortening resolved in an arbitrary direction, $S_H$ is multiplied by the cosine of the angle between the trend of the net-slip vector and the direction of interest. For this analysis, the Team derived the amount of shortening resolved in the due north direction for comparison with the longitudinal strain rates derived by McCaffrey et al. (2013).

7. The component of north-south shortening for all faults along a given longitudinal traverse is summed. The long-term average shortening rate is derived by dividing total shortening along the traverse by the period the time during which the deformation occurred. For this analysis it is assumed that the two models for the onset of deformation discussed in Section 8.4.3.5: 10 Ma and 6 Ma.

The results of this analysis and a comparison with McCaffrey et al.'s (2013) shortening rates are presented in Table 8.14 and the lines of transect are shown in Figure 8.85.

**Table 8.14**. Comparison of geologic and geodetic shortening rates in the Yakima Fold Belt, Eastern Washington

| Longitude | North-South Shortening Rate, 6 Ma start time (mm/yr) | North-South Shortening Rate, 10 Ma start time (mm/yr) | Secular North-South Shortening Rate, GPS Analysis (McCaffrey et al. 2013) (mm/yr) |
|---|---|---|---|
| 119° W | 0.03–0.04 | 0.02–0.05 | Not resolved |
| 120° W | 0.3 | 0.2 | 0.2 |
| 121° W | 0.3 | 0.2 | 0.7 |

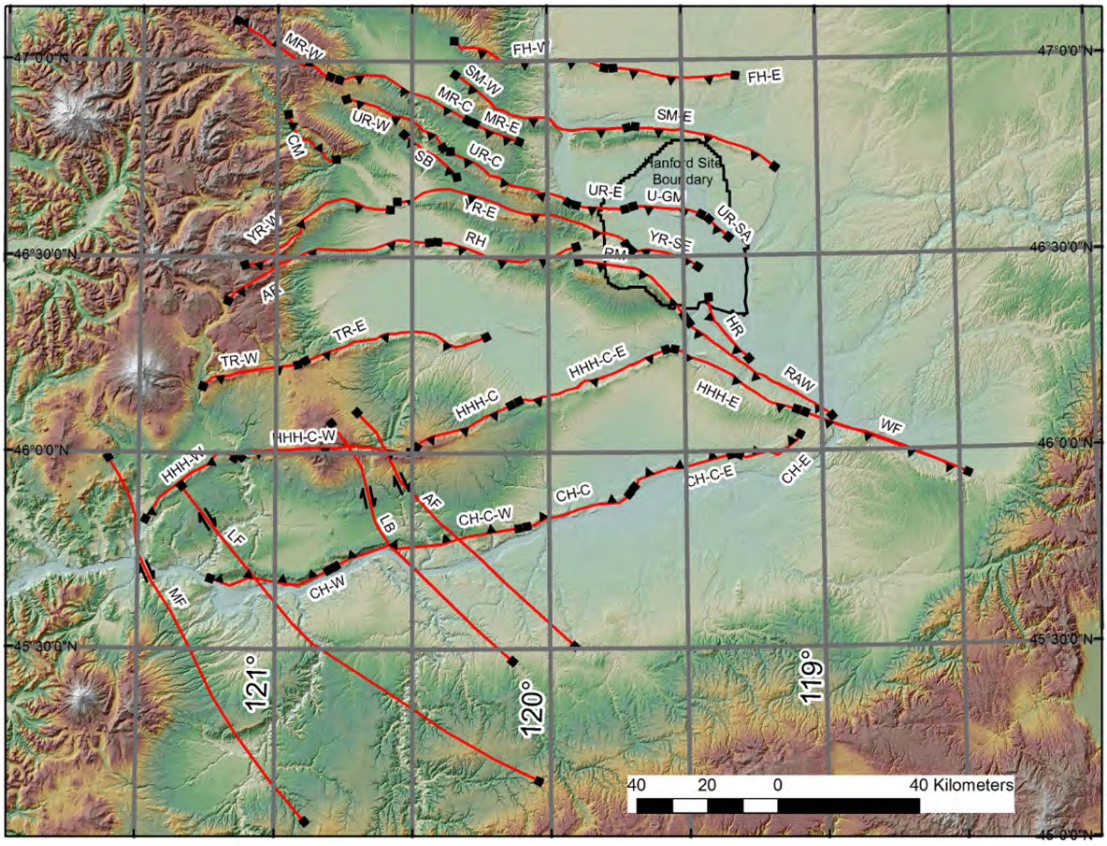


**Figure 8.85**. Map of the YFB region showing the lines of transect for the shortening analysis at 121°, 120°, and 119°W longitude.

The range in rates for the 119°W traverse reflects results from different models assuming pure reverse slip ($N$=1), oblique slip ($N$= 1.4), and strike slip (two models: $N$=2.2 and $N$=5.1). Multiple shortening rates similarly were calculated for reverse, oblique slip, and strike slip models along the 120°W and 121°W traverses, but the results are effectively the same when rounded to the nearest 0.1 mm/yr, so only a single value is shown in these cases.

The results of this analysis indicate that the secular GPS shortening rates are similar to the long-term average rates associated with the slip rates in the seismic source model. Both the GPS and geologic approaches find that the integrated rates of north-south shortening across the YFB are in the low tenths of millimeters per year, which implies that slip rates on individual thrust faults are likely to be a fraction of that; i.e., in the mid to high hundredths of millimeters per year. The best fit between the two approaches is in the central part of the YFB (i.e., longitude 120°W). The integrated geodetic shortening rate along 121°W at the west end of the YFB is still in the tenths of millimeters per year, but a factor of 2−3 higher than the geologic rate. Many of the GPS stations in this region used by McCaffrey et al. (2013) are located within the Cascades, west of the Yakima fold structures, and thus their velocities may reflect the influence of tectonic and magmatic processes that are not directly related to growth of the Yakima folds.

To summarize, secular shortening rates in the central YFB derived from geodetic data are similar to long-term average geologic shortening rates. Both approaches suggest that the integrated rate of shortening across the YFB is on the order of tenths of millimeters per year, implying slip rates on individual thrust and reverse faults on the order of hundredths of millimeters per year.

#### 8.4.3.7 Approaches to Assessing Recurrence: Slip Rate, Recurrence Interval

As discussed in Section 8.4.3, the logic tree that relates to the assessments of recurrence for fault sources has a node that provides for two alternative approaches to the assessment of earthquake recurrence, which are slip rate and recurrence intervals. All of the fault sources have geologic data that allow for the assessment of slip rate, but only three faults have sufficient paleoseismic data to allow for the assessment of recurrence intervals. The data used to assess slip rates are given in Section 8.4.3.6 and paleoseismic information that constrains the ages of paleo-earthquakes such that the times between earthquakes can be estimated is given in this section. Sufficient paleoseismic data to estimate recurrence intervals are available for three fault sources: the Ahtanum-Rattlesnake Hills, Toppenish, and RAW fault sources. These data are discussed in Sections 8.4.3.7.1, 8.4.3.7.2, and 8.4.3.7.3, respectively.

The TI Team's assessment of the relative weights assigned to the slip-rate approach to recurrence estimation and the paleoseismic recurrence interval approach is a function of the fault-specific data that are available to assess each quantity. In ideal circumstances with abundant paleoseismic data that define with low uncertainties both the presence of individual earthquakes and their timing the recurrence interval approach would be given high weight relative to the slip-rate approach. This is because a slip rate provides the average behavior of a fault over a given time period, but the recurrence interval approach can provide more direct evidence of the actual length of recurrence intervals during the most recent period of activity. Unfortunately, the paleoseismic data that are available for the three faults in the YFB have significant uncertainties in both the numbers of paleo-earthquakes present in the geologic record and in the timing of each earthquake. These uncertainties are discussed in the context of all available paleoseismic data related to each fault in Sections 8.4.3.7.1 through 8.4.3.7.3. In light of a thorough review of these data and their associated uncertainties, the TI Team arrived at the following assessment of the relative weights for the alternative recurrence approaches for the Ahtanum-Rattlesnake Hills and Toppenish fault sources:

| | |
|---|---|
| Slip-rate approach | [0.7] |
| Recurrence intervals approach | [0.3]. |

The data related to the identification of paleo-earthquakes and to their timing for the RAW fault source are highly uncertain at the present time. Therefore the TI Team assessed the weight for the recurrence interval approach to be lower than for the other two faults. The relative weights for the alternative recurrence approaches for the RAW fault source are as follows:

| | |
|---|---|
| Slip-rate approach | [0.95] |
| Recurrence intervals approach | [0.05]. |

The paleoseismic data used for the assessment of recurrence intervals are gathered at particular points and along a limited reach of a single segment of each fault. For this assessment, it is assumed that the data are applicable to the entire segment and assessments are made regarding the applicability for other segments of the fault source. For Ahtanum Ridge-Rattlesnake Hills and Toppenish Ridge, all segments of the fault source are assessed to be characterized by the same recurrence intervals that are defined along a single segment. However, the recurrence rates are weighted by the applicable moment rate for each segment, which is a function of the segment length, downdip width, and net-slip rate. The paleoseismic data gathered for the RAW source are assumed to apply to the entire RAW fault source because multiple segments have not been identified.

For the analysis, radiocarbon ages (reported in $^{14}$C yr BP) were converted to 2-sigma calibrated ages using CALIB http://intcal.qub.ac.uk/calib (Reimer et al. 2013). Luminescence (optically stimulated luminescence and infrared stimulated luminescence [IRSL]) ages for samples collected from the Ahtanum-Rattlesnake Hills and Toppenish Ridge trench, which were reported as 2 sigma ages (yr BP) (Campbell and Repasky 1998; Repasky et al. 1998) were corrected to years before 2014.

Given the identification of individual paleo-earthquakes and the uncertainty distribution defining their ages, the approach used to calculate recurrence intervals incorporates the uncertainties in the number of events and their timing. The approach used for estimation of the uncertainty distribution for the rate parameter $\lambda$ of a Poisson process follows the following general framework:

- Define a likelihood function that represents the probability of seeing the observed sample of data given a specified rate parameter $\lambda$.
- Compute the likelihood values for a full range of the rate parameter $\lambda$.
- Normalize these likelihood values to create a probability distribution for $\lambda$.
- Incorporate uncertainty in the input data by repeating the process for the weighted alternative data sets and computing a weighted combination of the resulting probability distributions for $\lambda$.
- Represent the resulting probability distribution by a discrete approximation for implementation in hazard analysis.

The likelihood functions used to implement this process depend upon the type of data available. For the three faults that have data related to recurrence intervals, the data are estimates of the timing of paleo-earthquakes. The approach used to calculate recurrence is the same as that used in the CEUS SSC project (NRC 2012a, NUREG-2115, Section 5.3.3.1), as summarized below.

The data available are estimates of the occurrence times of a sequence of $N$+1 earthquakes obtained from dating of paleoseismic features or known occurrence times from the historical record. The estimated dates for the $N$+1 earthquakes provide $N$ values of the times between earthquakes, $t_i$, plus the open interval since the most recent repeated large-magnitude earthquake, $t_0$. The Poisson process produces an exponential distribution for the time between occurrences:

$$f(t) = \lambda \exp\{-\lambda t\}$$

$$F(t) = 1 - \exp\{-\lambda t\} \tag{8.1}$$

This leads to the likelihood function for a rate parameter of $\lambda_i$ given the observed data ($t_i$, $i$ = 1, $N$, $t_0$):

$$L(\lambda_i | t_i, t_0) = \prod_{i=1}^{N} f(t_i) \times [1 - F(t_0)] = \lambda_i^N \exp\left\{-\lambda_i \times \left[\sum_{i=1}^{N} t_i + t_0\right]\right\} \tag{8.2}$$

The form of the likelihood function indicates that specification of the dates for the intermediate events is not needed because the term $\left[\sum_{i=1}^{N} t_i + t_0\right]$ is equal to the elapsed time since the oldest earthquake in the sequence.

The logic-tree structure is generally used to represent uncertainty in the inputs to a PSHA. In a logic tree, uncertainty distributions are represented by a (small) set of discrete alternatives with assigned probability weights. Miller and Rice (1983) provide a set of discrete approximations for arbitrary continuous probability distributions. Their five-point approximation was chosen to represent the distributions for $\lambda$ developed for the fault sources, as simplified by the NRC (2012a).

#### 8.4.3.7.1 Ahtanum-Rattlesnake Hills

The USGS Quaternary Fault database ranks the Ahtanum Ridge structures as Class A and B, similar to Toppenish Ridge and Saddle Mountains (Lidke 2003d; Lidke et al. 2003). The Rattlesnake Hills continue to the east of and largely on strike with Ahtanum Ridge (Lidke et al. 2003) (Figure 8.45). The Ahtanum Creek fault is inferred to dip south under Ahtanum Ridge and project upward toward the foot of the northern edge of the ridge, which is buried in young alluvium. Evidence for Quaternary faulting has been described by Geomatrix (1988, 1990), Campbell and Repasky (1998), and Repasky et al. (1998a, b).

Geomatrix (1988, 1990) reports scarps and lineaments suggestive of Pleistocene deformation along the northern flank of the ridge for about 30 km west and 6 km east of Union Gap. Scarps and graben structures south of the Ahtanum Creek fault appear to be similar to structures south of the Mill Creek fault along Toppenish Ridge (see Section 8.4.3.7.2), although they are more subdued. Geomatrix (1988, 1990) also describes an east-striking fault at Union Gap, just south of Yakima, that dips 43° N and places Miocene volcanic rocks on terrace gravels of the Yakima River with caliche questionably dated by Th/U as 30 ± 3 ka. The gravels are offset at least 7 m (Reidel et al. 1994). Touchet Beds containing the Mount St. Helens "S" tephra, dated at 13 ka (revised more recently to ~15.8–16 ka, see Appendix E, Table 4.2.7-1), are not faulted at this location, but faulted Touchet Beds were observed 1 km to the east (NP Campbell 1992, unpublished data cited by Reidel et al. 1994). Repasky and Campbell (1998)

suggest this is a backthrust to the Ahtanum Creek fault. How the backthrust and its activity relate to the inferred main south-dipping fault is unknown; it is likely, however, that the primary fault is at least as active as the subsidiary fault, and consequently the primary fault can be inferred to have been active in the late Pleistocene.

Repasky and Campbell (1998) report evidence for late Pleistocene to early Holocene movement along normal faults of a ridge-top graben south of the Ahtanum Creek fault (Figure 8.45). They suggest these faults probably are tensional features related to movement along the underlying Ahtanum Creek fault, similar to the graben features reported on Toppenish Ridge and the Saddle Mountains. Steeply north- and south-dipping normal faults accompanied by a sequence of colluvial wedges exposed in a trench (Trench RSH-1) across the graben indicate that three faulting events (represented by colluvial wedges A, B, and C) occurred in the graben during the past 109 kyr, with the latest event occurring 12 to 45 ka (probably ~15 ka based on soil stratigraphy) (Figure 8.86) (Repasky et al. 1998). If this event occurred simultaneously with the backthrust at Union Gap, the observation of faulted Touchet Beds 1 km east of Union Gap suggests that the most recent event post-dates ~17 ka (the maximum constraining age for deposition of Touchet Beds during the most recent phase of Missoula floods) and probably pre-dates eruption of the Mount St. Helens "S" tephra (Campbell and Repasky 1998). The penultimate event (represented by wedge B) sits on top of a soil that is probably too old to be Washtucna (20 to 40 ka) but may be equivalent to the "Chocolate soil" with an estimated age of 50 ka as suggested by the composite stratigraphy table presented by Repasky et al. (1998).

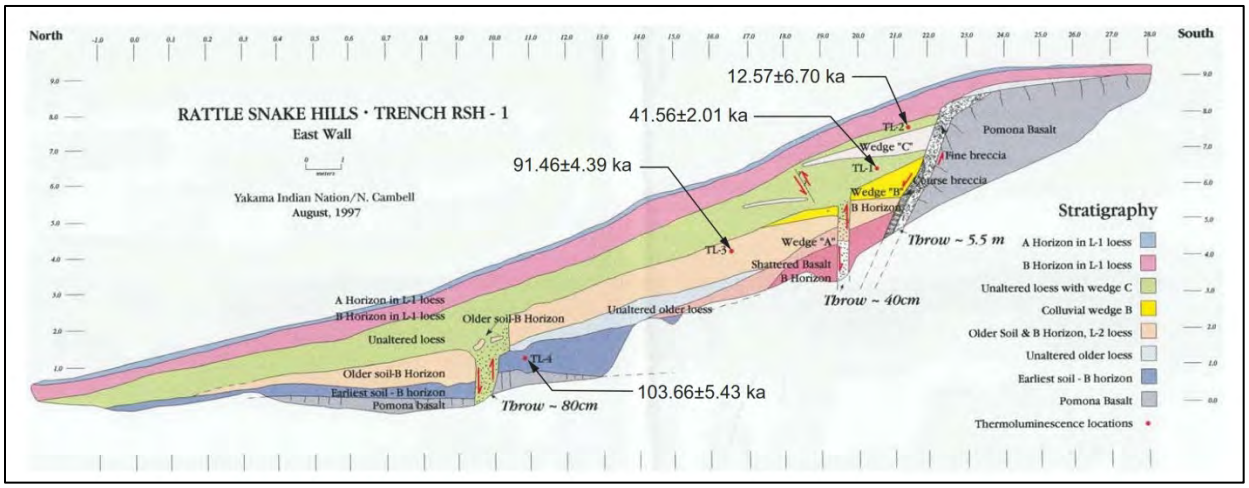


**Figure 8.86.** Log of Ahtanum-Rattlesnake Hill-Trench RSH-1 showing IRSL and thermoluminescence dates (from Repasky et al. 1998).

Based on the available dates and soil stratigraphy observations, the age constraints and weights (in brackets) in Table 8.15 are used to estimate the timing of the most recent event (Event C) and the intervals of time between the three surface faulting events recorded in the Ahtanum-Rattlesnake Hills trench.

**Table 8.15**. Constraining dates and timing of paleo-earthquakes inferred from Ahtanum-Rattlesnake Hills Trench RSH-1.

| Constraining Age | IRSL/TL Age (yr BP) (2-sigma) [(a)] | Years before 2014 |
|---|---|---|
| a | 12,570 ± 670 | 13.3 ka to 11.9 ka |
| b | 41,560 ± 2,010 | 43.6 ka to 39.6 ka |
| c | 91,460 ± 4,390 | 95.9 ka to 87.1 ka |
| d | 103,660 ± 5,430 | 109.1 ka to 98.2 ka |
| Paleo-earthquake | Estimate Age | Weight |
| Event 3 (wedge A) | uniform between c and d | [1.0] |
| Event 2 (wedge B) | uniform between b and c<br>uniform between b and 50 (± 5%) ka | [0.4]<br>[0.6] |
| Event 1 (wedge C) | uniform between a and b<br>uniform between a and 17 (± 5% ) ka | [0.3]<br>[0.7] |

(a) See Age Dating Report by S Mahan (January 2, 1998) (Repasky et al. 1998, Appendix B). Reported ages are corrected to years before 2014 by adding 16 years to reported ages.

TL = thermoluminescence.

#### 8.4.3.7.2 Toppenish Ridge

The USGS Quaternary Fault database ranks the Toppenish Ridge structures as Class A and B (Lidke and Bucknam 2002a, b; Lidke et al. 2003). Toppenish Ridge is limited to the area west of the Yakima Valley, and it rises west toward the Cascades east of Mount Adams (Figure 8.45). Evidence for Quaternary faulting has been described by Bentley et al. (1980), Campbell and Bentley (1981), WCC (1981c), Campbell et al. (1995), and Repasky et al. (1998, which includes a report by Campbell and Repasky as Appendix C). The structures consist of the Mill Creek thrust at the northern foot of Toppenish Ridge and subparallel normal faults that form grabens along the crest of the main anticline (Figure 8.87). Geomorphic expression of the Mill Creek thrust includes three east-striking zones of fault scarps following a sinuous pattern and extending for at least 24 km to as much as 32 km in the Satus Peak segment of Toppenish Ridge (Geomatrix 1988, 1990). The crestal graben south of the Mill Creek thrust disrupts north-flowing drainage and locally creates sag ponds containing as much as 1.5 m of ponded silt (Bentley et al. 1980). Trenches across the Mill Creek thrust have exposed a shallowly 20 to 40 degrees south-dipping thrust fault that places upper Miocene rocks over Pleistocene-Holocene soils and Pleistocene gravels and has clear evidence of repeated late Quaternary surface faulting (Campbell et al. 1995) (Figure 8.87 and Figure 8.88). Normal faults in the graben dip north and south 60 to 90 degrees, based on trench exposures.

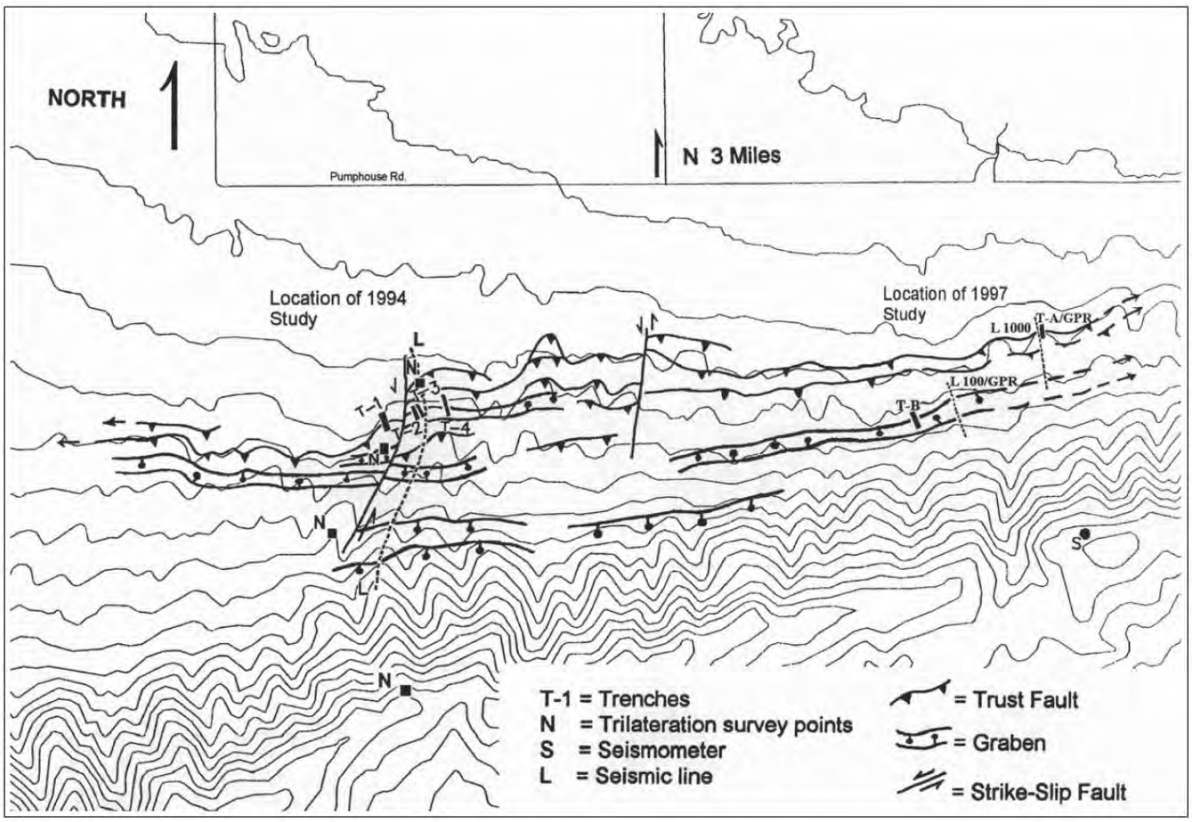


**Figure 8.87**. Location Map of the 1994 and 1997 study area on Toppenish Ridge showing locations of paleoseismic trenches (Modified from Repasky et al. 1998).

Campbell et al. (1995) and Campbell and Repasky (1998, Appendix C of Repasky et al. 1998) report three to possibly five events along the Mill Creek thrust, dated as 1) 0.5 to 1 ka, poor documentation; 2) 6 to 7 ka, very good documentation; 3) 10 to 11 ka, fair documentation; 4) 40 to 60 ka, good documentation; and 5) 145 to 180 ka, fair to good documentation. Evidence of a post-1000 ka event includes radiocarbon dates of 505 ± 160 $^{14}$C yr BP and 620 ± 135 $^{14}$C yr BP from organic matter in a ridge-top graben sag pond that were initially thought to closely constrain the timing of a surface faulting event. Repasky et al. (1998) concluded, however, that the dates and other evidence (slide movement and legends) for the post-1000-ka event were questionable and noted as well that this postulated event is not the most recent event that is well documented in trenches that exposed the Mill Creek thrust. A maximum limiting age for the most recent event on the Mill Creek thrust is well constrained by an IRSL age of 5,690 ± 390 yr BP on soil overridden by the Mill Creek thrust (Trench A) and a thermoluminescence (TL) age of 6,690 ± 680 yr BP from the A-horizon of a soil overridden by the Mill Creek thrust in Trench 1 (Figure 8.88 and Figure 8.89).

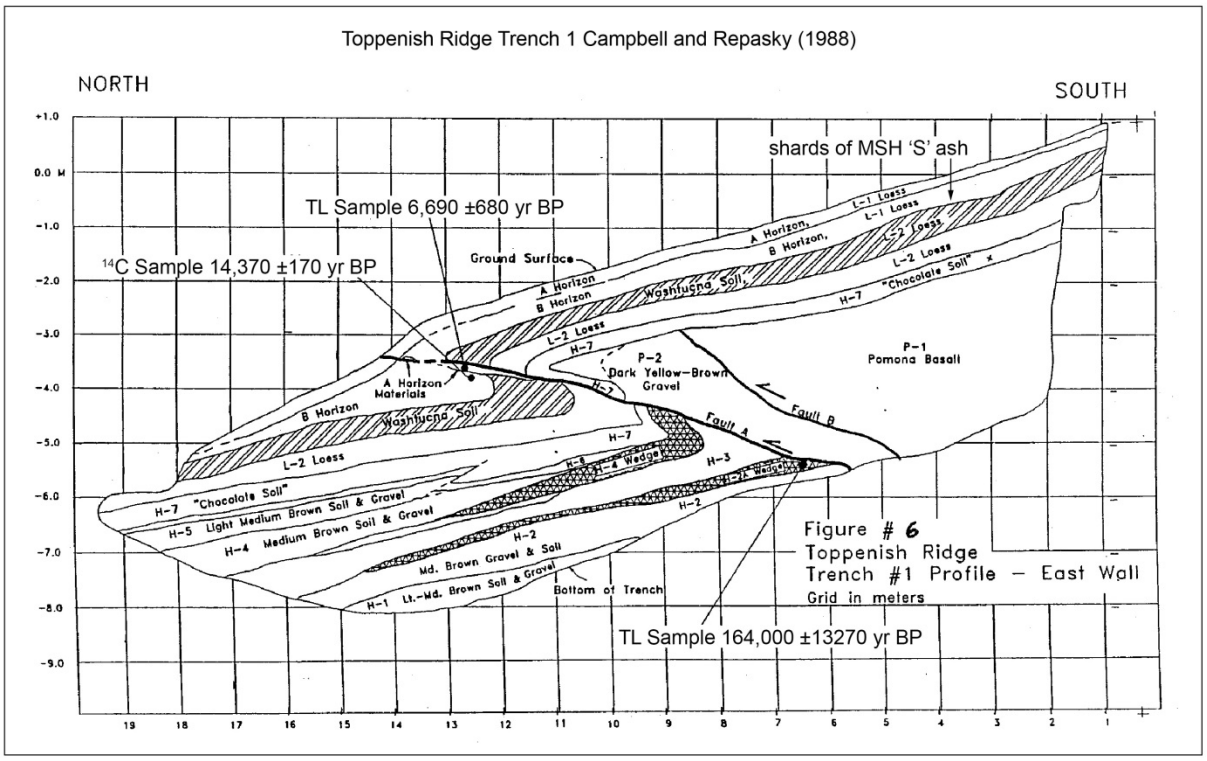


**Figure 8.88**. Log of the Trench 1 paleoseismic trench across the Mill Creek thrust, Toppenish Ridge (Campbell and Repasky 1988).

The timing of the penultimate event on the Mill Creek fault is not as well constrained. Repasky et al. (1998) do not provide a detailed discussion of the evidence to support the 10−11 ka age. The compilation table summarizing trench data for both Ahtanum-Rattlesnake Hills and Toppenish trenches (Campbell and Repasky 1998) suggests that the age is based on the age of a seed (9050 ± 50 $^{14}$C yr BP) collected from the basal part of the upper sedimentary package in Olney Lake. The compilation table states that the sample was collected from the base of an inferred earthquake-caused landslide; however, discussion of the Olney Lake stratigraphy (Repasky et al. 1998, Appendix D) indicates that the change in sedimentation is probably due to regional climate change. Based on conservative estimates of sedimentation rates and tephra observed in the lower units in the Olney Lake sedimentary section, Repasky et al. (1998) conclude the lake, which is inferred to be slide-created pond on Toppenish Ridge, formed over 20 ka and most likely prior to mid-Wisconsinan time (>33 ka), possibly during a tectonic surface-rupturing event 40 to 60 ka.

Colluvial wedges observed in Trench 1 are cited as evidence of two pre-Washtucna soil faulting events. Key sample ages used to evaluate timing of surface faulting events related to the Toppenish fault source are outlined in Table 8.16.

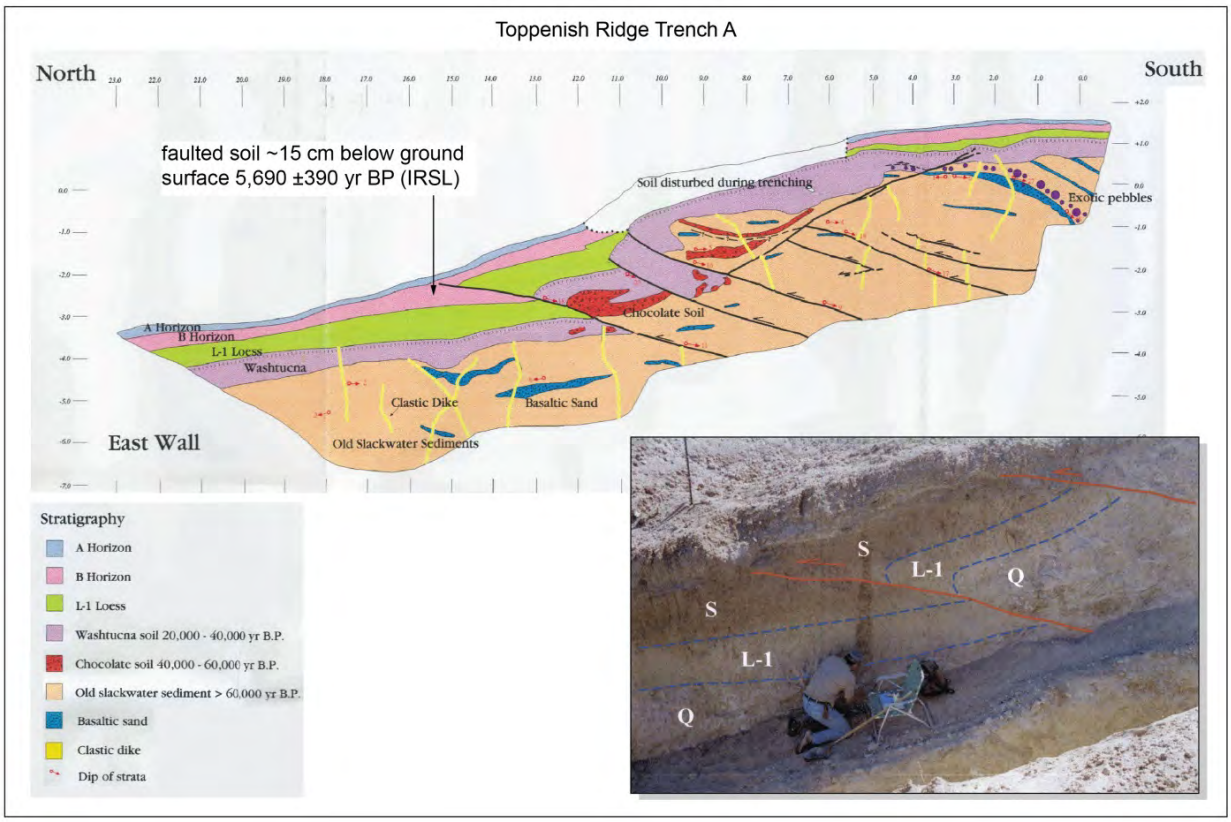


**Figure 8.89**. Log and photograph of paleoseismic Trench A across the Mill Creek thrust, Toppenish Ridge (modified from Repasky et al. 1998).

**Table 8.16**. Constraining dates used to estimate timing of paleo-earthquakes based on stratigraphy inferred from Toppenish Ridge trench and Olney Lake core data.

| Measured $^{14}$C yr BP | Calibrated (2 Sigma) [(a)] | Years before 2014 (2 Sigma) |
|---|---|---|
| 505 ± 160 | cal AD 1183: cal AD 1684 | 831 to 330 |
| 620 ± 135 | cal AD 1152: cal AD 1526 | 862 to 488 |
| 9050 ± 50 | cal BC 8348: cal BC 8201 | 10363 to 10216 |
| 10200 ± 280 | cal BC 10745: cal BC 9211 | 12760 to 11226 |
| Measured yr BP[(b)] | Years before 2014 | Years before 2014 |
| 5,690 + 390 (IRSL) | 5706 ± 390 | 6096 to 5316 |
| 164,000 ± 13,270 (TL) | 164,016 ± 13,270 | 177,286 to 150,746 |

(a) Calibrated using CALIB http://intcal.qub.ac.uk/calib/ ; calibration data set: intcal13.14c (Reimer et al. 2013)
(b) IRSL/TL ages Repasky et al. 1998 and Campbell and Repasky (1998) reports. Dating appendix to Repasky et al. (1998) by Dr. S. Mahan (USGS) dated January 1998. Therefore to correct dates to January 1, 2014, 16 years were added to the reported ages.

The data presented by Repasky et al. (1998) allow for alternative interpretations of the number and timing of earthquake sequences. Three options are considered as outlined in Table 8.17. One is to accept all five possible events as outlined by Repasky et al. (1998). The second and third options, which allow for fewer events and different timing, are based on review of the trench logs, report, and assessment of their supporting data. Repasky et al. (1998) suggest that the postulated event that formed a sag shortly before 500−1000 ka is not the most recent event observed on the Mill Creek thrust. In the second option, the deposition of the sediments in the sag is not considered to be definitive evidence of a major surface-rupturing event and the likelihood that the age of the sediments represents the timing of the most recent event is therefore given a weight of only [0.4]. The 5690 ± 390 yr BP (IRSL) date (corrected to 6096 to 5316 yr before 2014) closely pre-dates a surface-rupturing earthquake on the Mill Creek thrust. Evidence for the 10- to 11-ka event, which seems to rely predominantly on a change in the character of sedimentation in Olney Lake, is reassessed. Leopold et al. (Repasky et al. 1998, Appendix C) attribute this change to a regional climatic change, which is also inferred from sediments observed in Carp Lake. Stratigraphic relationships shown on the Trench A log, however, show a possible thickening of loess on the footwall block of the thrust that may be indicative of a preexisting scarp that formed post-Washtucna soil (post 20–40 ka). They also cite an age of 40−60 ka without any substantial explanation of the basis.

**Table 8.17**. Alternative interpretations of the number and timing of Toppenish Ridge surface faulting events.

| | | | |
|---|---|---|---|
| Option 1 | [wt. 0.5] | This option adopts all five events and estimated ages from Campbell and Repasky (1998) (Repasky et al.1998, Appendix C) (ages from trenches excavated in 1994 and 1997); except for Event 2, which is modified to capture the full range in uncertainty of the ages (years before 2014) of the samples collected in 1997 from Trench A and in 1994 from Trench 1 (Repasky et al. 1998). | |
| a | 0.5 ka | Event 1 | uniform between a and b |
| b | 1 ka | | |
| c | 5.3 ka | Event 2 | uniform between c and d |
| d | 7.4 ka | | |
| e | 10 ka | Event 3 | uniform between e and f |
| f | 11 ka | | |
| g | 40 ka | Event 4 | uniform between g and h |
| h | 60 ka | | |
| i | 145 ka | Event 5 | uniform i and j |
| j | 160 ka | | |
| Option 2 | [wt. 0.5] | This option does not include the 0.5–1.0-ka event, which is poorly documented. In this option the timing of the most recent event (MRE) is the youngest rupture of the Mills Creek thrust constrained by maximum and minimum ages (years before 2014) of dated samples from Trenches 1 and A, respectively. Based on the weak evidence for the latest Pleistocene event, the 10- to11-ka event is not included. The penultimate event is assumed to be represented by the H-4 wedge (Trench 1), which would pre-date formation of the Chocolate soil. Olney Lake may have formed in response to a seismically triggered earthquake during this event. The timing of the earliest event assumes that the age (thermoluminescence [TL] 164,000 ± 13,270 kyr BP) of the sample from the H-2A wedge represents the age of this surface rupture. | |
| a | 5.3 ka | | Minimum age based on age of Trench A sample (Modern soil buried during event) 5,690 + 390 yr BP (IRSL) |

**Table 8.17**. (contd)

| | | | | |
|---|---|---|---|---|
| | | Event 1 | | uniform between a and b |
| b | 7.4 ka | | | Maximum age based on age of Trench 1 sample (Modern soil buried during event) 6,690 ± 680 yr BP (TL) |
| c | 50 ka | | | Minimum limiting age is the age of the H-7/H-4 wedge contact (maximum age of Old Maid Coulee soil). The H-7 unit (Chocolate soil) could be equivalent to the Old Maid Coulee soil (~ 40–50 ka) or the Devils Canyon soil (~60–70 ka) of McDonald et al. (2012). |
| | | Event 2 | uniform between c and d | |
| d | 70 ka | | | Maximum limiting age is the age of the H-7/H-4 wedge contact (maximum age of Devils Canyon soil). |
| e | 150 ka | | | Maximum limiting age-TL sample from inferred scarp-derived colluvium (164,000 ± 13,270) (Trench 1). |
| | | Event 3 | uniform between e and f | |
| f | 178 ka | | | Maximum limiting age-TL sample from inferred scarp-derived colluvium (164,000 ± 13,270) |

#### 8.4.3.7.3 RAW (Finley Quarry)

A key locality for assessing the style of faulting and the timing of most recent faulting along the RAW fault source is a quarry exposure near Finley, Washington. Previous studies conducted during site characterization studies for both Columbia Generating Station and the Basalt Waste Isolation Project involved logging a quarry wall and a trench excavation in the quarry (Farooqui and Thoms 1980; WCC 1981a, b). The USGS, under the direction of Drs. Brian Sherrod and Richard Blakely, recently completed a paleoseismic log of the existing quarry wall exposure, additional mapping, geomorphic interpretation of high-resolution LiDAR data, and ground-based magnetic surveys in the vicinity of the Finley quarry. The results of the USGS studies are discussed by Sherrod et al. (In Review).

Sherrod et al. (In Review) interpret as many as four paleo-earthquakes along the Wallula fault (which as defined by Sherrod et al. includes Rattlesnake Mountain, the RAW structure, and the Wallula Gap fault). An evaluation of these new data and interpretations of the number and timing of surface faulting events are provided in Section 7.4.2 and Table 7.2 of Appendix E.

The timing of the oldest event(s) recognized from exposures in a trench excavated and logged by WCC (1981a) is not well constrained and thus is not used in the recurrence assessment for the RAW fault source based on recurrence interval data from Finley quarry. Evidence for the three youngest latest Pleistocene to Holocene postulated paleo-earthquakes recorded at Finley quarry is not conclusive. Alternative non-tectonic explanations of the observations and evidence (e.g., related to glacial outburst flood processes) cited for these events are outlined in Table 7.2 in Appendix E. Arguments can be made for zero to as many as three paleo-earthquakes post-dating an MIS 2 flood-related erosional unconformity that is estimated to be no older than 17 ± 1.8 ka. The hypotheses that zero or one paleo-earthquake post-date the MIS 2 unconformity are judged to be most likely; and in such cases there is not sufficient information to calculate meaningful recurrence intervals.

Recurrence intervals are calculated for hypothesized two [weight 0.8] and three [weight 0.2] post-MIS2 unconformity event scenarios. The constraining ages used to estimate the timing of the sequence of deposition and faulting are listed in Table 8.18.

**Table 8.18**. Constraining ages used to estimate the timing of the sequence of deposition and faulting.

| | | |
|---|---|---|
| a | 0.2 ka | Minimum initial settlement by non-Native Americans |
| b | 10 ka | Estimated maximum age for deposition of most of the upper loess unit (unit16, Figure 7.16 in Appendix E) above Glacier Peak G (GP G) tephra. The liquefaction feature as mapped by Sherrod et al. (In Review) appears to extend up into the Modern soil and thus post-dates deposition of unit 16. |
| c | 13.5 ka | Minimum limiting age of GP G tephra, which is dated at 13,710−13,410 cal yr BP (Kuehn 2009) (13774 to 13474 years before 2014) |
| d | 13.8 ka | Maximum limiting age of GP G tephra, which is dated at 13,710−13,410 cal yr BP (Kuehn 2009) (13774 to 13474 years before 2014) |
| e | 15.0 ka | Estimated maximum age of lower part of unit 13, which is interpreted to be a post-flooding loess by Sherrod et al. (In Review) or a cataclysmic flood deposit. This unit overlies the lower colluvium (unit 12). |
| f | 18.8 ka | Maximum limiting age of MIS 2 unconformity based on Th/U date of pedogenic carbonate formed in unit 11 (see discussion in Section 4.3.1.5 of Appendix E) prior to MIS 2 glacial outburst flooding event that formed unconformity. |
| | Three-Event Case | |
| Earthquake 1 occurs at a random time uniformly distributed between a and b. | | Assumes that the dike and sill d (as mapped by Sherrod et al. [In Review]) represent a post GP G seismically induced liquefaction event that was triggered by an earthquake on the RAW fault source. |
| Earthquake 2 occurs at a random time uniformly distributed between c and d. | | Assumes that unit 14 (upper colluvium interpreted to be a scarp-derived colluvium by Sherrod et al. [In Review]) was deposited concurrently or very shortly before GP G tephra. |
| Earthquake 3 occurs at a random time uniformly distributed between e and f. | | Assumes that unit 12 (lower colluvium) is a scarp-derived colluvium formed during a surface-rupturing event on the Faults F1/F2 (Sherrod et al. In Review) |
| | Two-Event Case | |
| Earthquake 1 occurs at a random time uniformly distributed between a and d. | | Assumes one event (either Earthquake 2 or 3 as described in the three-event case) |
| Earthquake 2 occurs at a random time uniformly distributed between e and f. | | Assumes that a surface-rupturing earthquake on Fault F2 occurred post-deposition of unit 12 and pre-deposition of units 13 and 14. |

### 8.4.3.8 Characteristic Magnitudes and Maximum Magnitudes

As discussed in detail in Section 8.4.3.9, the characteristic earthquake magnitude frequency distribution (Youngs and Coppersmith 1985; denoted as YC85) is adopted as being appropriate for use in defining the shape of earthquake recurrence curves for the fault sources. The YC85 model requires as input the slip rate and an estimate of the magnitude of the characteristic earthquake (Mchar). The functional form of the YC85 model expresses the magnitude range of the characteristic earthquake to be a 0.5 magnitude-wide uniform (boxcar) aleatory distribution centered on the mean Mchar for the fault of interest. The distribution is aleatory in the sense that all magnitudes within the distribution are expected

to occur and their relative frequency is the same. This means that the maximum magnitude, Mmax, in the YC85 model is 0.25 magnitude units larger than the mean Mchar. This section describes the assessment of Mchar for each of the fault sources and, by definition, Mmax is therefore also defined.

The assessment of characteristic earthquake magnitudes in paleoseismology typically involves consideration of the dimensions of rupture of paleo-earthquakes (e.g., rupture lengths, rupture areas, maximum and average displacement per event). In the case of the YFB faults, displacement per event paleoseismic data are not available, but data related to the possible lengths of past ruptures and the downdip widths of faulting are available. As discussed in Section 8.4.2, structural analysis of the topographic and geomorphic characteristics of the faults shows that they have a distinctive shape to the amplitude of cumulative structural relief along the strike of each fault. As shown in Figure 8.49 and discussed in that section, the ridge profiles show slip gradients that are very similar to the displacement profiles commonly associated with coseismic ruptures. Geologic studies have shown that repeated coseismic displacement distributions associated with characteristic earthquakes leads to long-term slip-rate profiles that have the same shape (e.g., Schwartz and Coppersmith 1984; Simoes et al. 2014). In addition to the ridge profiles, the geomorphic evidence for each YFB fault and fold shows distinctive patterns of deformation that are assessed to represent the surface evidence for faulting at depth. These regions of deformation are mapped as polygons (Figure 8.50) and their lateral extents conform to the patterns discerned from the ridge profiles. Based on this evidence as well as a variety of other indicators discussed in Section 8.4.2, the characteristic rupture lengths were assessed by the SSC TI Team for each fault source, as given in Table 8.8 and shown in Figure 8.51. It should be noted that the characteristic rupture lengths do not necessarily correspond exactly to the lengths of mapped sections along the fault, nor do they uniquely apply to any given section of the fault. Rather, the assessment of characteristic lengths was made in light of all possible segmentation points along the fault, the data quality, correspondence of multiple lines of evidence for particular segmentation points, etc. Further, the assessed characteristic lengths are judged by the TI Team to be applicable to the entire fault source and to have the potential to occur anywhere along its length. Therefore, ruptures in the hazard calculations are allowed to straddle segmentation points defined from structural relief evidence, but the seismic moment rates of each fault segment are held constant throughout the assumed occurrence of the full range of magnitudes and associated ruptures.

In addition to the characteristic rupture lengths, each fault is also defined by its average downdip width, which is a function of the assessed ranges of dip and seismogenic thickness. Therefore, a distribution of potential rupture lengths and rupture areas associated with characteristic earthquakes is available for each fault source. To develop estimates of Mchar, the important assessments are the selection of appropriate scaling relationships between magnitude and rupture length and rupture area, as well as the development of weights for the two alternative approaches.

The selection of magnitude to rupture length, and magnitude to rupture area scaling relationships was made in light of the tectonic environment of the YFB faults. The faults are dominantly reverse faults and characteristic lengths range from about 20 to 70 km. As reverse faults within a region that has seismogenic thickness up to 20 km, the downdip extent of rupture and associated rupture areas can be quite extensive for a given rupture length. As will be discussed in the context of Mmax, several worldwide historical reverse-faulting earthquake ruptures were reviewed by the TI Team to gain an understanding of the characteristics of such large ruptures from the standpoint of not only the dimensions of rupture, but also the nature of seismicity or segmentation evidence that might have been identified prior to the event.

After review of the literature, the TI Team concluded that the available scaling relationships relating moment magnitude to rupture length were limited. This is also the conclusion of other researchers who have attempted to compile, rate, and rank the existing relationships (e.g., Stirling et al. 2013) against a set of criteria. In all cases, the rating and ranking of relationships are subjective and the criteria applied by any given author are not necessarily the criteria that the TI Team would apply for application to PSHA. An additional point of importance for the Hanford PSHA is that sensitivity analyses showed that the selection of alternative rupture length/area relationships was not significant to the hazard results and not nearly as important to the uncertainty in the hazard as the uncertainty in the rupture dimensions themselves. In light of these issues, the TI Team selected two published scaling relationships relating rupture length to moment magnitude (Figure 8.90), which are both applicable to reverse and reverse-oblique faults:

Wells and Coppersmith (1994): WC94 [0.5]

**M** = 4.49 + 1.49 log L, where L is the rupture length at depth

N = 50, $\alpha$ = 0.26, magnitude range: 4.8 – 7.6, length range: 1 – 74 km

Wesnousky (2008): W08 [0.5]

**M** = 4.11 + 1.88 log L, where L is the rupture length

N = 6, $\alpha$ = 0.24, magnitude range: 5.8 – 7.6, length range: 4 – 72 km.

For both relationships, the number of earthquakes, N, is given, as are the magnitude range composing the data set, and the range of lengths in the data set. Note that the rupture length at depth (RLD) relationship from WC94 was selected based on the fact that the segment lengths and assessed characteristic lengths for the YFB faults are estimated without any direct knowledge of the surface rupture lengths of past earthquakes. The W08 relationship provides rupture lengths that are assessed based on a combination of geologic and seismologic (aftershocks) evidence. The two scaling relationships are assigned equal weights of [0.5].

A variety of rupture area versus magnitude scaling relationships have been proposed in the literature. An advantage is that the relationships generally show agreement within the magnitude ranges of interest for the Hanford PSHA. For example, Figure 8.91 plots the data compiled by Hanks and Bakun (2008), which are heavily dominated by plate boundary strike slip environments but include reverse and normal faulting as well. Also included are four scaling relationships, some of which were developed using slightly different data sets. With the exception of the Working Group on California Earthquake Probabilities (WGCEP) 2003 relationship, all of the relationships are essentially the same up to M~8 and rupture areas of about 10,000 $km^2$. Therefore, to avoid redundancy, only one of these relationships was selected for use in the SSC model—the one published by Hanks and Bakun (2008).

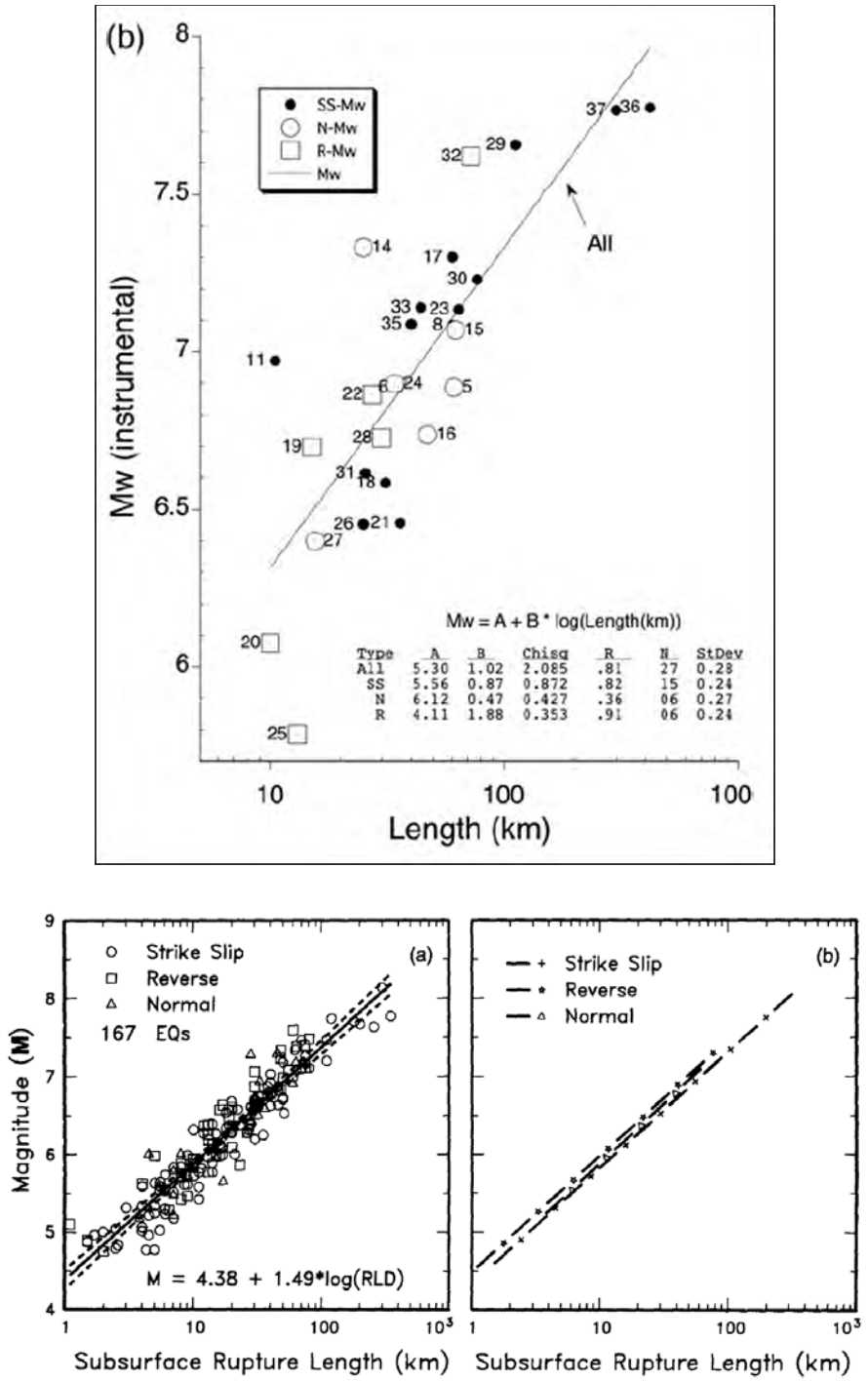


**Figure 8.90**. Scaling relationships between rupture length and moment magnitude. The upper panel is the relationship from Wesnousky 2008 and the lower panel is the relationship from Wells and Coppersmith 1994. In both cases, the relationship applicable to reverse faults was selected for use in estimating Mchar.

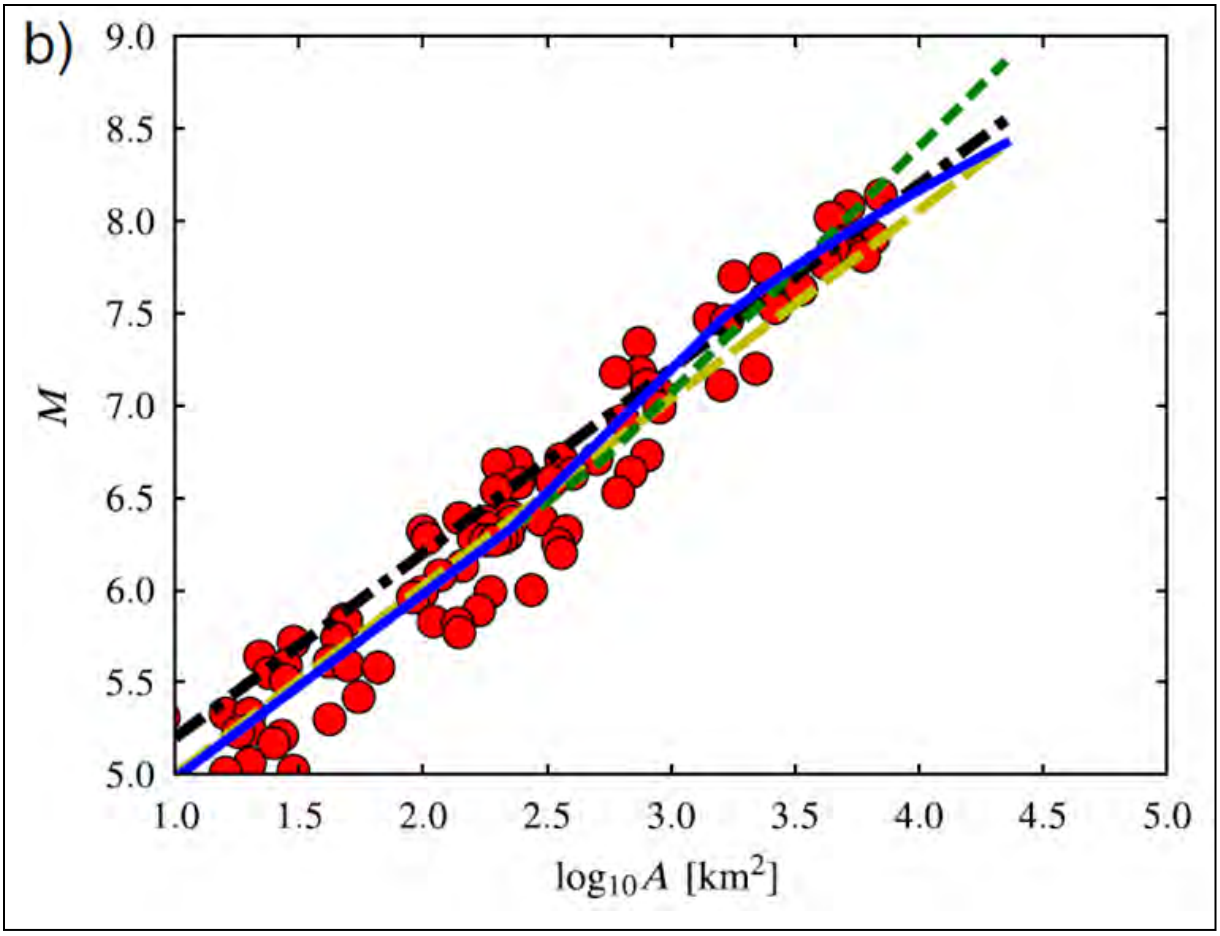


**Figure 8.91**. Scaling relationships between rupture area and moment magnitude (from Shaw 2013). Shown are the Hanks and Bakun 2008 database (red dots), relationships proposed by Wells and Coppersmith 1994 (yellow dashed line), Shaw 2009 (solid blue line), WGCEP 2003 (black dash-dot line), and Hanks and Bakun 2008 (short dash green line).

Given that the dominant style of faulting in the YFB region is reverse and reverse-oblique faulting, the TI Team considered a second rupture area scaling relationship developed specifically for use in reverse-faulting environments. Three alternatives were considered. The first was proposed by Yen and Ma (2011) as part of their study of static stress drops. Earthquakes in the data set are from Taiwan and include a variety of slip types including reverse faulting. Unfortunately, the rupture areas included are based on source inversions, rather than simple measurements of aftershocks, and this leads to considerable and unquantified uncertainties. A second relationship considered was proposed by Wu et al. (2013) based on earthquakes in Taiwan with fault types that were 53% thrust, 27% strike slip, and 20% normal. The conclusion was that the scaling was independent of fault type. Importantly, the magnitudes in the data set were derived from conversion of $M_L$ to $M_w$, rather than being based on instrumentally determined seismic moments. Likewise, the Taiwan region has very thick seismogenic crust (about 35 km) relative to most tectonic environments, including the YFB. Comparison of the Wu et al. relationship with other relationships shows much larger areas for a given magnitude, but these differences could be due to systematic differences in moment magnitudes because of the conversion used. In light of the uncertainties and possible systematic problems, both the Yen and Ma and the Wu et al. relationships were not selected for use in the SSC model.

A third area scaling relationship is the one proposed by Stirling et al. (2008). It is based on a suite of 28 New Zealand strike slip to reverse earthquakes on low slip-rate faults. The data were obtained from body-wave modeling studies of historical and contemporary earthquakes where fault mechanism, depth, source duration, and seismic moment were obtained and the magnitude range is Mw 5.6–7.8. In terms of application to the YFB, the authors recommend that "…the regression should be used for strike slip–to–convergent-dip-slip faults, not for major plate boundary faults. Performs well for strike slip to oblique slip faults other than the primary plate boundary faults (e.g., Alpine fault, San Andreas fault) and for strike slip to oblique slip faults in low seismicity regions, that is, larger magnitudes for given fault rupture lengths." Given these recommendations and the judged applicability to the YFB, the TI Team decided to include this rupture area scaling relationship.

The two rupture area scaling relationships selected for use in calculating characteristic magnitudes Mchar are as follows:

Hanks and Bakun (2008): HB08 [0.5]

**M** = log A + 3.98 (±0.03) for A≤ 537 $km^2$; and

**M** = 1.33 log A + 3:07 (±0.04) for A>537 $km^2$

N = 88, magnitude range: 5 – 8, area range: 10 – 10,000 $km^2$.

Stirling et al. (2008): S08 [0.5]

**M** = 4.18 + 2/3 log W + 4/3 log L (where L is rupture length, and W is width)

N = 28, magnitude range: 5.6 – 7.8, area range: 10 – 10,000 $km^2$.

Given the applicability of both of these scaling relationships to the YFB region, they were assigned equal weights of [0.5].

To incorporate the use of both the rupture length and rupture area scaling relationships, the relative weights between the two were also assessed. The rupture area relationships are assigned higher weight [0.7] than the rupture length relationships [0.3] for several reasons. Rupture area is an integral part of the definition of seismic moment and therefore believed to be a better indicator of moment magnitude. In a reverse-faulting environment, the downdip width of rupture may be considerable and—particularly for shallowly dipping faults and thick seismogenic crust—the entire rupture length might not be expressed at the surface. This could especially be true for moderate-magnitude earthquakes. Finally, the numbers of earthquakes in the rupture area relationships is significantly higher, thus leading to more confidence in their stability and general applicability.

Based on the assessed characteristic rupture lengths and the assessed downdip widths and associated rupture areas of each fault, Mchar distributions were developed using each of the four scaling relationships (Figure 8.92). Based on the relative weights assigned to the rupture length versus rupture area approach, as well as the weights assigned to each scaling relationship, a combined Mchar distribution was calculated, shown by the black histograms in Figure 8.81. Note that the typical uncertainty in Mchar spans a range of about 0.5 to 0.75 magnitude units.

As discussed previously in this section, the functional form of the YC85 magnitude frequency distribution, which was selected for the fault sources (Section 8.4.3.9.1), specifies that the Mmax is 0.25 magnitude units larger than Mchar. Given this definition, the distributions of Mmax for the various fault sources are summarized in Figure 8.93.

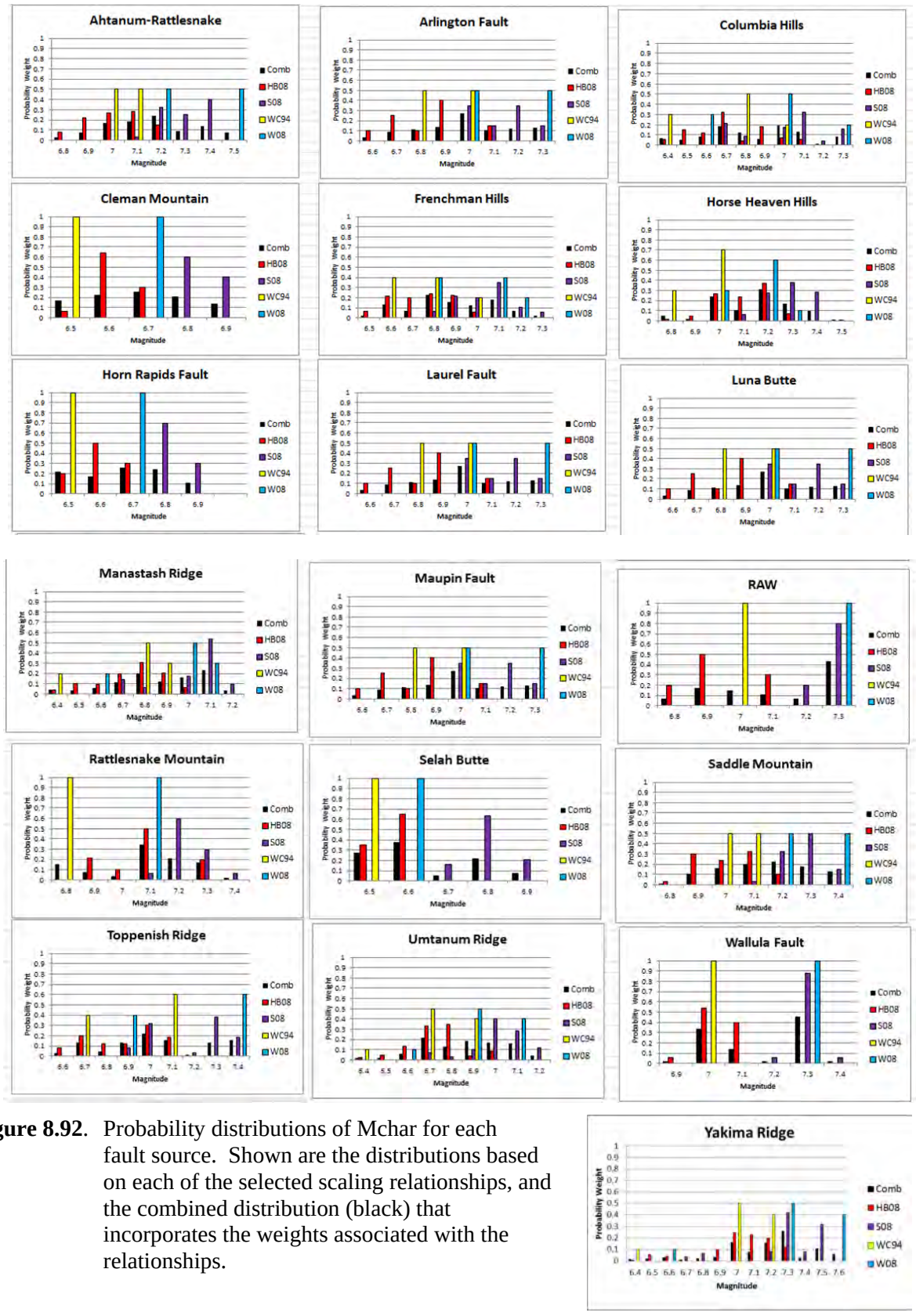


**Figure 8.92**. Probability distributions of Mchar for each fault source. Shown are the distributions based on each of the selected scaling relationships, and the combined distribution (black) that incorporates the weights associated with the relationships.

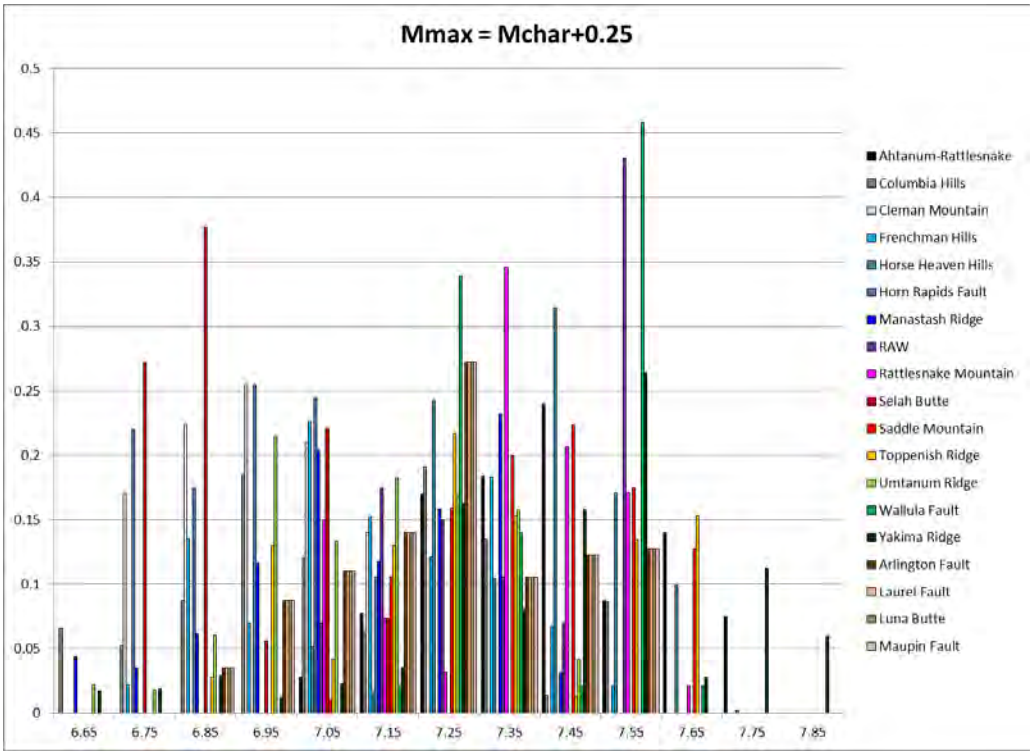


**Figure 8.93**. Probability distributions of Mmax for the fault sources.

As discussed in Section 8.4.3.9.2, the TI Team considered whether or not an alternative frequency magnitude distribution was appropriate that allowed for larger Mmax due to the linkages of multiple faults, as has been postulated for large strike slip faults in California. As discussed in that section, there is no technically defensible geologic evidence for such scenarios in the YFB, such scenarios are not observed for reverse fault systems based on historical evidence worldwide, and the Mmax distributions that are derived using the YC85 distribution already provide for reverse-faulting events that are about as large as have been observed in even the most active compressional systems. Therefore, the incorporation of such multiple fault linkages is not believed to be appropriate for the YFB fault sources.

### 8.4.3.9 Magnitude Frequency Distributions

Magnitude frequency distributions (MFDs) define the relative frequency of various earthquake magnitudes generated by a fault source. As such, they define the "shape" of the recurrence curve as it expresses the annual frequency of various magnitude earthquakes up to the maximum for a given fault source. Although it is a common observation that the appropriate MFD describing regional recurrence is an exponential distribution (Gutenberg and Richter 1956) that is truncated at the Mmax, the appropriate MFD for a fault source has been the subject of research for many years (e.g., Schwartz and Coppersmith 1984). As part of the evaluation process, the SSC TI Team considered four alternative MFDs for use in defining the recurrence for fault sources: a truncated exponential distribution, the maximum moment model (Wesnousky 1986), the characteristic earthquake distribution (Youngs and Coppersmith 1985), and the Wooddell, Abrahamson, Acevedo-Cabrera, Youngs (WAACY) model (Wooddell and Abrahamson 2013; WAACY 2014). The first three alternative models are shown in Figure 8.94 for a hypothetical fault using the same Mmax and seismic moment rate. The evaluation of these three models is discussed in Section 8.4.3.9.1. The evaluation of the WAACY model is discussed in Section 8.4.3.9.2. Given the

selection of the MFD for the fault sources, consideration is then given to non-Poissonian fault behavior (Section 8.4.3.10), and this is followed by the presentation of earthquake recurrence curves for each fault source (Section 8.4.3.11).

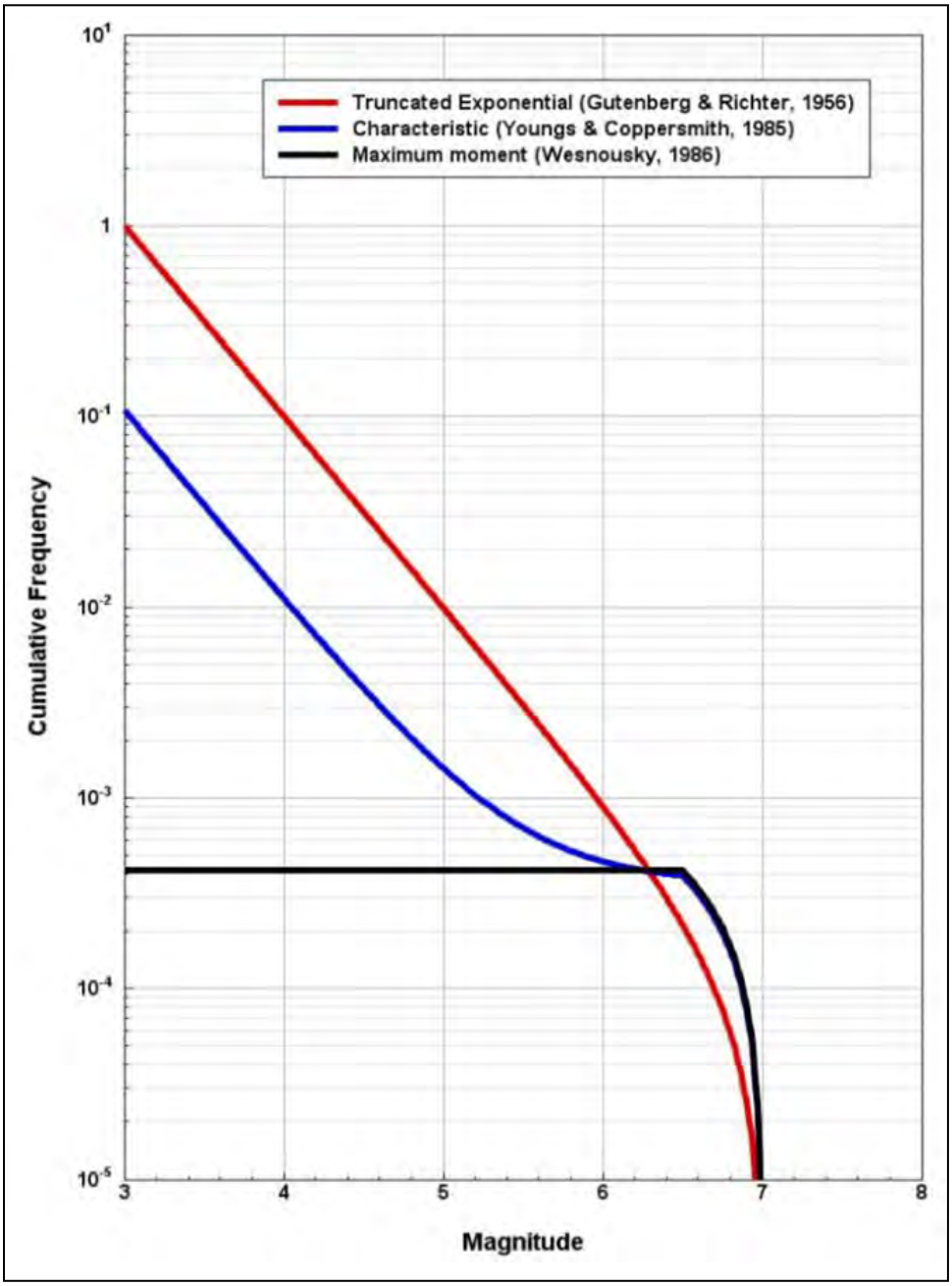


**Figure 8.94**. Alternative cumulative magnitude frequency distributions of earthquake recurrence for a given Mmax of 7 and for a constant seismic moment rate. (Modified from Youngs and Coppersmith 1985.)

#### 8.4.3.9.1 Exponential, Maximum Moment, and Characteristic Earthquake MFDs

Consistent with the SSHAC process, the TI Team evaluated the alternative MFDs that have been proposed for fault sources: a truncated exponential distribution, the maximum moment model, and the characteristic earthquake model (indicated by the notation YC85). This evaluation follows years of consideration of these models by other PSHAs for application in describing fault-specific recurrence. For example, the SSHAC Level 3 BC Hydro PSHA conducted a review of these alternatives and concluded that the exponential and maximum moment models (termed the "maximum magnitude" model in that study) should be assigned very low to zero weight. Similarly, the SSHAC Level 3 CEUS SSC project (NRC 2012a) concluded that the exponential model was not appropriate for fault sources or for repeated large-magnitude earthquake (RLME) sources based on comparisons with observed paleoseismic evidence and historical earthquake recurrence.

As can be seen in the simplified case given in Figure 8.94, the implications of the alternative MFDs can be discerned relative to the expected frequency of various magnitudes for a given slip rate. Such comparisons are useful in the case of the YFB fault sources because the slip-rate constraint is common for all fault sources. The exponential distribution shows a monotonic decrease (in logarithmic space) in the rate of earthquakes with increasing magnitude. In contrast, the maximum moment and YC85 models both show a characteristic earthquake whose frequency is somewhat higher than would be predicted from the exponential model. The maximum moment model does not provide for the occurrence of moderate or small-magnitude earthquakes smaller than the characteristic magnitude. In contrast, the YC85 model does provide for the exponential occurrence of these smaller earthquakes, but at a frequency that is lower than that given by the exponential model. From the standpoint of testing for these three models, two fundamental tests can be used for a given fault source. The first is the recurrence rate of characteristic earthquakes. If paleoseismic data are available regarding the size and rates of characteristic magnitudes, then that information can be compared with the implied rates of characteristic earthquakes coming from the three models to see which is most consistent. The second test is a comparison of the recurrence rates based on observed seismicity with the predicted rates from those three models in the small- to moderate-magnitude range. Such a comparison requires the identification of seismicity that occurs within a local zone near the fault to be meaningfully compared with a fault-specific recurrence model. Sampling over a larger region, say a zone within which the fault lies, could include sources other than the fault and thus would not provide a meaningful basis for comparison.

For the YFB faults, slip-rate data are available for all faults but paleoseismic information is only available for three of the faults (Section 8.4.3.7). Further, the data that are available are highly uncertain and relate only to the timing of surface-rupturing earthquakes and not to their magnitudes in a meaningful way. With respect to observed seismicity, the correlation of hypocenters with specific faults in the YFB region is difficult, as discussed in Sections 5.3 and 8.2.1.3. However, the high-quality earthquake hypocenter locations and the surface evidence for the downdip locations of the faults provided by the structural relief and topographic polygons (Section 8.4.3.2) provide a vehicle for identifying which earthquakes can be reasonably assigned to each fault. By doing so, the recurrence rates based on observed seismicity can then be compared with the recurrence rates that would be predicted from the three MFDs.

Shown in Figure 8.95 are the earthquake epicenters from the project catalog and the topographic polygons defined from the analysis of structural relief (Section 8.4.3.2). The interpretation of the structural relief is that the boundaries of these polygons define the limits of the region undergoing deformation associated with each fault. Hence, the boundary of the polygons defines the extent of the fault at depth projected to the surface. Earthquakes that occur within these polygons can then reasonably be assumed to be associated with the specific faults; the TI Team terms those regions the "capture areas" for seismicity. To account for the uncertainty represented by earthquakes lying near the capture area boundary, some boundaries were extended slightly to allow the nearby earthquakes to be included in the extended boundaries for purposes of this test. If anything, this would increase the numbers of earthquakes within each capture area and, as a result, increase the frequency of observed events.

The comparison of the rates of observed small-magnitude seismicity with the predicted recurrence based on a YC85 model and an exponential model is shown in Figure 8.96. The slip-rate and Mmax distributions are given based on the fault characterization. The results based on a maximum moment model are not shown but they would predict no earthquakes smaller than the characteristic magnitudes (the magnitudes where the cumulative recurrence curves are relatively flat). Also shown are the observed rates of small-magnitude earthquakes, as represented by the black and blue dots and the error bars that express the uncertainty in estimating a rate from the observed numbers of events within each magnitude bin. The black dots and bars are the rates derived for the capture areas and the blue dots and bars are for the extended capture areas. The mean recurrence curve based on an exponential MFD is shown by the brown line; the mean, 5th, and 95th percentile curves are shown for the YC85 model.

A number of observed earthquakes can be reasonably associated with each fault and the maximum moment model does not provide for these events. Therefore, the TI Team concluded that the model is not appropriate for the YFB faults and it was assigned zero weight. Consistently, for all faults, the exponential distribution overestimates the rate of observed seismicity. This observation has been made elsewhere and was one of the first reasons that the characteristic earthquake model was first proposed (e.g., Youngs and Coppersmith 1985; Youngs et al. 1992). For example, the same type of comparison is made in Figure 8.97 for several major faults in the San Francisco Bay Area between observed seismicity and predicted recurrence using slip rate with the YC85 model and the exponential model. Although the observed seismicity rates are considerably higher and therefore cover a larger range of magnitudes, the exponential model consistently overestimates the recurrence rates based on the observed seismicity record.

Based on the comparisons with observed seismicity, the exponential model was eliminated as an appropriate MFD for the YFB faults and the TI Team assigned the model zero weight.

In addition to the comparisons with observed seismicity, the YC85 model is also strongly supported by a recent examination of paleoseismic evidence by Hecker et al. (2013). A key element of the characteristic earthquake concept is the repeated occurrence of essentially the same size earthquake at particular points along a fault, as evidenced by observed multiple displacements in trenches along faults. Hecker et al. (2013) quantified the characteristic earthquake by exploring coefficient of variation (CV) values of surface rupture displacements. The data included 505 slip-at-a-point observations from 171 sites in 20 countries, and the average number of observations per site is about 3. Analysis of the variability of displacement amounts at individual sites in the empirical data showed a range of CVs of 0.40–0.55. The calculated CV for the YC85 model is 0.45–0.46, which is reasonably consistent with the empirical data. But the calculated CV for an exponential distribution, which would be expected to give

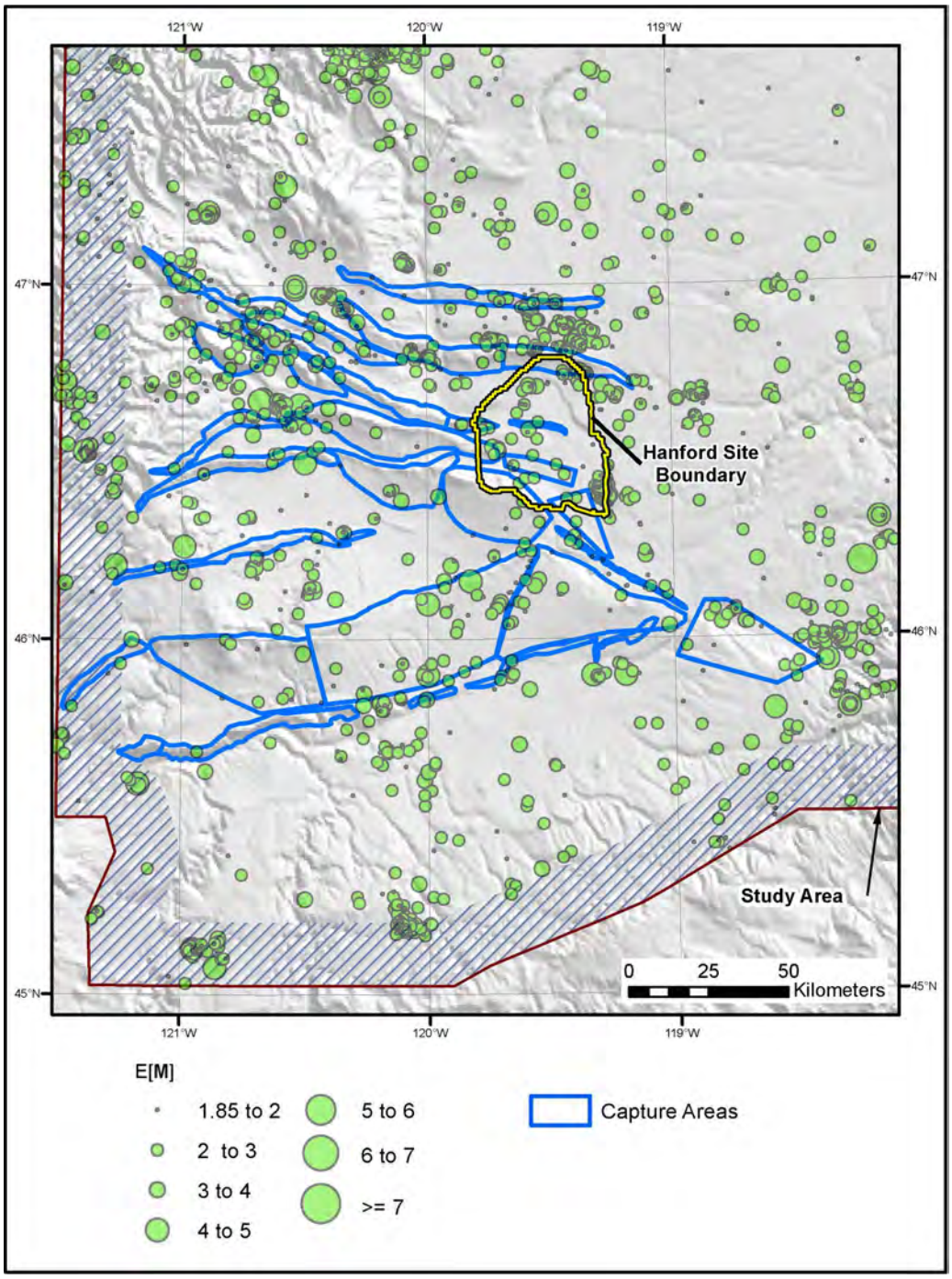


**Figure 8.95**. Map showing earthquake epicenters from project crustal catalog and topographic polygons defined from analysis of structural relief (Section 8.4.3.2). Boundaries to polygons define the regions within which the seismicity is postulated to be associated with the fault. Seismicity within these "capture areas" is used to assess earthquake recurrence rates.

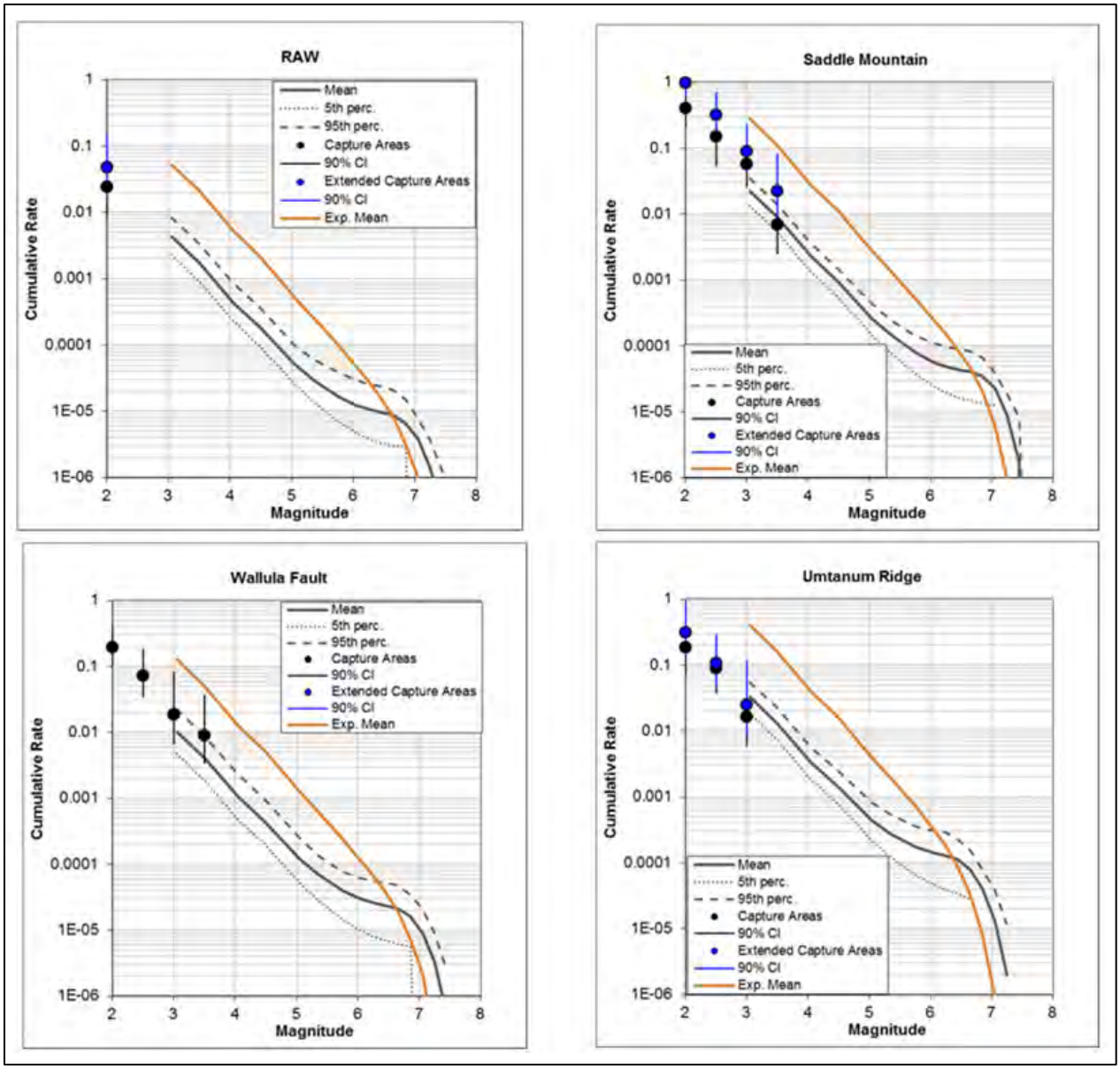


**Figure 8.96**. Comparison of the YC85 and exponential MFDs with observed seismicity rates for some fault sources in the YFB. Seismicity rates are based on observed counts of earthquakes lying within the seismicity capture areas and extended capture areas. The mean recurrence based on the exponential MFD is shown by the brown line and the mean, 5th, and 95th percentile recurrence curves are also shown for the YC85 model.

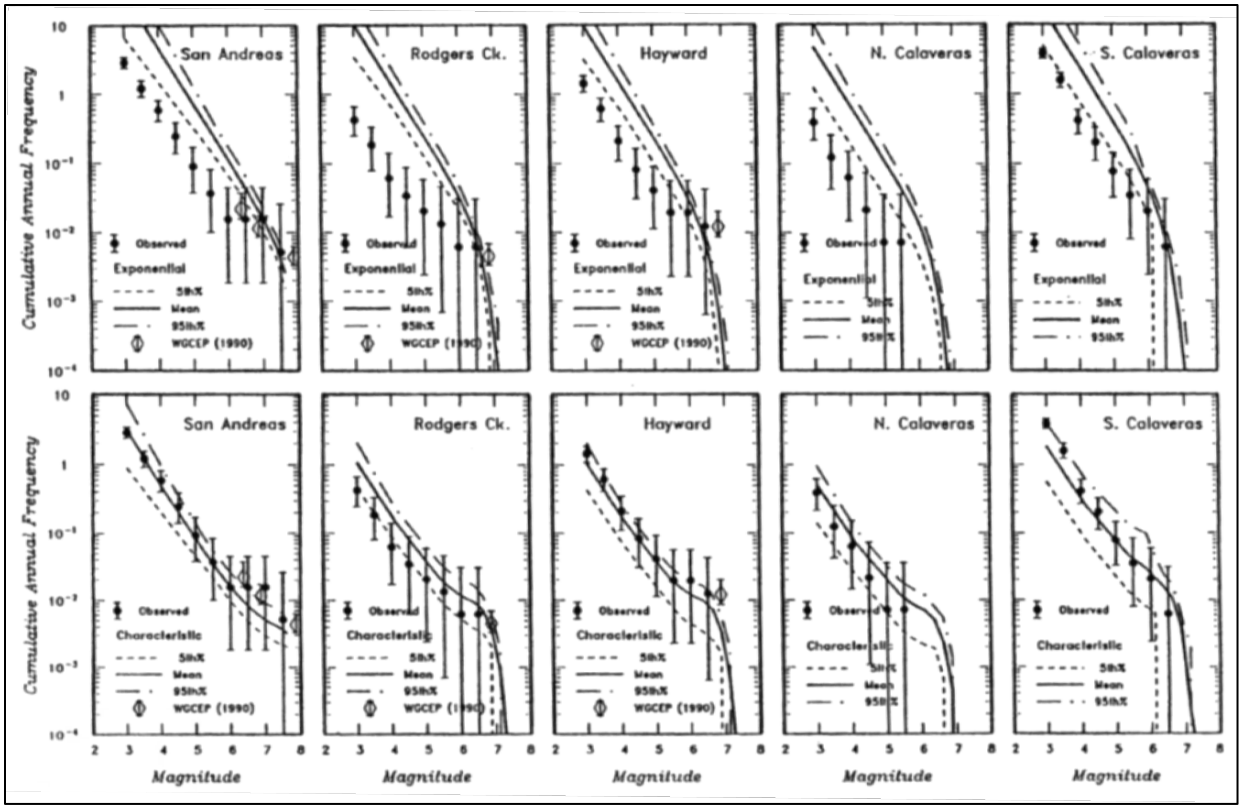


**Figure 8.97**. Comparison of observed seismicity rates (dots with error bars) with earthquake frequencies predicted from fault slip rate using the exponential model (top panels) and characteristic earthquake YC85 model (bottom panels) for individual fault sources (Youngs et al. 1992).

rise to a wider range of displacement events, is 0.66– 0.83. Hecker et al. conclude that the exponential distribution does not agree with fault-specific paleoseismic observations and that the YC85 model predicts a range of displacements that is reasonably consistent with the observations.

In light of the evaluations described above, the TI Team selected the YC85 model as an appropriate MFD for use in calculations of recurrence for YFB fault sources. The TI Team also considered an additional model that incorporates the YC85 shape but includes a larger Mmax "tail," as discussed in Section 8.4.3.9.2. Recurrence curves developed for all fault sources that incorporate the YC85 model as well as the concept of a renewal process (Section 8.4.3.10) are presented in Section 8.4.3.11.

### 8.4.3.9.2 WAACY Model

As discussed above, the characteristic earthquake (YC85) MFD specifies a Mchar "boxcar" distribution that is one-half magnitude unit wide, such that the Mmax is 0.25 magnitude units larger than Mchar. Such a Mmax distribution allows for multiple segments to rupture during an individual earthquake in a typical fault segmentation model. The consideration of interacting faults within the dominantly strike slip plate boundary regime of California has led to the consideration of possible multiple segment linkages in rare very large ruptures. It turn, these scenarios require specification of the relative frequency of each rupture scenario included in the hazard model and possible extension of Mmax

to account for such linkages. Wooddell and Abrahamson (2013) and Wooddell et al.[1] (2014) propose a generalized MFD that captures the characteristic magnitude behavior of the standard models while allowing for "rare, large magnitude, linked ruptures." The shape of the MDF is based on forward modeling of the coefficient of variation for slip at a point ($CV \leq 0.55$) that is consistent with the global data set of Hecker et al. (2013), but, at the same time, allows for rare, multi-fault ruptures. This is achieved by adding a tail to the YC85 base model to account for larger magnitudes due to multi-fault ruptures (Figure 8.98). Wooddell and Abrahamson (2013) explore the shape of the tail and a range of models is produced that do not violate constraints imposed by the observed CV values as well as the rates of the small- to moderate-magnitude earthquakes. Coupled with an assumption that the average slip over the full rupture is the same as the average slip on the segment closest to the study site, Wooddell et al. (2014) provide a simplification of the moment balance by only tallying the fraction of the moment released on the nearest segment; thus only the nearest fault segment to a site of interest requires full characterization. They also explore the hazard implications of this model and sensitivity to the selection of magnitude-displacement relationships, models for the probability of surface rupture, and other MFD model parameters.

The SSC TI Team considered the WAACY model as a possible alternative MFD for use with the fault sources. In particular, the WAACY model, which is identical to the YC85 model throughout the range of magnitudes including Mchar, could provide an alternative distribution to define Mmax if there were a need to include rare multi-fault linkages. Importantly, rupture scenarios would need to be envisioned that would entail the multi-fault linkages analogous to the strike slip plate boundary environment of California. Review of the geologic information regarding the paleoseismic history of individual ruptures, such as behavioral evidence for past ruptures, is lacking. As discussed in Section 8.4.3.8, there is virtually no evidence in the geologic record to assess the extent of past ruptures on faults of the YFB other than structural evidence related to differences in structural relief along strike and limited geomorphic data for faults like Toppenish Ridge and Ahtanum-Rattlesnake Hills that have experienced latest Pleistocene to Holocene surface ruptures. However, the TI Team considered whether tectonic models proposed for the region might require the use of a WAACY model to accommodate larger Mmax scenarios, such as those postulated in California.

As discussed in Section 4.1, the OWL has been recognized for decades as a crustal-scale feature with considerable length. As also discussed in that section, the OWL itself is composed of a series of individual structures. In turn, all of those faults in the YFB—including those that extend beyond the margins of what has been called the OWL—are included in the set of fault sources characterized in the SSC model. Further, as discussed in detail in Section 4.1, several lines of evidence preclude a "thin-skin" tectonic model, which might allow the presence of through-going structures in the deeper part of the crust that are not expressed at the surface. Therefore, by including and characterizing the faults that compose the OWL and assuming that all of those structures extend downdip throughout the seismogenic crust, there is no need to include some type of additional "OWL-type" feature as a seismic source.

[1] The acronym WAACY is used to designate the model using the initials of the co-authors.

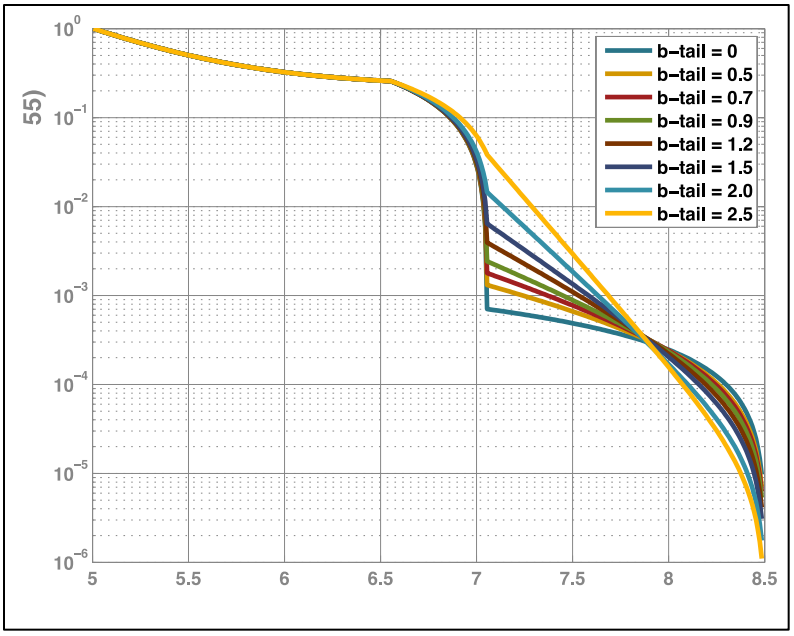


**Figure 8.98**. WAACY magnitude frequency distribution (Wooddell and Abrahamson 2013). The YC85 model is used with a Mchar of 6.75 and the upper tail is truncated at Mmax of 8.5. Alternative b-values for the tails are shown that are all consistent with a CV = 0.55.

Section 4.1 also summarizes a model proposed by Blakely et al. (2011) that draws an analogy between the OWL trend and a major strike slip fault, the Sakhalin Island fault, which extends from the forearc to the backarc region. Acknowledging that the scale of the OWL is significantly shorter than the Sakhalin Island fault, the analogy raises the issue of whether or not the OWL might likewise represent a large-scale strike slip fault that might need to be considered for inclusion as part of the application of a WAACY MFD. However, close examination of the Sakhalin Island fault and careful consideration of the seismologic and geologic evidence for the OWL indicate that the analogy between the two systems lacks technical support, as discussed further below.

The Sakhalin Island fault is part of a ~2,000-km-long fault system with numerous major strike slip faults. Faults of the system have been associated with abundant historical seismicity, including the 1995 $M_s$ 7.6 Neftegorsk earthquake. The fault displays abundant geomorphic evidence of Holocene activity, has slip rates of 1 to 4 mm/yr, and displays paleoseismic evidence of having generated multiple large-magnitude earthquakes (estimated as M 7.5 to 8) in Holocene time (e.g., Rogozhin and Rodina 2012). Recurrence intervals for M 7 earthquakes are estimated from a combination of historical and paleoseismic evidence at about 1,000 years (Rogozhin and Rodina 2012).

In comparison, the OWL shows questionable evidence of strike slip, only intermittent geomorphic evidence (often separated by tens of kilometers), and very questionable evidence for slip rates above the order 0.1 mm/yr. As discussed in Section 8.4.3.3 and Section 7 of Appendix E, the prevailing evidence based on studies of faults and folds within the YFB (which comprises most of the OWL) shows evidence of reverse faulting and, although there may be a component of oblique slip, there is no convincing evidence for through-going strike slip comparable to the Sakhalin Island fault system. Unlike the Sakhalin Island fault zone, there is no clear geomorphic evidence for a significant strike slip fault along the OWL in the YFB. Further, individual points cited by Blakely et al. (2011; 2013) for evidence of

strike slip are generally not supported by geologic observations. For example, as noted in Section 8.4.3.6.2, Rattlesnake Mountain is cited as showing geomorphic evidence of about 250 m of strike slip displacement. However, detailed Quaternary studies conclude that the postulated offsets are not supported and that there is very little if any evidence for lateral offset. Locally, at the location between Rattlesnake Mountain and Red Mountain (north end of the RAW fault), geologic relationships are able to preclude any significant lateral components of slip (Section 7.0 of Appendix E). Likewise, geologic and structural evidence compiled from geologic studies conducted over the past 30 years for the RAW and Wallula faults (Section 8.4.3.6; Section 7.0 of Appendix E) all conclude that the dominant component of slip is reverse. Likewise, regional studies of major structural elements that cross the OWL, such as the Hog Ranch-Naneum Ridge basement high, conclude that the OWL "crosses the north-south basement high but does not offset it, suggesting that any strike slip motion on the lineament preceded development of the north-south basement high" (Saltus 1993). Blakely et al. (2013) postulate that offsets of aeromagnetic anomalies associated with Ice Harbor dikes can be interpreted as representing slip rates as high as 0.8 mm/yr. Review of these postulated offsets by the TI Team leads to the conclusion that the smaller offsets of about 1 to 2 km are possible within the uncertainties of the data, but the postulated offset of 6.9 km is not technically supported.

Based on a review of all geologic, geomorphic, geophysical, and seismologic data, the TI Team concluded that the concept of a through-going strike slip fault comparable to the Sakhalin Island fault system extending from the Puget Sound area to the YFB region is not credible. Likewise, any implications of multi-fault linkages within a large strike slip zone are not applicable. Based on the fact that all of the reverse faults that compose the OWL are already part of the SSC model, no evidence exists that would require rupture scenarios entailing the rupture of multiple faults within the YFB. In the absence of local data, the TI Team considered documented reverse-faulting earthquakes as possible analogues.

The TI Team reviewed the information available for continental reverse-faulting ruptures associated with historical large-magnitude earthquakes worldwide (see Table 8.19) to examine the dimensions of rupture, rupture geometries, components of slip, pre- and post-main shock seismicity, etc. Part of the examination included consideration of whether extensive multi-fault linkages have been observed in association with the largest earthquakes. In general, it is difficult to determine whether the historical ruptures observed occurred along faults that had previously been considered as separate faults. In all cases, the larger ruptures occurred on faults that had been mapped previously and that showed clear evidence of Quaternary activity. In most cases, the large earthquakes in the historical record occurred on faults within very active compressional tectonic systems and with slip rates that are one to three orders of magnitude higher than the faults within the YFB. The largest historical reverse-faulting ruptures had rupture lengths of about 250 km, and most were less than 100 km. The list of historical large-magnitude historical ruptures is by no means exhaustive but it is believed to representative. It is possible that the historical record of worldwide reverse ruptures does not include "rare, multi-fault" ruptures that are intended to be represented in the WAACY model. However, in the judgment of the TI Team, it is more likely that the historical record is reasonably representative of the scales of ruptures that can be expected within even the most active reverse-faulting tectonic regimes.

**Table 8.19**. Historical reverse-faulting earthquakes reviewed for characteristics of rupture.

| Earthquake | Date | Moment Mag | Length | Dip | Primary References |
|---|---|---|---|---|---|
| Rikuu, Japan | 08/31/1896 | 7.2 | 37 | 45 | Matsuda et al. 1980 |
| Kebin Chon-Kemin, Kyrgyzstan | 01/03/1911 | 7.7 | 177 | 60 | Arrowsmith et al. 2005 |
| San Fernando, CA | 02/09/1971 | 6.7 | 15 | 45 | Allen et al. 1971; Wyss 1971; Allen et al. 1975; Langston 1978; Heaton 1982; Hanks 1974; Fuis et al. 2003; Tsutsumi and Yeats 1999; Hauksson et al. 1995; Rubin et al. 1998; USGS 1971; Kamb et al. 1971 |
| Cadoux, Australia | 06/02/1979 | 6.1 | 10 | 35 | Lewis et al. 1981; Fredrich et al. 1988 |
| El Asnam, Algeria | 10/10/1980 | 6.7 | 27 | 50 | Yielding et al. 1981; Swan 1988; Yielding et al. 1989; King and Yielding 1984 |
| Chi-Chi, Taiwan | 09/21/1999 | 7.4 | 100 | 70 | Lin et al. 2001; Zeng and Chen 2001; Shin and Teng 2001 |
| Kashmir, Pakistan | 10/04/2005 | 7.6 | 70 | 39 | Kaneda et al. 2008; Wesnousky 2008 |
| Wenchuan, China | 05/12/2008 | 7.9 | 240 | 50 | Xu et al. 2009, 2010; Yu et al. 2009, 2010; Qi et al. 2011 |

Because the WAACY model was developed to provide for the possible occurrence of "rare, multi-fault ruptures," which might be larger than those assessed to occur based on the YC85 model, the TI Team considered the rupture lengths, downdip widths, and magnitudes of those earthquakes that are assessed to occur on the fault sources given a YC85 model. Figure 8.99 shows the distributions for each fault source of Mchar and Mmax, which is 0.25 magnitude units larger than Mchar in the YC85 model. It should be noted that many of the faults have relatively shallow dips and, given the use of rupture area to estimate magnitude, the large downdip rupture widths lead to larger magnitudes. The distribution of Mchar for the faults shows considerable probability mass in the **M** 6.75 to 7.25 range, which is comparable to magnitudes of many of the historical earthquakes considered. The Mmax distribution has considerable probability mass in the range of magnitudes above **M** 7.5 up to nearly 8. These are comparable to the largest crustal reverse earthquakes in the historical record.

After consideration of the reverse-faulting analogues and the Mmax distributions that result from the application of the YC85 model to the fault sources of the YFB, the TI Team concluded that the distributions of Mmax were representative of the largest ruptures that could be reasonably supported for the reverse-faulting regime of the YFB. Unlike strike slip faults within an active plate boundary tectonic environment, there were no compelling reasons to ponder multi-fault linkages within the framework of a non-plate boundary compressional environment. In fact, even the high-activity compressional environments considered in the historical database did not appear to host such linkages.

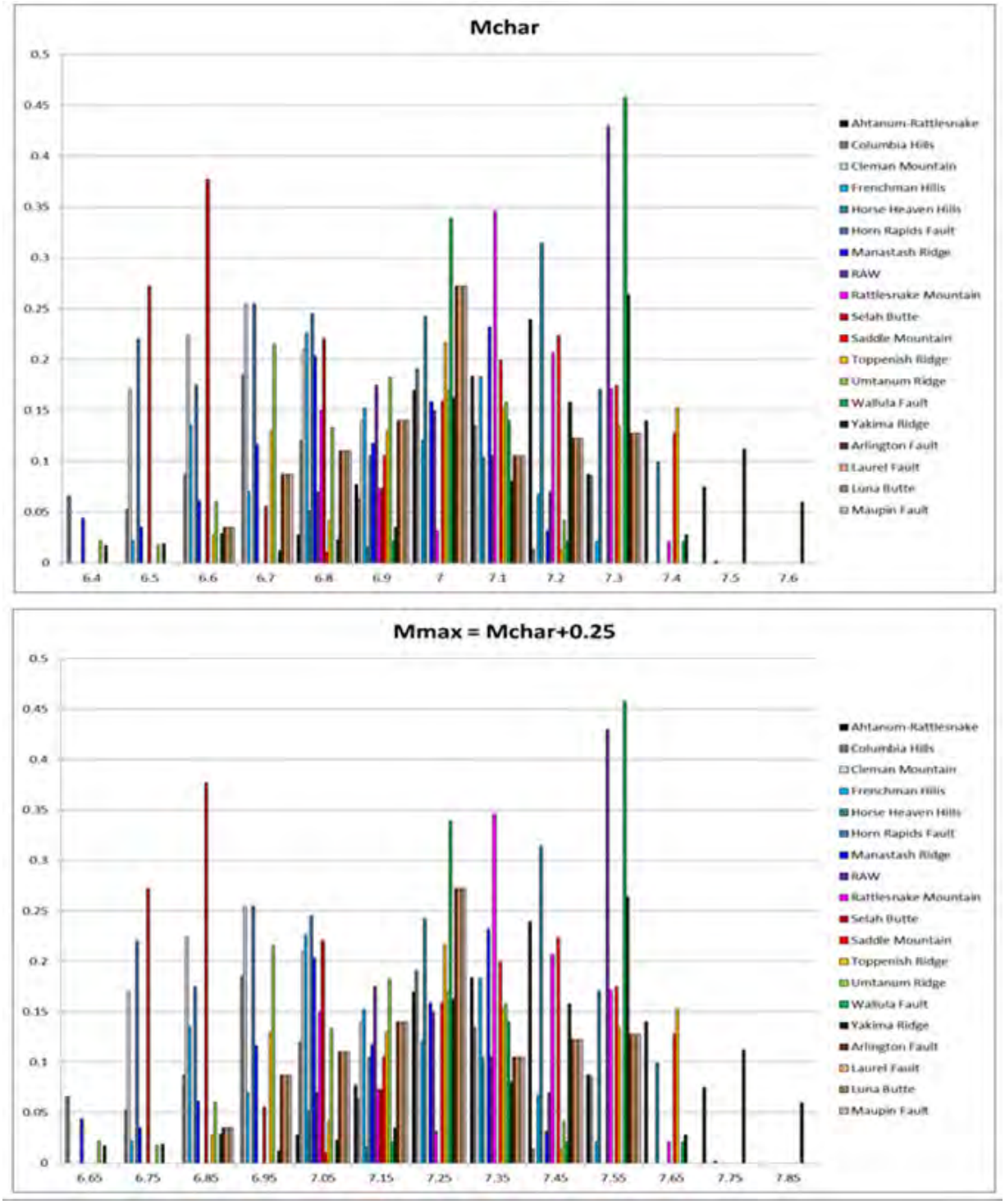


**Figure 8.99**. Histograms showing the Mchar and Mmax distributions for the fault sources in the SSC model.

The WAACY model is in development and has not yet seen common use in the PSHA community, nor has it been proposed for general usage in tectonic regimes that are unlike California. So, any implementation in the Hanford PSHA would require modification of the model components to be consistent with the tectonic regime of the Hanford region. For example, because the model is based on a

fault displacement hazard analysis at given sites along a fault of interest, key elements of the model are the relationships between average displacement and magnitude, the probability of detection of surface rupture, and the probability of surface rupture as a function of magnitude. All of these elements would need to be made compatible with the reverse-faulting regime of the YFB region. In addition, the current model as proposed provides no constraints on the b-value of the tail of the distribution or methods by which the b-value should be assessed.

After due consideration of the potential applicability of the WAACY MFD model to the fault sources in the SSC model and the need to have a different representation of the upper tail of the distribution, the TI Team concluded that the WAACY model was not needed to represent the full range of recurrence for the fault sources. Indeed, the WAACY model results would be identical to those from the YC85 model up to Mmax values that are believed to be reasonable for the YFB fault sources and in light of large historical crustal reverse-faulting earthquake ruptures. Therefore, the WAACY model was not included as an alternative MFD in the SSC model for fault sources.

#### 8.4.3.10 Renewal Processes and Recurrence Curves for Fault Sources

The Poisson assumption for the occurrence of earthquakes on a seismic source is the typical assumption used in PSHA. A Poisson process assumes that the occurrence of earthquakes is defined entirely by an average rate and that the rate is unchanged before or after the occurrence of earthquakes on a fault. In this sense, a Poisson process is "memoryless" with regard to the occurrence of earthquakes and is consistent with minimum information (maximum entropy) about when the next earthquake will occur. It is analogous to the assumption that the spatial distribution is uniform (equally likely) within a seismic source zone.

The Poisson distribution may not be consistent with the physics of earthquake generation on a fault source (e.g., elastic rebound) in which there is a quasi-steady buildup of stresses until the occurrence of an earthquake releases them and the process starts again. The Poisson process results in an exponential distribution for the time between earthquakes with a mode that is at zero. The physical process has often been modeled as a "renewal" process in which there is essentially steady-state loading and then earthquake unloading, such that, immediately after the occurrence of an earthquake, the probability of the next earthquake occurrence is essentially zero. The probability increases with time as the system is reloaded. In addition, the time interval between earthquakes is approximately periodic, with a uni-modal density function centered near the mean repeat time, rather than an exponential distribution. Hence, the issue is how to incorporate into PSHA the "knowledge" that the time between earthquakes is not exponentially distributed.

A renewal model that is currently favored for representing earthquake occurrences is the BPT model (Matthews et al. 2002). The BPT model has the desirable properties of zero hazard from the fault immediately after occurrence of an earthquake (neglecting aftershocks) followed by a buildup of probability with time to a maximum, then a decrease to a steady-state probability. These desirable properties are illustrated by the "hazard rate," which is the probability of occurrence in the next time increment given no occurrence in time $T_0/\mu_t$, where $\mu_t$ is the average time between earthquakes and $T_0$ is the time since the previous earthquake (Figure 8.100).

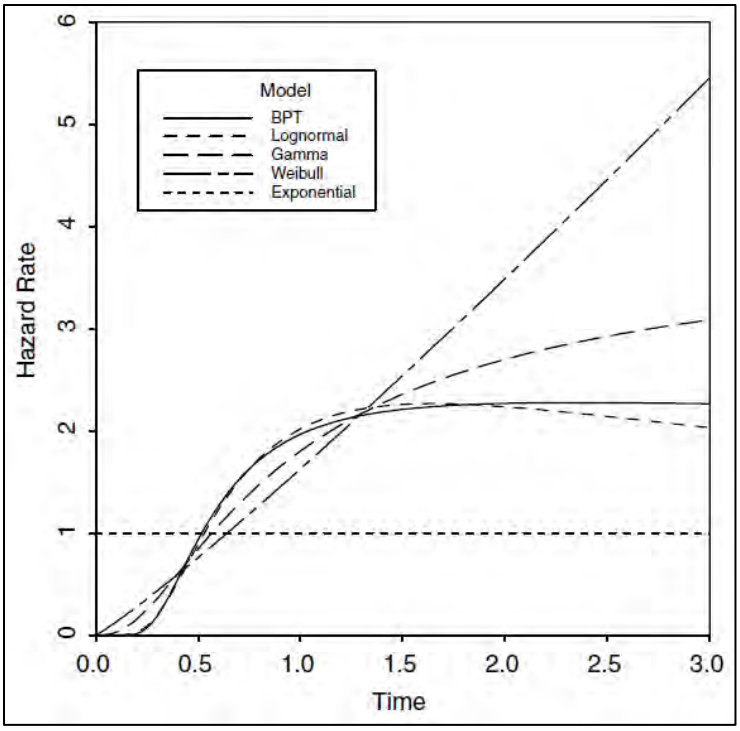


**Figure 8.100**. Hazard-rate functions for the BPT model and other recurrence distributions. The hazard rate is the probability of occurrence in the next time increment given no occurrence in time $T_0/\mu_t$, where $\mu_t$ is the average time between earthquakes and $T_0$ (labeled "Time") is the time elapsed since the previous earthquake. All distributions have mean 1 and standard deviation 0.5 (except the exponential distribution). A Poisson model is equivalent to the exponential model. (From Matthews et al. 2002)

An important consideration in a renewal model is the influence of the variability in the time between earthquakes. The CV in the time between earthquakes is defined by the parameter alpha, $\alpha$. The WGCEP (2003) suggests alpha values of 0.3, 0.5, or 0.7. As shown in Figure 8.101, the choice of alpha has a strong effect on the hazard rate.

Because of the importance of alpha, the TI Team considered the information that existed to estimate alpha. Most studies of alpha are for plate boundary faults that have high slip rates and relatively short recurrence intervals. The team considered those studies and concluded that, for the purposes of assessing alpha for the fault sources in the YFB, consideration should be given to the recurrence behavior of non-plate boundary faults. However, the data related to the timing of paleo-earthquakes on non-plate boundary faults is sparse and usually consists of no more than three to five events for any given fault. Therefore, the team decided that a collection of such faults should be used to assess a single distribution of alpha for use in the BPT model for YFB faults. Table 8.20 provides the event timing for non-plate boundary faults having at least three paleo-earthquakes (two intervals). Uncertainties in the age estimates are given by the respective authors of the studies and are incorporated into the analysis. Note that the long open intervals shown in brackets that precede the earliest dated events for some faults (e.g., >250 ka for Hyden) were not used in the analysis because of possible issues with completeness of the record or a departure from the current earthquake cycle (i.e., a period of quiescence).

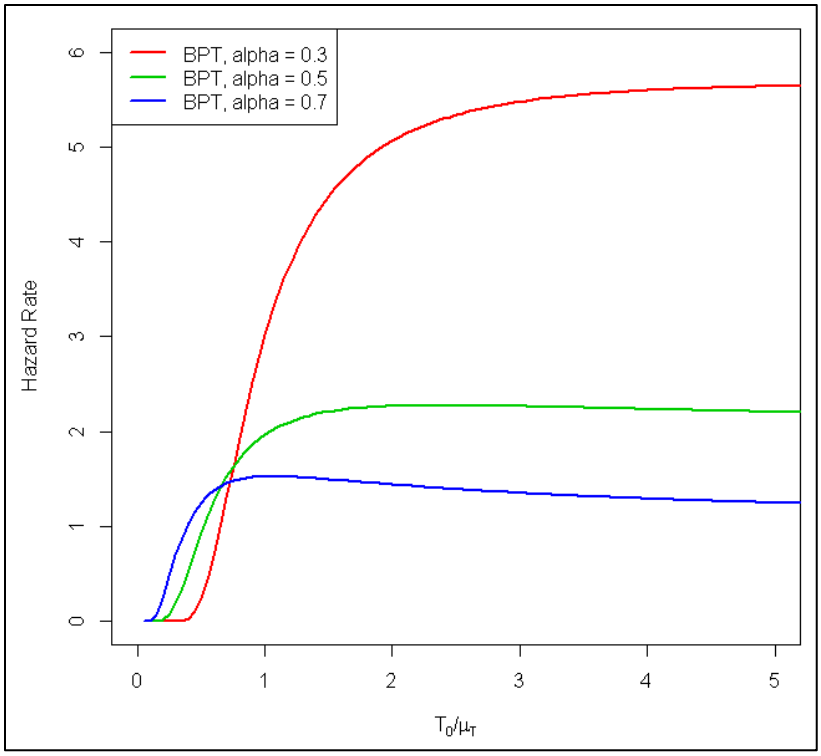


**Figure 8.101**. Influence of the alpha parameter on the hazard rate using the BPT model as a function of time $T_0/\mu_t$, where $\mu_t$ is the average time between earthquakes and $T_0$ is the time since the previous earthquake.

**Table 8.20**. Timing of paleo-earthquakes on non-plate boundary faults used in the analysis for alpha.

| Fault | Location | Event Timing (starting w/ MRE)[a] | Reference |
|---|---|---|---|
| Hyden | Australia | 30 ka<br>50–55 ka<br>90 ka<br>[>250 ka][b] | Crone et al. (2003)<br>Clark et al. 2011a |
| Lost River | Australia | 7 ka<br>15 ka<br>35 ka<br>[no event for > 1 Ma][b] | Estrada 2009[c] cited in<br>Clark et al. 2011a |
| Dumbleyung | Australia | 9 ka<br>16 ka<br>24 ka ??[d]<br>63 ka<br>[no event for > 1 Ma][b] | Estrada 2009 cited in<br>Clark et al. 2011a |
| Lake Edgar | Australia | 17 ka<br>25 ka<br>50 ka<br>[1–2 events in ~2 Ma][b] | Clark et al. 2011b cited in<br>Clark et al. 2011a |
| Cheraw | CO, USA | 8 ka<br>12 ka ??[d]<br>25 ka<br>[>100 ka][b] | Crone et al. 1997 |

**Table 8.20**. (contd)

| Fault | Location | Event Timing (starting w/ MRE)[(a)] | Reference |
|---|---|---|---|
| New Madrid | MO, USA | 1812 AD<br>1450 AD<br>900 AD<br>300 AD<br>2350 BC | (NUREG-2115, NRC 2012a) cited in Clark et al. 2011a |
| Toppenish Ridge | WA, USA | 505 ± 160 to 5,690 ± 390 yr BP??[(d)]<br>5,690 ± 390 yr BP to 7 ka<br>10–11 ka<br>40–60 ka<br>145–180 ka | Bentley et al. 1980; Campbell and Bentley 1981; Repasky and Campbell 1998 |
| Ahtanum Ridge | WA, USA | 12,570 ± 670 to 42,560 ± 2,010 yr<br>42,560 ± 2,010 to 91,460 ± 4,390 yr<br>91,460 ± 4,390 to 103,660 ± 5,430 yr | Repasky and Campbell 1998 |

(a) MRE is the most recent event; ranges shown should be considered uniform and are typically based on 2-sigma age-dating uncertainties.
(b) Long open interval not used in the analysis.
(c) Unpublished academic report. Available from Dan Clark, Geoscience Australia, Canberra.
(d) Questionable events are shown with "??". The analysis was run with and without these events.

Given the event timing and associated uncertainties, 1,000 possible catalogs of past earthquakes were simulated for each fault. The simulated catalogs were used to develop distributions for the coefficient of variation (COV) of time intervals between earthquakes. The resulting COV distributions are shown in Figure 8.102.

The COV results for individual faults indicate larger alpha values than have been used for plate boundary faults, such as those used in California by the WGCEP (2003). Based on the assumption that all faults in the data set represent a common alpha, the BPT model was fit to the simulated catalogs assuming different mean repeat times for each fault, but a common alpha. A distribution of alpha was developed from the relative likelihood of the fits to the simulated catalogs and that distribution is shown in Figure 8.103. In turn, the alpha distribution was represented by a five-point discrete distribution using Miller and Rice (1983), as shown in the figure.

In terms of the application to the Hanford PSHA, fault source recurrence is typically defined from the slip rate and the elapsed time, $T_0$, is unknown. In the general case for YFB fault sources, slip rate and the frequency magnitude distribution provide the average recurrence rate (i.e., the Poisson value). The BPT hazard rate provides the instantaneous frequency of earthquakes relative to the average rate and it varies with $T_0$ and alpha (Figure 8.104, upper panel). If $T_0$ is highly uncertain, an average over a wide range of $T_0$ can be used as a scale factor to apply to the Poisson rate to account for non-Poisson behavior, as shown in the lower panel of Figure 8.104. Based on the consideration of these temporal scale factors and the large uncertainties that exist in the elapsed times, a discrete distribution of "temporal model scale factors" was derived that serve as multipliers on the Poisson rate. These factors were used for all faults in the SSC model that lack information related to the timing of events. The temporal model scale factors are listed below:

1.55 [0.101]
1.3 [0.244]
1.1 [0.310]
0.9 [0.244]
0.75 [0.101].

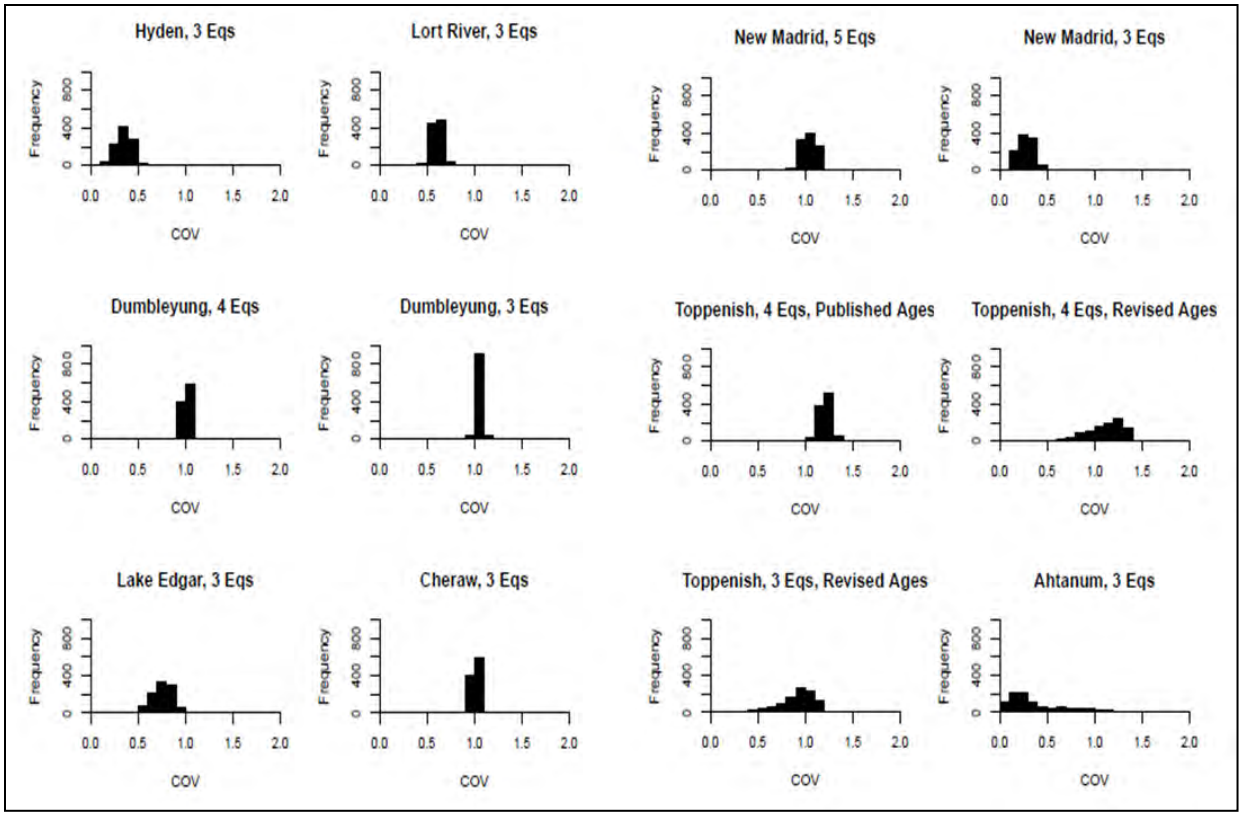


**Figure 8.102**. Probability density functions of the COV for each fault based on the event timing given in Table 8.18 and simulations of event catalogs.

The temporal model scale factors are applied only to the characteristic earthquakes in the YC85 recurrence model on the basis that these are the earthquakes that represent nearly all of the moment release on the fault and, therefore, are the earthquakes responding to the renewal process. The frequency of the smaller, exponentially distributed earthquakes is based on the average Poisson rate computed from the YC85 characteristic magnitude recurrence model.

Three fault segments in the SSC model have information related to the timing of earthquakes, and that can be used to assess recurrence intervals and elapsed time since the most recent earthquake. These segments have the necessary data required to directly apply the BPT model. The BPT model can be used to compute an equivalent Poisson rate applicable for the next 100 years (nominal period of interest) for inclusion in the hazard analysis. A question arises regarding how to combine the BPT recurrence on one segment with other segments on the same fault lacking recurrence interval data. That problem is addressed in the following way. It is assumed that the total earthquake rate on a fault is proportional to the sum of the slip rate for each segment times the segment area. The relative moment rate at any point along the fault is therefore determined by the product of the local slip rate and the local downdip fault width compared to the average for the entire fault. The relative frequency of earthquake ruptures of size **M** is determined by averaging the relative moment rate along the length of rupture at each possible rupture location. For the case where the earthquake recurrence is based on slip rate, this relative frequency approach is applied to earthquakes of all magnitudes. For the case where earthquake recurrence rate on one segment is based on the BPT model applied directly to recurrence interval data while the recurrence rate on adjacent segments is based on slip rate, the following process is used,

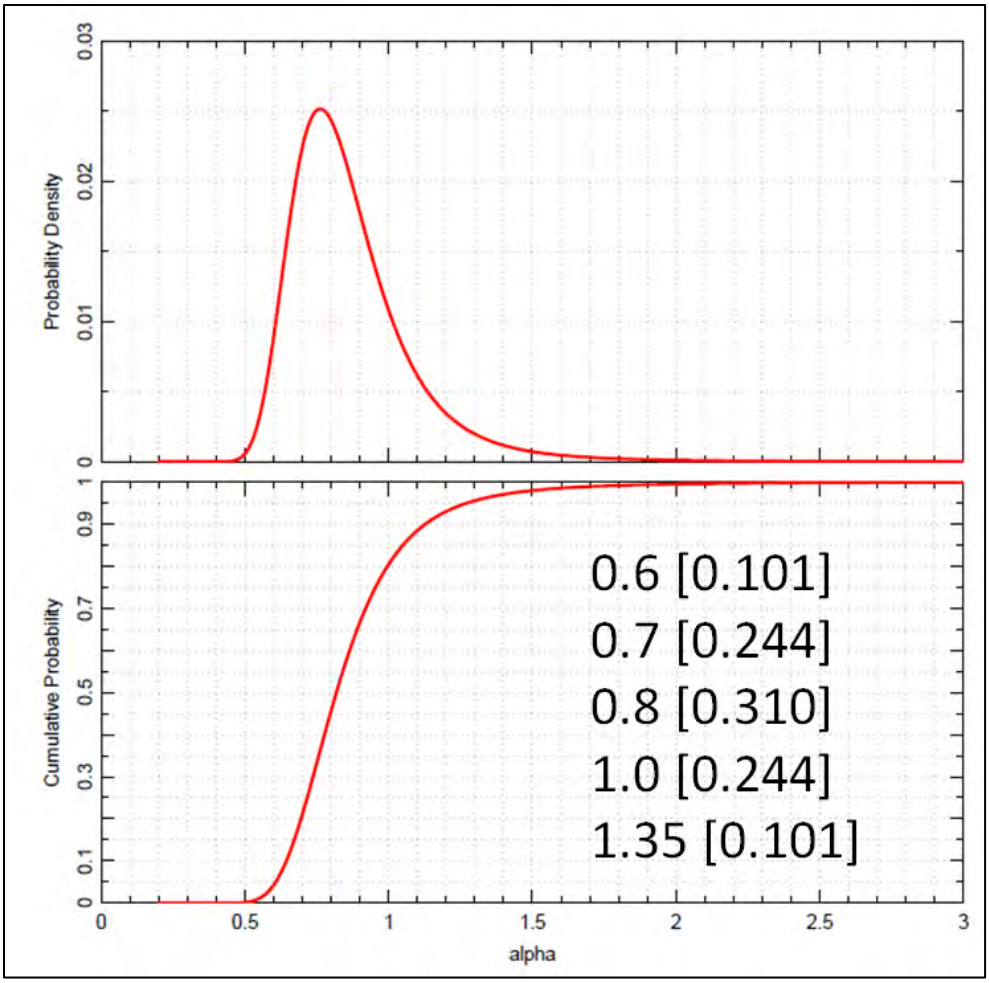


**Figure 8.103**. Distribution of alpha based on consideration of COVs from individual faults shown in Figure 8.102. Five-point discrete distribution is also shown.

illustrated using the Ahtanum-Rattlesnake Hills fault. The long-term average relative frequency of earthquake recurrence (relative moment release rate) on each segment is again obtained by the relative values of slip rate times segment area for each segment. The Poisson model is then fit to the recurrence interval data for the Ahtanum segment to obtain the long-term Poisson rate. The long-term Poisson rate for the Rattlesnake Hills segment is then obtained by multiplying the Ahtanum segment Poisson rate by the ratio of the relative moment release rate. The sum of these two values provides the long-term average Poisson rate for the fault as a whole. This rate is then fit using the Youngs and Coppersmith (1985) characteristic magnitude recurrence model to obtain the rates for the characteristic and exponentially distributed magnitudes. The rates for the exponentially distributed magnitudes are used directly and the relative frequency of these earthquakes along the fault is determined by the relative moment release rates, as described above. The frequency of characteristic earthquakes on the Rattlesnake Hills segment is obtained by multiplying the Poisson rate for this segment by the temporal scale factor, and the frequency of characteristic earthquakes in the Ahtanum segment is obtained directly from application of the BPT model. The total rate of characteristic earthquakes is then the sum of these two values. The relative frequency of the characteristic earthquakes along the length of the fault is now determined by the relative frequency of the characteristic earthquakes and will be different than that for the smaller, exponentially distributed earthquakes.

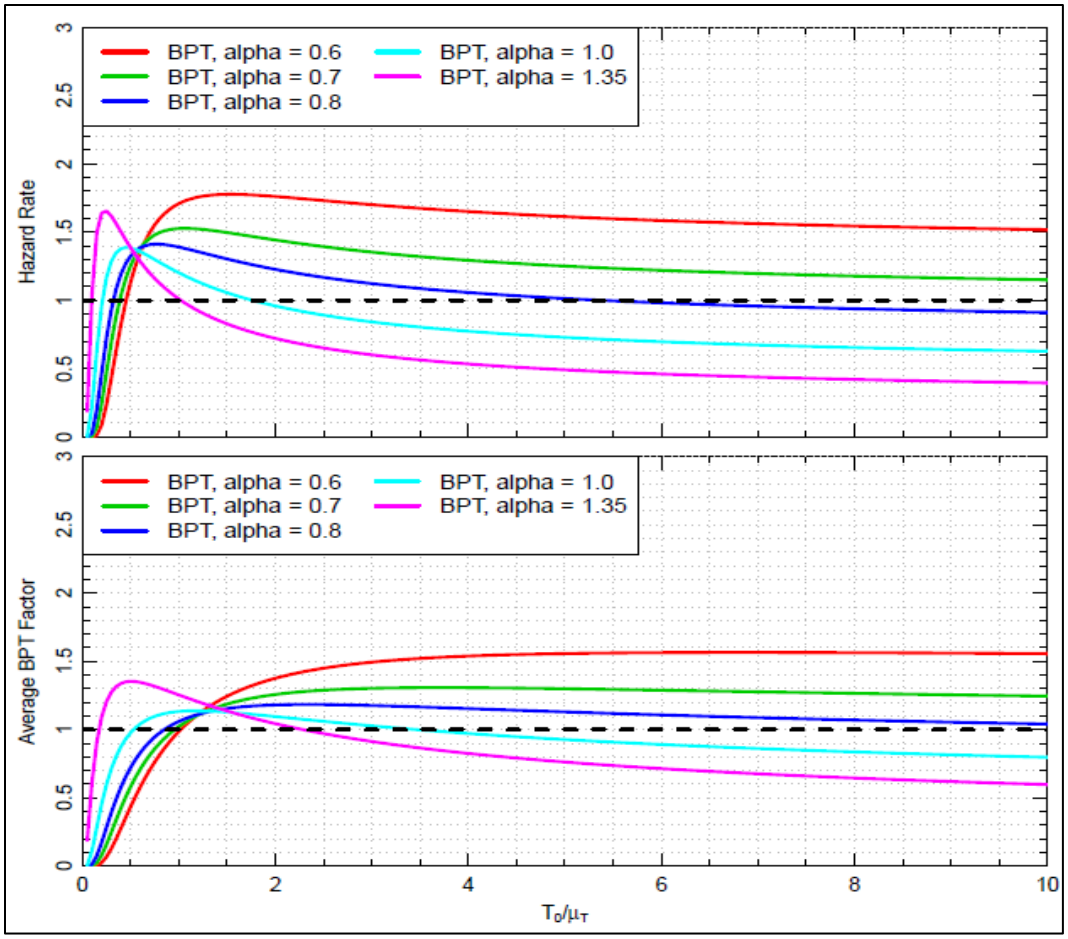


**Figure 8.104**. Variation in hazard rate for the BPT model as a function of alpha and elapsed time (expressed as $T_0/\mu_t$, where $\mu_t$ is the average time between earthquakes and $T_0$ is the time since the previous earthquake). The bottom panel shows the average temporal model scale factors for the BPT model, with the Poisson rate having a value of 1.0.

The average Poisson rates and BPT recurrence rates for the three fault segments were computed from the data described in Section 8.4.3.7. These data were used to simulate 1,000 earthquake catalogs for each segment. The simulated catalogs were then each used to obtain a Poisson recurrence rate, λ, and the BPT mean repeat time, μ, for each of the five values of α. The statistical uncertainty in λ and μ for each simulated catalog was computed using relative likelihoods. For the Poisson model, the estimated dates for the $N$+1 earthquakes provide $N$ values of the times between earthquakes, $t_i$, plus the open interval since the most recent earthquake, $t_0$. The Poisson process produces an exponential distribution for the time between occurrences:

$$f(t) = \lambda \exp\{-\lambda t\}$$

$$F(t) = 1 - \exp\{-\lambda t\} \qquad (8.3)$$

This leads to the likelihood function for the Poisson rate parameter of $\lambda_i$ given the observed data ($t_i$, $i$ = 1, $N$, $t_0$):

$$L(\lambda_i | t_i, t_0) = \prod_{i=1}^{N} f(t_i) \times [1 - F(t_0)] = \lambda_i^N \exp\left\{ -\lambda_i \times \left[ \sum_{i=1}^{N} t_i + t_0 \right] \right\} \tag{8.4}$$

The form of the likelihood function indicates that specification of the dates for the intermediate events is not needed because the term $\left[ \sum_{i=1}^{N} t_i + t_0 \right]$ is equal to the elapsed time since the oldest earthquake in the sequence.

For the BPT model, the time interval between earthquakes, *t*, is distributed and the probability density given by the following:

$$f(t) = \left( \frac{\mu}{2\pi\alpha^2 t^3} \right)^{1/2} \exp\left( -\frac{(t-\mu)^2}{2\mu_{In}\alpha^2 t} \right) \tag{8.5}$$

and cumulative probability given by

$$F(t) = \Phi[u_1(t)] + e^{2/\alpha^2} \Phi[-u_2(t)]$$

$$u_1(t) = \left( \sqrt{t/\mu} - \sqrt{\mu/t} \right) / \alpha$$

$$u_2(t) = \left( \sqrt{t/\mu} + \sqrt{\mu/t} \right) / \alpha \tag{8.6}$$

where $\mu$ is the mean inter-arrival time (repeat time), $\alpha$ is the aperiodicity coefficient, and $\Phi(\ )$ is the standard normal cumulative probability function. Given a sample of *N* time intervals and one open interval since the most recent earthquake, $t_0$, the likelihood function for the observed data set is given by

$$L(\mu, \alpha) = \prod_{i=1}^{N} f(t_i) \times [1 - F(t_0)] \tag{8.7}$$

with $f(t)$ and $F(t)$ given by Equations (8.5) and (8.6), respectively. The uncertainty distributions for the rate parameters of the Poisson and BPT models developed for each simulated catalog were then averaged over the 1,000 simulated catalogs to produce composite uncertainty distributions for λ and μ. The composite distributions were then represented by the Miller and Rice (1983) five-point discrete approximation described above. For the BPT model, the resulting values of μ are then used to compute an equivalent Poisson rate applicable as follows. The probability of an earthquake in the next time interval $\Delta t$ is given by the expression

$$P_{renewal}(\text{event in time } t_0 \text{ to } t_0 + \Delta t) = \frac{F(t_0 + \Delta t) - F(t_0)}{1 - F(t_0)} \tag{8.8}$$

The basic PSHA formulation used to assess the site hazard assumes that the occurrence of individual earthquakes conforms to a Poisson process. In order to combine the hazard from earthquakes defined by a renewal process into the total hazard, an equivalent Poisson rate is defined such that a Poisson process

will give a probability of at least one earthquake in time interval $\Delta t$ that is equal to the probability given by Equation (8.8). The equivalent Poisson rate, $\lambda_{renewal}$, is given by the following expression:

$$\lambda_{renewal} = -\ln\left[1 - P_{renewal}(\text{event in time } t_0 \text{ to } t_0 + \Delta t)\right] / \Delta t \tag{8.9}$$

A time period of 100 years was chosen as the time period of interest for application. The resulting distributions for Poisson and equivalent Poisson recurrence rates for the three fault segments are listed in Table 8.21.

**Table 8.21**. Distributions for Poisson recurrence rates and BPT equivalent Poisson recurrence rated for fault segments with recurrence interval data.

| | | BPT Equivalent Poisson Rate for α: | | | | |
|---|---|---|---|---|---|---|
| Weight | Poisson Rate | 0.6 | 0.7 | 0.8 | 1.0 | 1.35 |
| Ahtanum Ridge Segment | | | | | | |
| 0.101 | 7.300E-06 | 7.762E-08 | 1.259E-07 | 1.660E-07 | 2.138E-07 | 2.512E-07 |
| 0.244 | 1.630E-05 | 1.820E-06 | 2.399E-06 | 2.818E-06 | 3.162E-06 | 3.162E-06 |
| 0.310 | 2.750E-05 | 1.023E-05 | 1.148E-05 | 1.202E-05 | 1.202E-05 | 1.096E-05 |
| 0.244 | 4.320E-05 | 3.162E-05 | 3.020E-05 | 2.884E-05 | 2.570E-05 | 2.138E-05 |
| 0.101 | 7.010E-05 | 6.918E-05 | 6.026E-05 | 5.495E-05 | 4.677E-05 | 3.890E-05 |
| Toppenish Ridge – East Segment | | | | | | |
| 0.101 | 4.300E-06 | 1.000E-20 | 1.000E-20 | 1.000E-20 | 9.333E-17 | 4.677E-15 |
| 0.244 | 9.700E-06 | 1.000E-20 | 3.311E-16 | 2.692E-14 | 3.715E-12 | 1.202E-10 |
| 0.310 | 1.650E-05 | 4.786E-15 | 9.333E-13 | 2.884E-11 | 1.549E-09 | 3.090E-08 |
| 0.244 | 2.580E-05 | 1.514E-11 | 5.754E-10 | 6.457E-09 | 1.202E-07 | 1.230E-06 |
| 0.101 | 4.190E-05 | 2.512E-08 | 2.291E-07 | 9.120E-07 | 4.571E-06 | 1.862E-05 |
| RAW – Finley Quarry | | | | | | |
| 0.101 | 7.300E-06 | 7.762E-08 | 1.259E-07 | 1.660E-07 | 2.138E-07 | 2.512E-07 |
| 0.244 | 1.630E-05 | 1.820E-06 | 2.399E-06 | 2.818E-06 | 3.162E-06 | 3.162E-06 |
| 0.310 | 2.750E-05 | 1.023E-05 | 1.148E-05 | 1.202E-05 | 1.202E-05 | 1.096E-05 |
| 0.244 | 4.320E-05 | 3.162E-05 | 3.020E-05 | 2.884E-05 | 2.570E-05 | 2.138E-05 |
| 0.101 | 7.010E-05 | 6.918E-05 | 6.026E-05 | 5.495E-05 | 4.677E-05 | 3.890E-05 |

#### 8.4.3.11 Earthquake Recurrence Curves for Fault Sources

As discussed in Section 8.4.3, the logic trees for the fault sources include several elements leading to a distribution of net-slip rate based on long-term structural relief for each fault segment. Net-slip rate is combined with fault geometry and seismogenic thickness to arrive at a seismic moment rate for each fault segment, which is summed for all segments of the fault according to the relative lengths of each segment. This total moment rate for the fault source is then apportioned into earthquakes of various magnitudes according to a MFD. The YC85 distribution is selected for this purpose. Recurrence rates are calculated incorporating the renewal model process by multiplying all rates by the temporal model scale factors. The resulting recurrence curves for the fault sources are shown in Figure 8.105.

The recurrence curve for the Rattlesnake Mountain fault is based on the weighted combination of Quaternary and long-term slip rates. The curves based on each slip rate are shown in Figure 8.106. Three of the fault sources—the Ahtanum-Rattlesnake Hills, Toppenish Ridge, and RAW fault sources—have paleoseismic evidence of recurrence intervals. The recurrence curves for those faults based on recurrence intervals are shown in Figure 8.107.

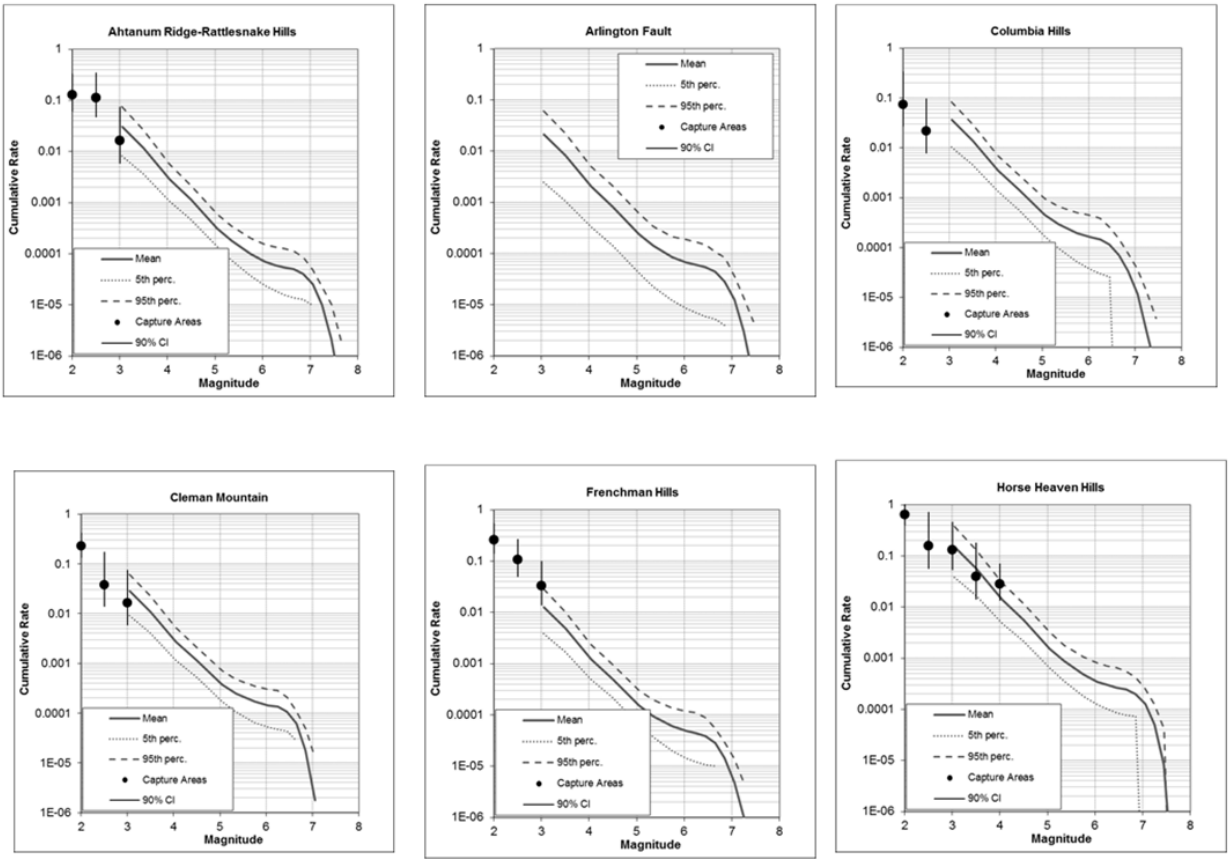


**Figure 8.105**. Earthquake recurrence curves for fault sources. Shown are the mean, 5th, and 95th percentile curves. Rates of observed seismicity are shown by the black dots and 90% confidence intervals (CIs).

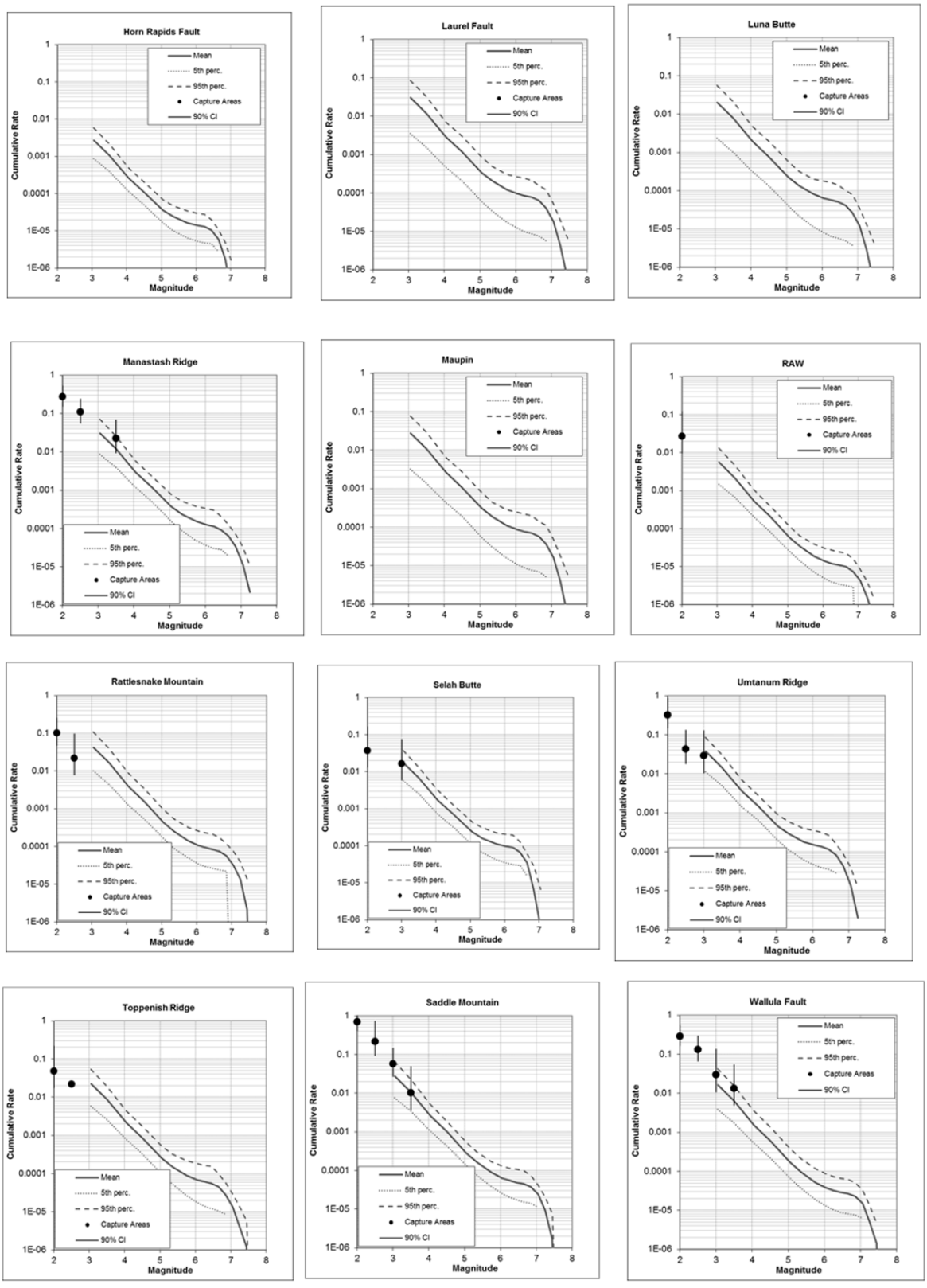


**Figure 8.105**. (contd)

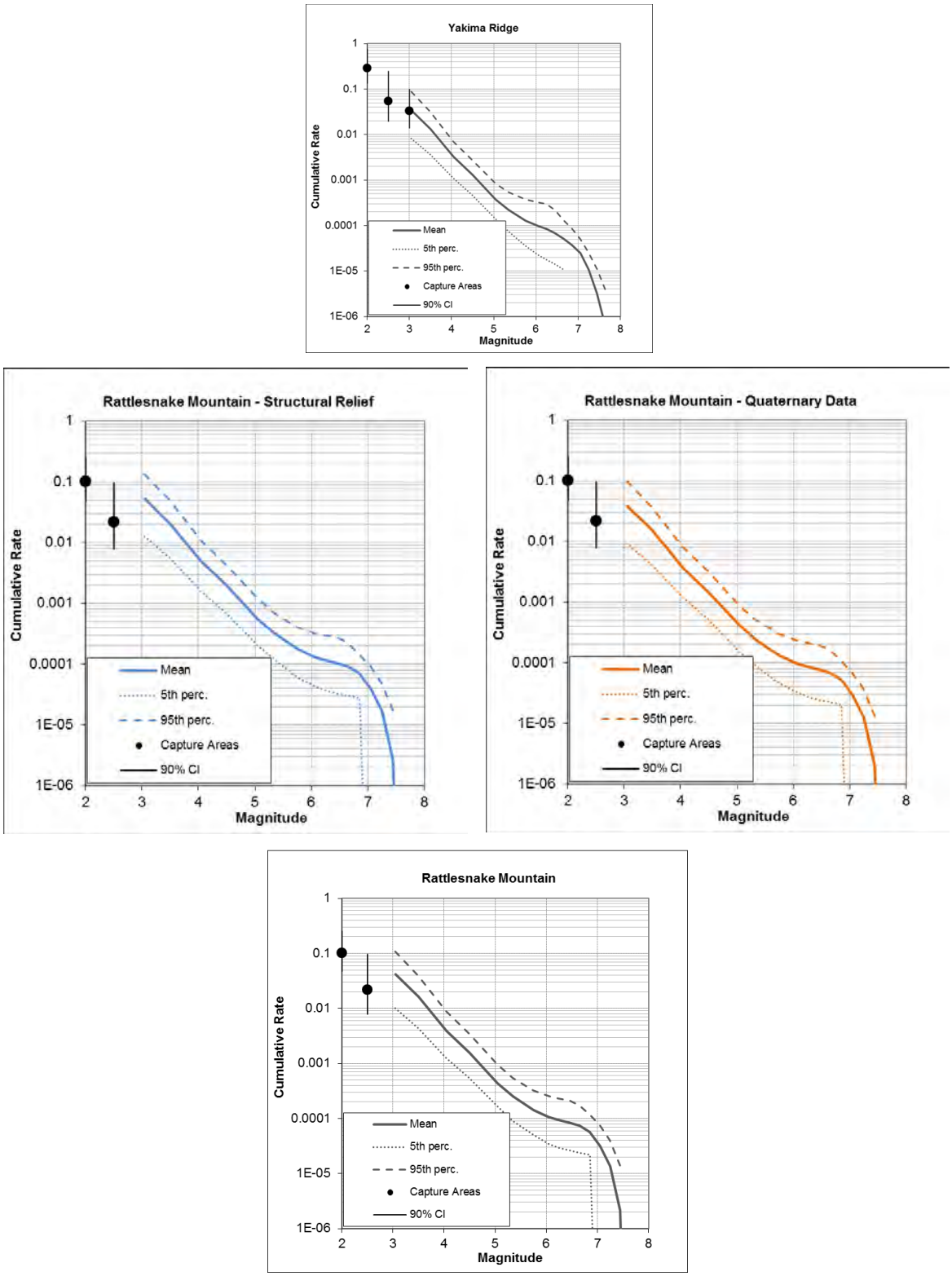


**Figure 8.106**. Earthquake recurrence curves for the Rattlesnake Mountain fault. Curves are shown based on long-term structural relief, Quaternary data, and the weighted combination of both data types.

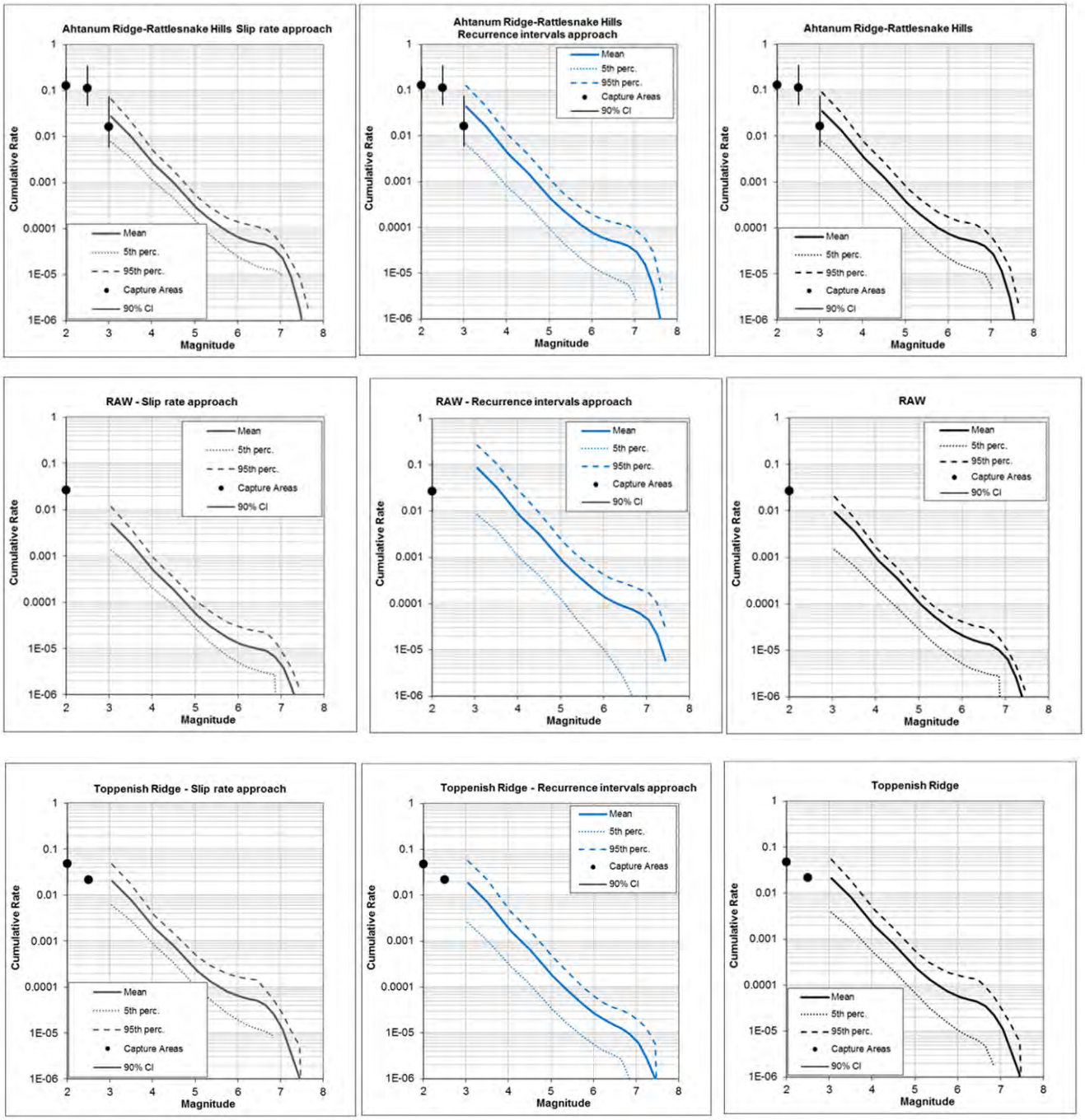


**Figure 8.107**. Earthquake recurrence curves for the faults having paleoseismic data related to recurrence intervals. Shown are the recurrence curves based on slip rate, recurrence intervals, and the weighted combination of both approaches.

## 8.5 References

Aki K and PG Richards. 1980. *Quantitative seismology: Theory and methods, 1*. WH Freeman and Co., New York.

Allen CR, GR Engen, TC Hanks, JM Nordquist, and WR Thatcher. 1971. Main shock and larger aftershocks of the San Fernando earthquake, February 9 through March 1, 1971, the San Fernando, California, earthquake of February 9, 1971. *U.S. Geological Survey Professional Paper* 733:17–20.

Allen CR, TC Hanks, and JH Whitcomb. 1975. Seismological studies of the San Fernando earthquake and their tectonic implications, San Fernando, California, earthquake of 9 February 1971. *California Division of Mines and Geology Bulletin* 196:257–262.

Anderson JL. 1987. The Structural Geology and Ages of Deformation of a Portion of the Southwest Columbia Plateau, Washington and Oregon. PhD Dissertation, University of Southern California, Los Angeles, California. (283 p., 7 pls., scale 1:24,000)

Anderson JL and TL Tolan. 1986. Ages of wrench faulting in interridge basins, southwest Columbia Plateau, Washington and Oregon. *Geological Society of America Abstracts with Programs* 18(2):82.

Anderson, JL, TL Tolan, and RE Wells. 2013. Strike-slip faults in the western Columbia River flood basalt province, Oregon and Washington. Pp. 325−347 in *The Columbia River Flood Basalt Province*, SP Reidel, VE Camp, ME Ross, JA Wolff, BS Martin, TL Tolan, and RE Wells (eds.), GSA Special Paper 497, Geological Society of America, Boulder, Colorado. DOI: 10.1130/2013.2497(13).

Armstrong RL, WH Taubeneck, and PO Hales. 1977. Rb-Sr and K-Ar geochronometry of Mesozoic granitic rocks and their Sr isotopic composition, Oregon, Washington, and Idaho. *Geological Society of America* 88:397−411.

Arrowsmith JR, CJ Crosby, CJ Korjenkov, AM Mamyrov, IE Povolotskaya. 2005. Surface rupture of the 1911 Kebin (Chon-Kemin) earthquake, Northern Tien Shan, Kyrgyzstan. Abstract T51F-05 (PowerPoint presentation), *American Geophysical Union Transactions* 86(52), Fall meeting supplement. Accessed August 25, 2011, at http://activetectonics.asu.edu/N_tien_shan/05AGU_kyrgyzstan_cjc.ppt.

Atwater T and J Stock. 1998. Pacific-North American plate tectonics of the Neogene southwestern United States – an update. *International Geology Reviews* 40:375−402.

Baker VR, BN Bjornstad, AJ Busacca, KR Fecht, EP Kiver, UL Moody, JG Rigby, DF Stradling, and AM Tallman. 1991. Quaternary Geology of the Columbia Plateau. In *Quaternary Nonglacial Geology: Conterminous U.S., The Geology of North America*, Volume K-2:215−250, RB Morrison (ed.). Geological Society of America, Boulder, Colorado.

Bakun WH, RA Haugerud, MG Hopper, and RS Ludwin. 2002. The December 1872 Washington State Earthquake. *Bulletin of the Seismological Society of America* 92(8):3239–3258.

Barnett DB, BN Bjornstad, KR Fecht, DC Lanigan, SP Reidel, and CF Rust. 2007. *Geology of the Waste Treatment Plant Boreholes.* PNNL-16407 Rev.1, Pacific Northwest National Laboratory, Richland Washington.

Barrash W, J Bond, and R Venkatakrishnan. 1983. Structural evolution of the Columbia Plateau in Washington and Oregon. *American Journal of Science* 283:897−935.

BC Hydro (BC Hydro Engineering). 2012. *Probabilistic Seismic Hazard Analysis (PSHA) Model. Volume 2: Seismic Source Characterization (SSC) Model*. Report No. E658, Vol. 2, WPR-3030, Vancouver, British Columbia.

Bentley RD. 1977. Stratigraphy of the Yakima basalts and structural evolution of the Yakima ridges in the western Columbia Plateau. In *Geological Excursions in the Pacific Northwest*, EH Brown and RC Ellis (eds.), pp. 339–390. Western Washington State University, Bellingham.

Bentley RD and JL Anderson. 1979. Right lateral strike-slip faults in the western Columbia Plateau, Washington (abstract). *EOS* 60(46):961.

Bentley RD, JL Anderson, NP Campbell, and DA Swanson. 1980. *Stratigraphy and Structure of the Yakima Indian Reservation, with Emphasis on the Columbia River Basalt Group.* U.S. Geological Survey (USGS) Open-File Report 80-200, U.S. Department of the Interior. Available at: http://pubs.er.usgs.gov/publication/ofr80200.

Biasi G, RJ Weldon II, and K Scharer. 2011. Rupture length and paleomagnitude estimates from point measurements of displacement—A model-based approach. In FA Audemard M, AM Michetti, and JP McCalpin (eds.), *Geological Criteria for Evaluating Seismicity Revisited: Forty Years of Paleoseismic Investigations and the Natural Record of Past Earthquakes.* Geological Society of America Special Paper 479:195–204. DOI: 10.1130/2011.2479(00).

Bjornstad BN, PD Thorne, BA Williams, GV Last, GS Thomas, MD Thompson, JL Ludwig, and DC Lanigan. 2010. *Hydrogeologic Model for the Gable Gap Area, Hanford Site*. PNNL-19702, Pacific Northwest National Laboratory, Richland, Washington.

Bjornstad BN, K Winsor, and SD Unwin. 2012. *A Summary of Fault Recurrence and Strain Rates in the Vicinity of the Hanford Site – Topical Report*. PNNL-17497, Pacific Northwest National Laboratory, Richland, Washington.

Blakely RJ, BL Sherrod, CS Weaver, RE Wells, and AC Rohay. 2013. The Wallula fault and tectonic framework of south-central Washington, as interpreted from magnetic and gravity anomalies. *Tectonophysics* 608:288−302. DOI: 10.1016/j.tecto.2013.11.006.

Blakely RJ, BL Sherrod, CS Weaver, RE Wells, AC Rohay, EA Barnett, and NE Knepprath. 2011. Connecting the Yakima fold and thrust belt to active faults in the Puget Lowland, Washington. *Journal of Geophysical Research: Solid Earth* 116: B07105. DOI: 10.1029/2010JB008091.

Burchfiel BC, DS Cowan, and GA Davis. 1992. Tectonic overview of the Cordilleran orogen in the western United States. In: *The Cordilleran Orogen: Conterminous U.S.* BC Burchfiel, PW Lipman, and ML Zoback (eds.), The Geology of North America, G-3:407-479. Geological Society of America, Boulder, Colorado.

Burns ER, DS Morgan, RS Peavler, and SC Kahle. 2011. Three-dimensional Model of the Geologic Framework for the Columbia Plateau Regional Aquifer System, Idaho, Oregon, and Washington. U.S. Geological Survey (USGS) Scientific Investigations Report 2010-5246, USGS, Tacoma, Washington.

Campbell NP and RD Bentley. 1981. Late Quaternary deformation of the Toppenish Ridge uplift in south-central Washington. *Geology* 9(11):519–524.

Campbell NP and T Repasky. 1998. *Earthquake Hazards in the Yakima Area – Results of the 1994 Through 1997 Studies.* Prepared by Newell P. Campbell, Consulting Geologist, Yakima, Washington, and Ted Repasky, Yakama Nation Water Program, Toppenish, Washington.

Catchings RD and WD Mooney. 1988. Crustal structure of the Columbia Plateau: evidence for continental rifting. *Journal of Geophysical Research* 93(B1):459−474.

Chiou BJ and RR Youngs. 2008. *An NGA model for the average horizontal component of peak ground motion and response spectra*. *Earthquake Spectra* 24(1):173−215.

Clark D, A McPherson, and DCN Collins. 2011a. *Australia's Seismogenic Neotectonic Record: A Case for Heterogeneous Intraplate Deformation*. Record 2011/11, Geoscience Australia, Canberra.

Clark DJ, M Cupper, M Sandiford, and K Kiernan. 2011b. Style and timing of late Quaternary faulting on the Lake Edgar Fault, southwest Tasmania, Australia: Implications for hazard assessment in intracratonic areas. Chapter 5 in *Geological Criteria for Evaluating Seismicity Revisited: Forty Years of Paleoseismic Investigations and the Natural Record of Past Earthquakes*, FA Audemard, AM Michetti, and JP McCalpin (eds.), GSA Special Publication 479, Geological Society of America, Boulder, Colorado.

Cornell CA and EH Van Marke. 1969. The major influences on seismic risk. *Proceedings of the Third World Conference on Earthquake Engineering*, Santiago, Chile A-1, 69−93.

Cozzens BD and GA Spinelli. 2012. A wider seismogenic zone at Cascadia due to fluid circulation in subducting oceanic crust. *Geology* 40(10):899–902.

Crone AJ, MN Machette, and JR Bowman. 1997. Episodic nature of earthquake activity in stable continental regions revealed by paleoseismicity studies of Australian and North American Quaternary faults. *Australian Journal of Earth Sciences* 44:203−214.

Crone AJ, PM De Martini, MN Machette, K Okumura, and JR Prescott. 2003. Paleoseismicity of Two Historically Quiescent Faults in Australia: Implications for Fault Behavior in Stable Continental Regions. *Bulletin of the Seismological Society of America* 93:1913−1934.

Das S and CH Scholz. 1983. Why large earthquakes do not nucleate at shallow depths. *Nature* 305:621−623.

Erickson L. 1987. *User's Manual for DIS3D: A Three-Dimensional Dislocation Program with Applications to Faulting in the Earth*. Geomechanics, Applied Earth Science Department, Stanford University, Stanford, California.

Energy Northwest. 1998. Appendix 2.5N, Late Cenozoic tectonics of the Pacific Northwest with special reference to the Columbia Plateau; in Section 2.5, Geology, Seismology and Geotechnical Engineering of the *Columbia Generating Station Final Safety Analysis Report*, Richland, Washington.

Estrada B. 2009. Neotectonic and paleoseismological studies in the southwest of Western Australia. The University of Western Australia, Perth (Unpublished).

Fagereng Å and VG Toy. 2011. *Geology of the earthquake source: an introduction*. Geological Society, London, Special Publications 2011, 359:1−16.

Farooqui SM and RE Thoms. 1980. *Geologic Evaluation of Selected Faults and Lineaments Pasco and Walla Walla Basins – Washington*. Shannon & Wilson, Inc., Lake Oswego, Oregon.

Faulds JE and CD Henry. 2008. Tectonic influences on the spatial and temporal evolution of the Walker Lane: an incipient transform fault along the evolving Pacific-North American plate boundary. *Arizona Geological Society Digest* 22:437−470.

Fecht KR, SP Reidel, and MA Chamness. 1992. Contour Map of the Top of the Basalt of the Hanford Site. Scale 1:62500. Washington State University Open-File Map 2014-1. (Contact Steve Reidel at Washington State University to obtain a copy.)

Fredrich J, R McCaffrey, and D Denham. 1988. Source parameters of seven large Australian earthquakes determined by body waveform inversion. *Geophysical Journal of the Royal Astronomical Society* 95:1–13.

Fuis GS and LA Wald. 2003. Rupture in south-central Alaska—the Denali fault earthquake of 2002. *U.S. Geological Survey Fact Sheet* 014-03 (March), 4 pp. Available at: http://pubs.usgs.gov/fs/2003/fs014-03/.

Gardner JN, MG Snow, and KR Fecht. 1981. *Geology of the Wallula Gap Area, Washington*. RHO-BWI-LD-9, Rockwell International, Rockwell Hanford Operations, Richland, Washington.

Geomatrix. 1988. *Seismotectonic Evaluation of the Northern Cascade Mounts Geomorphic Province for Bumping Lake, Tieton, Keechelus, Kachess, Cle Elum, and Clear Creek Dams*. Geomatrix Consultants, Inc., Oakland, California.

Geomatrix. 1990. *Seismotectonic Evaluation, Walla Walla Section of the Columbia Plateau Geomorphic Province*. Geomatrix Consultants, Inc., Oakland, California.

Geomatrix. 1995. *Seismic Design Mapping, State of Oregon*. Final Report prepared for the Oregon Department of Transportation, Salem, Oregon, under Personal Services Contract 11688, 5 plates, scale 1:1,250,000. Geomatrix Consultants, Inc., San Francisco, California.

Geomatrix. 1996. *Probabilistic Seismic Hazard Analysis – DOE Hanford Site, Washington*. Report prepared for WHC-SD-W236A-TI-002, Rev. 1, Westinghouse Hanford Company, Richland, Washington.

Gustafson EP. 2011. "Overview of paleontological resources within the Hanford Reach National Monument." In: *Hanford Reach National Monument Final Comprehensive Conservation Plan and Environmental Impact Statement Adams, Benton, Grant, and Franklin Counties, Washington.* U.S. Fish and Wildlife Service, Burbank, Washington.

Gutenberg B and C Richter. 1949. *Seismicity of the Earth and Associated Phenomenon*. Princeton University Press, Princeton, New Jersey.

Hanks TC. 1974. The Faulting Mechanism of the San Fernando Earthquake. *Journal of Geophysical Research* 79(8)1215−1229.

Hanks TC and WH Bakun. 2008. M − log A observations of recent large earthquakes. *Bulletin of the Seismological Society of America* 98(1):490–494.

Hauksson E, LM Jones, and K Hutton. 1995. The 1994 Northridge earthquake sequence in California: Seismological and tectonic aspects. *Journal of Geophysical Research: Solid Earth* (1978–2012), 100(B7):12335−12355.

Hauksson E, W Yang, and PM Shearer. 2012. Elucidating regional tectonic and secondary causes of seismicity in southern California: Application of waveform relocated seismicity and high precision focal mechanisms and other geophysical data sets (Abstract). *Seismological Research Letters* 83:364.

Heaton TH. 1982. The 1971 San Fernando earthquake: a double event? *Bulletin of the Seismological Society of America*. 72:2037–2062.

Hecker S, NA Abrahamson, and KE Wooddell. 2013. *Variability of Displacement at a Point: Implications for Earthquake-Size Distribution and Rupture Hazard on Faults*. *Bulletin of the Seismological Society of America* 103(2A):651−674.

Hyndman RD. 2013. Downdip landward limit of Cascadia great earthquake rupture. *Journal of Geophysical Research: Solid Earth* 118:5530–5549.

Jarchow CM, RD Catchings, and WJ Lutter. 1994. Large-explosive source, wide-recording aperture, seismic profiling on the Columbia Plateau, Washington. *Geophysics* 59(2):259–271.

JBA (Jack Benjamin & Associates), URS Corporation Seismic Hazards Group, Geomatrix Consultants, Inc., and Shannon & Wilson. 2012. *Probabilistic Seismic Hazard Analyses Project for the Mid-Columbia Dams*. Final Report prepared for the Public Utility Districts of Chelan, Douglas, and Grant Counties. Chelan County Public Utility District, Wenatchee, Washington.

Johnson SY, RJ Blakely, TM Brocher, RC Bucknam, PJ Haeussler, TL Pratt, AR Nelson, BL Sherrod, RE Wells, DJ Lidke, DJ Harding, and HM Kelsey (compilers). 2004. Fault number 570, Seattle fault zone, in Quaternary fault and fold database of the United States. U.S. Geological Survey website: http://gldims.cr.usgs.gov/webapps/cfusion/sites/qfault/qf_web_disp.cfm?qfault_or=1340&ims_cf_cd=cf&disp_cd=C.

Johnston AC, KJ Coppersmith, LR Kanter, and CA Cornell. 1994. *The Earthquakes of Stable Continental Regions*. EPRI TR-102261, five volumes. JF Schneider (ed.), final proprietary report for the Electric Power Research Institute, Palo Alto, California.

Kafka AL. 2007. Does seismicity delineate zones where future large earthquakes are likely to occur in intraplate environments? In: Continental Intraplate Earthquakes: Science, Hazard, and Policy Issues, S Stein & S Mazzotti (eds.), *Geological Society of America Special Paper 425*, 35−48.

Kamb B, LT Silver, MJ Abrams, BA Carter, TH Jordan, and JB Minister. 1971. "Pattern of faulting and nature of fault movement in the San Fernando earthquake." The San Fernando, California, earthquake of February 9, 1971; a preliminary report published jointly by the U.S. Geological Survey and the National Oceanic and Atmospheric Administration, Geological Survey Professional Paper 733, pp. 41–54, United States Government Printing Office, Washington, D.C.

Kaneda H, T Nakata, H Tsutsumi, H Kondo, N Sugito, Y Awata, SS Akhtar, A Majid, W Khattak, AA Awan, RS Yeats, A Hussain, M Ashraf, SG Wesnousky, and AB Kausar. 2008. Surface rupture of the 2005 Kashmir, Pakistan, earthquake and its active tectonic implications. *Bulletin of the Seismological Society of America* 98:521–557. DOI: 10.1785/0120070073.

Kao H, K Wang, R-Y Chen, I Wada, J He, and SD Malone. 2008. Identifying the rupture of the 2001 Nisqually, Washington, earthquake. *Bulletin of the Seismological Society of America* 98:1546−1558.

King GCP and G Yielding. 1984. The evolution of a thrust fault system: processes of rupture initiation, propagation and termination in the 1980 El Asnam (Algeria) earthquake. *Geophysical Journal of the Royal Astronomical Society* 77:915−933.

Kuehn SC, DG Froese, PE Carrara, FE Foit Jr., NJG Pearce, and P Rotheisler. 2009. Major- and trace-element characterization, expanded distribution, and a new chronology for the latest Pleistocene Glacier Peak tephras in western North America. *Quaternary Research* 71:201−216. DOI: 10.1016/j.yqres.2008.11.003.

Kulkarni R, I Wong, J Zachariasen, C Goldfinger, and M Lawrence. 2013. Statistical analyses of great earthquake recurrence along the Cascadia subduction zone. *Bulletin of the Seismological Society of America* 103(6):3205–3221.

Ladinsky TC. 2012. Late Quaternary Evolution of the Manastash Anticline and Manastash Range Front, Yakima Fold Belt, Washington: Influence of Tectonics and Climate. Master's thesis, Humbolt State University, Arcata, California.

Ladinsky TC and HM Kelsey. 2012. Late Quaternary Landscape Evolution and Deformation in the Forelimb Region of the Manastash Anticline, Yakima Fold Belt, Washington. U.S. Geological Survey, Reston, Virginia. Available at: http://earthquake.usgs.gov/research/external/reports/G10AC00686.pdf (June 2013).

Langston CA. 1978. The February 9, 1971 San Fernando earthquake: a study of source finiteness in teleseismic body waves. *Bulletin of the Seismological Society of America* 68:1–29.

Lewis JD, NA Daetwyler, JA Bunting, and JS Moncrieff. 1981. *The Cadoux Earthquake, 2 June 1979*. Report 11, Geological Survey of Western Australia, Department of Mines and Petroleum, East Perth, Western Australia.

Lidke DJ (compiler). 2003d. Fault Number 564a, Ahtanum Ridge Structures, Ahtanum Creek Fault. In *Quaternary Fault and Fold Database of the United States*. U.S. Geological Survey website, http://earthquake.usgs.gov/hazards/qfaults; accessed March 20, 2013.

Lidke DJ and RC Bucknam (compilers). 2002a. Fault Number 566a, Toppenish Ridge Structures, Mill Creek Fault. In *Quaternary Fault and Fold Database of the United States*. U.S. Geological Survey website, http://earthquake.usgs.gov/hazards/qfaults; accessed March 20, 2013.

Lidke DJ and RC Bucknam (compilers). 2002b. Fault Number 566b, Toppenish Ridge Structures, Folds and Other Faults of the Toppenish Ridge Uplift. In *Quaternary Fault and Fold Database of the United States*. Open-File Report 03-428, U.S. Geological Survey. Available at: http://earthquake.usgs.gov/hazards/qfaults; accessed March 20, 2013.

Lidke DJ, SY Johnson, PA McCrory, SF Personius, AR Nelson, RL Dart, LA Bradley, KM Haller, and MN Machette. 2003a. *Map and Data for Quaternary Faults and Folds in Washington State*. Open-File Report 03-428, U.S. Geological Survey. Available at: http://pubs.usgs.gov/of/2003/428/; accessed March 20, 2013.

Lin A, T Ouchi, A Chen, and T Maruyama. 2001. Co-seismic displacements, folding and shortening structures along the Chelungpu surface rupture zone occurred during the 1999 Chi-Chi (Taiwan) earthquake. *Tectonophysics* 330:225–244.

Lisiecki LE and ME Raymo. 2005. A Pliocene-Pleistocene stack of 57 globally distributed d180 records. *Paleooceanography* 20:PA1003. DOI: 10.1029/2004PA001071.

Matsuda T, H Yamazaki, T Nakata, and T Imaizumi. 1980. The surface faults associated with the Rikuu Earthquake of 1896. *Bulletin of the Earthquake Research Institute*, University of Tokyo 55:795–855.

Matthews MV, WL Ellsworth, and PA Reasenberg. 2002. A Brownian Model for Recurrent Earthquakes. *Bulletin of the Seismological Society of America* 92(6):2233–2250.

McCaffrey R, RW King, SJ Payne, and M Lancaster. 2013. Active tectonics of northwestern US inferred from GPS-derived surface velocities. *Journal of Geophysical Research*, Solid Earth 118:1−15. DOI: 10.1029/2012JB009473.

McCaffrey R, A Qamar, I King, RW Wells, R Khazardze, G Williams, CA Stevens, CW Vollick, and JJ Zwick. 2007. Fault locking, block rotation and crustal deformation in the Pacific Northwest. *Geophysical Journal International* 169:1315−1340.

McCalpin J. 1996. *Paleoseismology*. Academic Press, New York.

McCrory PA, JK Blair, DH Oppenheimer, and SR Walter. 2006. *Depth to the Juan de Fuca slab beneath the Cascadia subduction margin. A 3-D model for sorting earthquakes*. U.S. Geological Survey, Data Series 91, Version 1.2. Available at: http://pubs.usgs.gov/ds/91/.

McCrory PA, JL Blair, F Waldhauser, and DH Oppenheimer. 2012. Juan de Fuca slab geometry and its relation to Wadati-Benioff zone seismicity. *Journal of Geophysical Research: Solid Earth*, 117(B9):1978–2012.

McCrory PA, RD Hyndman, and JL Blair. 2014. Relationship between the Cascadia fore-arc mantle wedge, nonvolcanic tremor, and the downdip limit of seismogenic rupture. *Geochemistry Geophysics Geosystems* 15. DOI: 10.1002/ 2013GC005144, preview.

Miller AC and TR Rice. 1983. Discrete approximations of probability distributions. *Management Science* 29:352−362.

Montgomery SL. 2008. New exploration concepts highlight Columbia River basin's potential. *Oil and Gas Journal* 106(2):35–42.

Mori J and RE Abercrombie. 1997. Depth dependence of earthquake frequency-magnitude distributions in California: Implications for rupture initiation. *Journal of Geophysical Research: Solid Earth* (1978–2012), 102(B7):15081−15090.

Musson RMW. 2000. Evaluation of seismic hazard source models. In: JK Lapajne and R Vidrih (eds.), *Seismicity Modeling in Seismic Hazard Mapping*, pp. 53−66, Slovenian Geophysical Survey, Ljubljana.

Myers CW, SM Price, JA Caggiano, et al. 1979. *Geologic Studies of the Columbia Plateau – A Status Report*. RHO-BWI-ST-4, Rockwell Hanford Operations, Richland, Washington.

Nelson E. 2014. Spreadsheet to Convert Rake to Plunge & Trend. In *Computer Applications in Structural Geology*. Accessed at http://serc.carleton.edu/NAGTWorkshops/structure/computer_resources.html on April 14, 2014.

Newcomb RC. 1970. Tectonic Structure of the Main Part of the Columbia River Group, Washington, Oregon, and Idaho. U.S. Geological Survey Miscellaneous Geological Investigations Map I-587, scale 1:500,000, 1 sheet.

NRC (U.S. Nuclear Regulatory Commission). 1982. Safety evaluation report related to the operation of WPPSS Nuclear Project No. 2, Docket No. 50-397. NUREG-0892, Supplement No. 1, Washington, D.C.

NRC (U.S. Nuclear Regulatory Commission). 2012a. *Central and Eastern United States Seismic Source Characterization for Nuclear Facilities*. NUREG-2115, Washington, D.C.

NRC (U.S. Nuclear Regulatory Commission). 2012b. *Practical Implementation Guidelines for SSHAC Level 3 and 4 Hazard Studies*. NUREG-2117, Rev. 1, Washington, D.C.

Oskin M, J Stock, and A Martin-Barajas. 2001. Rapid localization of Pacific-North American plate motion in the Gulf of California. *Geology* 29:459−462.

Personius SF and DJ Lidke (compilers). 2003d. Fault Number 847, Arlington-Shutler Butte Fault. In *Quaternary Fault and Fold Database of the United States*. U.S. Geological Survey, http://earthquake.usgs.gov/hazards/qfaults; accessed March 20, 2013.

Personius SF and DJ Lidke (compilers). 2003c. Fault Number 579, Luna Butte Fault. In *Quaternary Fault and Fold Database of the United States*. U.S. Geological Survey, http://earthquake.usgs.gov/hazards/qfaults; accessed March 20, 2013.

Petersen MD, TE Dawson, R Chen, T Cao, CJ Wills, DP Schwartz, and AD Frankel. 2011. Fault displacement hazard for strike-slip faults. *Bulletin of the Seismological Society of America* 101(2):805−825.

Petersen MD, AD Frankel, SC Harmsen, CS Mueller, KM Haller, RL Wheeler, RL Wesson, Y Zeng, OS Boyd, DM Perkins, N Luco, EH Field, CJ Wills, and KS Rukstales. 2008. *Documentation for the 2008 Update of the United States National Seismic Hazard Maps*. USGS Open-File Report 2008-1128, U.S. Geological Survey, Reston, Virginia. Available at: http://pubs.er.usgs.gov/usgspubs/ofr/ofr081128.

Pezzopane SK. 1993. *Active Faults and Earthquake Ground Motions in Oregon*. University of Oregon, unpublished PhD dissertation, 208 p.

PNNL (Pacific Northwest National Laboratory). 2013a. Workshop Report Hanford Probabilistic Seismic Hazard Analysis Workshop 1: Hazard-Significant Issues and Available Data. PNNL-21985, Richland, Washington.

PNNL (Pacific Northwest National Laboratory). 2013b. *Workshop Report Hanford Probabilistic Seismic Hazard Analysis Workshop 2: Review of Database and Discussion of Alternative Models*. PNNL-22254, Richland, Washington.

PNNL (Pacific Northwest National Laboratory). 2014. Workshop Report Hanford Probabilistic Seismic Hazard Analysis Workshop 3: Feedback to Technical Integration Teams on Preliminary Models. PNNL-23141, Richland, Washington.

Qi W, Q Zuejun, L Qigui, J Freymueller, Y Shaomin, X Caijun, Y Yonglin, Y Xinzhao, T Kai, and C Gang. 2011. Rupture of deep faults in the 2008 Wenchuan earthquake and uplift of the Longmen Shan. *Nature Geoscience* 4:634–640. DOI: 10.1038/NGE01210.

Reidel SP. 1984. The Saddle Mountains: The evolution of an anticline in the Yakima Fold Belt. *American Journal of Science* 284(8):942–978.

Reidel SP. In Press. Geologic Map of the Iowa Flats 1:24,000 Quadrangle, Washington. U.S. Geological Survey, Olympia, Washington.

Reidel SP, NP Campbell, KR Fecht, and KA Lindsey. 1994. Late Cenozoic structure and stratigraphy of south-central Washington. In R Lasmanis and ES Cheney (eds.), Regional Geology of Washington State. *Washington Division of Geology and Earth Resources Bulletin* 80:159–180.

Reidel SP, RW Cross, and KR Fecht. 1983. "Constraints on Tectonic Models." Chapter 5 (pp. 5.1−5.19) in DOE 1983, *Preliminary Interpretation of the Tectonic Stability of the Reference Repository Location, Cold Creek Syncline, Hanford Site*. RHO-BW-ST-19P, Rockwell Hanford Operations, Richland Washington.

Reidel SP and KR Fecht (compilers). 1994. *Geologic Map of the Priest Rapids 1:100,000 Quadrangle, Washington*. Open-File Report 94-13, Division of Geology and Earth Resources, Washington State Department of Natural Resources, Olympia.

Reidel SP, KR Fecht, MC Hagood, and TL Tolan. 1989. The geologic evolution of the central Columbia Plateau. In *Volcanism and Tectonism in the Columbia River Flood-Basalt Province,* SP Reidel and PR Hooper (eds.), Special Paper 239, pp. 247–264. Geological Society of America, Boulder, Colorado.

Reidel SP, VG Johnson, and FA Spane. 2002. *Natural Gas Storage in Basalt Aquifers of the Columbia Basin, Pacific Northwest USA: A Guide to Site Characterization.* PNNL-13962, Pacific Northwest National Laboratory Richland, Washington.

Reimer PJ, E Bard, A Bayliss, JW Beck, PG Blackwell, CB Ramsey, CE Buck, H Cheng, RL Edwards, M Friedrich, PM Grootes, TP Guilderson, H Haflidason, I Hajdas, C Hatte, TJ Heaton, DL Hoffman, AG Hogg, RL Reimer, DA Richards, EM Scott, JR Southon, RA Staff, CSM Turney, and J van der Plicht. 2013. INTCAL13 and MARINE13 radiocarbon age calibration curves 0–50,000 years cal BP. *Radiocarbon* 55:1869−1887.

Repasky TR and NP Campbell. 1998. *Earthquake Hazard Study in the Vicinity of Toppenish Basin, South-Central Washington.* Technical report to U.S. Geological Survey, under Contract 1434-HQ-97-GR-03013, Department of Natural Resources, Yakama Indian Nation, Toppenish, Washington.

Repasky TR, NP Campbell, and AJ Busacca. 1998. *Earthquake Hazard Study in the Vicinity of Toppenish Basin, South-Central Washington (with Plates).* Department of Natural Resources, Yakama Indian Nation, Toppenish, Washington.

Robin TL and JD Hoover. 1982. Late Cenozoic deformation and volcanism in the Blue Mountains of central Oregon: microplate interactions? *Geology* 10:572−576.

Rogozhin EA and SN Rodina. 2012. Seismic Instruments. 48(4):333–341, © Allerton Press, Inc. Original Russian Text 2011, published in *Voprosy Ingenernoy Seismologii* 38(3):45–58.

Rubin CM, SC Lindvall, and TK Rockwell. 1998. Evidence for Large Earthquakes in Metropolitan Los Angeles. *Science* 281:398−402.

Saltus RW. 1993. Upper-crustal structure beneath the Columbia River Basalt Group, Washington: Gravity interpretation controlled by borehole and seismic studies. *Geological Society of America Bulletin* 105(9):1247−1259.

Scholz CH. 1998. Earthquakes and friction laws. *Nature* 391:37−42.

Schuster JE (compiler). 1994. Geologic map of the east half of the Toppenish 1:100,000 quadrangle, Washington. Open-File Report 94-10, 15 p., 1 pl., Division of Geology and Earth Resources, Washington State Department of Natural Resources, Olympia, Washington.

Schuster JE. 2000. Geologic map of Washington State. Washington Division of Geology and Earth Resources, Washington State Department of Natural Resources, Olympia, Washington.

Schuster JE. 2005. Geologic Map of Washington State. Geologic Map GM-35, 1:500,000 scale, Division of Geology and Earth Resources, Washington State Department of Natural Resources, Olympia, Washington.

Schuster JE, CW Gulick, SP Reidel, KR Fecht, and S Zurenko. 1997. Geologic Map of Washington – Southeast Quadrant. Geologic Map GM-45, Division of Geology and Earth Resources, Washington State Department of Natural Resources, Olympia, Washington.

Schwartz DP and KJ Coppersmith. 1984. Fault behavior and characteristic earthquakes: Examples from the Wasatch and San Andreas fault zones. *Journal of Geophysical Research* 89:5681−5698.

Shaw BE. 2009. Constant stress drop from small to great earthquakes in magnitude–area scaling. *Bulletin of the Seismological Society of America* 99(2A):871–875.

Shaw BE. 2013. Earthquake surface slip-length data is fit by constant stress drop and is useful for seismic hazard analysis. *Bulletin of the Seismological Society of America* 103(2A):876−893.

Sherrod BL, RB Blakely, JP Lasher, A Lamb, S Mahan, FF Foit Jr. and EA Barnett. In Review. Active Faulting on the Wallula Fault within the Olympic-Wallowa Lineament, Washington State, USA. *Journal of Geology*.

Shin T-C and T-L Teng. 2001. An Overview of the 1999 Chi-Chi, Taiwan, Earthquake. *Bulletin of the Seismological Society of America* 91(5):895–913.

Sibson RH and G Xie. 1998. Dip range for intracontinental reverse fault ruptures: Truth not stranger than friction? *Bulletin of the Seismological Society of America* 88(4):1014−1022.

Silverman BW. 1986. *Density Estimation for Statistics and Data Analysis*. Chapman and Hall, London, England.

Simoes M, Y-G Chen, DP Shinde, and AK Singhvi. 2014. Lateral variations in the long-term slip rate of the Chelungpu fault, Central Taiwan, from the analysis of deformed fluvial terraces. *Journal of Geophysical Research: Solid Earth* 119 (American Geophysical Union, Early View).

Stirling MW, MC Gerstenberger, NJ Litchfield, GH McVerry, WD Smith, J Pettinga, and P Barnes. 2008. Seismic hazard of the Canterbury region, New Zealand: New earthquake source model and methodology. *Bulletin of the New Zealand National Society for Earthquake Engineering* 41:51–67.

Stirling M, T Goded, K Berryman, and N Litchfield. 2013. Selection of Earthquake Scaling Relationships for Seismic-Hazard Analysis. *Bulletin of the Seismological Society of America* 103(6):2993−3011.

Stock C and EGC Smith. 2002. Adaptive kernel estimation and continuous probability representation of historical earthquake catalogs. *Bulletin of the Seismological Society of America* 92:913−922.

Suppe J and DA Medwedeff. 1990. Geometry and kinematics of fault-propagation folding. *Eclogae Geologicae Helvetiae* 83(3):409−454.

Swan FH. 1988. Temporal clustering of paleoseismic events on the Oued Fodda fault, Algeria. *Geology* 16(1092−1095).

Swanson DA, JL Anderson, RD Bentley, GR Byerly, JN Gardner, and TL Wright. 1979. Reconnaissance Geologic Maps of the Columbia River Basalt Group in Parts of Eastern Washington and Northern Idaho. U.S. Geological Survey Open-File Report 79-1363, scale 1:250,000, 12 sheets.

Swanson DA, JL Anderson, VE Camp, PR Hooper, WH Taubeneck, and TL Wright. 1981. Reconnaissance Geologic Map of the Columbia River Basalt Group, Northern Oregon and Western Idaho. U.S. Geological Survey Open-File Report 81-797, scale 1:250,000, 6 sheets.

Tanaka A. 2004. Geothermal gradient and heat flow data in and around Japan (II): Crustal thermal structure and its relationship to seismogenic layer. *Earth, Planets, and Space* 56:1195−1199.

Tanaka A and H Ito. 2002. Temperature at the base of the seismogenic zone and its relationship to the focal depth of the western Nagano Prefecture area. *Journal of the Seismological Society of Japan* 55:1−10 (in Japanese with English abstract).

Thorne PD, AC Rohay, and SP Reidel. 2014. *Development of a Basin Geologic and Seismic Property Model Used to Support Basin-Effects Modeling for the Hanford Probabilistic Seismic Hazards Analysis*. PNNL-23305, Pacific Northwest National Laboratory, Richland, Washington.

Tiampo KF, W Klein, H-C Li, A Mgnan, T Toya, SZL Kohen-Kadosh, JB Rundle, and C-C Chen. 2010. Ergodicity and Earthquake Catalogs: Forecast Testing and Resulting Implications. *Pure and Applied Geophysics* 167:763–782.

Tolan TL and SP Reidel (compilers). 1989. Structure map of a portion of the Columbia River flood-basalt province. In *Volcanism and Tectonism in the Columbia River Flood-Basalt Province*, SP Reidel and PR Hooper (eds.), Special Paper 239, plate bound inside back cover. Geological Society of America, Boulder, Colorado.

Tsutsumi H and RS Yeats. 1999. Tectonic setting of the 1971 Sylmar and 1994 Northridge earthquakes in the San Fernando Valley, California. *Bulletin of the Seismological Society of America* 89(5):1232−1249.

USACE (U.S. Army Corps of Engineers). 1983. *The Dalles and John Day Lakes earthquake and fault study—Design memorandum 26*. 19 plates, U.S. Army Corps of Engineers, Portland District, Portland Oregon.

USGS (U.S. Geological Survey). 1971. The San Fernando, California, earthquake of February 9, 1971. A preliminary report published jointly by the U.S. Geological Survey and the National Oceanic and Atmospheric Administration, USGS Professional Paper 733. United States Government Printing Office, Washington, D.C.

Wada I, S Mazzotti, and K Wang. 2010. Intraslab stresses in the Cascadia subduction zone from inversion of earthquake focal mechanisms. *Bulletin of the Seismological Society of America*. 100(5A):2002–2013.

Waitt RB. 1979. Late Cenozoic deposits, landforms, stratigraphy and tectonism in Kittitas Valley, Washington. U.S. Geological Survey Professional Paper 1127:18. U.S. Government Printing Office, Washington, D.C. Available at: http://pubs.er.usgs.gov/publication/pp1127.

Walsh TJ (compiler). 1986. Geologic map of the west half of the Yakima quadrangle, Washington. Open-File Report 86-4, 1 sheet, scale 1:100,000, with 9 p. text, Division of Geology and Earth Resources, Washington State Department of Natural Resources, Olympia, Washington.

Walsh TJ (compiler). 1986. Geologic map of the west half of the Toppenish quadrangle, Washington. Open-File Report 86-3, 1 sheet, scale 1:100,000, with 7 p. text, Division of Geology and Earth Resources, Washington State Department of Natural Resources, Olympia, Washington.

WCC (Woodward-Clyde Consultants). 1980a. *Seismic Attenuation Study for the Walla-Walla Basin, Washington*. Prepared for Department of the Army, Seattle District, Corps of Engineers, Seattle Washington, by WCC, San Francisco, California

WCC (Woodward-Clyde Consultants). 1980b. *Seismological Review of the July 16, 1936 Milton-Freewater Earthquake Source Region*. Prepared for the Washington Public Power Supply System, Richland, Washington, by WCC San Francisco, California.

WCC (Woodward-Clyde Consultants). 1981a. *Logs of Trenches at Finley Quarry*. Prepared for Washington Public Power Supply System under the direction of United Engineers & Constructors, Inc. by WCC, San Francisco, California.

WCC (Woodward-Clyde Consultants). 1981b. *Task D3 Quaternary Sediments Study of the Pasco Basin and Adjacent Areas*. Prepared for the Washington Public Power Supply System, Richland, Washington by WCC, San Francisco, California.

WCC (Woodward-Clyde Consultants). 1981c. *Task D5 Toppenish Ridge Study*. Prepared for the Washington Public Power Supply System, by WCC, San Francisco, California

Wech AG and KC Creager. 2008. Automatic detection and location of Cascadia tremor. *Geophysical Research Letters* 35, L20302 (Published Online).

Weichert DH. 1980. Estimation of the earthquake recurrence parameters for unequal observation periods for different magnitudes. *Bulletin of the Seismological Society of America* 70(4):1337−1346.

Wells DL and KJ Coppersmith. 1994. New empirical relationships among magnitude, rupture length, rupture width, rupture area, and surface displacement. *Bulletin of the Seismological Society of America* 84(4):974−1002.

Wells RE and R McCaffrey. 2013. Steady rotation of the Cascade arc. *Geology* 41:1027−1030. DOI: 10.1130/G34514.1.

Wesnousky SG. 1986. Earthquakes, Quaternary faults, and seismic hazard in California. *Journal Geophysical Research* 91:12587−12631.

Wesnousky SG. 2008. Displacement and geometrical characteristics of earthquake surface ruptures—Issues and implications for seismic-hazard analysis and the process of earthquake rupture. *Bulletin of the Seismological Society of America* 98:1609–1632.

WGCEP (Working Group on California Earthquake Probabilities). 2003. *Earthquake probabilities in the San Francisco Bay region*: 2002–2031. U.S. Geological Survey Open-File Report 03-214.

Witter RC, Y Zhang, K Wang, C Goldfinger, GR Priest, and JC Allan. 2012. Coseismic slip on the southern Cascadia megathrust implied by tsunami deposits in an Oregon lake and earthquake-triggered marine turbidities. *Journal of Geophysical Research* 117, B10303.

WLA (William Lettis & Associates, Inc.). 2000. *Down-Dip Geometry of Blind Thrust Faults Beneath the Syrian Arc Fold Belt*. Basic Data Report No. 20, Shivta-Rogem Site Investigation, prepared for the Israel Electric Corporation, Ltd. Walnut Creek, California.

Wong IG. 2005. Low potential for large intraslab earthquakes in the central Cascadia subduction zone. *Bulletin of the Seismological Society of America* 95(5):1880–1902.

Wooddell KE and NA Abrahamson. 2013. Constraints on magnitude-frequency distributions for evaluating the hazard of multi-segment ruptures. *Seismological Research Letters* 84(2):364.

Wooddell KE, NA Abrahamson, AL Acevedo-Cabrera, and RR Youngs. 2014. Hazard implementation of simplified seismic source characterization allowing for linked faults. *Seismological Research Letters* 85(2):471.

Wu WN, L Zhao, and YM Wu. 2013. Empirical relationships between aftershock zone dimensions and moment magnitudes for plate boundary earthquakes in Taiwan. *Bulletin of the Seismological Society of America* 103(1):424−436.

Wyss M. 1971. Preliminary Source Parameter Determination of the San Fernando Earthquake, the San Fernando, California, Earthquake of February 9, 1971. U.S. Geological Survey Professional Paper, 733, pp. 38−40, U.S. Government Printing Office, Washington, D.C.

Xu C, Y Liu, Y Wen, and R Wang. 2010. Coseismic slip distribution of the 2008 Mw 7.9 Wenchuan earthquake from joint inversion of GPS and InSAR data. *Bulletin of the Seismological Society of America* 100:2736–2749. DOI: 10.1785/0120090253.

Yen Y-T and K-F Ma. 2011. Source-scaling relationship for M 4.6–8.1 earthquakes, specifically for earthquakes in the collision zone of Taiwan. *Bulletin of the Seismological Society of America* 101(2):464–481.

Yielding G, JA Jackson, GCP King, H Sinvhal, C Vita-Finzi, and RM Wood. 1981. Relations between surface deformation, fault geometry, seismicity, and rupture characteristics during the El Asnam (Algeria) earthquake of 10 October 1980. *Earth and Planetary Science Letters* 56:287–304.

Yielding G, M Ouyed, GCP King, and D Hatzfeld. 1989. Active tectonics of the Algerian Atlas Mountains-evidence from aftershocks of the 1980 El Asnam earthquake. *Geophysical Journal International* 99:761−788.

Youngs RR and KJ Coppersmith. 1985. Implications of fault slip rates and earthquake recurrence models to probabilistic seismic hazard estimates. *Bulletin of the Seismological Society of America* 75(4):939−964.

Youngs RR, KJ Coppersmith, CL Taylor, MS Power, LA DiSilvestro, ML Angell, NT Hall, JR Wesling, and L Mualchin. 1992. A comprehensive seismic hazard model for the San Francisco Bay region. In: *Proceedings of the Second Conference on Earthquake Hazards in the Eastern San Francisco Bay Area*, G Borchardt, SE Hirschfeld, JJ Lienkaemper, P McClellan, PL Williams, and IG Wong (eds.), Special Publication 113, pp. 431−441, California Department of Conservation, Division of Mines and Geology, Sacramento, California.

Yu G, X Xu, Y Klinger, G Diao, G Chen, X Feng, C Li, A Zhu, R Yuan, T Guo, X Sun, X Tan, and Y An. 2010. Fault-scarp features and cascading-rupture model for the Mw 7.9 Wenchuan earthquake, eastern Tibetan Plateau, China. *Bulletin of the Seismological Society of America* 100: 2590–2614. DOI: 10.1785/0120090255.

Zeng Y and CH Chen. 2001. Fault rupture process of the 20 September 1999 Chi-Chi, Taiwan earthquake. *Bulletin of the Seismological Society of America* 91:1088–1098.

Zoback ML, RE Anderson, and GA Thompson. 1981. Cainozoic evolution of the state of stress and style of tectonism of the Basin and Range province of the western United States. *Royal Society of London Philosophical Transactions* A300:407−434.